

Electronic Thesis and Dissertation Repository

7-14-2021 3:00 PM

Development of Multifunctional Drug Delivery Systems for Locoregional Therapy

Xinyi Li, *The University of Western Ontario*

Supervisor: Wan, Wankei, *The University of Western Ontario*

A thesis submitted in partial fulfillment of the requirements for the Doctor of Philosophy degree
in Biomedical Engineering

© Xinyi Li 2021

Follow this and additional works at: <https://ir.lib.uwo.ca/etd>



Part of the [Biomaterials Commons](#)

Recommended Citation

Li, Xinyi, "Development of Multifunctional Drug Delivery Systems for Locoregional Therapy" (2021).
Electronic Thesis and Dissertation Repository. 7944.
<https://ir.lib.uwo.ca/etd/7944>

This Dissertation/Thesis is brought to you for free and open access by Scholarship@Western. It has been accepted for inclusion in Electronic Thesis and Dissertation Repository by an authorized administrator of Scholarship@Western. For more information, please contact wlsadmin@uwo.ca.

Abstract

Locoregional treatment is the specific delivery of therapeutics to their desired sites of action with minimized systemic adverse effects. In this approach, drug is administered through topical instillation, inhalation, intra-lesional or intra-arterial injection. Decades of experience in locoregional treatment have delivered meaningful benefits to patients with localized diseases (e.g., osteoarthritis, ocular disorders and liver cancers). However, improvements are required for this type of treatment to be more effective. For transarterial chemoembolization (TACE) therapy of hepatocellular carcinoma (HCC), the most current approaches do not allow repeat treatment as the drug delivery vehicle is not degradable. In addition, image contrast agents for visualization are administered separately, leading to uncertainty of the drug location.

In this thesis, the concept of a multifunctional ‘nano-on-micro’ delivery system was explored for enhanced TACE therapy. Magnetic hydrogels composed of poly(vinyl alcohol) (PVA) and iron oxide nanoparticles (IONPs) were prepared and shaped into microparticles using microfluidics. This system was able to deliver the anti-cancer drug, doxorubicin (DOX), with co-localized IONPs as a contrast agent to visualize drug location. Degradability of the PVA hydrogel carrier allows for repeat treatment. To enhance drug loading, we explored the use of silica nanoparticles (SiNPs) as an effective drug carrier. Loading was investigated using lysozyme as a model protein and applied to N-94, a therapeutic peptide for dry eye treatment. The results demonstrated SiNPs system could provide controlled drug release that is also degradable under simulated physiological conditions. Building on these results, silica (SiO₂) was introduced to prepare PVA-SiO₂-IONP microparticles. In addition to all the positive attributes of the original system, the PVA-SiO₂-IONP microbeads have increased drug loading and tunable release profile.

The concept of a multifunctional ‘nano-on-micro’ delivery system demonstrated for TACE therapy can be applied to other diseases where locoregional treatment is applicable.

Keywords

Multifunctional delivery system, locoregional therapy, transarterial chemoembolization, dry eye disease, drug eluting beads, nanoparticle, microparticle, hydrogel, nano-in-micro, microfluidics, embolization, magnetic targeting, magnetic resonance imaging, drug delivery, controlled release, degradation

Summary for Lay Audience

Locoregional therapy is a treatment strategy where therapeutics are delivered to sites of the diseases via topical instillation, inhalation or injection. This approach can potentially minimize the involvements of invasive surgery and systemic side effects. Transarterial chemoembolization (TACE) is a locoregional therapy that is used in the treatment of hepatocellular carcinoma (HCC), which is commonly known as liver cancer. Microbeads are used to block tumor blood vessels and to deliver therapeutic drugs to the tumor site. Most of the beads currently used cannot be removed after the anti-cancer drug is delivered, so repeat treatment would not be possible. Also, to determine the location of the beads, imaging contrast agents have to be injected separately to the proximity of beads' delivery site. This causes uncertainty as to the exact location of the treatment site.

For TACE therapy, we developed a poly(vinyl alcohol) (PVA) hydrogel-based multifunctional delivery system containing iron oxide nanoparticles (IONPs) and silica (SiO₂) particles that can deliver the drug and the image contrast agent within the same package. This allows the drug to be delivered effectively. In addition, the microparticles can be monitored via imaging more precisely. The delivery system is also degradable, which would allow repeat treatment at the same tumor site. These improvements would lead to enhanced treatment and better outcomes for the patients.

The concept of a multifunctional delivery system demonstrated for TACE therapy can be applied to other diseases where locoregional treatment is applicable.

Co-Authorship Statement

Chapter 1 and **Chapter 2** were written by Xinyi Li and edited by Dr. Wankei Wan.

Chapter 3: Experiments were carried out mainly by Xinyi Li. The high-speed camera images of the microfluidic fabrication were captured by Dawn Bannerman. The MRI images of the microparticles were provided by Dr. Ali Khan's lab. The manuscript was prepared by Xinyi Li and reviewed by Dr. Wankei Wan.

The research work in this chapter will be submitted to *Polymers* under the title: Development of multifunctional poly(vinyl alcohol) hydrogel microparticles for transarterial chemoembolization therapy. Xinyi Li is the first author.

Chapter 4: Xinyi Li developed the protocol for the preparation of SiNPs and SiNP-protein conjugates. Experiments on lysozyme were conducted by Xinyi Li. Experimental work on N-94 peptide and cell study was performed by Angela Chang in Dr. Cindy Hutnik's lab. This work was co-supervised by Dr. Wankei Wan and Dr. Cindy Hutnik. Xinyi Li and Angela Chang contributed equally to the manuscript.

A version of this chapter will be submitted to *Clinical & Experimental Ophthalmology* under the title: Lacritin peptide (N-94)-conjugated solid silica nanoparticles as a novel drug delivery system for dry eye disease. Xinyi Li shares the co-first authorship with Angela Chang.

Chapter 5: This chapter contains a research work that is complete. Experiments were performed by Xinyi Li under the supervision of Dr. Wankei Wan. This chapter was written by Xinyi Li and reviewed by Dr. Wankei Wan.

A paper under the title: Microfluidic fabrication of drug-eluting composite hydrogel microparticles is in the preparation stage. Xinyi Li will be the first author.

Chapter 6: This chapter was prepared by Xinyi Li and modified by Dr. Wankei Wan.

Acknowledgments

I want to start by thanking my supervisor Dr. Wan, for his guidance and support over the past years. Back in 2014, I came to Western University as a fourth-year student, excited and scared. I still vividly remember the days you were the instructor for several courses I was taking. You told me to step out the comfort zone and challenge myself, which were engraved in my heart, and encouraged me to push the boundaries and explore the unknown. Thank you for taking me as your student, this Ph.D. journey really shaped me into a better researcher.

My sincere thanks also go to my advisory committee members, Dr. Ali Khan, Dr. Elizabeth Gillies, Dr. Saman Maleki for providing insights and suggestions for my projects.

I would like to extend my appreciation towards Tim Goldhawk, Todd Simpson, Karen Nygard, Reza Khazae and Dr. Richard Gardiner for teaching and assisting me with the TEM and SEM. I am also grateful to Angela Chang and Hong Liu at Dr. Hutnik's lab for their collaboration on the bioactive protein project.

I would also like to express my gratitude to my colleagues Helium Mak and Betty Li. Thanks for providing advice on my projects, training me on a wide range of techniques and helping me both in the lab and daily life. I would also like to thank my friends Ruolan Fan, Xiao Li, Mengxing Lin, Xiaoyi Pan, Xuelian Xing, Yujie Zhang, Vincent Kong, Dong Zhang, Zhehao Jing, Jiangtian Li, Olivia Tong and Neda Aslankoochi for be willing to comfort me, support me and tolerate my unending complaints. I would also like to thank Aishik Chakraborty, Yasmeen Shamiya and Shruthi Polla Ravi, thanks for the company in the late stage of my Ph.D. journey. I have never felt such close to anyone, thank you everyone for opening my heart and making me someone important.

My special thanks go to Longyi Chen, for showing me persistence and courage. I have no doubt that you will be a good researcher, and I wish you a bright future in academia. My sincere thanks also go to Hui Wang. Thank you for teaching me care and patience. I will never forget all the happy and depressing days we have spent together. I couldn't imagine what my life would be if you were not here.

Last but not least, I want to give my biggest thanks to my parents. Thank you, mom and dad, for bringing me to this beautiful world. Having your unconditional love and support with me, I had the chance to meet so many amazing people, learnt plenty of invaluable knowledge and skills, and created uncountable wonderful memories.

Thank you to anyone who has ever shown up in my life. Thank you for helping me get to where I am today. My life would be so much less joyful without you!

Table of Contents

Abstract.....	ii
Summary for Lay Audience.....	iii
Co-Authorship Statement.....	iv
Acknowledgments.....	v
Table of Contents.....	vii
List of Tables.....	xiii
List of Figures.....	xiv
List of Abbreviations.....	xix
Chapter 1.....	1
1 Introduction.....	1
1.1 Background and Motivation.....	1
1.2 Objectives.....	4
1.3 Thesis Structure.....	5
1.4 References.....	7
Chapter 2.....	10
2 Literature Review.....	10
2.1 Hepatocellular Carcinoma and Transarterial Chemoembolization.....	10
2.2 Dry Eye Disease and Treatments.....	13
2.3 Chemotherapeutic Agents.....	16
2.4 Drug-eluting Microparticles and Commercial Products.....	17
2.5 Design Criteria for Drug-eluting Microparticles.....	19
2.5.1 Shape.....	20
2.5.2 Size and Size Distribution.....	21
2.5.3 Imageability/Detectability.....	21

2.5.4	Targetability	22
2.5.5	Controlled Release	24
2.5.6	Degradability.....	25
2.5.7	Delivery of Multiple Therapeutics	26
2.6	Design of Multifunctional Materials for Drug Delivery.....	26
2.7	Choice of Materials and Proposed Systems.....	30
2.7.1	Poly(vinyl alcohol).....	30
2.7.2	Iron Oxide Nanoparticles	33
2.7.3	Silica Particles.....	38
2.7.4	Proposed Systems	41
2.8	System Assembly using Microfluidics	43
2.8.1	Materials and Fabrication Techniques for Microfluidic Chips.....	43
2.8.2	Droplets Generation Mechanisms	45
2.8.3	Geometrical Design of Microchannels	47
2.8.4	Droplet Microfluidics in Drug Delivery	48
2.9	Clinical Applications and Future Translational Opportunities	50
2.10	References.....	51
Chapter 3	78
3	Development of Multifunctional PVA-IONP Microparticles for TACE.....	78
3.1	Introduction.....	78
3.2	Materials and Methods.....	80
3.2.1	Materials	80
3.2.2	Assembly of the Microfluidic Device.....	80
3.2.3	Preparation of Dispersed Phase	81
3.2.4	Microfluidic Fabrication of Microparticles	81
3.2.5	Microscopy Observation.....	81

3.2.6	Magnetic Properties	82
3.2.7	MR Contrast Effect	83
3.2.8	<i>In vitro</i> Degradation Measurements.....	83
3.2.9	Loading and <i>in vitro</i> Release of DOX	83
3.2.10	Statistical Analysis	84
3.3	Results.....	85
3.3.1	Droplets Generation and Size Analysis	85
3.3.2	Morphological, Elemental and Structural Features of Microparticles	86
3.3.3	Magnetic Properties	88
3.3.4	MR Contrast Effect.....	89
3.3.5	<i>In vitro</i> Degradation	90
3.3.6	DOX Loading and <i>in vitro</i> Release.....	92
3.4	Discussion.....	93
3.4.1	Fabrication of PVA-IONP Microparticles	93
3.4.2	Morphological, Elemental and Structural Features of Microparticles	94
3.4.3	Magnetic Properties	95
3.4.4	MR Contrast Effect.....	96
3.4.5	<i>In vitro</i> Degradation	96
3.4.6	DOX Loading and <i>in vitro</i> Release.....	97
3.5	Conclusion	98
3.6	References.....	98
Chapter 4	105
4	Development of a Multifunctional Bioactive Protein/Peptide Delivery System for Dry Eye Disease	105
4.1	Introduction.....	105
4.2	Materials and Methods.....	107

4.2.1	Materials	107
4.2.2	Preparation and Characterization of Protein/Peptide-SiNPs Conjugates	108
4.2.3	Protein Adsorption Kinetics and Isotherms	108
4.2.4	Protein/Peptide Release in the Absence of Cells	109
4.2.5	Dissolution of SiNPs in the Absence of Cells	110
4.2.6	Cell Culture	110
4.2.7	Determination of Optimal Pro-inflammatory Cytokines IFN γ & TNF Concentration	110
4.2.8	Effects of N-94 on HCECs	111
4.2.9	Effect of N-94-SiNPs on HCECs.....	111
4.2.10	Statistics	112
4.3	Results.....	113
4.3.1	Preparation and Characterization of Protein/Peptide-SiNPs Conjugates	113
4.3.2	Adsorption Kinetics and Isotherms.....	114
4.3.3	Protein/Peptide Release in the Absence of Cells	116
4.3.4	Dissolution of SiNPs in the Absence of Cells	118
4.3.5	Toxicity of N-94 to HCECs	118
4.3.6	Cytoprotective Effects of N-94 to HCECs.....	119
4.3.7	Toxicity of N-94-SiNPs to HCECs.....	121
4.3.8	Cytoprotective Effect of Released N-94 on Stressed HCECs	122
4.4	Discussion	123
4.5	Conclusions.....	126
4.6	References.....	126
Chapter 5.....		132
5	Development of Multifunctional PVA-SiO $_2$ -IONP Microparticles for TACE.....	132
5.1	Introduction.....	132

5.2	Materials and Methods.....	135
5.2.1	Materials	135
5.2.2	Preparation of PVA Solution	135
5.2.3	Preparation of Iron Chloride Solution.....	136
5.2.4	Preparation of PVA-SiO ₂ -Fe (II, III) Gel	136
5.2.5	Fabrication of the Flow-focusing Microfluidic Device	136
5.2.6	Fabrication of PVA-SiO ₂ -IONP Microparticles	136
5.2.7	Drug Concentration Effect on DOX loading	137
5.2.8	<i>In vitro</i> Release of DOX	138
5.2.9	Degradation of PVA-SiO ₂ -IONP Microparticles.....	138
5.2.10	Size Analysis.....	138
5.2.11	Scanning Electron Microscopy (SEM)/Energy-Dispersive X-ray (EDX)	139
5.2.12	Transmission Electron Microscopy (TEM)	139
5.2.13	Fourier Transform Infrared Spectroscopy (FTIR)	139
5.2.14	Vibrating Sample Magnetometry (VSM)	139
5.2.15	Statistical Analysis.....	139
5.3	Results.....	140
5.3.1	Microfluidic Fabrication of Size-tunable PVA-SiO ₂ -IONP Microparticles	140
5.3.2	Characterization of PVA-SiO ₂ -IONP Microparticles	141
5.3.3	Drug Concentration Effect on DOX Loading	144
5.3.4	<i>In vitro</i> Release of DOX	144
5.3.5	Degradation of Microparticles	145
5.4	Discussion.....	146
5.4.1	Microfluidic Fabrication of Size-tunable PVA-SiO ₂ -IONP Microparticles	146

5.4.2	Characterization of PVA-SiO ₂ -IONP Microparticles	148
5.4.3	Drug Concentration Effect on DOX Loading	150
5.4.4	<i>In vitro</i> Release of DOX	151
5.4.5	Degradation of Microparticles	152
5.5	Conclusion	152
5.6	References.....	153
Chapter 6	160
6	Conclusion and Recommendations	160
6.1	Summary and Conclusion	160
6.2	Significance of Research.....	162
6.3	Future Studies	163
6.4	References.....	165
Appendices	166
Curriculum Vitae	172

List of Tables

Table 2.1 Barcelona Clinic Liver Cancer (BCLC) staging system with treatment recommendations. Adapted from reference [6].	10
Table 2.2 Roles of TACE in the management of HCC.....	11
Table 2.3 Summary of commonly used cytotoxic anticancer drugs for TACE.	17
Table 2.4 Overview of commercially available DEBs.	18
Table 2.5 Overview of the degradable drug-eluting microparticles.	25
Table 2.6 Comparison of current DEBs with multifunctional microparticles.	51
Table 5.1 Drug concentration effect on DOX loading.....	144

List of Figures

Figure 1.1 Schematic of the interrelationship of the research work described in Chapter 3-5.	5
Figure 2.1 Schematic demonstration of TACE. Figure reprinted with permission from [18].	12
Figure 2.2 Design and processing of a multifunctional hydrogel system for biomedical applications.	28
Figure 2.3 Schematic of ferrogel preparation. (A) The blending method. (B) The <i>in situ</i> precipitation method. (C) The grafting-onto method.	37
Figure 2.4 Schematic drawing of a multifunctional PVA-IONP microparticle.	41
Figure 2.5 Schematic drawing of the bioactive protein delivery system.	42
Figure 2.6 Schematic drawing of a multifunctional PVA-SiO ₂ -IONP microparticle.	43
Figure 2.7 Schematic illustration of different channel geometries of a microfluidic device. (A) Co-flow; (B) T-junction; and (C) flow-focusing. Solid arrows indicate the flow direction.	48
Figure 3.1 Fabrication of PVA-IONP microbeads using a flow-focusing microfluidic channel. The red arrow indicates flow of the dispersed phase, the blue arrow indicates flow of the continuous phase, and the black arrow indicates the generated microbeads. Droplets were successfully fabricated using a flow-focusing microfluidic device.	85
Figure 3.2 (A) Optical microcopy image of fabricated PVA-IONP microbeads and (B) histogram of microbead equivalent spherical diameter fit to a Gaussian distribution. Microbeads were in a teardrop shape with a relatively narrow size distribution.	86
Figure 3.3 (A)-(C) SEM images of PVA-IONP microbeads. (A) displays a whole bead, (B) and (C) show surface morphology. (D) Whole microbead with a square specifying the location of EDX sampling. (E) EDX spectrum indicating the presence of iron in the PVA-IONP microbeads.	87

Figure 3.4 (A) TEM micrograph of PVA-IONP microbeads. The black arrow indicates an individual iron oxide nanoparticle, the red arrow indicates a polymer-rich region, and the blue arrow indicates a polymer-poor region. (B) Histogram of diameter of dispersed IONPs fit to a Gaussian distribution. IONPs were in spherical shape with minimum aggregation. IONPs were observed to distribute at the interface of polymer-rich and polymer-poor regions. 88

Figure 3.5 (A) Magnetic responsiveness of PVA-IONP microbeads upon introducing of a permanent magnet close to the sample. The microparticles were attracted by the magnet and would completely settle down due to gravity after the magnet was removed. (B) Magnetic susceptibility of the microbeads. The absence of a hysteresis loop indicates a superparamagnetic behavior of the PVA-IONP microbeads. The saturation magnetization M_s of the microbeads was measured to be 9.36 emu/g. 89

Figure 3.6 T_2 -weighted MRI images of microbeads at different quantities (3T, repetition time 350 ms, echo-time 3.5-15 ms). The white arrow indicates the presence of PVA-IONP microbeads and their contrast effect on T_2 -weighted images. 89

Figure 3.7 Degradation of the PVA-IONP beads. (A) Cumulative iron released from the microbeads. (B) and (C) are optical images of beads at day 0 and day 30, respectively. (D) SEM micrograph of beads at day 30. Degradation study was performed in DMEM at pH 5.5, 7.4 and 37 °C. More than 20% of total iron was released in 5 weeks for both conditions. The removal of IONPs can be further visualized through the color change of the microparticles. The PVA-IONP microparticles lost the original teardrop shape during the incubation. The release of IONPs and disintegration of the polymeric matrix indicate the degradation of the microbeads. 91

Figure 3.8 Profiles of cumulative percent doxorubicin release with time from PVA-IONP beads in PBS at pH 7.4, 5.5 and 37 °C. The DOX loading was 0.49 ± 0.02 mg/mL with a loading efficiency of $48.8 \pm 2.5\%$. Microparticles can provide a controlled release for DOX for 7 days. Acidic environment contributes to a faster and greater DOX release. 92

Figure 4.1 SEM of SiNPs used in (A) lysozyme and (B) N-94 study. Insert is the particle size distribution. 113

Figure 4.2 (A) SEM of lysozyme-loaded SiNPs. The red arrow indicates the presence of lysozyme. Insert: FTIR spectrum of SiNPs, lysozyme powder and lysozyme-SiNPs. The red arrow indicates the characteristic bands of proteins, and the black arrow indicates the characteristic bands of silica. (B) SEM of N-94-loaded SiNPs. The SEM micrographs and FTIR spectrum confirm the loading of lysozyme and N-94 onto the SiNPs surface. 114

Figure 4.3 (A) Adsorption kinetics and (B) isotherm at 296 K. Error bars for some data points are too small to be displayed. The black square shows the experimental data, and the red dash curve shows the best-fit curve. Kinetic data is fit with pseudo-second order kinetic ($R^2 > 0.99$). Isotherm data fits well with the Langmuir isotherm ($R^2 = 0.94$). 116

Figure 4.4 (A) Lysozyme release from SiNPs in PBS at pH 7.4 and 37 °C in the absence of cells. Lysozyme loading (i.e., M_∞) was 21.74 ± 2.32 mg/g. (B) N-94 release from SiNPs, N-94 loading (i.e., M_∞) was 44.94 ± 0.42 mg/g. SiNPs can provide controlled release for both lysozyme and N-94 over the course of 8 hours. Representative spectra of various masses (m/z or Da) of lacritin peptide (N-94) (C) prior to its conjugation to SiNPs, and (D) after release from SiNPs. The conjugation to SiNPs and release do not affect peptide integrity. 117

Figure 4.5 SEM images of SiNPs with an increasing immersion time in PBS, (A) $t=0$, (B) $t=10$ days, and (C) $t=30$ days. (D) Size variation of SiNPs after immersion in PBS for 0, 10, and 30 days. Each value is presented as mean \pm SD. Based on the one-way ANOVA test, size of SiNPs significantly decreased with a prolonged immersion time (*, $P < 0.05$), indicating the degradation of the nanoparticles. 118

Figure 4.6 Mean cellular metabolic activity (% relative to vehicle control \pm SD) of primary human corneal epithelial cells obtained from three donors (N=3) following treatment of lacritin peptide (N-94) (1, 10, 100, 1000, 10 000 nM). Vehicle control (dotted line, 100%) was cell culture medium treatment only. MTT assays were performed after 1, 2, 6, and 24-hour treatment durations. There were no significant differences in cellular metabolic activity between the varying concentrations and durations of N-94 treatment, including vehicle control. 119

Figure 4.7 . Mean cellular metabolic activity (% relative to vehicle control \pm SD) of primary human corneal epithelial cells obtained from three donors (N=3) following (A) insult by 100 U/mL of IFN γ and varying concentrations of TNF (0, 6.25, 12.5, 25, 50, 100 ng/mL) and (B) co-treatment of lacritin peptide (N-94) (0, 1, 10, 100, 1000, 10 000 nM) along with insult by 100 U/mL IFN γ and 12.5 ng/mL TNF. In both, vehicle control (dotted line, 100%) was cell culture medium treatment only. MTT assays were performed after 16- and 20-hour treatment durations. *, **, and *** indicate statistical significance versus insult only. ***, $P < 0.001$; **, $P < 0.01$; *, $P < 0.05$ 120

Figure 4.8 (A) Mean cellular metabolic activity (% relative to vehicle control \pm SD) and (B) mean lactate dehydrogenase (LDH) release (% relative to vehicle control \pm SD) of primary human corneal epithelial cells obtained from three donors (N=3) following treatment of lacritin peptide-conjugated silica nanoparticles (N-94-SiNPs) (1, 10, 100, 1000 nM). There was a vehicle control (dotted line, 100%) of phosphate-buffered saline and cell culture medium treatment only and a group of bare SiNP treatment only. MTT and LDH assays were performed after 16- and 20-hour treatment durations. There were no significant differences in cellular metabolic activity and LDH release between the various treatments and vehicle control at either time point. 121

Figure 4.9 (A) Mean cellular metabolic activity (% relative to vehicle control \pm SD) and (B) mean lactate dehydrogenase (LDH) release (% relative to vehicle control \pm SD) of primary human corneal epithelial cells obtained from three donors (N=3) following co-treatment of lacritin peptide (N-94) (0, 1, 10, 100, 1000 nM) released from silica nanoparticles along with 100 U/mL IFN γ and 12.5 ng/mL TNF. Vehicle control (dotted line, 100%) was phosphate-buffered saline and cell culture medium treatment only. MTT and LDH assays were performed after 16- and 20-hour treatment durations. *, **, and *** indicate statistical significance versus insult only. ***, $P < 0.001$; **, $P < 0.01$; *, $P < 0.05$ 122

Figure 5.1 Schematic illustration for the preparation of PVA-SiO $_2$ -IONP microparticles... 135

Figure 5.2 Relationship between particle diameter and flow rates. (A) Diameter as a function of dispersed phase, $Q_c=20$ mL/h, $Q_d=1-9$ mL/h. (B) Diameter as a function of continuous phase, $Q_d=1$ mL/h, 3 mL/h, $Q_c=5-45$ mL/h. (C)-(E): Optical microscope images and size distributions of microbeads fabricated under different flow rate conditions. For a fixed $Q_c=20$

mL/h, the particle size decreased first and then increased as the Q_d increased. At a fixed Q_d , the particle size decreased with an increased Q_c 140

Figure 5.3 (A) and (B): surface morphology of microparticles ($Q_d=3$ mL/h, $Q_c=20$ mL/h). (C) and (D): EDX spectrum of microparticles with a square indicating the area of analysis. (E) is the EDX elemental mapping of the entire sample in (C). The EDX analysis confirmed the presence of iron and silica content in the PVA-SiO₂-IONP microparticles. 141

Figure 5.4 TEM images of (A) silica sol and (B) PVA-SiO₂-IONP microbeads. Acid-catalyzed sol-gel process contributed to spherical silica microparticles with a diameter of $1.3 \pm 0.5 \mu\text{m}$. IONPs were 2.3 ± 0.8 nm in diameter and were well-dispersed in the microbeads. Due to the large variance of the dimension of silica microparticles and IONPs, individual silica microparticle cannot be displayed in (B) with IONPs..... 142

Figure 5.5 FTIR spectra of neat PVA, PVA-SiO₂ gel, and PVA-SiO₂-IONP microbeads. The emergence of C-O-Si peak and reduction of O-H peak indicates the condensation reaction between -OH groups of PVA and surface silanols of silica..... 143

Figure 5.6 Magnetization curve of PVA-SiO₂-IONP microparticles. The microparticles exhibited paramagnetic behavior. (B) Microparticles dispersed in PBS attracted by a permanent magnet. 144

Figure 5.7 *In vitro* drug release from DOX-loaded PVA-SiO₂-IONP microparticles: (A)-(C) effect of release conditions on DOX release; (B) effect of drug loading on DOX release. Within the same DOX loading subgroup, the release rate increased with a higher ionic concentration in buffer or a lower pH value. At the same buffer condition, microparticles with a higher DOX loading contributed to a slower and lower percentage of release. 145

Figure 5.8 SEM images of the PVA-SiO₂-IONP microparticles at two buffer conditions. Pictures were obtained after 0, 14, 35 and 56 days' immersion in the corresponding buffer. Error bar: 20 μm , except for day 14 PBS (error bar 100 μm). The degradation of microparticles at both buffer conditions was evidenced by the morphological change during the test period..... 146

Figure 6.1 Schematic of the research work described in Chapter 3-5. 160

List of Abbreviations

AAm	Acrylamide
AAS	Atomic absorption spectroscopy
ACM	Acetylated chitosan microspheres
AMF	Alternating magnetic field
ANOVA	Analysis of variance
APAP	Acetaminophen
APBA	3-aminophenylboronic acid
BCLC	Barcelona Clinic Liver Cancer
BMA	Butyl methacrylate
CM	Chitosan microspheres
CMC	Carboxymethylcellulose
CMCS	Carboxymethyl chitosan
CPT	Camptothecine
CT	Computed tomography
cTACE	Conventional transarterial chemoembolization
CV	Coefficient of variation
DEB	Drug-eluting bead
DED	Dry eye disease
DLS	Dynamic light scattering
DMEM	Dulbecco's modified Eagle's medium
DMSO	Dimethylsulfoxide
DNA	Deoxyribonucleic acid
DOX	Doxorubicin
DSC	Differential scanning calorimetry
EASL	European Association for the Study of the Liver
ECM	Extracellular matrix
EDX	Energy-dispersive X-ray
EORTC	Response Evaluation Criteria in Solid Tumors
FDA	Food and Drug Administration
FITC	Fluorescein isothiocyanate
FTC	Freeze-thaw cycle
FTIR	Fourier transform infrared spectroscopy
GRAS	Generally Recognized as Safe
HA	Hyaluronan
HAP	Hydroxyapatite
HCC	Hepatocellular carcinoma
HCEC	Human corneal epithelial cell
HEMA	2-hydroxyethyl methacrylate (HEMA)
HNT	Halloysite nanotubes

IEP	Isoelectric point
IFN γ	Interferon- γ
IL	Interleukin
IONP	Iron oxide nanoparticle
KGN	Kartogenin
Lap	Laponite
LD50	Lethal dose
LDH	Lactate dehydrogenase
LNP	Lipid nanoparticle
LTTC	Low temperature thermal cycling
MC	Methylcellulose
MMP	Matrix metalloproteinases
MRI	Magnetic resonance imaging
MRN	Magnetic resonance navigation
MRT	Magnetic resonance targeting
MS	Microsphere
MTT	Methyl thiazolyl tetrazolium
MW	Molecular weight
NIPAM	<i>N</i> -isopropylacrylamide
NP	Nanoparticle
NPX	Naproxen
P(MAA- <i>g</i> -EG)	Methacrylic acid grafted with poly(ethylene glycol)
PBS	Phosphate buffered saline
PC	Polycarbonate
PDI	Polydispersity index
PDMS	Poly(dimethylsiloxane)
PEG	Poly(ethylene glycol)
PEGMA	Poly(ethylene glycol) methacrylate
pHEMA	Poly(2-hydroxyethyl methacrylate)
PLGA	poly(lactic- <i>co</i> -glycolic acid)
PMMA	Poly(methyl methacrylate)
PNIPAm	Poly(<i>N</i> -isopropylacrylamide)
PVA	Poly(vinyl alcohol)
PVAc	Poly(vinyl acetate)
RFA	Radiofrequency ablation
ROS	Reactive oxygen species
SD	Standard deviation
SDC	Syndecan
SEC	Size exclusion chromatography
SEM	Scanning electron microscope
SiNP	Silica nanoparticle

SMANCS	Poly(styrene- <i>co</i> -maleic acid)-conjugated neocarzinostatin
SPION	Superparamagnetic iron oxide nanoparticle
TACE	Transarterial chemoembolization
TAE	Transarterial embolization
TEM	Transmission electron microscope
TEOS	Tetraethyl orthosilicate
TMZ	Temozolomide
TNF	Tumor necrosis factor
UV-vis	Ultraviolet–visible
VEGF	Vascular endothelial growth factor
VSM	Vibrating sample magnetometer

Chapter 1

1 Introduction

1.1 Background and Motivation

Drug release systems are drug depots that aim to confine the drug's pharmacological activity to the target site with a predetermined release profile. The ideal formulation should be able to (1) maintain the local concentration within the therapeutic window, (2) prolong drug release at the site of disease, (3) protect therapeutics from inactivation or degradation, (4) produce little or no systemic toxicity, (5) be tailored to the administration route and physiological features of the desired site of action [1].

Since the first drug-polymer system was introduced in the mid-1960s [2], controlled delivery technologies have undergone profound advancement over the past 60 years. This is represented by the move from short-term (1-2 day) delivery formulations in the form of tablets or ointments, towards long-term (6-12 months) and modulated formulations in micron or nanoscale dosage forms [3]. The choice of drug carriers also evolves from non-degradable polymers like silicone rubber and ethylene-vinyl acetate to a wide array of biodegradable polymers. Of note, hydrogels and nanocarriers composed of biodegradable materials dominated the research landscape in the past decade and have established promising clinical relevance, and the systems based on nanoparticles are projected to be leading the research on targeted delivery in the future [3,4].

Existing drug delivery systems can be categorized into two types based on the administration route and action mechanism. The first group is usually administered via oral or intravenous route and reaches the desired site of action through blood circulation. Typical delivery platforms are tablets [5] and nanoscale particles such as polymeric nanoparticles [6], lipids [7] and micelles [1]. Although controlled release formulations offered many advantages over the conventional dosage forms, they are suffering from suboptimal pharmacokinetic profiles or poor stability and low bioavailability [8,9]. The second group of delivery systems are characterized by wafers, hydrogels, and inhalable or injectable microparticles [10]. They can be implanted or injected within or adjacent to the

site of diseases, leading to locoregional drug delivery. Localized treatment regimens can circumvent hepatic first-pass metabolism and gastrointestinal enzymatic degradation and bypass different biological barriers, resulting in improved bioavailability [11].

The advancements in controlled release techniques expanded drug delivery options and fostered safer, more efficient and compliant treatments. In contrast to systemic delivery, locoregional drug delivery limits the presentation of the drug to a target site for its release and absorption. Drug administration can be achieved through implantation, injection or inhalation [10]. This delivery strategy provides a number of advantages over systemic administration such as minimally invasive administration, lower total drug dosage and fewer adverse side effects.

Locoregional drug delivery plays a well-defined role in the management of the diseases with localized nature. It remains one of the main strategies treating osteoarthritis [12], perturbed wounds [13] and a range of ocular disorders [14]. A wide range of treatment options is currently in clinical and preclinical investigations, including devices, macromolecular drugs (e.g., peptides and proteins) and small molecules [12,14,15]. Future research is likely to focus on expanding the drug spectrum, developing long-term controlled release formulations and addressing the safety concerns.

In addition, locoregional delivery of chemotherapeutics extends treatment options in case of solid tumors that are easily accessible. Patients undergoing intraductal administration of liposomal doxorubicin have shown higher drug concentration in the breast than intravenously injected groups, indicating reduced systemic toxicity [16]. In the case of ovarian cancer, Lu et al. found that intraperitoneal treatment provided sustained drug levels in the peritoneal cavity with lower systemic drug exposure [17]. Similarly, in the postsurgical management of glioblastoma, implantable Gliadel[®] wafer could provide a drug concentration up to 1200 times higher than the systemic route with no significant safety concerns [18,19]. Locoregional treatments have also demonstrated promising results as the alternative or adjuvant to other forms of treatment in managing lung and liver tumors [20,21].

Decades of experience in locoregional drug delivery have delivered meaningful benefits to an appreciable number of patients and imparted additional requirements for controlled release systems. First, the retention time of drug depots in the targeted site can be extended. Delivery systems with mucoadhesive and drug-protecting attributes would be highly desirable in such circumstances [22]. Second, drug permeation and absorption should be improved. In this context, drug carriers that are charged, lipophilic and small in dimension will be of great value [23,24]. In image-guided locoregional delivery like transarterial embolization (TACE), controlled release systems with CT/MRI detectability would be highly beneficial [25]. In addition, for the best treatment outcome, co-delivery systems might be necessary [25,26]. Last but not least, in consideration of biocompatibility and repeated drug administration, the delivery system should be able to degrade without forming toxic substances *in vivo*.

The realization of the desired drug delivery systems relies upon novel material strategies. The significant progress in nanotechnology and polymer science offers a great opportunity. It can combine the intrinsic strengths of macroscale systems (e.g., hydrogels) with properties (e.g., antimicrobial and imageable) of nanoparticles. This combinational system allows a multifunctional delivery formulation. A wide range of nanoparticles such as superparamagnetic iron oxide nanoparticles (SPIONs) [26–28], silica nanoparticles (SiNPs) [29–31], lipid nanoparticles (LNPs) [32] were successfully incorporated into hydrogels through physical or chemical interactions. The incorporation of nanocarriers provides a tool to alter the mechanical strength, drug release and hydrogel degradation. These manipulations can be done by varying the concentration of nano components in the gel matrix [30,31,33,34]. Compared with the delivery systems based on a single platform, combinational systems offer expanded spectrum of loadable drugs and prolonged drug release [35]. In addition, the nanoparticle-hydrogel interaction adds a degree of freedom in regulating drug release and polymer degradation [27].

To conclude, locoregional drug delivery has gained increasing importance for treating disease with localized nature. Drug delivery systems composed of hydrogels and nanoparticles demonstrate huge potential in fulfilling the stringent requirements placed on locoregional delivery. As the therapeutics and intervention techniques continue to

grow, it is expected that novel drug release systems will be in high demand. We believe the development and optimization of multifunctional drug delivery systems will deepen the understanding of fundamental science and, more importantly, lead to significant clinical impact in the coming decades.

1.2 Objectives

In previous work in our laboratory, we explored PVA-iron oxide nanoparticles (IONPs) nanocomposite hydrogels. We have shown that the incorporation of IONPs contributes to the crosslinking of the PVA and leads to a ‘degradable’ hydrogel system [27].

The overall objective of this thesis is to explore various formulations to improve and expand their applications in locoregional drug delivery. To achieve the objectives, a series of specific goals are set up and listed below.

1. To develop a range of delivery systems in the form of nanoparticles or composite hydrogels.
2. To characterize the delivery systems in terms of size, morphology, composition, and magnetic properties.
3. To investigate drug release profiles at different environmental conditions.
4. To study the degradation/dissolution of the drug carriers.

As shown in Figure 1.1, the first stage (Chapter 3) of this thesis is regarded as a continuation of our prior work. Magnetic PVA-IONP hydrogels were prepared and shaped into microparticles using microfluidics for doxorubicin delivery with IONPs co-localized for visualization of drug location at the tumor site. Degradability of the carrier also allows for repeat TACE treatment. In the second stage (Chapter 4), non-porous silica nanoparticles (SiNPs) were explored as a carrier for bioactive protein and peptide N-94 for the treatment of dry eye disease. Finally, a modified microbeads formulation composed of silica microparticles, IONP and PVA hydrogel (PVA-SiO₂-IONP) was developed and characterized for doxorubicin delivery. The optimized system demonstrated an increased drug loading and tunable release profile compared to the original PVA-IONP system (Chapter 5).

- Chapter 3 Development of Multifunctional PVA-IONP Microparticles for TACE

This chapter introduces the design of PVA-IONP microparticles as potential drug-eluting beads (DEBs) in TACE treatment. Microparticles were fabricated via microfluidic technique. The MRI images of microbeads of various concentrations were taken to examine the contrast enhancement. Doxorubicin loading and release were performed. Degradation studies were performed in the acidic and physiological pH conditions.

- Chapter 4 Development of a Multifunctional Bioactive Protein/Peptide Delivery System for Dry Eye Disease

This chapter describes the work on SiNPs as protein carriers in the application of dry eye treatment. Adsorption kinetics and isotherm were studied and modelled using lysozyme as the model protein. The release profile of lysozyme and a bioactive peptide, N-94, were studied and compared. Dissolution of SiNPs was investigated in a period of one month. Cell studies were performed to examine the functional equipotency of N-94 to its parent protein, lacritin, and the biocompatibility of the delivery system.

- Chapter 5 Development of Multifunctional PVA-SiO₂-IONP Microparticles for TACE

This chapter presents the modification and improvements of PVA-IONP microbeads. Silica microparticles were introduced into the composite hydrogel. The dependency of particle diameter on flow rates of the continuous phase and dispersed was explored. The effect of drug loading, pH and ionic concentration on the drug elution profile were investigated. The dissolution of PVA-SiO₂-IONP microparticles was qualitatively characterized.

- Chapter 6 Conclusions and Recommendations

This chapter provides the summary, significance and future directions of the research presented in Chapter 3-5.

1.4 References

- [1] F. Pittella, H. Cabral, Y. Maeda, P. Mi, S. Watanabe, H. Takemoto, H.J. Kim, N. Nishiyama, K. Miyata, K. Kataoka, Systemic siRNA delivery to a spontaneous pancreatic tumor model in transgenic mice by PEGylated calcium phosphate hybrid micelles, *Journal of Controlled Release*. 178 (2014) 18–24.
- [2] R.S. Langer, N.A. Peppas, Present and future applications of biomaterials in controlled drug delivery systems, *Biomaterials*. 2 (1981) 201–214.
- [3] K. Park, Controlled drug delivery systems: past forward and future back, *J Control Release*. 190 (2014) 3–8.
- [4] Y.F. Tan, L.L. Lao, G.M. Xiong, S. Venkatraman, Controlled-release nanotherapeutics: State of translation, *Journal of Controlled Release*. 284 (2018) 39–48.
- [5] S. Kumar, A.K. Singh, S.K. Prajapati, V.K. Singh, Formulation and Evaluation of once daily sustained release matrix tablets of Aceclofenac using natural gums, *Journal of Drug Delivery and Therapeutics*. 2 (2012).
- [6] S. Acharya, S.K. Sahoo, PLGA nanoparticles containing various anticancer agents and tumour delivery by EPR effect, *Adv. Drug Deliv. Rev.* 63 (2011) 170–183.
- [7] T.X. Nguyen, L. Huang, M. Gauthier, G. Yang, Q. Wang, Recent advances in liposome surface modification for oral drug delivery, *Nanomedicine*. 11 (2016) 1169–1185.
- [8] S. Senapati, A.K. Mahanta, S. Kumar, P. Maiti, Controlled drug delivery vehicles for cancer treatment and their performance, *Signal Transduct Target Ther.* 3 (2018).
- [9] N.R. Mathias, M.A. Hussain, Non-invasive Systemic Drug Delivery: Developability Considerations for Alternate Routes of Administration, *Journal of Pharmaceutical Sciences*. 99 (2010) 1–20.
- [10] F. Ramazani, C.F. van Nostrum, G. Storm, F. Kiessling, T. Lammers, W.E. Hennink, R.J. Kok, Locoregional cancer therapy using polymer-based drug depots, *Drug Discov. Today*. 21 (2016) 640–647.
- [11] G. Pulivendala, S. Bale, C. Godugu, Inhalation of sustained release microparticles for the targeted treatment of respiratory diseases, *Drug Deliv Transl Res.* 10 (2020) 339–353.
- [12] P. Maudens, O. Jordan, E. Allémann, Recent advances in intra-articular drug delivery systems for osteoarthritis therapy, *Drug Discovery Today*. 23 (2018) 1761–1775.

- [13] R. Dimatteo, N.J. Darling, T. Segura, In situ forming injectable hydrogels for drug delivery and wound repair, *Adv. Drug Deliv. Rev.* 127 (2018) 167–184.
- [14] A. Patel, K. Cholkar, V. Agrahari, A.K. Mitra, Ocular drug delivery systems: An overview, *World J Pharmacol.* 2 (2013) 47–64.
- [15] J.W. Park, S.R. Hwang, I.-S. Yoon, Advanced Growth Factor Delivery Systems in Wound Management and Skin Regeneration, *Molecules.* 22 (2017).
- [16] V. Stearns, T. Mori, L.K. Jacobs, N.F. Khouri, E. Gabrielson, T. Yoshida, S.L. Kominsky, D.L. Huso, S. Jeter, P. Powers, K. Tarpinian, R.J. Brown, J.R. Lange, M.A. Rudek, Z. Zhang, T.N. Tsangaris, S. Sukumar, Preclinical and Clinical Evaluation of Intraductally Administered Agents in Early Breast Cancer, *Science Translational Medicine.* 3 (2011) 106ra108.
- [17] Z. Lu, M. Tsai, D. Lu, J. Wang, M.G. Wientjes, J.L.-S. Au, Tumor-penetrating microparticles for intraperitoneal therapy of ovarian cancer, *J. Pharmacol. Exp. Ther.* 327 (2008) 673–682.
- [18] T.A. Juratli, G. Schackert, D. Krex, Current status of local therapy in malignant gliomas — A clinical review of three selected approaches, *Pharmacology & Therapeutics.* 139 (2013) 341–358.
- [19] T. AOKI, R. NISHIKAWA, K. SUGIYAMA, N. NONOGUCHI, N. KAWABATA, K. MISHIMA, J. ADACHI, K. KURISU, F. YAMASAKI, T. TOMINAGA, T. KUMABE, K. UEKI, F. HIGUCHI, T. YAMAMOTO, E. ISHIKAWA, H. TAKESHIMA, S. YAMASHITA, K. ARITA, H. HIRANO, S. YAMADA, M. MATSUTANI, A Multicenter Phase I/II Study of the BCNU Implant (Gliadel® Wafer) for Japanese Patients with Malignant Gliomas, *Neurol Med Chir (Tokyo).* 54 (2014) 290–301.
- [20] R. Rosière, T. Berghmans, P. De Vuyst, K. Amighi, N. Wauthoz, The Position of Inhaled Chemotherapy in the Care of Patients with Lung Tumors: Clinical Feasibility and Indications According to Recent Pharmaceutical Progresses, *Cancers (Basel).* 11 (2019).
- [21] L. Shen, M. Xi, L. Zhao, X. Zhang, X. Wang, Z. Huang, Q. Chen, T. Zhang, J. Shen, M. Liu, J. Huang, Combination Therapy after TACE for Hepatocellular Carcinoma with Macroscopic Vascular Invasion: Stereotactic Body Radiotherapy versus Sorafenib, *Cancers (Basel).* 10 (2018).
- [22] S. Duggan, W. Cummins, O. O’ Donovan, H. Hughes, E. Owens, Thiolated polymers as mucoadhesive drug delivery systems, *European Journal of Pharmaceutical Sciences.* 100 (2017) 64–78.
- [23] A. Vashist, A. Kaushik, A. Vashist, R.D. Jayant, A. Tomitaka, S. Ahmad, Y.K. Gupta, M. Nair, Recent trends on hydrogel based drug delivery systems for infectious diseases, *Biomater. Sci.* 4 (2016) 1535–1553.

- [24] S. Zhang, H. Gao, G. Bao, Physical Principles of Nanoparticle Cellular Endocytosis, *ACS Nano*. 9 (2015) 8655–8671.
- [25] A.L. Lewis, S.L. Willis, M.R. Dreher, Y. Tang, K. Ashrafi, B.J. Wood, E.B. Levy, K.V. Sharma, A.H. Negussie, A.S. Mikhail, Bench-to-clinic development of imageable drug-eluting embolization beads: finding the balance, *Future Oncology*. 14 (2018) 2741–2760.
- [26] M.P. Kesavan, S. Ayyanaar, V. Vijayakumar, J. Dhavethu Raja, J. Annaraj, K. Sakthipandi, J. Rajesh, Magnetic iron oxide nanoparticles (MIONs) cross-linked natural polymer-based hybrid gel beads: Controlled nano anti-TB drug delivery application, *J Biomed Mater Res A*. 106 (2018) 1039–1050.
- [27] A.D. Bannerman, X. Li, W. Wan, A ‘degradable’ poly(vinyl alcohol) iron oxide nanoparticle hydrogel, *Acta Biomaterialia*. 58 (2017) 376–385.
- [28] D.-H. Kim, T. Choy, S. Huang, R.M. Green, R.A. Omary, A.C. Larson, Microfluidic Fabrication of MEAN-Eluting Magnetic Microspheres, *Acta Biomater*. 10 (2014) 742–750.
- [29] R. Guo, X. Du, R. Zhang, L. Deng, A. Dong, J. Zhang, Bioadhesive film formed from a novel organic–inorganic hybrid gel for transdermal drug delivery system, *European Journal of Pharmaceutics and Biopharmaceutics*. 79 (2011) 574–583.
- [30] P. Zhao, H. Liu, H. Deng, L. Xiao, C. Qin, Y. Du, X. Shi, A study of chitosan hydrogel with embedded mesoporous silica nanoparticles loaded by ibuprofen as a dual stimuli-responsive drug release system for surface coating of titanium implants, *Colloids and Surfaces B: Biointerfaces*. 123 (2014) 657–663.
- [31] H.H.C. de Lima, V.L. Kupfer, M.P. Moisés, M.R. Guilherme, J. de C Rinaldi, S.L. Felisbino, A.F. Rubira, A.W. Rinaldi, Bionanocomposites based on mesoporous silica and alginate for enhanced drug delivery, *Carbohydr Polym*. 196 (2018) 126–134.
- [32] C. Desfrancois, R. Auzély, I. Texier, Lipid Nanoparticles and Their Hydrogel Composites for Drug Delivery: A Review, *Pharmaceutics (Basel)*. 11 (2018).
- [33] A.K. Gaharwar, C.P. Rivera, C.-J. Wu, G. Schmidt, Transparent, elastomeric and tough hydrogels from poly(ethylene glycol) and silicate nanoparticles, *Acta Biomaterialia*. 7 (2011) 4139–4148.
- [34] A. Nasajpour, S. Ansari, C. Rinaldi, A.S. Rad, T. Aghaloo, S.R. Shin, Y.K. Mishra, R. Adelung, W. Swieszkowski, N. Annabi, A. Khademhosseini, A. Moshaverinia, A. Tamayol, A Multifunctional Polymeric Periodontal Membrane with Osteogenic and Antibacterial Characteristics, *Advanced Functional Materials*. 28 (2018).
- [35] T.R. Hoare, D.S. Kohane, Hydrogels in drug delivery: Progress and challenges, *Polymer*. 49 (2008) 1993–2007.

Chapter 2

2 Literature Review

2.1 Hepatocellular Carcinoma and Transarterial Chemoembolization

Hepatocellular carcinoma (HCC) is the most common primary malignancy of the liver and the third most common cause of cancer-related mortality in the world [1,2]. The treatment allocation for HCC is dependent on the stage of disease, liver function, and performance status. Table 2.1 provides an overview of the most commonly used HCC management guideline- Barcelona Clinic Liver Cancer (BCLC) staging system. With improved surveillance strategy of patients with cirrhosis and chronic liver disease and advanced diagnostic methods, more patients are detected at early-stage HCC [3].

Curative treatments, including hepatic resection, liver transplantation, and radiofrequency ablation (RFA) are recommended for patients diagnosed with early-stage HCC [4]. For HCC that is not amenable to curative procedures, palliative therapies via TACE or systematic chemotherapy are offered [5].

Table 2.1 Barcelona Clinic Liver Cancer (BCLC) staging system with treatment recommendations. Adapted from reference [6].

Stage	Tumour characteristic	Treatment strategy
Stage 0: very early stage	Single ≤ 2 cm	Curative treatments: hepatic resection
Stage A: early stage	Single < 5 cm or ≤ 3 nodules ≤ 3 cm	Curative treatments: liver transplantation or percutaneous ablation [e.g. percutaneous ethanol injection (PEI) and radiofrequency ablation (RFA)]
Stage B: intermediate stage	Multinodular	Palliative treatments: transarterial chemoembolization (TACE)
Stage C: advanced stage	Vascular invasion or extrahepatic spread	Palliative treatments: systemic therapy with sorafenib
Stage D: terminal stage	Any form	Best supportive care or the inclusion of patients in clinical trials

Transarterial chemoembolization plays multiple roles in the clinical management of HCC, as summarized in Table 2.2. In accordance with the BCLC guideline, TACE is the

first-line treatment for patients with intermediate stage HCC (BCLC stage B) [6]. TACE is used in cases with recurrent HCC after curative treatments [7,8]. TACE has also been used as a bridge for patients waiting to fulfill criteria for transplantation when donor becomes available [9,10]. Moreover, TACE represents a valuable component in multimodal treatments for downsizing large tumors [11].

Table 2.2 Roles of TACE in the management of HCC.

Palliative treatment for intermediate stage HCC (BCLC stage B)
Treatment/prevention tool for recurrent HCC after curative treatments by surgery or ablation
Bridging or downstaging tool to liver transplantation
Neoadjuvant therapy to downsize tumor prior to liver resection
Combined therapy with other interventional treatments

The principle of TACE revolves around the dual blood supply of the liver. The normal tissue of the liver receives most (75%-85%) of its blood supply from the portal vein and receives the remaining from the hepatic artery. On the other hand, liver tumors receive ~90% of their blood supply from the hepatic artery [5]. It has been reported that the embolization via hepatic arteries would have minimal ischemic damage on normal hepatic parenchyma, as its dominant blood supply from a portal vein is unaffected [12]. In addition, unlike oral or intravenous delivery, the chemotherapeutic effect of the drugs is reserved as this approach bypasses the first-pass metabolism [13].

The success of the TACE procedure heavily relies on imaging techniques and requires a multidisciplinary tumor board consist of a surgeon, clinical oncologist and interventional radiologist [14]. In a typical TACE therapy, pre-treatment imaging consisting of a multiphasic computed tomography (CT) or dynamic contrast-enhanced magnetic resonance imaging (MRI) of the liver must be obtained preferably within four weeks of the planned TACE intervention [15]. The pre-treatment imaging aims to acquire anatomic information to aid in planning the procedure [15,16]. Figure 2.1 schematically describes the TACE procedure. During a TACE, patients will be given a local anesthetic. The interventional radiologist places a catheter into the patient's femoral artery and moves the catheter up until it reaches the hepatic artery in the liver. Three-dimensional vascular

images (angiogram) are necessary to identify the appropriate tumor-feeding branches. An X-ray is taken by infusing radio-opaque contrast agents through the catheter. Drugs/drug carriers and embolic materials are delivered separately or simultaneously depending on the techniques and delivery systems. The injection is stopped when the stasis flow of contrast agents existed. Angiography is repeated, and embolization is continued until all blushed tumors disappeared [17]. In post-procedure care, CT scans are performed to determine tumor response recurrence 4-8 weeks after the procedure. Sequential TACE procedures can be performed in 4-16 weeks if any recurrent tumor is identified [12].

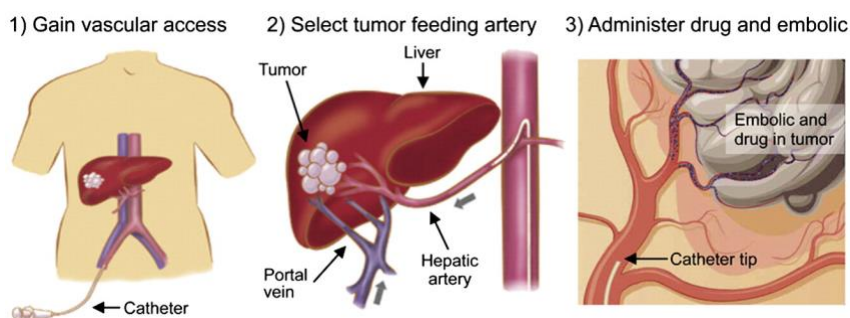


Figure 2.1 Schematic demonstration of TACE. Figure reprinted with permission from [18].

TACE can be classified as conventional TACE (cTACE) and drug eluting beads (DEB)-TACE. The cTACE involves an arterial infusion of an emulsion containing chemotherapeutics in iodinated oil (Lipiodol®) followed by injection of embolic agents to occlude the same tumor vasculature. A major advantage of cTACE is its radiopaque iodinated oil allows intra-procedure visualization of the drugs, which is helpful to optimize the imaging guidance. The drawbacks of cTACE include the rapid release of drug from Lipiodol associated with the weak bonding between the doxorubicin and the carriers [19]. Other drawbacks underline the unstable and unpredictable post-treatment outcomes, which might be due to the variants in the procedure, as cTACE is not a well-standardized procedure and can be largely dependent on the medical specialists' experience, treatment devices available and the therapeutic agents injected [20].

The limitations of cTACE led to its gradual replacement by DEB-TACE. DEB-TACE takes advantage of drug-impregnated microspheres and allows the simultaneous delivery

of chemotherapeutic agents together with vessel occlusion. The DEBs essentially serve as a drug carrier, contrast agent and embolic agent. The integration of multiple functions is achieved by the appropriate design of the size and composition of the matrix. DEBs are typically in the diameter of 40-900 μm , making them large enough for vascular embolization [21]. Drug loading is performed prior to the TACE procedure by immersion methods and typically takes 20 min to 2 h to complete depending on the bead size and materials [22,23]. The loading is driven by ionic interactions between the drug molecules with polymeric backbone. The contrast medium could be incorporated by physical mixing with DEBs [24,25] or via covalent coupling with the polymeric backbone [26]. Imageable DEBs can also be prepared by entrapment of iron oxide nanoparticles (IONPs) [27–29]. Of note, DEB-TACE is performed in a more standardized way as compared to cTACE, both during preparation and administration. The standardization leads to more homogenous and stable patient data [30]. In some clinical studies, DEB-TACE has shown improved tolerability, better tumor response and lower systemic toxicity than cTACE [31,32].

2.2 Dry Eye Disease and Treatments

Dry eye disease (DED) is a multifactorial disease of the tear and ocular surface, characterized by hyperosmolarity, tear film instability, ocular surface inflammation, and visual discomfort [33]. These changes in tear composition activate stress signaling pathways in the ocular surface epithelium and resident immune cells, which triggers the production of inflammatory mediators to recruit and activate immune cells and produce cytokines, such as interleukin (IL)- 1β , IL-6, and tumor necrosis factor (TNF)- α [34]. The secretion of cytokines would initiate a vicious cycle and further damage the cornea and lacrimal glands, decline the tear function and worsen the symptoms [34,35].

The current DED treatments focus on minimizing the inflammation and supplementing the tear film components [36]. The topical application of lubricating agents, anti-inflammatory therapeutics, biological tear components through eye drops remains the commonest intervention option for patients with dry eye [37]. For this treatment, punctal

plug insertion is encouraged to prolong the resident time of aqueous and artificial tears on the ocular surface [38].

The topical administration is often associated with two challenges: the low ocular bioavailability of the drug and the unfavorable long-term use of the commonly prescribed therapeutics [36,37]. Less than 5% of topically applied drug doses can reach deeper ocular tissues due to the complex anatomical and physiological barriers of eyes [39]. Reflex tearing, blinking, nasolachrymal drainage and metabolic degradation impede sufficient time residence and deep drug permeation [40]. As a result, frequent dosing of the drugs at high concentrations is required to deliver sufficient therapeutic effects. The poor patient adherence and high drug dosage could result in extreme fluctuations in drug ocular concentrations and systemic drug distribution, leading to undesirable side effects [37].

To prolong the ocular residence time of the therapeutics and minimize the oscillations in the drug concentrations, numerous drug delivery systems have been developed. Nanomicelles, nanoparticles, liposomes, and hydrogels were loaded with drugs and can provide an effective drug concentration in the eye for a week [41]. In addition to being used solely, such systems could be included in other devices such as contact lens. The liposome-laden lens have demonstrated a controlled drug release over a period of 8 days [40].

The potential risks associated with the long-term use of commonly prescribed drugs posed a challenge for DED treatment via topical route. Steroids are one of the most effective and rapid medications for DED. However, prolonged use is not recommended due to the risks of developing an ocular infection, glaucoma, and cataract [42]. Topical instillation of cyclosporine can lead to complications such as lid maceration and corneal epitheliopathy [43]. Another alternative treatment is lifitegrast, the only U.S. Food and Drug Administration (FDA)-approved drug for both signs and symptoms of DED [44]. The adverse events consist of ocular irritation and hyperthermia. Systemic effects are headaches, erythema, and musculoskeletal pain. Clinical studies on long-term safety profiles are still quite limited and represent an essential avenue for future investigation.

The adverse ocular events associated with commonly prescribed molecules have encouraged research and development of biotherapeutics as alternatives. Among them, bioactive tear proteins have emerged as promising candidates.

Lacritin is a growth-factor-like tear protein (~ 25 kDa) that is selectively downregulated in dry eye [45,46]. It is produced by human lacrimal acinar cells, corneal, conjunctival, and salivary epithelia [47]. Lacritin has demonstrated mitogenic and cytoprotective properties on human corneal epithelial cells (HCECs) and can promote basal tearing that is sustained for at least 4 hours when topically instilled in rabbits [46–48]. It was found that lacritin's C-terminal is mitogenic and has an amphipathic α -helical structure [49]. In addition, its C terminus targets cell surface syndecan-1 (SDC1), a transmembrane protein that regulates mitogenic signaling, making lacritin a potential cell-targeting strategy for DED.

Various C-terminal fragments of lacritin have been produced via chemical synthesis. For example, N-65 represents a lacritin truncation mutant lacking 65 N-terminal amino acids [50]. Other lacritin peptides such as N-55, N-74, N-94, and N-104 were synthesized, as described elsewhere [51]. The synthetic surrogates have demonstrated antimicrobial properties and they are effective in stabilizing the tear lipid layer and maintaining epithelial homeostasis [52].

The combinational use of protein-based therapeutic agents with drug delivery systems offers a promising tool to treat DED. The topical administration of lacritin molecules or its fragments may contribute to a restored tear film microenvironment, particularly under dry eye conditions where they are deficient [47]. As biomolecules are prone to decomposition on the inflammatory and oxidative ocular surface, the use of drug delivery systems, in return, can potentially protect and allow sustained availability of protein therapeutics [53].

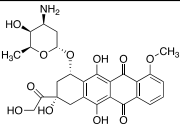
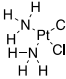
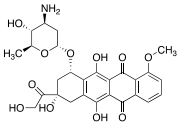
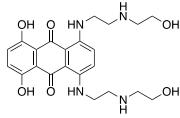
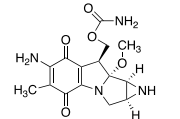
For dry eye treatment, future efforts should be dedicated to discovering safer drug molecules and more effective delivery options. The replacement of steroid therapy with natural tear components can provide a long-term solution by physiologically rescuing the ocular surface without provoking any noticeable adverse effects. On the other hand, the

advancement in carrier systems is expected to facilitate the delivery of drugs, concentrate drugs at the target site, and prolong their corneal residence time, ultimately reducing dose and dosing frequency.

2.3 Chemotherapeutic Agents

For TACE, the most common sole-agent anticancer drugs used are the anthracycline group. In published cohort and randomized studies, anthracycline antibiotic doxorubicin (DOX) takes up 36% of the cases while epirubicin represents 12% of the records. Other popular chemotherapy agents include cisplatin (31% of the cases), mitoxantrone (8%), mitomycin (8%), and poly(styrene-*co*-maleic acid)-conjugated neocarzinostatin (SMANCS, 5%) [54]. The chemical formula and structure of commonly used anticancer drugs are shown in Table 2.3. Notably, the criteria to decide the dosing regimen is not standardized: some physicians prefer to determine it based on patient's body surface area, weight, tumor burden or bilirubin level, while others prefer to use a fixed dose [55]. The usual dose for DOX is 40-100 mg while cisplatin between 50-100 mg [14,15]. Some randomized clinical studies showed no significant differences in survival rate between the single-drug treatment of DOX and cisplatin or epirubicin [56–59]. Moreover, to date, there is no evidence of the superiority of any single cytotoxic anticancer drug over other drugs or for mono-drug chemotherapy versus combination chemotherapy [14,15].

Table 2.3 Summary of commonly used cytotoxic anticancer drugs for TACE.

Generic name	Chemical formula	Molecular weight (g/mol)	Structure
Doxorubicin	$C_{27}H_{29}NO_{11}$	543.5	
Cisplatin	$Cl_2H_6N_2Pt$	300.0	
Epirubicin	$C_{27}H_{29}NO_{11}$	543.5	
Mitoxantrone	$C_{22}H_{28}N_4O_6$	444.5	
Mitomycin	$C_{15}H_{18}N_4O_5$	334.3	

While the dosing regimen is not standardized, the EASL-EORTC [(European Association for the Study of the Liver) or (Response Evaluation Criteria in Solid Tumors)] clinical practice guidelines provide a general rule for the dose of DOX. The recommended DOX dose per treatment is 50-75 mg to a maximum value of 150 mg (75 mg/m² body surface area) [60]. Patients may receive 3- 4 TACE treatments within six months, with each session being ~3 to 4 weeks apart. The maximum recommended lifetime dose of DOX is 900 mg (450 mg/m²), in correlation to the cardiac toxicity when the drug is administered systemically [61].

2.4 Drug-eluting Microparticles and Commercial Products

Over the previous decades, several DEBs have become commercially available (Table 2.4). The most commonly used microparticles in clinical practice are DC BeadTM/LC BeadTM (Biocompatibles, United Kingdom), the radio-opaque version of DC Bead: DC Bead LUMITM (Bosten Scientific, United States), HepaSphereTM/QuadrasphereTM

(BioSphere Medical, France), OncozeneTM/Embozene TANDEMTM (Varian Medical Systems, United States), and LifePearl[®] (Terumo International Systems, Belgium). Commercial DEBs are typically offered in a size range (e.g., 70-150 μm , 100-300 μm , 300-500 μm , 500-700 μm). The most common bead sizes are 100-300 μm , 300-500 μm and 500-700 μm [62], while DEBs in 100-300 μm provide the a better treatment response and fewer major complications than beads with larger diameters [63,64].

Table 2.4 Overview of commercially available DEBs.

Product	Company	Material	Drug-binding groups	Maximal drug loading		Other functions			Size available (μm)
				Doxorubicin	Irinotecan	Embolization	Imageability	Degradability	
DC Bead TM and LC Bead TM	Biocompatibles, United Kingdom	Polyvinyl alcohol- <i>co</i> -Poly(2-acrylamido-2-methylpropane sulfonate)	Sulfonate groups	45 mg/mL hydrated beads	50 mg/mL hydrated beads	Y	N	N	70-150 100-300 300-500 500-700
DC Bead LUMI TM	Boston Scientific, United States	Iodine covalently bonded to DC Bead	Sulfonate groups	37.5 mg/mL hydrated beads	50 mg/mL hydrated beads	Y	Y	N	40-90 70-150 100-300
HepaSphere TM and QuadraSphere TM	BioSphere Medical, France	Polyvinyl acetate- <i>co</i> -polymethylacrylate	Carboxylate groups	0.9 mg/mg dry beads 40 mg/mL hydrated beads	1.8 mg/mg dry beads	Y	N	N	(Dry state) 30-60 50-100 100-150 150-200 (Hydrated state) 120-240 200-400 400-600 400-800
Oncozene TM and Embozene TANDEM TM	Varian Medical Systems, United States	Poly(methyl methacrylate) core coated with [bis(trifluoroethoxy) phosphazene]	Carboxylate groups	50 mg/mL hydrated beads	50 mg/L hydrated beads	Y	N	N	40 \pm 10 75 \pm 15 100 \pm 25
LifePearl [®]	Terumo Interventional Systems, Belgium	Poly (ethylene glycol) modified with 3-sulfopropyl acrylate	Sulfonate groups	37.5 mg/mL hydrated beads	50 mg/mL hydrated beads	Y	N	N	100 \pm 25 200 \pm 50 300 \pm 50 400 \pm 50

Y: yes, N: no.

Commercial DEBs carry negative charges and allow the loading of chemodrugs with counter ions (e.g., DOX, epirubicin and cisplatin). DC BeadTM is made of PVA functionalized with sulfonate groups on the bead surface [65]. DC BeadTM microparticles are usually packaged in 2 mL vials at a hydrated state in a sodium phosphate solution and provide a DOX loading capacity of up to 45 mg/mL [64,65]. DC Bead LUMITM is derived from DC BeadTM and the PVA backbone is covalently bonded with imaging moieties iodine, therefore allows standard fluoroscopy and CT imaging [66]. HepaSphereTM is a poly(vinyl alcohol-*co*-acrylic acid) microsphere packaged in a dry state. This type of beads expands to four times in volume upon exposure to saline. The presence of carboxylate groups allows binding of positively charged drugs throughout the

beads and can achieve a DOX loading ~40 mg/mL beads [22]. Likewise, TANDEM™ is composed of poly(methylacrylic acid) microspheres with perfluorinated coating. The pendant carboxylate groups allow up to 50 mg/ml loading of DOX [67,68]. LifePearl® beads consist of a poly(ethylene glycol) (PEG) modified with sulfonate groups and can provide a DOX loading at ~37.5 mg/ml [69].

The *in vitro* drug loading and eluting profile provide helpful information to determine the dosing regimen and predict the pharmacokinetics of the drugs. Baere et al. conducted a comparative study of the four DEBs (DC Bead™, HepaSphere™, Embozene TANDEM™ and LifePearl®) [22]. All four types of DEBs can reach maximum loading in ~ 2 h, with larger particles generally take a longer time to reach the plateau. The drug elution profile was examined under sink condition in flow cells, all four types of DEBs exhibited incomplete drug release, and the maximum release achieved within 5 hours. The results also showed a decline in eluted DOX, indicating degradation and adsorption of DOX at neutral pH [70].

The future direction in DEBs is in the development of size-tunable, imageable, degradable beads. DEBs that are in support of combination treatments is another research focus. The design criteria and rationales for DEBs will be discussed in detail in the following section.

2.5 Design Criteria for Drug-eluting Microparticles

Multiple parameters that could significantly affect the clinical benefits of DEB-TACE. The morphological characteristics can affect the vascular distribution and occlusive behavior of the microparticles. Imageability/detectability is useful in guiding the intervention. More importantly, the co-localization of contrast agent with drug allows a more precise tracking of drug distribution relative to the position of the tumor. Targetability allows tumor-specific delivery through magnetic resonance navigation (MRN), potentially minimizing the unwanted toxicity to healthy tissue. Advantages of controlled release formulations include an effective drug concentration in tumor tissue and reduction of systemic exposure. The purpose of having degradable DEBs is to prevent tumor hypoxia and allow repeated interventions. Moreover, the ability to deliver

multiple therapeutics is desired as it could enable comprehensive and multimodal therapies for certain cancer patients. A multifunctional delivery system, as its name suggests, can exert multiple functions with one platform. Such system is highly advantageous for the locoregional treatment of complex diseases, such as cancer. In this section, the design considerations for multifunctional drug-eluting microparticles are rationally discussed.

2.5.1 Shape

The shape of DEBs has a significant impact on the efficacy and safety of the TACE treatment. Non-spherical poly(vinyl alcohol) (PVA) particles emerged in the 1970s as a permanent embolic option complementing degradable gelatin sponge. It was marketed as Ivalon® and distributed as a sheet or block form. For each use, PVA particles were manually produced by a sawblade or a rotating rasp. And the shavings were subsequently filtered with sieves and sorted into particles of different sizes [71]. The resulting PVA particles are irregular in shape due to the preparation method. This led to two issues: (1) the actual size does not coincide with the dimension provided by the vendor and (2) the tendency for aggregation. Derdeyn et al. [72] studied the size of PVA particles and found that many were larger than the advertised minimum size. This could mislead the radiologist in selecting the agent compatible with the dimension of vessels to be occluded. In addition, the PVA particles possessed a huge size deviation. The oblong particles may have an extremely short axis ($< 20 \mu\text{m}$) or sharp fragments. Such fractions could cause off-target embolization or end-organ damage [73]. The irregular surface and broad size distribution also led to clumps that made catheter administration very difficult. In addition, this tendency to form aggregates resulted in a larger effective size, which contributed to a more proximal rather than distal occlusion [74]. Nevertheless, particulate non-spherical PVA holds its utility in widespread scenarios where proximal occlusion is desired, such as in embolizing uterine fibroid, managing epistaxis, treating solid organ bleeding [75,76]. In situations where deeper tissue penetration is required, spherical particles would be the more suitable option.

The clinical disadvantages of irregular-shaped PVA particles prompted the development of calibrated microspheres. During the past three decades, a number of commercial

products have become available. Depending on the purpose of the application, commercial products can be classified into two categories: bland embolic agents (e.g., Contour SE™, Embosphere® and Bead Block®) and embolic DEBs (e.g., DC/LC Bead™, HepaSphere/QuadraSphere™, Embozene TANDEM™ and LifePearl®). Microspheres with calibrated sizes have demonstrated improved distal penetration and physiologic outcomes than non-spherical PVA particles, hence becoming a preferred choice for physicians [77–79].

2.5.2 Size and Size Distribution

Size and size distribution are critical in determining flow behavior and physiologic outcome of the DEB-TACE treatments. Smaller particles tend to penetrate deeper into the vasculature and reach more distal locations [78,80]. Regarding the size distribution, most commercial products are offered in a size range (e.g., 70-150 µm, 100-300 µm, and 300-500 µm) rather than in one size. A broad size range did not render significant targeting disadvantages over a narrow one. In a comparative study conducted by Laurent et al., microspheres with a broader size distribution demonstrated similar vasculature distribution in animal models as compared to narrow microparticles [81]. This study suggests that microparticles with a broad size range might provide the same level of vessel embolization as unisize beads.

Moreover, the size and shape of DEBs play a critical role in regulating the drug-eluting profile. Smaller DEBs provide faster release than larger ones due to the greater surface-to-volume ratio [82]. In addition, irregular-shaped DEBs produced a faster drug release rate compared to microspheres. This might be associated with a larger surface area [83,84]. As such, the geometrical factors of DEBs must be considered in the development of DEBs to achieve the desired embolization and drug delivery outcome.

2.5.3 Imageability/Detectability

As stated in section 2.1, vascular imaging plays an integral role in TACE by providing intra-procedural guidance for catheters, confirming complete occlusion, and post-procedural monitoring on beads distribution and tumor progression [85,86]. DEBs with intrinsic CT and (or) magnetic resonance imaging (MRI) detectability, in this regard, can

possibly be used as an indicator of drug/bead distribution and fulfil the imaging needs without multiple usages of toxic contrast agents. Imageable drug delivery systems were initially prepared by mixing radiopaque Lipiodol emulsions with the drug. However, animal studies revealed the discordance between the contrast and drug. More specifically, the spatial distribution of contrast agents did not correlate with the distribution of the drug. This could be due to the instability of the formulation and rapid passage of the drug to the systemic circulation after administration, as the bonding between the Lipiodol emulsion and the drug is relatively weak [5,30,87].

DEBs with integrated contrast agents are therefore highly sought-after in clinical practice. Since the chemotherapeutics and contrast components are held together, the location of DEBs represents the exact drug location. In addition, the intensity of the signal can be an indicator of local drug concentration. The most common approach to constructing an imageable DEB system is by incorporating magnetic nanoparticles (NPs) into the hydrogel matrix. The generation of large magnetic dipoles thereby local magnetic field gradient within the NPs will strongly alter the relaxation times of surrounding water protons, resulting an enhanced imaging contrast [88]. Commonly used magnetic NPs are superparamagnetic iron oxide nanoparticles (SPIONs), tantalum NPs, cobalt NPs, and lanthanide moieties [89].

2.5.4 Targetability

Targeted drug delivery represents another future direction for locoregional therapy, and this can be achieved by magnetic targeting. In this approach, magnetic particles are embedded in the drug carriers to localize the drugs at the site of action. The drug-carrier complex is first injected intra-arterially. High-gradient, external magnetic fields generated by rare earth permanent magnets are used to maneuver magnetic particles to achieve an exclusive drug accumulation at the tumor site [90]. The magnetic carriers contain SPIONs have demonstrated improved tumor suppressive behaviors in treating brain [91,92], lung [93] and bone cancers [94]. The limitations with magnetic targeting are that the gradient-induced forces decline rapidly with the distance from the magnet, and it is also difficult to tailor the shape of the gradient field to the anatomy. These

drawbacks limit the application of magnetic targeting to superficial tumors or small animals.

Magnetic resonance navigation (MRN), also referred to as magnetic resonance targeting (MRT), has been developed to overcome the weakness of magnetic targeting. Clinical MRI coils are explored as the source of steering (propelling) force. The distance from the magnet is no longer a restraint as MRI gradient coils can offer constant amplitude over depth as distant as 50 cm [95]. The physical principle behind MRT is to use the three orthogonal gradient coils inside the MRI bore to induce a 3D directional magnetic force to propel the magnetic particles along a predefined trajectory [96]. The majority of the state-of-art facilities use MRI machines with a magnetic field strength of 1.5 or 3T [97]. The clinical magnets (≥ 1.5 T) are considered to be sufficient for saturating the ferromagnetic materials throughout the body so a maximum magnetic force/response could be exerted on the particles [96,98].

A significant challenge with MRN is that the magnetic gradient amplitudes are insufficient for navigating smaller particles. For navigation purposes, MRI gradient coils need to generate a propelling force that could overcome the drag force. The magnetic force increases at a cubic power with the particle radius (proportional to the volume), while drag force increases in a linear fashion in laminar flow (e.g., small arteries, arterioles or capillaries) [96,99]. This suggests that larger millimeter particles can be navigated more efficiently than smaller particles. Additional gradient coils (also referred to as steering coils) could be installed in the MRI bore to acquire stronger magnetic gradients to navigate smaller particles. Upgraded gradient coils could strengthen the magnetic gradients of a 1.5-T clinical scanner from 40 mT/m to up to 400 mT/m [95]. The configurational modification allowed efficient steering of microparticles with a diameter of 11 μm in a y-shaped microfluidic channel.

As the SPIONs inside the DEBs can also serve as the contrast agents to guide the delivery, simultaneous steering and imaging are possible with a tailored MRI pulse sequence. Felfoul et al. designed an MRI pulse sequence that reserved 90% of the maximum propelling force that can be applied while imaging [100]. The author

demonstrated simultaneous steering and tracking of millimeter particles using a vascular network phantom. However, this study was lack of clinical relevance as it was conducted in the absence of flowing fluid. Further research should include the simulation of physiological fluids and tests on animal models to examine the clinical viability of the combination of steering and imaging.

In summary, the validity and efficacy of MRN have been demonstrated *in vitro* and *in vivo*. MRN provides a promising approach to deliver drugs in a non-invasive and highly targeted fashion. In imaging arena, coil configuration, control scheme, and pulse sequence must be upgraded for clinical use. In the realm of material science, efforts could be made in finding the suitable type and combination of polymers and magnetic components to ensure both imageability and targetability.

2.5.5 Controlled Release

The drug release profile has huge impact on clinical outcome of TACE. Due to the weak association between the drug and oil, Lipiodol emulsions render rapid drug release *in vivo* and quickly elevate plasma drug concentration. This burst release could lead to post-embolization syndrome and inadequate treatments [101,102].

In contrast, DEBs allow controlled drug release mainly through two mechanisms: (1) ion exchange between the positively charged drug and the same charge ions in the release medium and (2) diffusion of the drug through the polymeric network and into the release medium. Commercial DEBs including DC Bead™, HepaSphere™, Embozene TANDEM™ and LifePearl® are made of the ionic polymeric matrix, and the drug release typically follows the first mechanism [103]. The second release mechanism is prevalent in DEBs composed of non-ionic polymers, such as poly(vinyl alcohol) [104]. For drug delivery systems consisted of degradable polymers (e.g., PLGA and chitosan), other mechanisms such as erosion/ degradation of the matrix cohabits with the diffusion and can dominate over diffusion in many cases [105,106].

DEBs with controlled release functions could improve safety and efficacy of TACE through maintaining the drug concentration in tumor tissue within a therapeutic range and

lowering its levels in the systemic circulation. In a phase II clinical trial, DEB-TACE group significantly decreased the drug-related systemic and liver toxicity versus the cTACE group. In addition, the response rate and disease control rate was higher in the DEB-TACE group [31].

2.5.6 Degradability

As suggested by Ha et al., TACE was performed every 6-8 weeks to eradicate tumors until thromboses and/or metastases were developed or patients cannot tolerate more hepatic damage [107]. Degradable DEBs could be beneficial in TACE to (1) prevent extended periods of tumor hypoxia, as it can stimulate the expression of vascular endothelial growth factor (VEGF), which adversely promote tumor growth [108], and to (2) allow repeat treatments.

Over the past decade, numerous multifunctional DEBs composed of degradable materials were explored (Table 2.5). Such systems are typically composed of hydrogel matrix with cleavable linkers that can disintegrate in the presence of acidic hydrolysis, enzyme or reactive oxygen species (ROS) environment *in vivo* [109]. Future work could be dedicated to the study of degradation rate, degradation products and the effect of degradation on angiogenesis.

Table 2.5 Overview of the degradable drug-eluting microparticles.

Material	Particle diameter (μm)	Drug	Loading capacity	<i>In vitro</i> drug release		<i>In vitro</i> degradation		Reference
				Release medium	Results	Degradation medium	Results	
Chitosan	132	DOX	CMs: 115 mg/g, ACMs: 107 mg/g	PBS (pH 7.2) at 37 °C Sodium citrate buffer (pH 4.0) at 37 °C	pH 7.2: CMs: 70% at plateau at 20 h ACMs: 80% at plateau at 28 h pH 4.0: CMs: 80% at plateau at 6 h ACMs: 90% at plateau at 16 h	HAc-NaAc buffer (pH 6.0) containing 0.5 mg/ml lysozyme at 45 °C	Weight loss: CMs: 40.7%, ACMs: 58.1%	111
Chitosan and carboxymethyl cellulose	100-1000	DOX	66-77 mg/g MSs (depending on size)	0.9% normal saline (pH=6), acetate buffer (pH=5.2), PBS (pH=7.4) at 37 °C	pH 6: 34.7% at plateau at day 2 pH 5.2: 23.5% at day 2, 39% at plateau at day 14 pH 7.4: 19.6% at plateau at day 2	0.01 M PBS (pH 7.4) containing 4 mg/ml lysozyme	14-88 days (depending on size)	112
Gellan gum	200-730	DOX	28 mg/g beads	0.02 M PBS (pH 7.4) at 37 °C	7.3 $\mu\text{g}/\text{ml}$ at day 45	N/A		113
Silk fibroin and alginate	142	Adriamycin hydrochloride	N/A	PBS (pH 7.4) at 37 °C	80% at 80 h	PBS (pH 7.4) at 37 °C	Weight 4.1% at day 7, 20.8% at day 21	114
PLGA	26.36 \pm 6.39	DOX	Encapsulation efficiency ^a 50%	PBS; pH 5.5, 6.8, and 7.4 at 37 °C	pH 5.5: 35% at plateau at day 3 pH 6.8: 48% at plateau at day 3 pH 7.4: 73% at plateau at day 3	50% (v/v) FBS in PBS (pH 7.4) at 37 °C	MSs developed irregular shape and multiple pores on the surface after 2 weeks incubation, diameter decreased by 20%	115
PLGA and hyaluronic acid-ceramide (HACE)	27 \pm 4	DOX	Encapsulation efficiency 65%	PBS; pH 5.5, 6.8, 7.4 at 37 °C	pH 5.5: 28% at day 1, 42% at day 7 pH 6.8: 21% at day 1, 33% at day 7 pH 7.4: 2.5% at day 1, 25% at day 7	50% (v/v) FBS in PBS (pH 7.4) at 37 °C	MSs developed irregular shape and multiple pores after 14-day incubation	116
PEGMA and PEG-PLGA	300-500	DOX	Encapsulation efficiency 92%	N/A	N/A	Phosphate buffer at 37 °C	100% weight loss at day 2	117

$$^a \text{ encapsulation efficiency (\%)} = \frac{\text{actual amount of DOX in microspheres}}{\text{mass of feed drug}} \times 100\%$$

DOX: Doxorubicin, CMs: chitosan microspheres, ACMs: acetylated CMs, PLGA poly(lactide-*co*-glycolide) (PLGA), MSs: microspheres, PEG: poly(ethylene glycol), PEGMA: poly(ethylene glycol) methacrylate, N/A: not available.

2.5.7 Delivery of Multiple Therapeutics

The co-delivery of multiple therapeutics with complementary modes of action represents another future direction for DEBs. TACE leaves the chemotherapy-damaged HCC cells under hypoxic conditions, transforming the cancer cells into a more aggressive phenotype [110]. Studies have demonstrated the embolization stimulated the expression of VEGF that will promote angiogenesis [111]. Systemic administration of antiangiogenic drugs such as thalidomide [111], vandetanib [112] and sorafenib/sunitinib (both are antitumoral and anti-angiogenic) [113,114] combined with TACE have demonstrated satisfying angiogenesis-suppressing effects in animal models. It is therefore logical to locoregionally co-deliver these drugs with anti-tumor agents using DEBs [115]. Forster et al. loaded DC BeadTM with several drug combinations and compared their treatment safety and efficacy [116]. The co-delivery of two drugs displayed synergistic activity and reduced cellular toxicity versus the single-drug loaded DEBs. Other types of therapeutics such as anti-inflammatory agents (e.g., ibuprofen) can be considered as they may reduce post-embolization inflammation and pain [117].

2.6 Design of Multifunctional Materials for Drug Delivery

Science, technology and medicine are continuously looking for new and improved treatments for diseases, which tremendously catalyzed research on less toxic, effective and cost-effective drug delivery options [118]. The mixing of known materials: nanoparticles and hydrogels, offers a simple and effective material strategy to address the clinical needs.

The structural combination of nanoparticles with hydrogels creates a composite platform, often referred to as nanocomposite hydrogel or nanoparticle-hydrogel composite [119]. Such material bears great potential to integrate the desirable properties of both

components (i.e., nanoparticle and hydrogel) into a single system and enable additional functions through the nanoparticle-hydrogel interactions [120].

Nanocomposite hydrogels can be prepared through four main routes. For the first route, nanoparticles are entrapped in the polymeric network by the gelation of hydrogel monomers in the presence of preformed NPs [119]. Alternatively, the incorporation of NPs can be accomplished after hydrogel gelation by allowing the polymeric network to swell and ‘breathe in’ the suspended NPs [121]. Moreover, the NPs could be introduced into the gel matrix by loading the hydrogels with the metallic nanoparticle precursors, followed by a reduction reaction to form metal NPs [122,123]. Another approach to prepare nanocomposite hydrogels is to use NPs as hydrogel crosslinkers (referred to as the grafting-onto method in section 2.7.2). Depending on the end groups, the particles are anchored in the hydrogels through covalent or non-covalent bonds (e.g., ionic or coordination interactions) with the polymeric chains [124,125].

The properties of the nanocomposite hydrogels are dependent on the innate properties of the individual components and particle-hydrogel interactions. As shown in Figure 2.2, commonly used nanoparticles and hydrogels with their desirable properties are listed. Nanoparticles can bring many unique functions: magnetic responsiveness [99], diagnostic imaging [126], electrical conductivity [127], antimicrobial activity [128], and compatibility with both hydrophilic and hydrophobic drugs [129]. Hydrogels are known for their stimuli-responsive [130], mechanical toughness [131], bioadhesive [132,133] and controlled release properties [130]. To satisfy the application requirements, the materials and the preparation methods must be carefully selected.

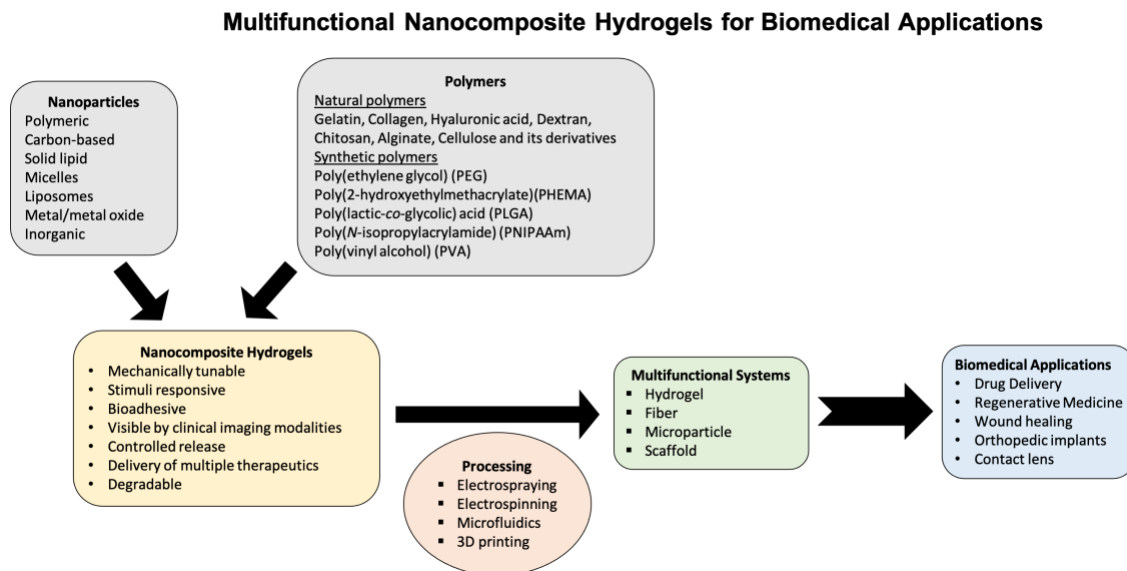


Figure 2.2 Design and processing of a multifunctional hydrogel system for biomedical applications.

The structural and dimensional diversity between the nanocomponents and hydrogels provide an effective strategy for the independent delivery of one or more drugs. A composite system containing PLGA nanoparticles and hyaluronan (HA)/methylcellulose (MC) hydrogel allowed fast drug release from the hydrogel while slow release from the nanocarriers [134]. This unique feature was adopted by Zhao et al. to deliver two types of drugs independently [135]. The authors achieved dual drug delivery by formulating PTX-loaded PLGA NPs into temozolomide (TMZ)-loaded hydrogel. The co-delivery of PTX and TMZ resulted in a synergistic effect on glioblastoma cells. In addition to loading one drug in hydrogel while the other in nanocarriers, an independent delivery can be achieved by incorporating distinct drug-loaded carriers. For example, Patel et al. prepared curcumin-encapsulated poly(L-lysine-*b*-L-phenylalanine) micelles and amphotericin B-encapsulated poly(L-glutamic acid-*b*-L-phenylalanine) micelles, separately [136]. Hydrogel matrix was created by cross-linking the pendant groups of the polypeptides using genipin as a crosslinker. The different pH responsiveness of the two nanocarriers permitted independent and switchable release of the corresponding drug. The drug release rate can also be tuned by varying the dosage of genipin. The realization of dual drug

delivery might be helpful in post-surgical cancer management or wound healing, as it may provide a synergistic effect.

The constitution of nanocomposite hydrogels can potentially address the challenges in which the nanoparticles or hydrogels are used alone. For example, the incorporation of lipophilic nanocarriers can potentially address the incompatibility of hydrogels with hydrophobic therapeutics. In turn, the presence of hydrogel can prolong the drug release from nanoparticles. Yu et al. utilized lipid nanocarriers to encapsulate a hydrophobic drug, quercetin, and reached an encapsulation efficiency greater than 97% [137]. The drug-loaded nanoparticles were then physically embedded in a mixture of carboxymethyl chitosan (CMCS) and Pluronic[®] F-127. The resulting delivery system provided a slower release rate than that of drug-lipid nanoparticles in the absence of hydrogel. This was believed to be contributed by the three-dimensional and water-dense polymeric network, which imposed a longer diffusion path and additional diffusion barrier to drug molecules [138]. In a comparative study, drug release was performed on two formulations: kartogenin (KGN)-loaded halloysite nanotubes (HNT) and KGN-HNT embedded in laponite (Lap) hydrogel (KGN-HNT-Lap) [139]. The release kinetics showed that the composite formulation greatly prolonged the KGN release compared with KGN-HNT system. The authors substantiated that the hydrogel could act as an inert medium to slow down KGN release.

In addition, the nanoparticle and polymeric network interactions can render the composite material with unique properties that are not found in individual components. For example, Bannerman et al. developed a composite hydrogel comprised of IONPs and PVA [140]. The biostable PVA developed degradation behavior under an acidic and iron-chelating environment. It was believed that the IONPs participated in the cross-linking of PVA. As a result, the gradual removal of IONPs would weaken the PVA matrix and allowed the degradation to occur. Nasajpour and coworkers fabricated a microfibrinous membrane of zinc oxide (ZnO) NPs in PCL [141]. It was found that the composite membranes degraded faster than plain PCL membranes (pH 7.4 and 8.5). The authors believed that the incorporation of ZnO NPs created cavities within the polymer matrix,

which may facilitate water diffusion into the PCL. Moreover, the hydrophilic nature of ZnO NPs may also play a role in promoting PCL-water interaction [141].

Taken together, the combination of nanoparticles with hydrogels provides a multifunctional platform for drug delivery applications. Such platform endows function integration from each component and can potentially overcome the limitations of nanoparticle and hydrogel systems when they are used independently. Moreover, it provides an additional degree of freedom in designing or tailoring delivery systems through nanoparticle-polymer interactions.

With the employment of different material processing techniques, the biomedical application of nanocomposite hydrogels has gone far beyond what a macroscopic system can reach (Figure 2.2). Electrospaying [142], electrospinning [143], microfluidics [144] and 3D printing [145] have been used to produce drug delivery systems in the forms of fiber, microbead and scaffold. The diversity in the geometry could even expand the application spectrum of nanocomposite hydrogels into regenerative medicine and multimodal cancer treatments [146–148].

2.7 Choice of Materials and Proposed Systems

2.7.1 Poly(vinyl alcohol)

Poly(vinyl alcohol) (PVA) is one of the most commercially important water-soluble thermoplastics in use. It has widespread pharmaceutical and biomedical applications, including drug carriers, scaffolds, wound dressing, contact lens and orthopedic implants [149].

PVA must be stabilized by crosslinking to form a hydrogel before many of its applications in biomedical research. Hydrogels are regarded as hydrophilic, crosslinked polymeric networks that are able to imbibe larger amounts of fluids and swell when placed in water or biological fluids without losing their structure [150]. The crosslinking strategies for PVA can be classified as physical and chemical crosslinking.

Chemical crosslinking use crosslinkers to form covalent bonds between PVA's secondary hydroxyl groups. Commonly used crosslinkers are monoaldehydes (e.g., acetaldehyde and formaldehyde), bifunctional aldehydes (e.g., glutaraldehyde and glyoxal)[151] and dicarboxylic acids (e.g., citric acid and maleic acid) [152,153]. The hydroxyl groups of PVA react with the crosslinking agents to form intermolecular acetal bridges (bonds) where crosslinking could occur [154]. In addition to crosslinkers, sulfuric acid, acetic acid or methanol must be used to form the acetal bridges. PVA hydrogel formed by chemical crosslinking always retains toxic crosslinkers, which could result in unwanted biological effects. The residue of initiators, stabilizers and chain transfer agents could also hinder the *in vivo* application of PVA [155].

High energy irradiation offers an alternative approach to prepare chemically crosslinked PVA. During this process, electron beam or γ irradiation is used to generate free radicals on the polymeric chain. The radicals would subsequently combine through covalent bonds to form a crosslinked network. The advantages of this strategy are: no crosslinkers are required; no residual impurities; the degree of crosslinking and the pore size of PVA gels are tunable by radiation dose and concentration of the polymer solution [156]. The limitation with this method is that the radiation exposure may damage the bioactive payloads if the crosslinking is performed after the loading [157].

Physically crosslinked PVA prepared by freezing-thawing technique has generated significant interest in biomedical research due to the avoidance of toxic crosslinking agents and impurities. In a typical preparation, a homogenous PVA solution is placed under repeated freezing and thawing cycles. The gel obtained from such cryogenic treatment is often referred to as a cryogel [158]. Phase separation and crystallization are the major mechanisms for cryogel formation and impact independently during the freeze-thaw cycles [159]. The formation of the crosslinked microstructure consists of multiple stages. During the freezing process, ice crystals formed within the homogenous PVA solution. The water volume expansion and phase separation expel PVA into close contact with each other and result in the formation of polymer-rich regions and polymer-poor regions. In the polymer-rich regions, PVA chains come into close contact with each other, facilitating the intra- and intermolecular interaction through hydrogen bonding

[159,160]. Repeated freezing processes allow polymer chains to fold into highly structured crystallites in PVA-rich regions as network junctions. In thawing stages, ice crystals melt, leaving water-filled micrometer-sized pores that make up the polymer-poor regions [158].

A number of process parameters in the preparation could be used to tailor the structure and properties of PVA cryogels. These parameters include but are not limited to temperature limits of thermal cycling, number of freezing-thawing cycles, polymer concentration in the solution and molecular weight of PVA [161]. These parameters affect the properties through chain mobility and intermolecular hydrogen bonding, resulting in variations in the size and number of crystallites. PVA cryogels with more crystalline structures (higher crystallinity) generally display a smaller porosity and higher rigidity [155,158].

Among all the characteristics, the diffusivity of PVA gels attracted particular attention in the areas of drug delivery. The porous polymeric network of PVA cryogels, which consists of crystalline regions (~3nm) and amorphous regions (~19 nm), regulates the transport process of drugs throughout the matrix [158]. The research concluded that the diffusion of solutes from hydrogels is related to the mesh size (i.e., the open space between polymer chains), which is inversely correlated to crystallinity. Hydrogels with higher crystallinity generally have smaller mesh sizes, which would impede the release of entrapped macromolecular drugs [162]. Small drug molecules with a dimension smaller than the mesh can move freely through the network, while the migration of larger molecules such as proteins will be retarded [163,164]. As such, the mesh size can be an effective tool for modulating drug loading and controlled release.

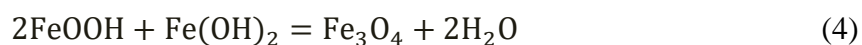
The biodegradation, in contrast to the stability, represents an event where the materials degrade, the products become resorbed and disappear via metabolic routes [165]. Biodegradable/bioresorbable materials are particularly advantageous to be used for DEBs as they allow multiple benefits such as reduced tissue inflammation, controlled drug release, and repeatable interventions [166]. PVA-based commercial DEBs: DC Bead[®] and DC Bead LUMI[®] are not degradable. Luckily, material compounding and blending

provides two effective strategies to make PVA gels degradable. Bannerman et al. introduced IONPs to the PVA hydrogels through *in situ* co-precipitation [140]. IONPs were allowed to interact with PVA chains during the subsequent freezing-thawing cycles and provide a certain degree of crosslinking to PVA. As a result, the gradual dissolution of IONPs in an acidic environment would weaken the linkages and lead to the dissolution/degradation of PVA. Another approach to construct degradable PVA hydrogels is through blending. PVA has been blended with degradable hydrogels such as chitosan [167], sodium alginate [168] and gelatin [150]. As intermolecular hydrogen bonding is formed throughout the polymer blends, the degradation of the other polymers can unfold the crystal chains and result in PVA dissolution [169,170].

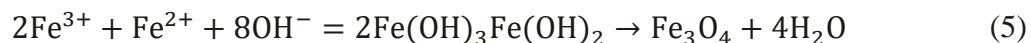
2.7.2 Iron Oxide Nanoparticles

Nanotechnologies have emerged as a powerful tool in cancer therapy and the diagnosis of diseases [171]. Among all the nanomaterials, iron oxide nanoparticles (IONPs) have gained particular interests due to their excellent magnetic properties and biocompatibility. IONPs have been extensively investigated for widespread biomedical applications, such as magnetic drug targeting, magnetic resonance imaging (MRI), gene therapy and hyperthermia/thermal ablation [172]. The most studied IONPs are magnetite (Fe_3O_4), maghemite ($\gamma\text{-Fe}_2\text{O}_3$) and hematite ($\alpha\text{-Fe}_2\text{O}_3$) nanoparticles (NPs).

IONPs are commonly prepared by two chemical approaches: co-precipitation and thermal decomposition. Co-precipitation involves the simultaneous precipitation of ferrous (Fe^{2+}) and ferric (Fe^{3+}) ions in an alkaline environment. The mechanism of magnetite NPs formation can be described by the following reactions [122]:



The overall reaction can be represented by:



The size, shape and composition of the magnetite NPs can therefore be tuned by altering the experimental parameters, including $\text{Fe}^{2+}/\text{Fe}^{3+}$ molar ratio [173], pH [122], temperature [174], choices of iron precursors (e.g., chloride, sulfate or nitrate) and alkaline agents (e.g., NaOH, NH_4OH or isopropanolamine) [175–177]. While the co-precipitation process is the most simple and efficient approach to synthesize IONPs, the products often develop a low degree of crystallinity and large size distribution [177].

In contrast to co-precipitation, thermal decomposition is performed in a non-aqueous environment and can better control the size, shape, and polydispersity of IONPs [178]. In a thermal decomposition reaction, organic complexes of iron (e.g., iron oleate, iron oxyhydroxide or iron pentacarbonyl) decompose at elevated temperatures in the presence of non-polar solvents and surfactant capping agents [179]. Surfactants are crucial in this process because they modulate the nucleation and growth of the IONPs to ensure good mono-dispersity [180]. The concerns with thermal decomposition are high temperatures and toxic residuals of the organic chemicals employed [178]. In addition, the non-hydrolytic nature of the reaction renders IONPs with hydrophobic surfaces, which imparts additional modification steps to make water-dispersible and stable IONPs that are suitable for biomedical applications [181]. Of note, for both synthesis routes, with the addition of oxidizing agents (e.g., HNO_3), $\gamma\text{-Fe}_2\text{O}_3$ or $\alpha\text{-Fe}_2\text{O}_3$ can be synthesized [182].

Iron oxide nanoparticles must be endowed with the specific characteristics required for targeted biomedical applications. The first and foremost properties are always biocompatibility and toxicity [183]. IONPs are generally considered as safe, biocompatible and non-toxic materials. The median lethal dose (LD_{50}) of the bare IONPs is 300-600 mg/kg body weight. Dextran coating could effectively improve the stability and biocompatibility of IONPs and increase this number to 2,000-6,000 mg/kg [184]. Due to the broad safety margin of IONPs, a number of surface-coated IONPs have been clinically approved as MRI contrast agents, such as ferumoxide, ferumoxtran and ferumoxytol [185].

The biodistribution of IONPs is dependent on the administration route and physicochemical factors, such as size, porosity, charge and surface chemistry [186]. For intravenously injected IONPs, they are removed from the circulation majorly by the mononuclear phagocyte system. It has been reported that IONPs with a hydrodynamic size (d_H) > 100 nm quickly accumulate in the liver and spleen through macrophage phagocytosis. In contrast, particles with d_H < 10-15 nm are most likely to be eliminated through the kidney in a non-phagocytizing pathway [183]. The internalized IONPs are metabolized in the lysosomes. The acidic pH environment and intracellular iron chelators (e.g., phosphate, nucleotides and dicarboxylic acids) can solubilize IONPs into free irons [187]. These irons would subsequently enter the intracellular iron pool and be utilized in the production of hemoglobin and transferrin, thereby becoming part of the normal iron pool [185]. The excess irons are stored in ferritin or exported by ferroportin, in order to maintain the iron concentration within limits to avoid toxicity [188,189].

Another crucial property to support the biomedical applications is the magnetic properties, particularly superparamagnetism, as it is highly relevant to MRI, hyperthermia and magnetic drug targeting. In the presence of a magnetic field, the magnetic moments of superparamagnetic materials could align with the direction of the field without any remanence magnetization. Fe_3O_4 and $\gamma-Fe_2O_3$ NPs are the two major superparamagnetic iron oxide nanoparticles (SPIONs) employed in research and clinical studies. Their high saturation magnetization values (M_s 70-100 emu/g) [190–192] allow generation of large magnetic dipoles thereby local magnetic field gradient within the NPs, which will strongly alter the spin-spin (i.e., transverse, T_2) relaxation times of surrounding water protons, resulting an enhanced imaging contrast [88]. Generally, SPIONs (~16-200 nm) are used as negative contrast agents for T_2 -weighted MRI, while smaller (<15 nm) IONPs are effective as T_1 (i.e., positive) contrast agents [193]. In addition, the relatively high M_s values of SPIONs would also allow precise spatial control over the particles in the blood using an external magnetic field generated by a magnet or MRI coil. This activity has been translated into magnetic drug targeting and MRN, as described in section 2.5.4. The current challenges with MRN are in designing gradient coils to ensure stronger propelling force [194].

Moreover, SPIONs can respond to an alternating magnetic field and convert the magnetic energy to heat within the particles. The heat generated can be used to elevate the temperature of the surrounding tissue. The effectiveness of hyperthermia relies on the fact that a temperature between 41-43 °C can cause tumor cell death, as they are less tolerant to heat than normal cells [195,196]. In hyperthermia treatments, SPIONs can be administered intravenously or intratumorally. Particle concentration should be large enough to deliver a sufficient heating effect.

Despite the great potential of IONPs in diagnostic imaging and drug delivery, the limitations with using such particles as an individual delivery system are also obvious: poor colloidal stability, short blood circulation, burst release, limited drug loading capacity, plasma protein adsorption, and unregulated biodistribution and pharmacokinetics [183].

To address these limitations and further expand the applications of IONPs, a composite platform named ferrogel (i.e., the combination of hydrogels with IONPs) was developed [197]. Ferrogels can be prepared mainly via three routes: blending, *in situ* co-precipitation, and grafting-onto. They can be further classified into polymer-first (*in situ* co-precipitation) and particle-first (blending and grafting-onto) approaches [198]. The scheme for the three approaches is shown in Figure 2.3. Depending on the choice of materials and the preparation methods, IONPs can form different interactions with the hydrogel matrix. The blending method consists of a sequential preparation, where IONPs are synthesized separately and added to a hydrogel precursor solution. The mixture is then stabilized by the crosslinking of the hydrogel. While being facile, the blending method fails to achieve a uniform nanoparticle distribution within the polymeric network. Moreover, particles remain attached mainly through physical entanglement and hydrogen bonding with the polymer chains [199]. Due to the limited particle-hydrogel interactions, IONPs might diffuse out from the hydrogel upon swelling [200]. In the *in situ* co-precipitation process, the hydrogel matrix acts as the reactor. In detail, hydrogels are firstly crosslinked through chemical or physical routes. The IONP precursors (Fe^{2+} and Fe^{3+}) are prepared in a stoichiometric ratio and mixed with the crosslinked hydrogel to form a homogenous solution [122]. The gels are subsequently immersed into an alkali

solution for the IONPs to precipitate. The mechanism with which IONPs are immobilized in the gel was not fully elucidated. However, it is believed that the IONPs participate in the polymeric network formation through hydrogen bonding with the hydrogel chains [140,201,202]. *In situ* co-precipitation provides improved IONP dispersion in the hydrogels. However, this method is limited to alkali-resistant polymers and should also be avoided in hydrogel systems containing bioactive compounds, such as proteins and cells, as the harsh environment may damage their bioactivity [203]. Compared to blending and *in situ* precipitation methods, the grafting-onto approach provides particle-hydrogel interactions through covalent bonds in addition to hydrogen bonds and van der Waals forces [204]. In the grafting-onto method, IONPs serve as the crosslinkers to the hydrogel monomers. In detail, IONPs are initially functionalized with reactive moieties (e.g., $-NH_2$ and $-COOH$). The nanoparticles are then added into a monomer solution to form covalent bonds with the monomers when polymerized. As the IONPs are covalently bonded to the network, the stability of ferrogel is guaranteed [125]. In the future, the grafting-onto method would benefit from research efforts in simplifying the preparation cycle and fabrication process [200].

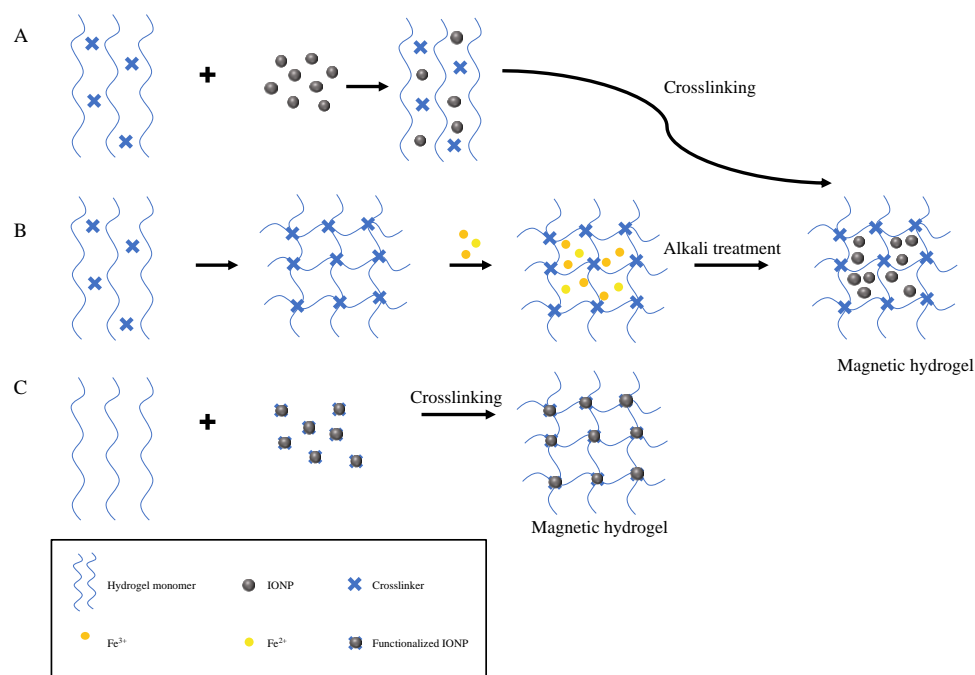


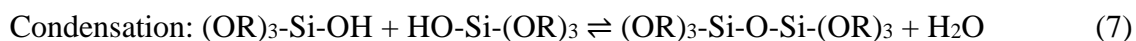
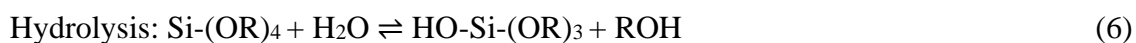
Figure 2.3 Schematic of ferrogel preparation. (A) The blending method. (B) The *in situ* precipitation method. (C) The grafting-onto method.

Overall, IONPs have been helpful in the development of multimodal therapeutic strategies, enabling a simultaneous exertion of therapeutic effect, hyperthermia and diagnostic imaging. Further research could focus on the development of self-healing materials and magnetically sensitive smart hydrogels [203]. Despite the wide range of applications, the cytotoxicity and long-term fate of magnetic materials, including individual particles and ferrogels, have yet to be fully revealed. As such, *in vivo* studies using animal models should be continued to supplement *in vitro* findings.

2.7.3 Silica Particles

Considerable research efforts have been made in developing silicate materials for biomedical applications. Silica (also known as silicon dioxide, SiO₂) has been "generally recognized as safe" by the FDA for more than five decades and is widely used in the food industry as a color or formulation stabilizer [205,206]. Among all types of silica, SiNPs plays a particularly critical role in fulfilling the rigorous clinical requirements for disease diagnosis and controlled drug release. The presence of abundant surface silanols (Si-OH) allows the conjugation of various organic functional groups, rendering SiNPs with a high level of versatility for drug delivery applications [207].

SiNPs are predominantly synthesized via the sol-gel process. Both hydrolysis and condensation can be acid- or base-catalyzed. Sol-gel process typically involves the hydrolysis and condensation of alkoxide precursors [e.g., Si(OC₂H₅)₄ or TEOS] in the presence of alcohols (e.g., ethanol), water and catalysts (e.g., NaOH or HCl). The simplified reactions that form SiNPs can be represented by [208]:



where R=alkyl group

The reaction forms a discrete, colloidal suspension (i.e., sol). The colloidal particles (1-100 nm) within the sol then condense to form an interconnected, rigid network with pores and polymeric chains (i.e., gel). The viscosity of the solution increases sharply at gelation and can eventually form a solid object in the shape of the mold [209]. The final product

of the sol-gel process is profoundly affected by the rate of hydrolysis and condensation reaction [210]. In an acidic environment, hydrolysis is slow. The silica tends to form a linear, weakly crosslinked network. Gelation proceeds by the formation of additional branches and the entanglement of polymeric chains. As a result, acid-catalyzed sol-gel generally leads to a gel structure [211]. In contrast, hydrolysis and condensation are fast in the basic-catalyzed process [208]. This results in the rapid formation of highly branched and non-interpenetrable clusters [209]. The clusters collide and lead to larger aggregates through hydrogen bonding and van der Waals interactions. At a critical concentration, the aggregates will precipitate in the form of discrete species as SiNPs [210]. Various mechanical (e.g., centrifugation) and physical (e.g., oven drying and alcohol dehydration) techniques can accelerate the water removal hence the formation of SiNPs [211].

As the pH conditions lead to silica networks with distinct properties, it is not surprising to see that each catalytic condition has its own characteristic applications. Acid-based sol-gel synthesis is predominately utilized in the development of nanocomposite hydrogels. Namely, the reaction occurs in the presence of hydrogels to form SiNPs-embedded hydrogels. The relatively slow hydrolysis step would result in molecular chains contain sufficient silanol groups to participate in hydrogen bonding with the hydrogel polymers [209]. The formation of SiNPs-hydrogel interaction affects the intramolecular bonding of the polymeric chains; therefore could help modify the mechanical properties and permeability of the gels [212–214]. For example, a silica/PVA composite hydrogel was prepared by *in situ* sol-gel synthesis [213]. SiNPs possessed good dispersion in the hydrogel matrix and developed strong interaction with PVA through Si-O-C bonds. Results showed that SiNPs served as a stiffness enhancer to PVA. A greater mass percentage of SiNPs in the PVA increased Young's modulus by up to ~14 folds. Similarly, silica/PVA nanocomposite hydrogel was prepared and electrospun into nanofibers [215]. The author found that the *in situ* formation of SiNPs contributed to the crosslinking of PVA, which reduced the -OH available for hydrogen bonding with water. As a result, the PVA exhibited improved aqueous stability.

Base-catalyzed mechanism is widely employed in the preparation of discrete SiNPs. Such a process is considered simple, fast and allows precise size and morphology control [216]. Stöber and Fink pioneered this approach in synthesizing non-porous silica spheres in the range of 50-2000 nm [217]. The authors found that particle size was dependent on the type of alcoholic solvents, silica precursors, and the concentration of water and ammonium hydroxide. The resulting non-porous silica particles are extensively used as hydrogel nanofillers [218], stabilizing agents [205,206] and matrix for protein adsorption study [219]. The applications of non-porous silica particles have been extended into drug carriers after surface modification with appropriate functional groups [220].

Base-catalyzed sol-gel process has also been adopted to prepare mesoporous SiNPs (i.e., SiNPs with pores sizes in the range of 2-50 nm) [221,222]. Amphiphilic copolymers or cationic surfactants are essential in the synthesis of porous SiNPs, as they serve as pore template and determine pore size. Templates with longer chain lengths typically result in larger pores [223]. As the drug transportation within non-functionalized porous SiNPs is through diffusion, the pore size and volume must be carefully designed to modulate the payload loading and release. Greater pore size and volume generally result in larger loading and faster release than particles with smaller pores [224]. This could be explained by the steric hindrance effects inside the mesopores [225]. Mesoporous SiNPs with extra-large pores (~25 nm) are extremely helpful in the loading and release of proteins, enzymes and DNA vaccines [223,226,227].

Sol-gel SiNPs, either in porous or non-porous form, are semicrystalline material and susceptible to hydrolytic attack, which encourages the degradation and clearance of SiNPs *in vivo*. The degradation process contains multiple stages: hydration, hydrolysis and ion exchange. The silica framework will eventually be converted to silicic acid ($\text{Si}(\text{OH})_4$, pKa 9.6), a water-soluble compound [228]. The rate of dissolution is largely dependent on the physicochemical properties of the particles [229], pH [230] and composition of the dissolution media [231]. Silicic acid is non-toxic and has a natural promoting effect on bone mineral density [232]. The degradation product can diffuse through the bloodstream or the lymphatic system. The ultimate excretion is through urine by the kidney [233].

In conclusion, SiNPs have gained growing interests as an advanced platform for biomedical applications. For future directions, more studies are expected in the evaluation of the toxicity, biological stability, and efficacy of SiNP-based delivery systems. Innovations could be made in designing targeted, stimuli-responsive platforms for gene and vaccine delivery [234].

2.7.4 Proposed Systems

This thesis covers three multifunctional delivery systems. The research work of Chapter 3 and Chapter 5 is based on composite hydrogel microparticles, while Chapter 4 contains work on the silica nanoparticles.

Chapter 3 PVA-IONP microparticles

Chapter 3 describes a multifunctional ‘nano-on-micro’ drug delivery system. Figure 2.4 shows the composition of the system. In detail, magnetite (Fe_3O_4) nanoparticles were immobilized in the PVA matrix via *in situ* co-precipitation followed by freezing-thawing process. The targeted particle size is 100-300 μm , as the beads in this size range are preferred in clinics due to the effective local necrosis and less systemic complications compared to larger ones [62–64].

PVA-IONP Microparticles

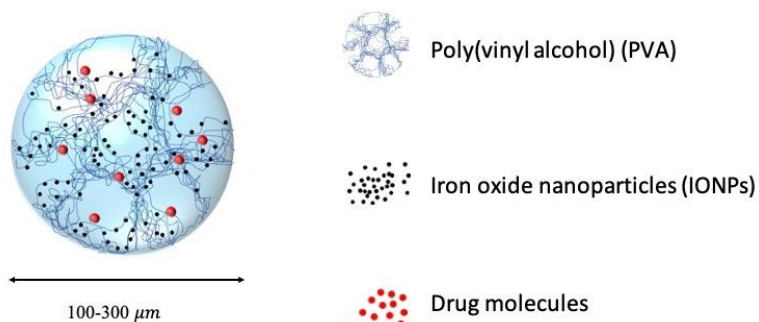


Figure 2.4 Schematic drawing of a multifunctional PVA-IONP microparticle.

The PVA-IONP microbeads are promising candidates for embolic DEBs in TACE therapy due to the following reasons: the avoidance of toxic chemical crosslinkers; the

ability to embolized tumor-supplying vessels; drug loading and controlled release capacities; the co-localization of drug with contrast agent; the potential for targeted drug delivery through image-guided magnetic resonance navigation (MRN) of the superparamagnetic microparticles; the possibility for repeatable TACE treatments, as the degradation of microbeads can occur with the dissolution of IONPs and the disintegration of PVA matrix.

Chapter 4 SiO₂ nanoparticles

The protein delivery system is based on non-porous SiNPs, as shown in Figure 2.5. SiNPs were synthesized by Stöber process and loaded with bioactive proteins via adsorption. SiNPs interact with proteins through hydrogen bonding and electrostatic interactions. The targeted size of the protein carrier is 100-400 nm, as it can provide a reasonable residence time on the ocular surface [235–237]. Such delivery system can potentially fulfill several roles: protection from protein decomposition, sustained release and tunable release profile. The system is hypothesized to be helpful in topical delivery of protein therapeutics to treat dry eye disease by reducing the dosing frequency and allowing personalized drug dosage.

SiNP-Bioactive Protein System

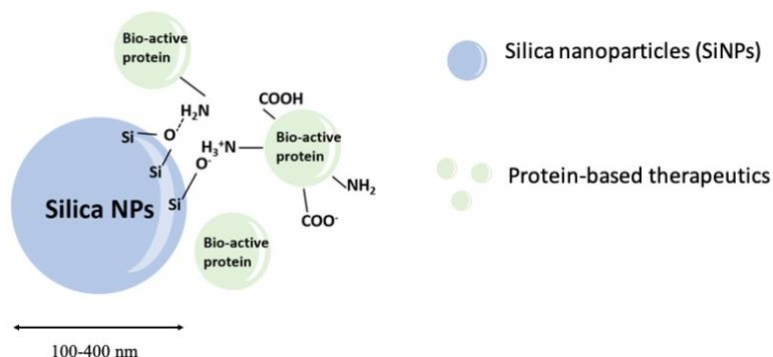


Figure 2.5 Schematic drawing of the bioactive protein delivery system.

Chapter 5 PVA-SiO₂-IONP microparticles

The formulation described in this chapter is a continuation and optimization of the PVA-IONP system. The multifunctional drug carrier in Chapter 5 is comprised of a PVA matrix, loaded with IONPs and SiO₂ microparticles (Figure 2.6). Similar to the PVA-IONP system, PVA-SiO₂-IONP microparticles are anticipated to be beneficial for application as DEBs for TACE treatment.

PVA-SiO₂-IONP Microparticles

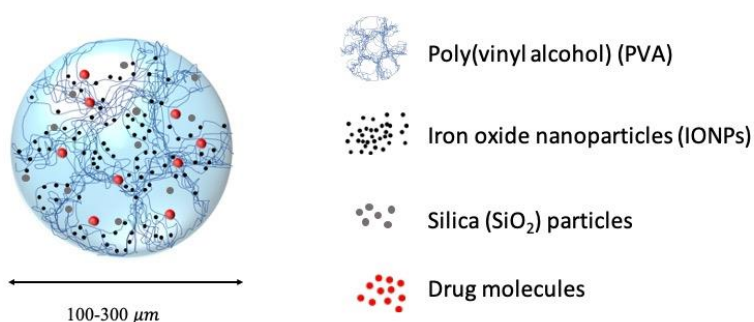


Figure 2.6 Schematic drawing of a multifunctional PVA-SiO₂-IONP microparticle.

2.8 System Assembly using Microfluidics

Microfluidics will be used to produce our microparticulate multifunctional drug carriers. The materials and fabrication techniques for microfluidic chips, droplet generation mechanisms, and channel configurations will be reviewed in this section. The advantages of using microfluidics in fabricating drug delivery systems will also be discussed. The detailed fabrication approach will be described in Chapter 3 and Chapter 5.

2.8.1 Materials and Fabrication Techniques for Microfluidic Chips

Poly(dimethylsiloxane) (PDMS) is the most common microfluidic material employed in research laboratories due to its convenient fabrication by soft lithography and reasonable cost [238]. Devices with 3D structures or multilayers can be prepared via curing individual pieces at mild temperatures (40-70 °C) and stacking [239]. The ability to exchange oxygen and carbon dioxide expands its application into cell-related research

(e.g., biological interactions, cell sorting, bioanalysis and diagnostics) [240–242]. However, the alkyl groups attached to PDMS's Si-O backbone lead to nonspecific adsorption and swelling. More specifically, hydrophobic molecules and biomolecules could adhere to channel walls and lead to channel clogging and inaccuracy in the measurements [243,244]. Another drawback is the incompatibility with organic solvents [245]. Upon exposure to organic solvents such as acetone, swelling of the channel would affect droplet generation and device deformation [246]. Surface modifications of the PDMS with hydrophilic moieties can address these issues, but the challenges arose in maintaining the long-term stability and hydrophilicity of the modified surface [247,248].

PMMA has gained interests as an alternative to PDMS. PMMA is particularly useful for disposable chips because of its fairly good rigidity, chemical resistance, transparency and biocompatibility [249]. In general, PMMA microfluidic microdevices consist of channel plates and cover plates that need to be sealed together. The channel plate can be created using a wide range of techniques [250], including hot embossing, laser ablation, imprinting, molding and solvent etching, making them desirable for mass manufacturing. However, creating uniform surface bonding of the two plates without deforming the channel structure represents a significant barrier for industrial fabrication. A number of approaches have been explored: thermal, solvent, adhesive, or polymerization bonding have demonstrated robust bonding [250]. Similar to PDMS, biocompatible PMMA microdevices with predefined geometry are extremely useful in bio-related fields. However, the hydrophobic nature of PMMA resulted in nonspecific adsorption and poor wetting properties at the channel wall. To overcome these challenges, various surface modification [251] and bulk modification [252] methods been developed.

Hydrogel is another class of material that can be used to make microfluidics. Chips made from hydrogels have particular interests in biological applications and biomimicking due to their similarity with extracellular matrix (ECM). The porous, 3D and water-rich polymeric environment allows the diffusion of cell nutrients and growth factors, making it a promising substrate for cell culture and encapsulation [253]. Gel-based microfluidic devices can be fabricated by soft lithography, flow solidification and gel photopolymerization [254]. The limitations with gel-based microchips are: (1) low spatial

resolution in microfabrication (micrometer scale) compared with other polymers (nanometer scale), (2) limited capacity supporting thick layer cell culture, (3) channel sealing (surface bonding) is difficult [254–256]. Efforts in exploring alternative micropatterning and integrative methods as well as materials could possibly address these challenges in the future.

Inorganic materials, including silicon and glass have been used for microchips even before the concept of 'microfluidics' has emerged. Silicon and glass microfluidic channels are typically made by photolithography and chemical etching [257]. Due to their good thermostability and solvent resistance, silicon/glass microdevices become a key platform for lab-on-chip design, droplet generation and bio-separation [258]. The drawbacks with such devices are associated with the sealing of the two plates and the relatively expensive and time-consuming fabrication process [257,259]. A picosecond pulsed laser system has been adopted and demonstrated feasibility in addressing the issues mentioned above [259].

2.8.2 Droplets Generation Mechanisms

Droplet microfluidics (or droplet-based microfluidics) is a subdivision of microfluidics that aims at producing and manipulating individual droplets. The generation of slugs or discrete volumes in microchannels relies upon immiscible multiphases [260]. A continuous phase is referred to the liquid in which droplets flow, while a dispersed phase is the droplet phase.

The mechanisms of droplet formation have been studied in depth. Reynolds number (R_e) is the dimensionless parameter in fluid mechanics used to predict flow patterns [261]. It correlates the relative effect of inertia forces to viscous forces [262]. R_e is defined as:

$$R_e = \frac{\rho D v}{\mu} \quad (8)$$

where ρ is the density of the fluid, D is the diameter of the passageway, v is the velocity of the liquid, and μ is the viscosity of the liquid. Laminar flow represents a flow with parallel streamlines without disruption. Turbulent flow characterizes non-linear, irregular fluctuations for mixing in the liquid. The limit of laminar flow between laminar and

turbulent flows is marked by R_e of $\sim 1,800-2,000$ [263]. As the diameter D and velocity v are relatively small for the fluids in the microchannels, droplet microfluidics typically falls in a low Reynolds number (usually much less than 100, often less than 1.0) laminar regime [264,265]. As such, inertial effects in the flow are negligible-the flow is dominated by viscous stresses [265].

In a microfluidic device, the confinement of the channels enhances the surface-to-volume ratio of the fluids, which consequently leads to the enhancement of surface tension and fluid viscous force [264]. The negligible inertial effects leave interfacial tension and viscosity in competition with each other [266]. When the two immiscible phases were introduced together, the continuous phase disrupts the dispersed phase due to the viscous forces. The mixing would introduce nonlinearity and instability at the junction of two microchannels where the dispersed phase would break into droplets or plugs due the tendency of surface tension to minimize the interfacial area [267,268].

The relative effect of viscous force and surface tension can be measured by the capillary number C_a :

$$C_a = \frac{\mu v}{\gamma} \quad (9)$$

where μ is the viscosity of the continuous phase, v is the superficial velocity of the continuous phase, and γ is the interfacial tension or surface tension between the two fluidic phases. At low capillary numbers, surface tension dominates, and the droplets remain spherical (dripping model). As the C_a increases, viscous forces increase. The shear stress applied to the droplet is large enough to overcome the surface tension. The initially spherical droplet becomes ellipsoidal plugs and eventually breaks into smaller droplets further downstream (jetting model) [269–271]. The balance of the two forces determines the flow pattern whether droplets (dripping) or plugs (jetting) form under a given condition. In general, droplets generated in dripping regimes are smaller in diameter with narrower size distribution [271,272]. As such, the dripping mode is preferred in droplet microfluidics.

2.8.3 Geometrical Design of Microchannels

The droplet generation mechanisms are adapted to guide the microparticles fabrication. Both passive and active techniques can be used to produce uniform and evenly distributed droplet volumes ranging from femtoliters to nanoliters. In active droplet production, microchannels in predesigned configurations are required to enhance the viscous shear force to secure the continuous formation of droplets.

Three primary microfluidic channel geometries are used: co-flow, T-junction and flow-focusing (Figure 2.7). In a co-flow geometry, also called coaxial flow, a cylindrical glass capillary is coaxially inserted into square glass tubes. The dispersed phase flows in the capillary in parallel to the continuous phase placed in a larger-diameter glass tube. The continuous phase surrounds the dispersed phase, and the droplets are generated mainly by the instability of the dispersed phase due to surface tension (Rayleigh-Plateau instability) [268]. The size of droplets can be tuned by the fluid properties and flow rates [271]. The cylindrical geometry of the center capillary limits the geometry of co-flow devices to a 3D architecture. In contrast, the T-junction and flow-focusing are applicable in planar geometries but possess more complicated droplet breakup mechanisms [266]. T-junction design is a subdivision of cross-flow designs, where the dispersed phase is sheared at an angle θ ($0^\circ < \theta < 180^\circ$). In the T-junction category, the dispersed and continuous phase flow in orthogonal channels meet at a cross-junction. The viscosity of two fluids, interfacial tension and channel geometries can affect the droplet formation [273]. The flow-focusing design is similar to co-flow. The continuous streams flow on both sides of the dispersed phase to a focus unit, where the three streams are forced through in a condensed passageway. The extended pressure and shear stress generated by the continuous phase breaks the dispersed phase inside or downstream of the orifice [274]. The droplet size can be controlled by the viscosity of the two phases, flow rates and inlet pressure [275]. In general, passive technique allows the coefficient of variation (CV), defined as the standard deviation in size divided by the mean droplet diameter, to remain less than 3% [276].

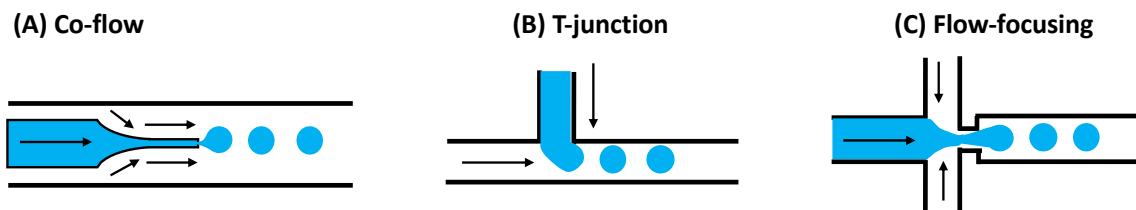


Figure 2.7 Schematic illustration of different channel geometries of a microfluidic device. (A) Co-flow; (B) T-junction; and (C) flow-focusing. Solid arrows indicate the flow direction.

Active methods implement external forces to exert local actuation to break up the fluid stream physically. The co-flow, T-junction and flow-focusing channel geometries still apply, and additional pneumatic, acoustic forces and magnetic forces are introduced to produce droplets on demand [277]. Active mixing purposely creates chaotic motion in the device, which promotes mass transfer. This expands the application of microfluidics into bioreactors for cells or bacteria since it accommodates fast and adequate oxygen and nutrients transfer [278].

2.8.4 Droplet Microfluidics in Drug Delivery

Droplet-based microfluidics enables precise and reproducible production of micro- or nanocarriers as drug delivery systems. This technique renders several advantages over conventional bulk production, including tailored particle size and encapsulation of various types of drugs.

Tailor microparticle size to tumor arterial anatomy

DEB size is one of the key parameters that would affect the procedure outcome. Animal studies have suggested that smaller size DEBs (70-150 μm) had deeper tissue penetration and greater drug coverage (i.e. amount of tissue exposed to drug) than the beads in the standard size range (100-300 μm) [279]. Eddy and Casarett claimed that tumor vessels maintained a capillary-like structure. Capillaries are typically less than 12 μm in diameter, and some vessels that could progressively dilated and reached diameters ~ 200 μm based on their studies on the hamster [280]. It has been advised that the human tumor blood vessels were much larger in diameter than what would be predicted based on

animal models [281]. Moreover, the diameter of tumor is also histology- and location-dependent [18]. These variants in tumor vasculature suggest that providing DEBs in several size ranges is necessary.

Microfluidic fabrication allows reproducible fabrication of particles of size over a broad size range (10-1000 μm). Particles of different sizes can be simply prepared by tuning the flow rates or properties of the dispersed phase or continuous phase [282,283]. The particles are highly uniform in size with CV < 3% [276]. Microparticles in defined geometry could be advantageous in DEB application, as they can provide predictable drug eluting profile and embolization outcome.

Encapsulation of various types of drugs

In microfluidics, drug molecules could be encapsulated into the carriers through single emulsions, multiple emulsions or hierarchical porous particles. For single emulsion templated particles, drugs can be suspended in a dispersed phase and encapsulated into the particles through forming oil (O)-in water (W) or W/O emulsions [284,285]. For double emulsion systems, W/O/W configuration is typically used. Drugs are encapsulated in the internal water phase of the double emulsion and can improve the stability and solubility of the drugs [286,287]. In addition to encapsulation, porous nanoparticles-in-microcarriers provide another approach for high drug loading via physical adsorption at pore surfaces [288,289].

Microfluidics techniques expand the material selection and ease the loading of drugs with various properties. In conventional preparation of delivery systems, hydrophilic drugs are generally loaded into hydrogel particles [106], while lipophilic drugs are mostly limited to liposomes and solid lipid nanoparticles [290]. With the aid of microfluidic techniques, both hydrophilic and lipophilic payloads can be encapsulated into the delivery vehicles [144]. Multiple drugs loading can be realized by microfluidic fabrication of microparticles with multiple compartments for separate encapsulation of drugs. For example, core-shell particles were prepared via double emulsion templates, hydrophilic therapeutics DOX was loaded into gelatin methacryloyl (GelMA) cores, while hydrophobic actives camptothecine (CPT) was loaded into the PLGA shells [291].

Similarly, Winkler et al. prepared Janus particles for simultaneous delivery of a hydrophilic-hydrophobic drug pair. Acetaminophen (APAP, hydrophilic) was entrapped in inner water droplets within an oil phase containing naproxen (NPX, hydrophobic), the W/O emulsion was then stabilized in another aqueous solution to form a W/O/W emulsion [292]. He et al. fabricated dual-/triple-compartmental microparticles using a novel W/W template [293]. Each compartment is a W/W droplet consist of calcium alginate (Ca-Alg) as the shell material and sodium carboxymethylcellulose (CMC) as the inner fluids. The compartments were aligned by needles and then fixed via Ca^{2+} crosslinking in the outer layer of Ca-Alg. The dual compartments in the resultant capsules were used separately to load two distinct model drugs.

2.9 Clinical Applications and Future Translational Opportunities

Multifunctional microparticles offered several improvements to the current DEBs (Table 2.6). Namely, the prepared system could be delivered through a catheter or even MRN. The co-localization of contrast agent and drug allows a more precise tracking of the drug distribution relative to the tumor site through MR imaging. This would provide useful information for intra- and post-procedural evaluation of the TACE procedure. Moreover, the delivery system can potentially render a controlled drug release to maintain an effective local drug dosage. The IONPs and silica particles participate in the crosslinking of PVA and render additional functionality through the particle-PVA interactions. More specifically, the composite hydrogel would disintegrate as the IONPs and (or) silica dissolve, which would allow the elimination from the embolization site with due course of time, which would allow repeatable TACE treatments. Besides, one or more drugs can be possibly loaded. In addition to treating the intermediate HCC, multifunctional microparticles can be applied in managing colorectal liver metastases [294].

Table 2.6 Comparison of current DEBs with multifunctional microparticles.

Functions	Current DEBs	Multifunctional Microparticles
Embolization	✓	✓
Targetability	Catheter delivery	Catheter delivery/ magnetic resonance navigation
Imageability/detectability	Contrast agent administered separately	Contrast agent is inside the bead
Controlled release	✓	✓
Degradability	×	✓
Multiple drug delivery	×	Possible

New polymeric platforms must be developed to allow the integration of multiple desirable functions described in section 2.5. The development of novel material strategies will also expand the drugs amendable to hydrogel-based systems. A combinational treatment regimen might be possible with a wide range of functional particles and bioactive molecules becoming compatible with the DEBs. Several microparticulate platforms have demonstrated the viability for combined regimens, including hyperthermia-TACE [295] and stem cell therapy-chemotherapy [296]. These may improve the clinical outcome of the treatments.

Multifunctional nanoparticles provide protection and sustained availability to therapeutics compared to free dosage forms. Improvements could be made through surface functionalization and introducing porous structure [211]. Nanocarriers can be used alone or incorporated into existing platforms, such as hydrogels or contact lenses to construct drug-eluting medical devices. Future studies on the safety and effectiveness must be warranted to validate their potential benefits.

2.10 References

- [1] S.P. Choo, W.L. Tan, B.K.P. Goh, W.M. Tai, A.X. Zhu, Comparison of hepatocellular carcinoma in Eastern versus Western populations, *Cancer*. 122 (2016) 3430–3446.
- [2] P. Rawla, T. Sunkara, P. Muralidharan, J.P. Raj, Update in global trends and aetiology of hepatocellular carcinoma, *Contemp Oncol (Pozn)*. 22 (2018) 141–150.

- [3] P. Fitzmorris, A.K. Singal, Surveillance and Diagnosis of Hepatocellular Carcinoma, *Gastroenterol Hepatol (N Y)*. 11 (2015) 38–46.
- [4] Y.-X.J. Wáng, B. De, J.-M. Idée, S. Ballet, Transcatheter embolization therapy in liver cancer: An update of clinical evidences, *Chinese Journal of Cancer Research*. 27 (2015) 96–121.
- [5] P. Giunchedi, M. Maestri, E. Gavini, P. Dionigi, G. Rassa, Transarterial chemoembolization of hepatocellular carcinoma. Agents and drugs: an overview. Part 1, *Expert Opin Drug Deliv*. 10 (2013) 679–690.
- [6] K. Han, J.H. Kim, Transarterial chemoembolization in hepatocellular carcinoma treatment: Barcelona clinic liver cancer staging system, *World J Gastroenterol*. 21 (2015) 10327–10335.
- [7] J.-H. Zhong, L.-Q. Li, Postoperative adjuvant transarterial chemoembolization for participants with hepatocellular carcinoma: A meta-analysis, *Hepatol Res*. 40 (2010) 943–953.
- [8] Q.-Q. Zu, S. Liu, C.-G. Zhou, Z.-Q. Yang, J.-G. Xia, L.-B. Zhao, H.-B. Shi, Chemoembolization of Recurrent Hepatoma After Curative Resection: Prognostic Factors, *American Journal of Roentgenology*. 204 (2015) 1322–1328.
- [9] A. Bouchard-Fortier, R. Lapointe, P. Perreault, L. Bouchard, G. Pomier-Layrargues, Transcatheter arterial chemoembolization of hepatocellular carcinoma as a bridge to liver transplantation: a retrospective study, *Int J Hepatol*. 2011 (2011) 974514.
- [10] M. Lesurtel, B. Müllhaupt, B.C. Pestalozzi, T. Pfammatter, P.-A. Clavien, Transarterial chemoembolization as a bridge to liver transplantation for hepatocellular carcinoma: an evidence-based analysis, *Am J Transplant*. 6 (2006) 2644–2650.
- [11] T.J. Vogl, N.N.N. Naguib, N.-E.A. Nour-Eldin, P. Rao, A.H. Emami, S. Zangos, M. Nabil, A. Abdelkader, Review on transarterial chemoembolization in hepatocellular carcinoma: palliative, combined, neoadjuvant, bridging, and symptomatic indications, *Eur J Radiol*. 72 (2009) 505–516.
- [12] A. Rammohan, J. Sathyanesan, S. Ramaswami, A. Lakshmanan, P. Senthil-Kumar, U.P. Srinivasan, R. Ramasamy, P. Ravichandran, Embolization of liver tumors: Past, present and future, *World J Radiol*. 4 (2012) 405–412.
- [13] S. Puppala, Technical update on transcatheter arterial chemoembolization, *Hepatoma Research*. 5 (2019).
- [14] K. Tam, The Roles of Doxorubicin in Hepatocellular Carcinoma, *ADMET and DMPK*. 1 (2013) 29–44.

- [15] T. Baere, Y. Arai, R. Lencioni, J.-F. Geschwind, W. Rilling, R. Salem, O. Matsui, M. Soulen, Treatment of Liver Tumors with Lipiodol TACE: Technical Recommendations from Experts Opinion, *CardioVascular and Interventional Radiology*. 39 (2016) 334–343.
- [16] T. de Baere, F. Deschamps, C. Teriitheau, P. Rao, K. Conengrapht, M. Schlumberger, S. Leboulleux, E. Baudin, L. Hechellhammer, Transarterial chemoembolization of liver metastases from well differentiated gastroenteropancreatic endocrine tumors with doxorubicin-eluting beads: preliminary results, *J Vasc Interv Radiol*. 19 (2008) 855–861.
- [17] G.-H. Zhou, J. Han, J.-H. Sun, Y.-L. Zhang, T.-Y. Zhou, C.-H. Nie, T.-Y. Zhu, S.-Q. Chen, B.-Q. Wang, Z.-N. Yu, H.-L. Wang, L.-M. Chen, W.-L. Wang, S.-S. Zheng, Efficacy and safety profile of drug-eluting beads transarterial chemoembolization by CalliSpheres® beads in Chinese hepatocellular carcinoma patients, *BMC Cancer*. 18 (2018) 644.
- [18] A.L. Lewis, M.R. Dreher, Locoregional drug delivery using image-guided intra-arterial drug eluting bead therapy, *J Control Release*. 161 (2012) 338–350.
- [19] M. Varela, M.I. Real, M. Burrel, A. Forner, M. Sala, M. Brunet, C. Ayuso, L. Castells, X. Montañá, J.M. Llovet, J. Bruix, Chemoembolization of hepatocellular carcinoma with drug eluting beads: Efficacy and doxorubicin pharmacokinetics, *Journal of Hepatology*. 46 (2007) 474–481.
- [20] A. Facciorusso, Drug-eluting beads transarterial chemoembolization for hepatocellular carcinoma: Current state of the art, *World J Gastroenterol*. 24 (2018) 161–169.
- [21] P. Giunchedi, M. Maestri, E. Gavini, P. Dionigi, G. Rassu, Transarterial chemoembolization of hepatocellular carcinoma--agents and drugs: an overview. Part 2, *Expert Opin Drug Deliv*. 10 (2013) 799–810.
- [22] T. de Baere, S. Plotkin, R. Yu, A. Sutter, Y. Wu, G.M. Cruise, An In Vitro Evaluation of Four Types of Drug-Eluting Microspheres Loaded with Doxorubicin, *J Vasc Interv Radiol*. 27 (2016) 1425–1431.
- [23] I.R. Dubbelboer, E. Lilienberg, E. Ahnfelt, E. Sjögren, N. Axén, H. Lennernäs, Treatment of intermediate stage hepatocellular carcinoma: a review of intrahepatic doxorubicin drug-delivery systems, *Ther Deliv*. 5 (2014) 447–466.
- [24] C.G. Johnson, Y. Tang, A. Beck, M.R. Dreher, D.L. Woods, A.H. Negussie, D. Donahue, E.B. Levy, S.L. Willis, A.L. Lewis, B.J. Wood, K.V. Sharma, Preparation of Radiopaque Drug-Eluting Beads for Transcatheter Chemoembolization, *J Vasc Interv Radiol*. 27 (2016) 117-126.e3.
- [25] Y. Okamoto, T. Hasebe, K. Bito, K. Yano, T. Matsumoto, K. Tomita, A. Hotta, Fabrication of radiopaque drug-eluting beads based on Lipiodol/biodegradable-

- polymer for image-guided transarterial chemoembolization of unresectable hepatocellular carcinoma, *Polymer Degradation and Stability*. 175 (2020) 109106.
- [26] K. Ashrafi, Y. Tang, H. Britton, O. Domenge, D. Blino, A.J. Bushby, K. Shuturminska, M. den Hartog, A. Radaelli, A.H. Negussie, A.S. Mikhail, D.L. Woods, V. Krishnasamy, E.B. Levy, B.J. Wood, S.L. Willis, M.R. Dreher, A.L. Lewis, Characterisation of a novel intrinsically radiopaque Drug-eluting Bead for image-guided therapy: DC Bead LUMI™, *J Control Release*. 250 (2017) 36–47.
- [27] H. Wang, X.-Y. Qin, Z.-Y. Li, L.-Y. Guo, Z.-Z. Zheng, L.-S. Liu, T.-Y. Fan, Preparation and evaluation of MRI detectable poly (acrylic acid) microspheres loaded with superparamagnetic iron oxide nanoparticles for transcatheter arterial embolization, *International Journal of Pharmaceutics*. 511 (2016) 831–839.
- [28] Q. Wang, S. Liu, F. Yang, L. Gan, X. Yang, Y. Yang, Magnetic alginate microspheres detected by MRI fabricated using microfluidic technique and release behavior of encapsulated dual drugs, *IJN*. 12 (2017) 4335–4347.
- [29] D.-H. Kim, J. Chen, R.A. Omary, A.C. Larson, MRI Visible Drug Eluting Magnetic Microspheres for Transcatheter Intra-Arterial Delivery to Liver Tumors, *Theranostics*. 5 (2015) 477–488.
- [30] A. Nicolini, S. Crespi, L. Martinetti, Drug delivery embolization systems: a physician's perspective, *Expert Opinion on Drug Delivery*. 8 (2011) 1071–1084.
- [31] J. Lammer, K. Malagari, T. Vogl, F. Pilleul, A. Denys, A. Watkinson, M. Pitton, G. Sergent, T. Pfammatter, S. Terraz, Y. Benhamou, Y. Avajon, T. Gruenberger, M. Pomoni, H. Langenberger, M. Schuchmann, J. Dumortier, C. Mueller, P. Chevallier, R. Lencioni, PRECISION V Investigators, Prospective randomized study of doxorubicin-eluting-bead embolization in the treatment of hepatocellular carcinoma: results of the PRECISION V study, *Cardiovasc Intervent Radiol*. 33 (2010) 41–52.
- [32] Y.-S. Liu, M.-C. Ou, Y.-S. Tsai, X.-Z. Lin, C.-K. Wang, H.-M. Tsai, M.-T. Chuang, Transarterial chemoembolization using gelatin sponges or microspheres plus lipiodol-doxorubicin versus doxorubicin-loaded beads for the treatment of hepatocellular carcinoma, *Korean J Radiol*. 16 (2015) 125–132.
- [33] A.J. Villatoro, V. Fernández, S. Claros, C. Alcoholado, M. Cifuentes, J. Merayo-Llves, J.A. Andrades, J. Becerra, Regenerative Therapies in Dry Eye Disease: From Growth Factors to Cell Therapy, *Int J Mol Sci*. 18 (2017).
- [34] X. Zhang, V. Jeyalatha M, Y. Qu, X. He, S. Ou, J. Bu, C. Jia, J. Wang, H. Wu, Z. Liu, W. Li, Dry Eye Management: Targeting the Ocular Surface Microenvironment, *Int J Mol Sci*. 18 (2017).
- [35] S.C. Pflugfelder, C.S. de Paiva, The Pathophysiology of Dry Eye Disease: What We Know and Future Directions for Research, *Ophthalmology*. 124 (2017) S4–S13.

- [36] P. Thulasi, A.R. Djalilian, Update in Current Diagnostics and Therapeutics of Dry Eye Disease, *Ophthalmology*. 124 (2017) S27–S33.
- [37] A. Guzman-Aranguez, B. Fonseca, G. Carracedo, A. Martin-Gil, A. Martinez-Aguila, J. Pintor, Dry Eye Treatment Based on Contact Lens Drug Delivery: A Review, *Eye & Contact Lens*. 42 (2016) 280–288.
- [38] A.R. Brissette, Z.D. Mednick, K.D. Schweitzer, M.D. Bona, S.A. Baxter, Punctal Plug Retention Rates for the Treatment of Moderate to Severe Dry Eye: A Randomized, Double-Masked, Controlled Clinical Trial, *American Journal of Ophthalmology*. 160 (2015) 238-242.e1.
- [39] R. Gaudana, J. Jwala, S.H.S. Boddu, A.K. Mitra, Recent Perspectives in Ocular Drug Delivery, *Pharm Res*. 26 (2009) 1197–1216. 008-9694-0.
- [40] A. Patel, K. Cholkar, V. Agrahari, A.K. Mitra, Ocular drug delivery systems: An overview, *World J Pharmacol*. 2 (2013) 47–64.
- [41] P. Agarwal, J.P. Craig, I.D. Rupenthal, Formulation Considerations for the Management of Dry Eye Disease, *Pharmaceutics*. 13 (2021) 207.
- [42] C. Yang, W. Sun, Y. Gu, A clinical study of the efficacy of topical corticosteroids on dry eye, *J Zhejiang Univ Sci B*. 7 (2006) 675–678.
- [43] M. Hingorani, L. Moodaley, V.L. Calder, R.J. Buckley, S. Lightman, A randomized, placebo-controlled trial of topical cyclosporin A in steroid-dependent atopic keratoconjunctivitis, *Ophthalmology*. 105 (1998) 1715–1720.
- [44] I.V. Lollett, A. Galor, Dry eye syndrome: developments and lifitegrast in perspective, *Clin Ophthalmol*. 12 (2018) 125–139.
- [45] R. Karnati, D.E. Laurie, G.W. Laurie, Lacritin and the tear proteome as natural replacement therapy for dry eye, *Exp Eye Res*. 117 (2013) 39–52.
- [46] N. Wang, K. Zimmerman, R.W. Raab, R.L. McKown, C.M.L. Hutnik, V. Talla, M.F. Tyler, J.K. Lee, G.W. Laurie, Lacritin Rescues Stressed Epithelia via Rapid Forkhead Box O3 (FOXO3)-associated Autophagy That Restores Metabolism, *J Biol Chem*. 288 (2013) 18146–18161.
- [47] S. Samudre, F.A. Lattanzio, V. Lossen, A. Hosseini, J.D. Sheppard, R.L. McKown, G.W. Laurie, P.B. Williams, Lacritin, a novel human tear glycoprotein, promotes sustained basal tearing and is well tolerated, *Invest. Ophthalmol. Vis. Sci*. 52 (2011) 6265–6270.
- [48] M.M. Feng, J. Baryla, H. Liu, G.W. Laurie, R.L. McKown, N. Ashki, D. Bhayana, C.M.L. Hutnik, Cytoprotective effect of lacritin on human corneal epithelial cells exposed to benzalkonium chloride in vitro, *Curr Eye Res*. 39 (2014) 604–610.

- [49] P. Ma, S.L. Beck, R.W. Raab, R.L. McKown, G.L. Coffman, A. Utani, W.J. Chirico, A.C. Rapraeger, G.W. Laurie, Heparanase deglycanation of syndecan-1 is required for binding of the epithelial-restricted prosecretory mitogen lacritin, *J. Cell Biol.* 174 (2006) 1097–1106.
- [50] R.L. McKown, E.V. Coleman Frazier, K.K. Zadrozny, A.M. Deleault, R.W. Raab, D.S. Ryan, R.K. Sia, J.K. Lee, G.W. Laurie, A cleavage-potentiated fragment of tear lacritin is bactericidal, *J Biol Chem.* 289 (2014) 22172–22182.
- [51] Y. Zhang, N. Wang, R.W. Raab, R.L. McKown, J.A. Irwin, I. Kwon, T.H. van Kuppevelt, G.W. Laurie, Targeting of heparanase-modified syndecan-1 by prosecretory mitogen lacritin requires conserved core GAGAL plus heparan and chondroitin sulfate as a novel hybrid binding site that enhances selectivity, *J. Biol. Chem.* 288 (2013) 12090–12101.
- [52] G.A. Georgiev, M.S. Gh., J. Romano, K.L. Dias Teixeira, C. Struble, D.S. Ryan, R.K. Sia, J.P. Kitt, J.M. Harris, K.-L. Hsu, A. Libby, M.G. Odrich, T. Suárez, R.L. McKown, G.W. Laurie, Lacritin proteoforms prevent tear film collapse and maintain epithelial homeostasis, *Journal of Biological Chemistry.* 296 (2021) 100070.
- [53] M. Dogru, T. Kojima, C. Simsek, K. Tsubota, Potential Role of Oxidative Stress in Ocular Surface Inflammation and Dry Eye Disease, *Invest. Ophthalmol. Vis. Sci.* 59 (2018) DES163–DES168.
- [54] L. Marelli, R. Stigliano, C. Triantos, M. Senzolo, E. Cholongitas, N. Davies, J. Tibballs, T. Meyer, D.W. Patch, A.K. Burroughs, Transarterial therapy for hepatocellular carcinoma: which technique is more effective? A systematic review of cohort and randomized studies, *Cardiovasc Intervent Radiol.* 30 (2007) 6–25.
- [55] S.W. Shin, The Current Practice of Transarterial Chemoembolization for the Treatment of Hepatocellular Carcinoma, *Korean J Radiol.* 10 (2009) 425–434.
- [56] S. Kawai, J. Okamura, M. Ogawa, Y. Ohashi, M. Tani, J. Inoue, Y. Kawarada, M. Kusano, Y. Kubo, C. Kuroda, Prospective and randomized clinical trial for the treatment of hepatocellular carcinoma--a comparison of lipiodol-transcatheter arterial embolization with and without adriamycin (first cooperative study). The Cooperative Study Group for Liver Cancer Treatment of Japan, *Cancer Chemother Pharmacol.* 31 Suppl (1992) S1-6.
- [57] S. Kawai, M. Tani, J. Okamura, M. Ogawa, Y. Ohashi, M. Monden, S. Hayashi, J. Inoue, Y. Kawarada, M. Kusano, Y. Kubo, C. Kuroda, Y. Sakata, Y. Shimamura, K. Jinno, A. Takahashi, K. Takayasu, K. Tamura, N. Nagasue, Y. Nakanishi, M. Makino, M. Masuzawa, Y. Yumoto, T. Mori, T. Oda, Prospective and randomized trial of lipiodol-transcatheter arterial chemoembolization for treatment of hepatocellular carcinoma: a comparison of epirubicin and doxorubicin (second cooperative study). The Cooperative Study Group for Liver Cancer Treatment of Japan, *Semin Oncol.* 24 (1997) S6-38-S6-45.

- [58] H. Kasugai, J. Kojima, M. Tatsuta, S. Okuda, Y. Sasaki, S. Imaoka, M. Fujita, S. Ishiguro, Treatment of hepatocellular carcinoma by transcatheter arterial embolization combined with intraarterial infusion of a mixture of cisplatin and ethiodized oil, *Gastroenterology*. 97 (1989) 965–971.
- [59] S. Watanabe, M. Nishioka, Y. Ohta, N. Ogawa, S. Ito, Y. Yamamoto, Prospective and randomized controlled study of chemoembolization therapy in patients with advanced hepatocellular carcinoma. Cooperative Study Group for Liver Cancer Treatment in Shikoku area, *Cancer Chemother Pharmacol*. 33 Suppl (1994) S93-96.
- [60] R. Lencioni, P. Petruzzi, L. Crocetti, Chemoembolization of Hepatocellular Carcinoma, *Semin Intervent Radiol*. 30 (2013) 3–11.
- [61] J. Kettenbach, A. Stadler, I. v Katzler, R. Schernthaner, M. Blum, J. Lammer, T. Rand, Drug-Loaded Microspheres for the Treatment of Liver Cancer: Review of Current Results, *Cardiovasc Intervent Radiol*. 31 (2008) 468–476.
- [62] R.C.G. Martin, J. Joshi, K. Robbins, D. Tomalty, R. O'Hara, C. Tatum, Transarterial Chemoembolization of Metastatic Colorectal Carcinoma with Drug-Eluting Beads, Irinotecan (DEBIRI): Multi-Institutional Registry, *Journal of Oncology*. 2009 (2009) e539795.
- [63] S.-Y. Lee, H.-Y. Ou, C.-Y. Yu, T.-L. Huang, L.L.-C. Tsang, Y.-F. Cheng, Drug-eluting bead transarterial chemoembolization for hepatocellular carcinoma: does size really matter?, *Diagn Interv Radiol*. 26 (2020) 230–235.
- [64] H.C. Nam, B. Jang, M.J. Song, Transarterial chemoembolization with drug-eluting beads in hepatocellular carcinoma, *World J Gastroenterol*. 22 (2016) 8853–8861.
- [65] A.L. Lewis, M.V. Gonzalez, A.W. Lloyd, B. Hall, Y. Tang, S.L. Willis, S.W. Leppard, L.C. Wolfenden, R.R. Palmer, P.W. Stratford, DC Bead: In Vitro Characterization of a Drug-delivery Device for Transarterial Chemoembolization, *Journal of Vascular and Interventional Radiology*. 17 (2006) 335–342.
- [66] K. Ashrafi, Y. Tang, H. Britton, O. Domenge, D. Blino, A.J. Bushby, K. Shuturminska, M. den Hartog, A. Radaelli, A.H. Negussie, A.S. Mikhail, D.L. Woods, V. Krishnasamy, E.B. Levy, B.J. Wood, S.L. Willis, M.R. Dreher, A.L. Lewis, Characterization of a novel intrinsically radiopaque Drug-eluting Bead for image-guided therapy: DC Bead LUMI™, *Journal of Controlled Release*. 250 (2017) 36–47.
- [67] G. Richter, B. Radeleff, C. Stroszczyński, P. Pereira, T. Helmberger, M. Barakat, P. Huppert, Safety and Feasibility of Chemoembolization with Doxorubicin-Loaded Small Calibrated Microspheres in Patients with Hepatocellular Carcinoma: Results of the MIRACLE I Prospective Multicenter Study, *Cardiovasc Intervent Radiol*. 41 (2018) 587–593.

- [68] K. Malagari, T. Kiakidis, M. Pomoni, H. Moschouris, E. Emmanouil, T. Spiridopoulos, V. Sotirchos, S. Tandeles, D. Koundouras, A. Kelekis, D. Filippiadis, A. Charokopakis, E. Bouma, A. Chatziioannou, S. Dourakis, J. Koskinas, T. Karampelas, K. Tamvakopoulos, N. Kelekis, D. Kelekis, Pharmacokinetics, Safety, and Efficacy of Chemoembolization with Doxorubicin-Loaded Tightly Calibrated Small Microspheres in Patients with Hepatocellular Carcinoma, *Cardiovasc Intervent Radiol.* 39 (2016) 1379–1391.
- [69] C. Aliberti, R. Carandina, D. Sarti, L. Mulazzani, V. Catalano, A. Felicioli, P. Coschiera, G. Fiorentini, Hepatic Arterial Infusion of Polyethylene Glycol Drug-eluting Beads for Primary and Metastatic Liver Cancer Therapy, *Anticancer Research.* 36 (2016) 3515–3521.
- [70] D.C. Wu, C.M. Ofner, Adsorption and Degradation of Doxorubicin from Aqueous Solution in Polypropylene Containers, *AAPS PharmSciTech.* 14 (2012) 74–77.
- [71] M. Herrera, J. Rysavy, F. Kotula, B. Rusnak, W.R. Castaneda-Zuniga, K. Amplatz, Ivalon shavings: technical considerations of a new embolic agent., *Radiology.* (1982).
- [72] C.P. Derdeyn, C.J. Moran, D.T. Cross, H.H. Dietrich, R.G. Dacey, Polyvinyl alcohol particle size and suspension characteristics., *American Journal of Neuroradiology.* 16 (1995) 1335–1343.
- [73] J. Handa, S. Nakasu, I. Matsuda, Facial nerve palsy following therapeutic embolization, *Surg Neurol.* 14 (1980) 377–380.
- [74] S. Vaidya, K.R. Tozer, J. Chen, An Overview of Embolic Agents, *Semin Intervent Radiol.* 25 (2008) 204–215.
- [75] <http://fyra.io>, Particulate Embolics, *Endovascular Today.* (n.d.).
<https://evtoday.com/articles/2013-apr/particulate-embolics> (accessed May 12, 2021).
- [76] A. Poursaid, M.M. Jensen, E. Huo, H. Ghandehari, Polymeric materials for embolic and chemoembolic applications, *Journal of Controlled Release.* 240 (2016) 414–433.
- [77] J.-P. Pelage, A. Laurent, M. Wassef, M. Bonneau, D. Germain, R. Rymer, P. Flaud, J. Martal, J.-J. Merland, Uterine artery embolization in sheep: comparison of acute effects with polyvinyl alcohol particles and calibrated microspheres, *Radiology.* 224 (2002) 436–445.
- [78] A. Laurent, M. Wassef, J.-P. Saint Maurice, J. Namur, J.-P. Pelage, A. Seron, R. Chapot, J.-J. Merland, Arterial distribution of calibrated tris-acryl gelatin and polyvinyl alcohol microspheres in a sheep kidney model, *Invest Radiol.* 41 (2006) 8–14.

- [79] G.C. Chua, M. Wilsher, M.P.A. Young, I. Manyonda, R. Morgan, A.-M. Belli, Comparison of particle penetration with non-spherical polyvinyl alcohol versus trisacryl gelatin microspheres in women undergoing premyomectomy uterine artery embolization, *Clin Radiol.* 60 (2005) 116–122.
- [80] A.L. Lewis, M.R. Dreher, V. O’Byrne, D. Grey, M. Caine, A. Dunn, Y. Tang, B. Hall, K.D. Fowers, C.G. Johnson, K.V. Sharma, B.J. Wood, DC BeadM1™: towards an optimal transcatheter hepatic tumour therapy, *J Mater Sci: Mater Med.* 27 (2015) 13.
- [81] A. Laurent, E. Velzenberger, M. Wassef, J.-P. Pelage, A.L. Lewis, Do Microspheres with Narrow or Standard Size Distributions Localize Differently in Vasculature? An Experimental Study in Sheep Kidney and Uterus, *Journal of Vascular and Interventional Radiology.* 19 (2008) 1733–1739.
- [82] L. Du, Y. Huang, Q. Zhang, Y. Zhou, J. Huang, L. Yan, Z. Yu, A. Qin, H. Yang, M. Chen, L. Liang, B. Bian, X. Li, J. Fu, Synthesis and assessment of drug-eluting microspheres for transcatheter arterial chemoembolization, *Acta Biomaterialia.* 88 (2019) 370–382.
- [83] Y. Hu, Q. Wang, J. Wang, J. Zhu, H. Wang, Y. Yang, Shape controllable microgel particles prepared by microfluidic combining external ionic crosslinking, *Biomicrofluidics.* 6 (2012) 026502.
- [84] Y.-S. Lin, C.-H. Yang, Y.-Y. Hsu, C.-L. Hsieh, Microfluidic synthesis of tail-shaped alginate microparticles using slow sedimentation, *ELECTROPHORESIS.* 34 (2013) 425–431.
- [85] M.W. Wilson, N. Fidelman, O.M. Weber, A.J. Martin, R.L. Gordon, J.M. LaBerge, R.K. Kerlan, K.A. Wolanske, M. Saeed, Experimental Renal Artery Embolization in a Combined MR Imaging/Angiographic Unit, *Journal of Vascular and Interventional Radiology.* 14 (2003) 1169–1175.
- [86] R.S. Hussein, W. Tantawy, Y.A. Abbas, MRI assessment of hepatocellular carcinoma after locoregional therapy, *Insights Imaging.* 10 (2019).
- [87] J.W. Choi, H.-J. Cho, J.-H. Park, S.Y. Baek, J.W. Chung, D.-D. Kim, H.-C. Kim, Comparison of Drug Release and Pharmacokinetics after Transarterial Chemoembolization Using Diverse Lipiodol Emulsions and Drug-Eluting Beads, *PLOS ONE.* 9 (2014) e115898.
- [88] J.X.J. Zhang, K. Hoshino, Chapter 7 - Nanomaterials for molecular sensing, in: J.X.J. Zhang, K. Hoshino (Eds.), *Molecular Sensors and Nanodevices (Second Edition)*, Academic Press, 2019: pp. 413–487.
- [89] H.B. Na, I.C. Song, T. Hyeon, Inorganic Nanoparticles for MRI Contrast Agents, *Adv. Mater.* 21 (2009) 2133–2148.

- [90] A. Nacev, C. Beni, O. Bruno, B. Shapiro, The behaviors of ferromagnetic nanoparticles in and around blood vessels under applied magnetic fields, *Journal of Magnetism and Magnetic Materials*. 323 (2011) 651–668.
- [91] E. Carena, V. Barceló, A. Morancho, L. Levander, C. Boada, A. Laromaine, A. Roig, J. Montaner, A. Rosell, In vitro angiogenic performance and in vivo brain targeting of magnetized endothelial progenitor cells for neurorepair therapies, *Nanomedicine: Nanotechnology, Biology and Medicine*. 10 (2014) 225–234.
- [92] C. Yu, M. Ra, A. B, T. Al, L. Ms, Multifunctional nanoparticles for brain tumor imaging and therapy., *Adv Drug Deliv Rev*. 66 (2013) 42–57.
- [93] D.N. Price, L.R. Stromberg, N.K. Kunda, P. Muttill, In Vivo Pulmonary Delivery and Magnetic-Targeting of Dry Powder Nano-in-Microparticles, *Mol. Pharmaceutics*. 14 (2017) 4741–4750.
- [94] J. Ge, Y. Zhang, Z. Dong, J. Jia, J. Zhu, X. Miao, B. Yan, Initiation of Targeted Nanodrug Delivery in Vivo by a Multifunctional Magnetic Implant, *ACS Appl. Mater. Interfaces*. 9 (2017) 20771–20778.
- [95] J.-B. Mathieu, S. Martel, Steering of aggregating magnetic microparticles using propulsion gradients coils in an MRI Scanner, *Magn Reson Med*. 63 (2010) 1336–1345.
- [96] S. Martel, J.-B. Mathieu, O. Felfoul, A. Chanu, E. Aboussouan, S. Tamaz, P. Pouponneau, L. Yahia, G. Beaudoin, G. Soulez, M. Mankiewicz, Automatic navigation of an untethered device in the artery of a living animal using a conventional clinical magnetic resonance imaging system, *Appl. Phys. Lett.* 90 (2007) 114105.
- [97] M.E. Ladd, P. Bachert, M. Meyerspeer, E. Moser, A.M. Nagel, D.G. Norris, S. Schmitter, O. Speck, S. Straub, M. Zaiss, Pros and cons of ultra-high-field MRI/MRS for human application, *Progress in Nuclear Magnetic Resonance Spectroscopy*. 109 (2018) 1–50.
- [98] R.R. Shah, T.P. Davis, A.L. Glover, D.E. Nikles, C.S. Brazel, Impact of magnetic field parameters and iron oxide nanoparticle properties on heat generation for use in magnetic hyperthermia, *J Magn Magn Mater*. 387 (2015) 96–106.
- [99] Kumar, Magnetic navigation and tracking of multiple ferromagnetic microrobots inside an arterial phantom setup for MRI guided drug therapy, *Biocybernetics and Biomedical Engineering*. 37 (2017) 347–356.
- [100] O. Felfoul, A.T. Becker, G. Fagogenis, P.E. Dupont, Simultaneous steering and imaging of magnetic particles using MRI toward delivery of therapeutics, *Scientific Reports*. 6 (2016) 33567.

- [101] P. Wiggermann, W. a. Wohlgemuth, M. Heibl, A. Vasilj, M. Loss, A. g. Schreyer, C. Stroszczynski, E. m. Jung, Dynamic evaluation and quantification of microvascularization during degradable starch microspheres transarterial Chemoembolisation (DSM-TACE) of HCC lesions using contrast enhanced ultrasound (CEUS): A feasibility study, *Clinical Hemorheology & Microcirculation*. 53 (2013) 337–348.
- [102] M.J. Song, H.J. Chun, D.S. Song, H.Y. Kim, S.H. Yoo, C.-H. Park, S.H. Bae, J.Y. Choi, U.I. Chang, J.M. Yang, H.G. Lee, S.K. Yoon, Comparative study between doxorubicin-eluting beads and conventional transarterial chemoembolization for treatment of hepatocellular carcinoma, *J. Hepatol.* 57 (2012) 1244–1250.
- [103] F. Melchiorre, F. Patella, L. Pescatori, F. Pesapane, E. Fumarola, P. Biondetti, P. Brambillasca, C. Monaco, A.M. Ierardi, G. Franceschelli, G. Carrafiello, DEB-TACE: a standard review, *Future Oncol.* 14 (2018) 2969–2984.
- [104] C.-J. Kim, P.I. Lee, Composite Poly(vinyl alcohol) Beads for Controlled Drug Delivery, *Pharm Res.* 9 (1992) 10–16.
- [105] F.Y. Han, K.J. Thurecht, A.K. Whittaker, M.T. Smith, Bioerodable PLGA-Based Microparticles for Producing Sustained-Release Drug Formulations and Strategies for Improving Drug Loading, *Front. Pharmacol.* 7 (2016).
- [106] A. Mitra, B. Dey, Chitosan Microspheres in Novel Drug Delivery Systems, *Indian J Pharm Sci.* 73 (2011) 355–366.
- [107] Y. Ha, J.B. Lee, J.H. Shim, K.M. Kim, Y.-S. Lim, H.-K. Yoon, Y.M. Shin, H.C. Lee, Validation and reappraisal of the assessment for retreatment with transarterial chemoembolization score for unresectable non-metastatic hepatocellular carcinoma in a hepatitis b virus-endemic region, *Eur Radiol.* 26 (2016) 3510–3518.
- [108] J. Lu, B.-Y. Zhong, H.-D. Zhu, J.-H. Guo, G.-J. Teng, Embolotherapy of unresectable hepatocellular carcinoma: Eastern perspective, *Chinese Clinical Oncology.* 8 (2019) 60.
- [109] G. Saravanakumar, J. Kim, W.J. Kim, Reactive-Oxygen-Species-Responsive Drug Delivery Systems: Promises and Challenges, *Adv Sci (Weinh).* 4 (2016).
- [110] K.W. Kim, A.D. Van den Abbeele, Evolution of Transarterial Chemoembolization for the Treatment of Liver Cancer, *Radiology.* 293 (2019) 704–706.
- [111] G. Dong, Q. Zheng, M. Ma, S. Wu, R. Zhang, R. Yao, Y. Dong, H. Ma, D. Gao, S. Ye, J. Cui, Z. Ren, R. Chen, Angiogenesis enhanced by treatment damage to hepatocellular carcinoma through the release of GDF15, *Cancer Med.* 7 (2018) 820–830.

- [112] A. Denys, P. Czuczman, D. Grey, Z. Bascal, R. Whomsley, H. Kilpatrick, A.L. Lewis, Vandetanib-eluting Radiopaque Beads: *In vivo* Pharmacokinetics, Safety and Toxicity Evaluation following Swine Liver Embolization, *Theranostics*. 7 (2017) 2164–2176.
- [113] W. Li, S. Kong, J. Su, J. Huang, H. Xue, Efficacy of transcatheter arterial chemoembolization combined with sorafenib in inhibiting tumor angiogenesis in a rabbit VX2 liver cancer model, *Journal of Interventional Medicine*. 3 (2020) 27–33.
- [114] K. Fuchs, P.E. Bize, O. Dormond, A. Denys, E. Doelker, G. Borchard, O. Jordan, Drug-eluting beads loaded with antiangiogenic agents for chemoembolization: In vitro sunitinib loading and release and in vivo pharmacokinetics in an animal model, *Journal of Vascular and Interventional Radiology*. 25 (2014) 379-387.e2.
- [115] P. Bize, R. Duran, K. Fuchs, O. Dormond, J. Namur, L. Decosterd, O. Jordan, E. Doelker, A. Denys, Antitumoral Effect of Sunitinib-eluting Beads in the Rabbit VX2 Tumor Model, *Radiology*. 280 (2016) 150361.
- [116] R.E.J. Forster, Y. Tang, C. Bowyer, A.W. Lloyd, W. Macfarlane, G.J. Phillips, A.L. Lewis, Development of a combination drug-eluting bead: towards enhanced efficacy for locoregional tumour therapies, *Anticancer Drugs*. 23 (2012) 355–369.
- [117] J. Namur, M. Wassef, J.P. Pelage, A. Lewis, M. Manfait, A. Laurent, Infrared microspectroscopy analysis of ibuprofen release from drug eluting beads in uterine tissue, *J Control Release*. 135 (2009) 198–202.
- [118] D. Weatherall, B. Greenwood, H.L. Chee, P. Wasi, Science and Technology for Disease Control: Past, Present, and Future, in: D.T. Jamison, J.G. Breman, A.R. Measham, G. Alleyne, M. Claeson, D.B. Evans, P. Jha, A. Mills, P. Musgrove (Eds.), *Disease Control Priorities in Developing Countries*, 2nd ed., World Bank, Washington (DC), 2006. <http://www.ncbi.nlm.nih.gov/books/NBK11740/> (accessed May 31, 2021).
- [119] W. Gao, D. Vecchio, J. Li, J. Zhu, Q. Zhang, V. Fu, J. Li, S. Thamphiwatana, D. Lu, L. Zhang, Hydrogel Containing Nanoparticle-Stabilized Liposomes for Topical Antimicrobial Delivery, *ACS Nano*. 8 (2014) 2900–2907.
- [120] A.K. Gaharwar, N.A. Peppas, A. Khademhosseini, Nanocomposite hydrogels for biomedical applications, *Biotechnology and Bioengineering*. 111 (2014) 441–453.
- [121] V. Thomas, M.M. Yallapu, B. Sreedhar, S.K. Bajpai, Breathing-in/breathing-out approach to preparing nanosilver-loaded hydrogels: Highly efficient antibacterial nanocomposites, *Journal of Applied Polymer Science*. 111 (2009) 934–944.
- [122] M. Mascolo, Y. Pei, T. Ring, Room Temperature Co-Precipitation Synthesis of Magnetite Nanoparticles in a Large pH Window with Different Bases, *Materials*. 6 (2013) 5549–5567.

- [123] Y. Xiang, D. Chen, Preparation of a novel pH-responsive silver nanoparticle/poly(HEMA-PEGMA-MAA) composite hydrogel, *European Polymer Journal*. 43 (2007) 4178–4187.
- [124] Q. Wang, Z. Gao, A constitutive model of nanocomposite hydrogels with nanoparticle crosslinkers, *Journal of the Mechanics and Physics of Solids*. 94 (2016) 127–147.
- [125] P. Ilg, Stimuli-responsive hydrogels cross-linked by magnetic nanoparticles, *Soft Matter*. 9 (2013) 3465–3468.
- [126] S.D. Anderson, V.V. Gwenin, C.D. Gwenin, Magnetic Functionalized Nanoparticles for Biomedical, Drug Delivery and Imaging Applications, *Nanoscale Research Letters*. 14 (2019) 188.
- [127] E. Mostafavi, D. Medina-Cruz, K. Kalantari, A. Taymoori, P. Soltantabar, T.J. Webster, Electroconductive Nanobiomaterials for Tissue Engineering and Regenerative Medicine, *Bioelectricity*. 2 (2020) 120–149.
- [128] K. Yang, Q. Han, B. Chen, Y. Zheng, K. Zhang, Q. Li, J. Wang, Antimicrobial hydrogels: promising materials for medical application, *IJN*. 13 (2018) 2217–2263.
- [129] J.K. Patra, G. Das, L.F. Fraceto, E.V.R. Campos, M. del P. Rodriguez-Torres, L.S. Acosta-Torres, L.A. Diaz-Torres, R. Grillo, M.K. Swamy, S. Sharma, S. Habtemariam, H.-S. Shin, Nano based drug delivery systems: recent developments and future prospects, *Journal of Nanobiotechnology*. 16 (2018) 71.
- [130] N. Sood, A. Bhardwaj, S. Mehta, A. Mehta, Stimuli-responsive hydrogels in drug delivery and tissue engineering, *Drug Delivery*. 23 (2016) 748–770.
- [131] H. Zhao, M. Liu, Y. Zhang, J. Yin, R. Pei, Nanocomposite hydrogels for tissue engineering applications, *Nanoscale*. 12 (2020) 14976–14995.
- [132] J. Li, F. Yu, G. Chen, J. Liu, X.-L. Li, B. Cheng, X.-M. Mo, C. Chen, J.-F. Pan, Moist-Retaining, Self-Recoverable, Bioadhesive, and Transparent in Situ Forming Hydrogels To Accelerate Wound Healing, *ACS Appl. Mater. Interfaces*. 12 (2020) 2023–2038.
- [133] M.C. Giano, Z. Ibrahim, S.H. Medina, K.A. Sarhane, J.M. Christensen, Y. Yamada, G. Brandacher, J.P. Schneider, Injectable bioadhesive hydrogels with innate antibacterial properties, *Nature Communications*. 5 (2014) 4095.
- [134] M.D. Baumann, C.E. Kang, J.C. Stanwick, Y. Wang, H. Kim, Y. Lapitsky, M.S. Shoichet, An injectable drug delivery platform for sustained combination therapy, *Journal of Controlled Release*. 138 (2009) 205–213.
- [135] M. Zhao, E. Bozzato, N. Joudiou, S. Ghiassinejad, F. Danhier, B. Gallez, V. Pr at, Codelivery of paclitaxel and temozolomide through a photopolymerizable

- hydrogel prevents glioblastoma recurrence after surgical resection, *Journal of Controlled Release*. 309 (2019) 72–81.
- [136] M. Patel, T. Kaneko, K. Matsumura, Switchable release nano-reservoirs for co-delivery of drugs via a facile micelle–hydrogel composite, *J. Mater. Chem. B*. 5 (2017) 3488–3497.
- [137] Y. Yu, R. Feng, S. Yu, J. Li, Y. Wang, Y. Song, X. Yang, W. Pan, S. Li, Nanostructured lipid carrier-based pH and temperature dual-responsive hydrogel composed of carboxymethyl chitosan and poloxamer for drug delivery, *International Journal of Biological Macromolecules*. 114 (2018) 462–469.
- [138] C.-C. Lin, A.T. Metters, Hydrogels in controlled release formulations: network design and mathematical modeling, *Adv. Drug Deliv. Rev.* 58 (2006) 1379–1408.
- [139] M. Massaro, G. Buscemi, L. Arista, G. Biddeci, G. Cavallaro, F. D’Anna, F. Di Blasi, A. Ferrante, G. Lazzara, C. Rizzo, G. Spinelli, T. Ullrich, S. Riela, Multifunctional Carrier Based on Halloysite/Laponite Hybrid Hydrogel for Kartogenin Delivery, *ACS Med Chem Lett*. 10 (2019) 419–424.
- [140] A.D. Bannerman, X. Li, W. Wan, A ‘degradable’ poly(vinyl alcohol) iron oxide nanoparticle hydrogel, *Acta Biomaterialia*. 58 (2017) 376–385.
- [141] A. Nasajpour, S. Ansari, C. Rinoldi, A.S. Rad, T. Aghaloo, S.R. Shin, Y.K. Mishra, R. Adelung, W. Swieszkowski, N. Annabi, A. Khademhosseini, A. Moshaverinia, A. Tamayol, A Multifunctional Polymeric Periodontal Membrane with Osteogenic and Antibacterial Characteristics, *Advanced Functional Materials*. 28 (2018).
- [142] J. Wang, J.A. Jansen, F. Yang, Electrospraying: Possibilities and Challenges of Engineering Carriers for Biomedical Applications—A Mini Review, *Front. Chem.* 7 (2019).
- [143] A. Kausar, Polymeric nanocomposite via electrospinning: Assessment of morphology, physical properties and applications, *Journal of Plastic Film & Sheeting*. 37 (2021) 70–92.
- [144] S. Damiati, U.B. Kompella, S.A. Damiati, R. Kodzius, Microfluidic Devices for Drug Delivery Systems and Drug Screening, *Genes (Basel)*. 9 (2018).
- [145] H. Mao, L. Yang, H. Zhu, L. Wu, P. Ji, J. Yang, Z. Gu, Recent advances and challenges in materials for 3D bioprinting, *Progress in Natural Science: Materials International*. 30 (2020) 618–634.
- [146] S. Saghadzadeh, C. Rinoldi, M. Schot, S.S. Kashaf, F. Sharifi, E. Jalilian, K. Nuutila, G. Giatsidis, P. Mostafalu, H. Derakhshandeh, K. Yue, W. Swieszkowski, A. Memic, A. Tamayol, A. Khademhosseini, Drug delivery systems and materials

- for wound healing applications, *Advanced Drug Delivery Reviews*. 127 (2018) 138–166.
- [147] L.-L. Bu, J. Yan, Z. Wang, H. Ruan, Q. Chen, V. Gunadhi, R.B. Bell, Z. Gu, Advances in drug delivery for post-surgical cancer treatment, *Biomaterials*. 219 (2019) 119182.
- [148] S.V. Murphy, A. Atala, 3D bioprinting of tissues and organs, *Nat Biotechnol*. 32 (2014) 773–785.
- [149] M.I. Baker, S.P. Walsh, Z. Schwartz, B.D. Boyan, A review of polyvinyl alcohol and its uses in cartilage and orthopedic applications, *J Biomed Mater Res B Appl Biomater*. 100 (2012) 1451–1457.
- [150] R. Rodríguez-Rodríguez, H. Espinosa-Andrews, C. Velasquillo-Martínez, Z.Y. García-Carvajal, Composite hydrogels based on gelatin, chitosan and polyvinyl alcohol to biomedical applications: a review, *International Journal of Polymeric Materials and Polymeric Biomaterials*. 69 (2020) 1–20.
- [151] G.G. Xu, C.Q. Yang, Y. Deng, Combination of bifunctional aldehydes and poly(vinyl alcohol) as the crosslinking systems to improve paper wet strength, *Journal of Applied Polymer Science*. 93 (2004) 1673–1680.
- [152] J.M. Gohil, A. Bhattacharya, P. Ray, Studies On The Crosslinking Of Poly (Vinyl Alcohol), *J Polym Res*. 13 (2006) 161–169.
- [153] D. Nataraj, R. Reddy, N. Reddy, Crosslinking electrospun poly (vinyl) alcohol fibers with citric acid to impart aqueous stability for medical applications, *European Polymer Journal*. 124 (2020) 109484.
- [154] R.V. Gadhave, P.A. Mahanwar, P.T. Gadekar, Effect of glutaraldehyde on thermal and mechanical properties of starch and polyvinyl alcohol blends, *Des Monomers Polym*. 22 (2019) 164–170.
- [155] C.M. Hassan, N.A. Peppas, Structure and Applications of Poly(vinyl alcohol) Hydrogels Produced by Conventional Crosslinking or by Freezing/Thawing Methods, in: *Biopolymers · PVA Hydrogels, Anionic Polymerisation Nanocomposites*, Springer, Berlin, Heidelberg, 2000: pp. 37–65.
- [156] J.-O. Jeong, J.-S. Park, E.J. Kim, S.-I. Jeong, J.Y. Lee, Y.-M. Lim, Preparation of Radiation Cross-Linked Poly(Acrylic Acid) Hydrogel Containing Metronidazole with Enhanced Antibacterial Activity, *Int J Mol Sci*. 21 (2019).
- [157] W.E. Hennink, C.F. van Nostrum, Novel crosslinking methods to design hydrogels, *Advanced Drug Delivery Reviews*. 54 (2002) 13–36.
- [158] W. Wan, A.D. Bannerman, L. Yang, H. Mak, Poly(Vinyl Alcohol) Cryogels for Biomedical Applications, in: O. Okay (Ed.), *Polymeric Cryogels: Macroporous Gels*

with Remarkable Properties, Springer International Publishing, Cham, 2014: pp. 283–321.

- [159] J.L. Holloway, A.M. Lowman, G.R. Palmese, The role of crystallization and phase separation in the formation of physically cross-linked PVA hydrogels, *Soft Matter*. 9 (2012) 826–833.
- [160] F. Yokoyama, I. Masada, K. Shimamura, T. Ikawa, K. Monobe, Morphology and structure of highly elastic poly(vinyl alcohol) hydrogel prepared by repeated freezing-and-melting, *Colloid and Polymer Science*. 264 (1986) 595–601.
- [161] S. Gupta, S. Goswami, A. Sinha, A combined effect of freeze--thaw cycles and polymer concentration on the structure and mechanical properties of transparent PVA gels, *Biomed Mater*. 7 (2012) 015006.
- [162] T.R. Hoare, D.S. Kohane, Hydrogels in drug delivery: Progress and challenges, *Polymer*. 49 (2008) 1993–2007.
- [163] M.H. Hettiaratchi, A. Schudel, T. Rouse, A.J. García, S.N. Thomas, R.E. Guldberg, T.C. McDevitt, A rapid method for determining protein diffusion through hydrogels for regenerative medicine applications, *APL Bioeng*. 2 (2018)..
- [164] J. Li, D.J. Mooney, Designing hydrogels for controlled drug delivery, *Nat Rev Mater*. 1 (2016).
- [165] P. Kassanos, B.G. Rosa, M. Keshavarz, G.-Z. Yang, Chapter 2 - From wearables to implantables—clinical drive and technical challenges, in: E. Sazonov (Ed.), *Wearable Sensors (Second Edition)*, Academic Press, Oxford, 2021: pp. 29–84.
- [166] K. Fuchs, R. Duran, A. Denys, P.E. Bize, G. Borchard, O. Jordan, Drug-eluting embolic microspheres for local drug delivery – State of the art, *Journal of Controlled Release*. 262 (2017) 127–138.
- [167] U.D. Kamacı, M. Kamacı, Preparation of polyvinyl alcohol, chitosan and polyurethane-based pH-sensitive and biodegradable hydrogels for controlled drug release applications, *International Journal of Polymeric Materials and Polymeric Biomaterials*. 69 (2020) 1167–1177.
- [168] M. Bahadoran, A. Shamloo, Y.D. Nokoarani, Development of a polyvinyl alcohol/sodium alginate hydrogel-based scaffold incorporating bFGF-encapsulated microspheres for accelerated wound healing, *Scientific Reports*. 10 (2020) 7342.
- [169] S.K. Mallapragada, N.A. Peppas, Crystal unfolding and chain disentanglement during semicrystalline polymer dissolution, *AIChE Journal*. 43 (1997) 870–876.
- [170] S.K. Mallapragada, N.A. Peppas, Dissolution mechanism of semicrystalline poly(vinyl alcohol) in water, *Journal of Polymer Science Part B: Polymer Physics*. 34 (1996) 1339–1346.

- [171] V.K. Chaturvedi, A. Singh, V.K. Singh, M.P. Singh, *Cancer Nanotechnology: A New Revolution for Cancer Diagnosis and Therapy*, *Curr Drug Metab.* 20 (2019) 416–429.
- [172] S.M. Dadfar, K. Roemhild, N.I. Drude, S. von Stillfried, R. Knüchel, F. Kiessling, T. Lammers, *Iron Oxide Nanoparticles: Diagnostic, Therapeutic and Theranostic Applications*, *Adv Drug Deliv Rev.* 138 (2019) 302–325.
- [173] A.P. LaGrow, M.O. Besenhard, A. Hodzic, A. Sergides, L.K. Bogart, A. Gavriilidis, N.T.K. Thanh, *Unravelling the growth mechanism of the coprecipitation of iron oxide nanoparticles with the aid of synchrotron X-Ray diffraction in solution*, *Nanoscale.* 11 (2019) 6620–6628.
- [174] B.H. Hui, M.N. Salimi, *Production of Iron Oxide Nanoparticles by Coprecipitation method with Optimization Studies of Processing Temperature, pH and Stirring Rate*, *IOP Conf. Ser.: Mater. Sci. Eng.* 743 (2020) 012036.
- [175] C. Pereira, A.M. Pereira, C. Fernandes, M. Rocha, R. Mendes, M.P. Fernández-García, A. Guedes, P.B. Tavares, J.-M. Grenèche, J.P. Araújo, C. Freire, *Superparamagnetic MFe₂O₄ (M = Fe, Co, Mn) Nanoparticles: Tuning the Particle Size and Magnetic Properties through a Novel One-Step Coprecipitation Route*, *Chem. Mater.* 24 (2012) 1496–1504.
- [176] H. Rashid, M.A. Mansoor, B. Haider, R. Nasir, S.B.A. Hamid, A. Abdulrahman, *Synthesis and characterization of magnetite nano particles with high selectivity using in-situ precipitation method*, *Separation Science and Technology.* 55 (2020) 1207–1215.
- [177] D. Kovář, A. Malá, J. Mlčochová, M. Kalina, Z. Fohlerová, A. Hlaváček, Z. Farka, P. Skládal, Z. Starčuk, R. Jiřík, O. Slabý, J. Hubálek, *Preparation and Characterisation of Highly Stable Iron Oxide Nanoparticles for Magnetic Resonance Imaging*, *Journal of Nanomaterials.* 2017 (2017) e7859289.
- [178] F.N. Sayed, V. Polshettiwar, *Facile and Sustainable Synthesis of Shaped Iron Oxide Nanoparticles: Effect of Iron Precursor Salts on the Shapes of Iron Oxides*, *Scientific Reports.* 5 (2015) 9733.
- [179] M. Unni, A. Uhl, S. Savliwala, B.H. Savitzky, R. Dhavalikar, N. Garraud, D.P. Arnold, L.F. Kourkoutis, J. Andrew, C. Rinaldi, *Thermal Decomposition Synthesis of Iron Oxide Nanoparticles with Diminished Magnetic Dead Layer by Controlled Addition of Oxygen*, *ACS Nano.* 11 (2017) 2284–2303.
- [180] R. Hufschmid, H. Arami, R.M. Ferguson, M. Gonzales, E. Teeman, L.N. Brush, N.D. Browning, K.M. Krishnan, *Synthesis of phase-pure and monodisperse iron oxide nanoparticles by thermal decomposition*, *Nanoscale.* 7 (2015) 11142–11154.
- [181] M.O. Besenhard, A.P. LaGrow, A. Hodzic, M. Kriechbaum, L. Panariello, G. Bais, K. Loizou, S. Damilos, M. Margarida Cruz, N.T.K. Thanh, A. Gavriilidis, *Co-*

- precipitation synthesis of stable iron oxide nanoparticles with NaOH: New insights and continuous production via flow chemistry, *Chemical Engineering Journal*. 399 (2020) 125740.
- [182] N. Ajinkya, X. Yu, P. Kaithal, H. Luo, P. Somani, S. Ramakrishna, Magnetic Iron Oxide Nanoparticle (IONP) Synthesis to Applications: Present and Future, *Materials* (Basel). 13 (2020).
- [183] H. Arami, A. Khandhar, D. Liggitt, K.M. Krishnan, In vivo delivery, pharmacokinetics, biodistribution and toxicity of iron oxide nanoparticles, *Chem. Soc. Rev.* 44 (2015) 8576–8607.
- [184] S. Wada, L. Yue, K. Tazawa, I. Furuta, H. Nagae, S. Takemori, T. Minamimura, New local hyperthermia using dextran magnetite complex (DM) for oral cavity: experimental study in normal hamster tongue, *Oral Diseases*. 7 (2001) 192–195.
- [185] A.S. Thakor, J.V. Jokerst, P. Ghanouni, J.L. Campbell, E. Mittra, S.S. Gambhir, Clinically Approved Nanoparticle Imaging Agents, *J Nucl Med*. 57 (2016) 1833–1837.
- [186] S. Laurent, A.A. Saei, S. Behzadi, A. Panahifar, M. Mahmoudi, Superparamagnetic iron oxide nanoparticles for delivery of therapeutic agents: opportunities and challenges, *Expert Opinion on Drug Delivery*. 11 (2014) 1449–1470.
- [187] S. Fakhri, M. Podinovskaia, X. Kong, H.L. Collins, U.E. Schaible, R.C. Hider, Targeting the Lysosome: Fluorescent Iron(III) Chelators To Selectively Monitor Endosomal/Lysosomal Labile Iron Pools, *J. Med. Chem.* 51 (2008) 4539–4552.
- [188] C. Camaschella, A. Nai, L. Silvestri, Iron metabolism and iron disorders revisited in the hepcidin era, 1. 105 (2020) 260–272.
- [189] S. Waldvogel-Abramowski, G. Waeber, C. Gassner, A. Buser, B.M. Frey, B. Favrat, J.-D. Tissot, Physiology of Iron Metabolism, *Transfus Med Hemother*. 41 (2014) 213–221.
- [190] R. Valenzuela, M.C. Fuentes, C. Parra, J. Baeza, N. Duran, S.K. Sharma, M. Knobel, J. Freer, Influence of stirring velocity on the synthesis of magnetite nanoparticles (Fe₃O₄) by the co-precipitation method, *Journal of Alloys and Compounds*. 488 (2009) 227–231.
- [191] V.C. Karade, A. Sharma, R.P. Dhavale, R.P. Dhavale, S.R. Shingte, P.S. Patil, J.H. Kim, D.R.T. Zahn, A.D. Chougale, G. Salvan, P.B. Patil, APTES monolayer coverage on self-assembled magnetic nanospheres for controlled release of anticancer drug Nintedanib, *Scientific Reports*. 11 (2021) 5674.

- [192] L. Maldonado-Camargo, M. Unni, C. Rinaldi, Magnetic Characterization of Iron Oxide Nanoparticles for Biomedical Applications, *Methods Mol Biol.* 1570 (2017) 47–71.
- [193] H. Wei, O.T. Bruns, M.G. Kaul, E.C. Hansen, M. Barch, A. Wiśniowska, O. Chen, Y. Chen, N. Li, S. Okada, J.M. Cordero, M. Heine, C.T. Farrar, D.M. Montana, G. Adam, H. Ittrich, A. Jasanoff, P. Nielsen, M.G. Bawendi, Exceedingly small iron oxide nanoparticles as positive MRI contrast agents, *PNAS.* 114 (2017) 2325–2330.
- [194] J.-B. Mathieu, S. Martel, Magnetic microparticle steering within the constraints of an MRI system: proof of concept of a novel targeting approach, *Biomed Microdevices.* 9 (2007) 801–808.
- [195] A.C. Silva, T.R. Oliveira, J.B. Mamani, S.M. Malheiros, L. Malavolta, L.F. Pavon, T.T. Sibov, E. Amaro, A. Tannús, E.L. Vidoto, M.J. Martins, R.S. Santos, L.F. Gamarra, Application of hyperthermia induced by superparamagnetic iron oxide nanoparticles in glioma treatment, *Int J Nanomedicine.* 6 (2011) 591–603.
- [196] D. Chang, M. Lim, J.A.C.M. Goos, R. Qiao, Y.Y. Ng, F.M. Mansfeld, M. Jackson, T.P. Davis, M. Kavallaris, Biologically Targeted Magnetic Hyperthermia: Potential and Limitations, *Front. Pharmacol.* 9 (2018).
- [197] L.M. Sanchez, V.A. Alvarez, J.S. Gonzalez, Ferrogels : Smart Materials for Biomedical and Remediation Applications, in: *Handbook of Composites from Renewable Materials*, John Wiley & Sons, Ltd, n.d.: pp. 561–579.
- [198] S.R.S. Veloso, R.G.D. Andrade, E.M.S. Castanheira, Review on the advancements of magnetic gels: towards multifunctional magnetic liposome-hydrogel composites for biomedical applications, *Advances in Colloid and Interface Science.* 288 (2021) 102351.
- [199] P. Thoniyot, M.J. Tan, A.A. Karim, D.J. Young, X.J. Loh, Nanoparticle–Hydrogel Composites: Concept, Design, and Applications of These Promising, Multi-Functional Materials, *Advanced Science.* 2 (2015) 1400010.
- [200] Y. Li, G. Huang, X. Zhang, B. Li, Y. Chen, T. Lu, T.J. Lu, F. Xu, Magnetic Hydrogels and Their Potential Biomedical Applications, *Advanced Functional Materials.* 23 (2013) 660–672.
- [201] G. Li, Y. Du, Y. Tao, H. Deng, X. Luo, J. Yang, Iron(II) cross-linked chitin-based gel beads: Preparation, magnetic property and adsorption of methyl orange, *Carbohydrate Polymers.* 82 (2010) 706–713.
- [202] M.P. Kesavan, S. Ayyanaar, V. Vijayakumar, J. Dhaweethu Raja, J. Annaraj, K. Sakthipandi, J. Rajesh, Magnetic iron oxide nanoparticles (MIONs) cross-linked natural polymer-based hybrid gel beads: Controlled nano anti-TB drug delivery application, *J Biomed Mater Res A.* 106 (2018) 1039–1050.

- [203] Z. Liu, J. Liu, X. Cui, X. Wang, L. Zhang, P. Tang, Recent Advances on Magnetic Sensitive Hydrogels in Tissue Engineering, *Front. Chem.* 8 (2020).
- [204] C. Dannert, B.T. Stokke, R.S. Dias, Nanoparticle-hydrogel composites: From molecular interactions to macroscopic behavior, *Polymers.* 11 (2019).
- [205] A.Y. Gore, G.S. Banker, Surface Chemistry of Colloidal Silica and a Possible Application to Stabilize Aspirin in Solid Matrixes, *Journal of Pharmaceutical Sciences.* 68 (1979) 197–202.
- [206] G. Ragnarsson, A.W. Hölzer, J. Sjögren, The influence of mixing time and colloidal silica on the lubricating properties of magnesium stearate, *International Journal of Pharmaceutics.* 3 (1979) 127–131.
- [207] C. Xu, C. Lei, C. Yu, Mesoporous Silica Nanoparticles for Protein Protection and Delivery, *Front. Chem.* 7 (2019).
- [208] L.P. Singh, S.K. Bhattacharyya, R. Kumar, G. Mishra, U. Sharma, G. Singh, S. Ahalawat, Sol-Gel processing of silica nanoparticles and their applications, *Advances in Colloid and Interface Science.* 214 (2014) 17–37.
- [209] A.M. Buckley, M. Greenblatt, The Sol-Gel Preparation of Silica Gels, *J. Chem. Educ.* 71 (1994) 599.
- [210] S.H. Soytaş, O. Oğuz, Y.Z. Menciloğlu, 9 - Polymer Nanocomposites With Decorated Metal Oxides, in: K. Pielichowski, T.M. Majka (Eds.), *Polymer Composites with Functionalized Nanoparticles*, Elsevier, 2019: pp. 287–323.
- [211] I.A. Rahman, V. Padavettan, Synthesis of Silica Nanoparticles by Sol-Gel: Size-Dependent Properties, Surface Modification, and Applications in Silica-Polymer Nanocomposites—A Review, *Journal of Nanomaterials.* (2012).
- [212] R. Guo, X. Du, R. Zhang, L. Deng, A. Dong, J. Zhang, Bioadhesive film formed from a novel organic–inorganic hybrid gel for transdermal drug delivery system, *European Journal of Pharmaceutics and Biopharmaceutics.* 79 (2011) 574–583.
- [213] H. Pingan, J. Mengjun, Z. Yanyan, H. Ling, A silica/PVA adhesive hybrid material with high transparency, thermostability and mechanical strength, *RSC Advances.* 7 (2017) 2450–2459.
- [214] C. Shao, H.-Y. Kim, J. Gong, B. Ding, D.-R. Lee, S.-J. Park, Fiber mats of poly(vinyl alcohol)/silica composite via electrospinning, *Materials Letters.* 57 (2003) 1579–1584.
- [215] T. Pirzada, S.A. Arvidson, C.D. Saquing, S.S. Shah, S.A. Khan, Hybrid Silica–PVA Nanofibers via Sol–Gel Electrospinning, *Langmuir.* 28 (2012) 5834–5844.

- [216] S.L. Greasley, S.J. Page, S. Sirovica, S. Chen, R.A. Martin, A. Riveiro, J.V. Hanna, A.E. Porter, J.R. Jones, Controlling particle size in the Stöber process and incorporation of calcium, *Journal of Colloid and Interface Science*. 469 (2016) 213–223.
- [217] W. Stöber, A. Fink, E. Bohn, Controlled growth of monodisperse silica spheres in the micron size range, *Journal of Colloid and Interface Science*. 26 (1968) 62–69.
- [218] M. Levin, A. Sonn-Segev, Y. Roichman, Structural changes in nanoparticle-hydrogel composites at very low filler concentrations, *The Journal of Chemical Physics*. 150 (2019) 064908.
- [219] R.M. Greer, B.A. Scruggs, R.A. May, B.D. Chandler, Patterning High Surface Area Silica with Lysozyme: Adsorption Kinetics, Fluorescence Quenching, and Protein Readsorption Studies To Evaluate the Templated Surface, *Langmuir*. 25 (2009) 7161–7168.
- [220] G. Sanità, B. Carrese, A. Lamberti, Nanoparticle Surface Functionalization: How to Improve Biocompatibility and Cellular Internalization, *Front Mol Biosci*. 7 (2020).
- [221] X. Du, S.Z. Qiao, Dendritic Silica Particles with Center-Radial Pore Channels: Promising Platforms for Catalysis and Biomedical Applications, *Small*. 11 (2015) 392–413.
- [222] Y. Sun, K. Ma, T. Kao, K.A. Spoth, H. Sai, D. Zhang, L.F. Kourkoutis, V. Elser, U. Wiesner, Formation pathways of mesoporous silica nanoparticles with dodecagonal tiling, *Nature Communications*. 8 (2017) 252.
- [223] N. Ž. Knežević, J.-O. Durand, Large pore mesoporous silica nanomaterials for application in delivery of biomolecules, *Nanoscale*. 7 (2015) 2199–2209.
- [224] J. Li, S. Shen, F. Kong, T. Jiang, C. Tang, C. Yin, Effects of pore size on in vitro and in vivo anticancer efficacies of mesoporous silica nanoparticles, *RSC Adv*. 8 (2018) 24633–24640.
- [225] R.-A. Mitran, M. Deaconu, C. Matei, D. Berger, Chapter 11 - Mesoporous Silica as Carrier for Drug-Delivery Systems, in: S.S. Mohapatra, S. Ranjan, N. Dasgupta, R.K. Mishra, S. Thomas (Eds.), *Nanocarriers for Drug Delivery*, Elsevier, 2019: pp. 351–374.
- [226] V.-C. Niculescu, Mesoporous Silica Nanoparticles for Bio-Applications, *Front. Mater*. 7 (2020).
- [227] B.G. Cha, J.H. Jeong, J. Kim, Extra-Large Pore Mesoporous Silica Nanoparticles Enabling Co-Delivery of High Amounts of Protein Antigen and Toll-like Receptor 9 Agonist for Enhanced Cancer Vaccine Efficacy, *ACS Cent. Sci*. 4 (2018) 484–492.

- [228] J.G. Croissant, Y. Fatieiev, N.M. Khashab, Degradability and Clearance of Silicon, Organosilica, Silsesquioxane, Silica Mixed Oxide, and Mesoporous Silica Nanoparticles, *Advanced Materials*. 29 (2017) 1604634.
- [229] T. Diedrich, A. Dybowska, J. Schott, E. Valsami-Jones, E.H. Oelkers, The Dissolution Rates of SiO₂ Nanoparticles As a Function of Particle Size, *Environ. Sci. Technol.* 46 (2012) 4909–4915.
- [230] G. Giovaninni, C.J. Moore, A.J. Hall, H.J. Byrne, V. Gubala, pH-Dependent silica nanoparticle dissolution and cargo release, *Colloids Surf B Biointerfaces*. 169 (2018) 242–248.
- [231] E. Mahon, D.R. Hristov, K.A. Dawson, Stabilising fluorescent silica nanoparticles against dissolution effects for biological studies, *Chem. Commun.* 48 (2012) 7970–7972.
- [232] R. Jugdaohsingh, J.J. Powell, 80 - Moderate Beer Consumption: Effects on Silicon Intake and Bone Health, in: V.R. Preedy (Ed.), *Beer in Health and Disease Prevention*, Academic Press, San Diego, 2009: pp. 787–794.
- [233] K.S. Finnie, D.J. Waller, F.L. Perret, A.M. Krause-Heuer, H.Q. Lin, J.V. Hanna, C.J. Barbé, Biodegradability of sol–gel silica microparticles for drug delivery, *J Sol-Gel Sci Technol.* 49 (2009) 12–18.
- [234] Z. Li, J.C. Barnes, A. Bosoy, J.F. Stoddart, J.I. Zink, Mesoporous silica nanoparticles in biomedical applications, *Chem. Soc. Rev.* 41 (2012) 2590–2605.
- [235] T. Irimia, M.V. Ghica, L. Popa, V. Anuța, A.-L. Arsene, C.-E. Dinu-Pîrvu, Strategies for Improving Ocular Drug Bioavailability and Corneal Wound Healing with Chitosan-Based Delivery Systems, *Polymers (Basel)*. 10 (2018).
- [236] Y. Chen, H. Chen, J. Shi, In vivo bio-safety evaluations and diagnostic/therapeutic applications of chemically designed mesoporous silica nanoparticles, *Adv Mater.* 25 (2013) 3144–3176.
- [237] Q. He, Z. Zhang, F. Gao, Y. Li, J. Shi, In vivo Biodistribution and Urinary Excretion of Mesoporous Silica Nanoparticles: Effects of Particle Size and PEGylation, *Small*. 7 (2011) 271–280.
- [238] J. Friend, L. Yeo, Fabrication of microfluidic devices using polydimethylsiloxane, *Biomicrofluidics*. 4 (2010).
- [239] G.S. Fiorini, D.T. Chiu, Disposable microfluidic devices: fabrication, function, and application, *BioTechniques*. 38 (2005) 429–446.
- [240] X. Mu, W. Zheng, J. Sun, W. Zhang, X. Jiang, Microfluidics for Manipulating Cells, *Small*. 9 (2013) 9–21.

- [241] D. Kim, X. Wu, A.T. Young, C.L. Haynes, Microfluidics-Based in Vivo Mimetic Systems for the Study of Cellular Biology, *Acc Chem Res.* 47 (2014) 1165–1173.
- [242] H.-H. Lai, W. Xu, N.L. Allbritton, Use of a virtual wall valve in polydimethylsiloxane microfluidic devices for bioanalytical applications, *Biomicrofluidics.* 5 (2011) 024105.
- [243] H.M. Wyss, D.L. Blair, J.F. Morris, H.A. Stone, D.A. Weitz, Mechanism for clogging of microchannels, *Phys Rev E Stat Nonlin Soft Matter Phys.* 74 (2006) 061402.
- [244] E.S. Park, C. Jin, Q. Guo, R.R. Ang, S.P. Duffy, K. Matthews, A. Azad, H. Abdi, T. Todenhöfer, J. Bazov, K.N. Chi, P.C. Black, H. Ma, Continuous Flow Deformability-Based Separation of Circulating Tumor Cells Using Microfluidic Ratchets, *Small.* 12 (2016) 1909–1919.
- [245] J.N. Lee, C. Park, G.M. Whitesides, Solvent Compatibility of Poly(dimethylsiloxane)-Based Microfluidic Devices, *Anal. Chem.* 75 (2003) 6544–6554.
- [246] A. Gokaltun, M.L. Yarmush, A. Asatekin, O.B. Usta, Recent advances in nonbiofouling PDMS surface modification strategies applicable to microfluidic technology, *Technology (Singap World Sci).* 5 (2017) 1–12.
- [247] A. Gökaltun, Y.B. (Abraham) Kang, M.L. Yarmush, O.B. Usta, A. Asatekin, Simple Surface Modification of Poly(dimethylsiloxane) via Surface Segregating Smart Polymers for Biomicrofluidics, *Scientific Reports.* 9 (2019) 7377.
- [248] T. Trantidou, Y. Elani, E. Parsons, O. Ces, Hydrophilic surface modification of PDMS for droplet microfluidics using a simple, quick, and robust method via PVA deposition, *Microsystems & Nanoengineering.* 3 (2017) 1–9.
- [249] E. Gencturk, S. Mutlu, K.O. Ulgen, Advances in microfluidic devices made from thermoplastics used in cell biology and analyses, *Biomicrofluidics.* 11 (2017).
- [250] Y. Chen, L. Zhang, G. Chen, Fabrication, modification, and application of poly(methyl methacrylate) microfluidic chips, *Electrophoresis.* 29 (2008) 1801–1814.
- [251] S.L. Llopis, J. Osiri, S.A. Soper, Surface modification of poly(methyl methacrylate) microfluidic devices for high-resolution separations of single-stranded DNA, *ELECTROPHORESIS.* 28 (2007) 984–993.
- [252] J. Wang, A. Muck, M.P. Chatrathi, G. Chen, N. Mittal, S.D. Spillman, S. Obeidat, Bulk modification of polymeric microfluidic devices, *Lab Chip.* 5 (2005) 226–230.
- [253] E.M. Ahmed, Hydrogel: Preparation, characterization, and applications: A review, *Journal of Advanced Research.* 6 (2015) 105–121.

- [254] X. Zhang, L. Li, C. Luo, Gel integration for microfluidic applications, *Lab Chip*. 16 (2016) 1757–1776.
- [255] D. Vera, M. García-Díaz, N. Torras, M. Álvarez, R. Villa, E. Martinez, Engineering Tissue Barrier Models on Hydrogel Microfluidic Platforms, *ACS Appl. Mater. Interfaces*. 13 (2021) 13920–13933.
- [256] A. Beck, F. Obst, M. Busek, S. Grünzner, P.J. Mehner, G. Paschew, D. Appelhans, B. Voit, A. Richter, Hydrogel Patterns in Microfluidic Devices by Do-It-Yourself UV-Photolithography Suitable for Very Large-Scale Integration, *Micromachines*. 11 (2020) 479.
- [257] Z. Qi, L. Xu, Y. Xu, J. Zhong, A. Abedini, X. Cheng, D. Sinton, Disposable silicon-glass microfluidic devices: precise, robust and cheap, *Lab Chip*. 18 (2018) 3872–3880.
- [258] E. Roy, A. Pallandre, B. Zribi, M.-C. Horny, F.D. Delapierre, A. Cattoni, J.G. and A.-M. Haghiri-Gosnet, *Overview of Materials for Microfluidic Applications*, IntechOpen, 2016.
- [259] K.L. Wlodarczyk, D.P. Hand, M.M. Maroto-Valer, Maskless, rapid manufacturing of glass microfluidic devices using a picosecond pulsed laser, *Scientific Reports*. 9 (2019) 20215.
- [260] S. Sohrabi, N. Kassir, M.K. Moraveji, Droplet microfluidics: fundamentals and its advanced applications, *RSC Adv*. 10 (2020) 27560–27574.
- [261] O. Reynolds, XXIX. An experimental investigation of the circumstances which determine whether the motion of water shall be direct or sinuous, and of the law of resistance in parallel channels, *Philosophical Transactions of the Royal Society of London*. 174 (1883) 935–982.
- [262] B.E. Rapp, Chapter 9 - Fluids, in: B.E. Rapp (Ed.), *Microfluidics: Modelling, Mechanics and Mathematics*, Elsevier, Oxford, 2017: pp. 243–263.
- [263] G.L. Morini, M. Lorenzini, S. Salvigni, M. Spiga, Analysis of laminar-to-turbulent transition for isothermal gas flows in microchannels, *Microfluidics and Nanofluidics*. 7 (2009) 181–190.
- [264] D. Liu, H. Zhang, F. Fontana, J.T. Hirvonen, H.A. Santos, Current developments and applications of microfluidic technology toward clinical translation of nanomedicines, *Advanced Drug Delivery Reviews*. 128 (2018) 54–83.
- [265] P. Garstecki, M.J. Fuerstman, H.A. Stone, G.M. Whitesides, Formation of droplets and bubbles in a microfluidic T-junction—scaling and mechanism of breakup, *Lab Chip*. 6 (2006) 437–446.

- [266] C.N. Baroud, F. Gallaire, R. Dangla, Dynamics of microfluidic droplets, *Lab Chip*. 10 (2010) 2032–2045.
- [267] J.H. Xu, G.S. Luo, S.W. Li, G.G. Chen, Shear force induced monodisperse droplet formation in a microfluidic device by controlling wetting properties, *Lab Chip*. 6 (2006) 131–136.
- [268] J.K. Nunes, S.S.H. Tsai, J. Wan, H.A. Stone, Dripping and jetting in microfluidic multiphase flows applied to particle and fiber synthesis, *J Phys D Appl Phys*. 46 (2013).
- [269] M.K. Mulligan, J.P. Rothstein, The effect of confinement-induced shear on drop deformation and breakup in microfluidic extensional flows, *Physics of Fluids*. 23 (2011) 022004.
- [270] D. Dendukuri, K. Tsoi, T.A. Hatton, P.S. Doyle, Controlled Synthesis of Nonspherical Microparticles Using Microfluidics, *Langmuir*. 21 (2005) 2113–2116.
- [271] A.S. Utada, A. Fernandez-Nieves, H.A. Stone, D.A. Weitz, Dripping to Jetting Transitions in Coflowing Liquid Streams, *Phys. Rev. Lett.* 99 (2007) 094502.
- [272] R.K. Shah, H.C. Shum, A.C. Rowat, D. Lee, J.J. Agresti, A.S. Utada, L.Y. Chu, J.W. Kim, A. Fernandez-Nieves, C.J. Martinez, D.A. Weitz, Designer emulsions using microfluidics, *Materials Today*. 11 (2008) 18–27.
- [273] J.D. Wehking, M. Gabany, L. Chew, R. Kumar, Effects of viscosity, interfacial tension, and flow geometry on droplet formation in a microfluidic T-junction, *Microfluid Nanofluid*. 16 (2014) 441–453.
- [274] T. Schneider, G.H. Chapman, U.O. Häfeli, Effects of chemical and physical parameters in the generation of microspheres by hydrodynamic flow focusing, *Colloids and Surfaces B: Biointerfaces*. 87 (2011) 361–368.
- [275] M. Seo, Z. Nie, S. Xu, M. Mok, P.C. Lewis, R. Graham, E. Kumacheva, Continuous Microfluidic Reactors for Polymer Particles, *Langmuir*. 21 (2005) 11614–11622.
- [276] W. Li, L. Zhang, X. Ge, B. Xu, W. Zhang, L. Qu, C.-H. Choi, J. Xu, A. Zhang, H. Lee, D.A. Weitz, Microfluidic fabrication of microparticles for biomedical applications, *Chem. Soc. Rev.* 47 (2018) 5646–5683.
- [277] E.-S. Shanko, Y. van de Burgt, P.D. Anderson, J.M.J. den Toonder, Microfluidic Magnetic Mixing at Low Reynolds Numbers and in Stagnant Fluids, *Micromachines (Basel)*. 10 (2019).
- [278] L.J. Frey, D. Vorländer, D. Rasch, H. Ostsieker, B. Müller, M. Schulze, R. Schenkendorf, T. Mayr, J.-H. Grosch, R. Krull, Novel electrodynamic oscillation

- technique enables enhanced mass transfer and mixing for cultivation in micro-bioreactor, *Biotechnology Progress*. 35 (2019) e2827.
- [279] M.R. Dreher, K.V. Sharma, D.L. Woods, G. Reddy, Y. Tang, W.F. Pritchard, O.A. Chiesa, J.W. Karanian, J.A. Esparza, D. Donahue, E.B. Levy, S.L. Willis, A.L. Lewis, B.J. Wood, Radiopaque Drug-Eluting Beads for Transcatheter Embolotherapy: Experimental Study of Drug Penetration and Coverage in Swine, *Journal of Vascular and Interventional Radiology*. 23 (2012) 257-264.e4.
- [280] H.A. Eddy, G.W. Casarett, Development of the vascular system in the hamster malignant neurilemmoma, *Microvasc Res*. 6 (1973) 63–82.
- [281] Visualizing tumor blood vessels - National Cancer Institute, (2016). <https://www.cancer.gov/news-events/cancer-currents-blog/2016/intravital-microscopy> (accessed May 16, 2021).
- [282] Q. Xu, M. Hashimoto, T.T. Dang, T. Hoare, D.S. Kohane, G.M. Whitesides, R. Langer, D.G. Anderson, Preparation of Monodisperse Biodegradable Polymer Microparticles Using a Microfluidic Flow-Focusing Device for Controlled Drug Delivery, *Small*. 5 (2009) 1575–1581.
- [283] D.-H. Kim, T. Choy, S. Huang, R.M. Green, R.A. Omary, A.C. Larson, Microfluidic fabrication of 6-methoxyethylamino numonafide-eluting magnetic microspheres, *Acta Biomaterialia*. 10 (2014) 742–750.
- [284] E. Gundogdu, I.G. Alvarez, E. Karasulu, Improvement of effect of water-in-oil microemulsion as an oral delivery system for fexofenadine: in vitro and in vivo studies, *Int J Nanomedicine*. 6 (2011) 1631–1640.
- [285] T. Kong, J. Wu, M. To, K. Wai Kwok Yeung, H. Cheung Shum, L. Wang, Droplet based microfluidic fabrication of designer microparticles for encapsulation applications, *Biomicrofluidics*. 6 (2012) 034104.
- [286] X. Qi, L. Wang, J. Zhu, Z. Hu, J. Zhang, Self-double-emulsifying drug delivery system (SDEDDS): a new way for oral delivery of drugs with high solubility and low permeability, *Int J Pharm*. 409 (2011) 245–251.
- [287] X. Qi, L. Wang, J. Zhu, Water-in-oil-in-water double emulsions: an excellent delivery system for improving the oral bioavailability of pidotimod in rats, *J Pharm Sci*. 100 (2011) 2203–2211.
- [288] X. Zhao, Y. Liu, Y. Yu, Q. Huang, W. Ji, J. Li, Y. Zhao, Hierarchically porous composite microparticles from microfluidics for controllable drug delivery, *Nanoscale*. 10 (2018) 12595–12604.
- [289] W. Li, Y. Li, Z. Liu, N. Kerdsakundee, M. Zhang, F. Zhang, X. Liu, T. Bauleth-Ramos, W. Lian, E. Mäkilä, M. Kemell, Y. Ding, B. Sarmiento, R. Wiwattanapatapee, J. Salonen, H. Zhang, J.T. Hirvonen, D. Liu, X. Deng, H.A.

- Santos, Hierarchical structured and programmed vehicles deliver drugs locally to inflamed sites of intestine, *Biomaterials*. 185 (2018) 322–332.
- [290] C. Vilos, L.A. Velasquez, Therapeutic Strategies Based on Polymeric Microparticles, *Journal of Biomedicine and Biotechnology*. 2012 (2012) e672760.
- [291] Y. Li, D. Yan, F. Fu, Y. Liu, B. Zhang, J. Wang, L. Shang, Z. Gu, Y. Zhao, Composite core-shell microparticles from microfluidics for synergistic drug delivery, *Sci. China Mater.* 60 (2017) 543–553.
- [292] J.S. Winkler, M. Barai, M.S. Tomassone, Dual drug-loaded biodegradable Janus particles for simultaneous co-delivery of hydrophobic and hydrophilic compounds, *Exp Biol Med (Maywood)*. 244 (2019) 1162–1177.
- [293] F. He, W. Wang, X.-H. He, X.-L. Yang, M. Li, R. Xie, X.-J. Ju, Z. Liu, L.-Y. Chu, Controllable Multicompartmental Capsules with Distinct Cores and Shells for Synergistic Release, *ACS Appl. Mater. Interfaces*. 8 (2016) 8743–8754.
- [294] A.L. Lewis, B. Hall, Toward a better understanding of the mechanism of action for intra-arterial delivery of irinotecan from DC Bead(TM) (DEBIRI), *Future Oncology*. 15 (2019) 2053–2068.
- [295] D. Zahn, A. Weidner, K. Saatchi, U.O. Häfeli, S. Dutz, Biodegradable magnetic microspheres for drug targeting, temperature controlled drug release, and hyperthermia, *Current Directions in Biomedical Engineering*. 5 (2019) 161–164.
- [296] H.A. Pearce, Y.S. Kim, E. Watson, K. Bahrami, M.M. Smoak, E.Y. Jiang, M. Elder, T. Shannon, A.G. Mikos, Development of a modular, biocompatible thiolated gelatin microparticle platform for drug delivery and tissue engineering applications, *Regenerative Biomaterials*. (2021).
- [297] B. Amoyav, O. Benny, Controlled and tunable polymer particles' production using a single microfluidic device, *Appl Nanosci*. 8 (2018) 905–914.

Chapter 3

3 Development of Multifunctional PVA-IONP Microparticles for TACE¹

3.1 Introduction

Hepatocellular carcinoma (HCC) is the most common primary liver cancer and the third most common cause of cancer-related death [1]. Potentially curative treatments, including liver transplantation, surgical resection, or radiofrequency ablation, are reserved for patients with early-stage HCC. However, 50% of patients with HCC are diagnosed at intermediate or advanced stages due to the poor prognosis, precluding curative-intent options [2].

Transarterial chemoembolization (TACE) plays a vital role in the clinical management of HCC. According to the most frequently used BCLC algorithm for HCC, TACE is recognized as first-line therapy for patients with multinodular HCC and preserved liver function (BCLC stage B) [3,4]. Besides, TACE is commonly recommended as the bridging therapy to downstage patients waiting for liver transplantation [5]. The role of TACE in HCC management continues to evolve, as TACE was evidenced to be an effective option in managing recurrent HCC after curative treatments [6,7].

TACE combines transarterial embolization (TAE) with the infusion of chemotherapeutics. It can be performed through conventional TACE (cTACE) and drug-eluting beads TACE (DEB-TACE). cTACE involves the catheter-guided delivery of antineoplastic drugs using Lipiodol-based emulsion, followed by administration of embolic agents to achieve a synergistic effect of drug cytotoxicity and ischemia [8]. For DEB-TACE, embolic particles are loaded with anti-tumor drugs before their transarterial administration. As such, a simultaneous exertion of both therapeutic and embolic effects can be possible. Although clear evidence of the superiority of DEB-TACE over cTACE

¹ A version of this chapter will be submitted to *Polymers* under the title: Development of multifunctional poly(vinyl alcohol) hydrogel microparticles for transarterial chemoembolization therapy. Xinyi Li will be the first author.

is yet to be found, the former technique offers a favorable pharmacokinetic profile with an improved loading capacity and release profile, along with a more standardized and repeatable hospital protocol [9–12].

The most commonly used commercial DEBs are DC Bead™ (Biocompatibles, United Kingdom) and HepaSphere™ (BioSphere Medical, France), Embozene Tandem™ (Varian Medical Systems, United States) and LifePearl® (Terumo International Systems, Belgium). These products are non-degradable, making repeat treatment impossible. Also, imaging contrast agents have to be administered separately, leaving the location of the beads and therefore the anti-tumor drugs rather imprecise.

Over the past decade, there has been a growing interest in designing magnetic and degradable DEBs. Magnetic characteristic allows post-operational evaluation of particle biodistribution and tumour response. Superparamagnetism would be preferred as it permits magnetic resonance imaging (MRI)-guided TACE. Degradable DEBs could address the concerns of non-target embolization, ischemia-induced angiogenesis, and allow repeatable treatments [13,14]. In addition, the integration of multiple functions, including embolization, imageability, controlled release and degradation, would ideally permit a safer, more effective and repeatable TACE treatment.

Physically crosslinked PVA hydrogel prepared using the low temperature thermal cycling (LTTC) process has many desirable properties for DEB-TACE therapy [15]. However, PVA hydrogel is known to be biostable and nondegradable. Our prior work demonstrated that it is possible to design a ‘degradable’ PVA hydrogel with incorporated iron oxide nanoparticles (IONPs) using the LTTC process. In this composite system, IONPs contribute to the crosslinking of the PVA-IONP hydrogel. Since IONPs can degrade and become soluble under physiological conditions and the slightly acidic tumor environment, the composite hydrogel would ‘degrade’ via removal of the crosslinks and redissolution [16]. The anti-cancer drug, doxorubicin (DOX), can be loaded into this hydrogel system for locoregional delivery.

In this work, we first fabricated iron-containing PVA hydrogels in the form of microbeads using the microfluidic technique. Superparamagnetic iron oxide nanoparticles were formed and anchored into the microbeads through *in situ* co-precipitation and LTTC process. The morphological and structural characteristics of the resulting PVA-IONP microparticles were examined by electron microscopy. The magnetic properties, MRI contrast effect, and degradation were evaluated. Finally, DOX loading and *in vitro* release were studied in simulated healthy tissue and tumorous conditions. PVA-IONP microparticles obtained can successfully integrate multiple functions into a single system, therefore it could be promising to be used as DEBs for TACE.

3.2 Materials and Methods

3.2.1 Materials

Poly(vinyl alcohol) (MW 146,000-186,000, 99+% hydrolyzed), iron (III) chloride (FeCl_3), iron (II) chloride tetrahydrate ($\text{FeCl}_2 \cdot 4\text{H}_2\text{O}$) and phosphate-buffered saline were purchased from Sigma-Aldrich, sodium hydroxide (NaOH) pellets and Dulbecco's modified Eagle's medium (DMEM) were obtained from ThermoFisher Scientific. Hydrochloric acid (36.5%-38%) was acquired from Caledon. Span80 was obtained from Fluka. Doxorubicin hydrochloride was purchased from Cayman Chemicals. Phosphate buffer solution (pH 5.5) was prepared by a procedure reported elsewhere [17]. The rest of the chemicals were all in ACS reagent grade and purchased from Sigma-Aldrich.

3.2.2 Assembly of the Microfluidic Device

A planar microchannel was milled out of a poly(methyl methacrylate) (PMMA) slab (50 x 25 x 12 mm) with a flow-focusing configuration. The continuous phase flow channel dimensions were about 500 μm in width, while the measured channel dimensions for the dispersed phase were about 200 μm . A second PMMA slab (50 x 25 x 12 mm) was sealed onto the slab containing channels by screws. Liquids were supplied to the microfluidic channel separately using two syringe pumps (NE-1000, New Era Pump Systems Inc.). A 0.038" outer diameter tubing (Intramedic polyethylene tubing, BD) was connected to the outlet hole to guide the droplets.

3.2.3 Preparation of Dispersed Phase

Dispersed phase containing IONP precursors were prepared as described elsewhere [16]. Briefly, a 5.88 wt.% PVA stock solution was prepared by dissolving PVA powder in a reactor at 90°C for 3 hours. Iron chloride solution was prepared by dissolving 6.20 g FeCl₃ and 3.80 g FeCl₂•4H₂O in 20 mL distilled water. The iron solution and PVA solution were then mixed proportionally to make a final mixture containing 5 wt.% PVA, 1 wt.% FeCl₃ and 0.6 wt.% FeCl₂•4H₂O. The resultant mixture was filtered through a 5µm filter (Acrodisc® syringe filter, Pall Laboratory) and used as the dispersed phase.

3.2.4 Microfluidic Fabrication of Microparticles

Undecane containing 1 wt.% Span80 was used as the continuous phase. The flow rate of the continuous phase was set at 20 mL/h, while the dispersed phase flow rate was kept at 1 mL/h. The continuous phase was flushed through the microfluidic device for at least 30 seconds to convert the microchannel wall to completely hydrophobic. Droplets were collected after a steady state was reached (~5min). A high-speed camera (Redlake MotionScope M with a frame rate up to 1000 frames/sec) was used to image the beads formation process.

The microdroplets generated were subsequently guided to a container containing 0.5 mol/L sodium hydroxide (NaOH) solution, whereby IONPs formed and the droplets solidified. The resulting microbeads were further collected and washed with 50v/v% ethanol in water several times and subject to six freeze-thaw cycles (FTCs) (from 20°C to -20°C then to 20°C at 0.1°C/min, held for one hour at the temperature limits). After that, the microbeads were stored in phosphate-buffered saline (PBS) at room temperature until future use.

3.2.5 Microscopy Observation

Morphological observation and size analysis were first acquired from an optical microscope (Olympus BX60) equipped with an OMRX A35100U camera. Samples were prepared by dropping microbeads suspension on the microscope glass slides. The area of the beads was measured manually using Image J software for over 100 samples (see

Appendix A for an image used in this measurement) and then converted into an equivalent spherical diameter using the following equation:

$$d = 2\sqrt{A/\pi} \quad (1)$$

where d is the equivalent spherical diameter and A is the measured sectional area of the microbead.

Surface morphology was examined with a scanning electron microscope (SEM, LEO (Zeiss) 1540XB FIB/SEM). Microbeads were dehydrated through to 100% ethanol by incrementally increasing ethanol concentration. Critical point drying (Samdri PVT-3B) was performed on the microbeads loaded onto a p-type silicon wafer with 0-10 Ohm-cm resistivity and orientation of 100 (University Wafers). Before imaging, samples were sputtered with a 5 nm osmium coating (Plasma Coater, Filgen). EDX was also performed on these samples for elemental analysis.

Transmission electron microscopy (TEM, PhillipsCM10) was performed to reveal the beads' microstructure and acquire the size and shape of internal IONPs. TEM samples were prepared by dropping the microbead suspension onto the Formvar carbon-coated 400 mesh copper grids (Electron Microscopy Sciences) and dried in air.

3.2.6 Magnetic Properties

The PVA-IONP microbeads (75.24 mg/mL) were suspended were placed in a microcentrifuge tube (ThermoFisher Scientific) filled with 1 mL PBS solution. A permanent magnet was then introduced close to the tube for a selected time interval. The movement of microbeads towards the magnet and their settling upon magnet removal was recorded using a camera.

The hysteresis loop of dried microparticles was tested using a vibrating sample magnetometer (VSM, LakeShore 7407, Lake-ShoreCryotronics Inc.) at 298 K.

3.2.7 MR Contrast Effect

For the MR images, PVA-IONP microbeads were placed in 1.5mL centrifuge tubes at varying masses. Neat 5wt% PVA hydrogel was homogenized and used as the control. All tubes were filled with agar phantom material described elsewhere [18] and then placed in a large plastic container also containing agar phantom material.

MRI contrast enhancement was examined using a clinical 3T MRI scanner (Siemens Healthcare, Erlangen, Germany). Scans were performed at 350 ms repetition, 3.5-15 ms echo-time, 3mm (axial) and 4mm (coronal) section thickness, 4.8 mm (axial) and 3.6 mm (coronal) intersection spacing, 88x192 matrix size and 65x141mm field of view to acquire T₂-weighted images.

3.2.8 *In vitro* Degradation Measurements

Degradation of the PVA-IONP microbeads was studied by placing 1.5mL hydrated beads (76 mg/mL) into a dialysis kit (2mL Mini Dialysis Kit, 1kDa, GE Healthcare) and performing dialysis against 3 mL DMEM (pH=7.4, used as received; pH=5.5, adjusting pH using HCl) at 37 °C. At predetermined time points, the solution outside the dialysis kit was collected, and the amount of released iron content was analyzed using atomic absorption spectroscopy (AAS, Varian Spectra AA-55) at the wavelength of 248.3 nm. Once the degradation medium was removed, the dialysis kit was placed in an equal volume of fresh release medium. Each experiment was carried out in triplicate. To determine the percentile of released iron, the total iron content of microbeads was extracted by dissolving the microbeads using diluted HCl. The solubilized iron content was subsequently quantified using AAS.

3.2.9 Loading and *in vitro* Release of DOX

Loading of DOX was achieved by soaking PVA-IONP hydrated microbeads (0.25 mL) into a doxorubicin solution (equivalent DOX concentration 0.25 mg/mL, 1mL) at room temperature overnight. The resulted products were collected by a permanent magnet and washed several times with PBS to removed non-specifically absorbed drugs.

The amount of doxorubicin in the supernatant was quantified using a UV spectrophotometer (Cary 60 UV-Vis, Agilent Technologies Inc.) at 485 nm. The loading capacity of doxorubicin was determined by Equation 2:

$$\text{Doxorubicin loading} \left(\frac{\text{mg}}{\text{mL}} \right) = (W_0 - W_t) / V_b \quad (2)$$

Loading efficiency was determined by Equation 3 as follows:

$$\text{Loading efficiency (\%)} = \frac{(W_0 - W_t)}{W_0} \times 100\% \quad (3)$$

where W_0 is the initial weight of DOX in solution, W_t is the weight of DOX in the supernatant, and V_b is the volume of hydrated PVA-IONP beads.

To study the *in vitro* release of DOX, drug-loaded microbeads were resuspended into 15 mL release buffer (PBS, pH=7.4 and phosphate buffer, pH 5.5) and then placed in a shaking water bath (New Brunswick Scientific, USA) maintained at 37 °C with gentle shaking (rpm=110). At predetermined release intervals, a supernatant of 1 mL was withdrawn from each sample and analyzed as described before. Subsequently, 1 mL of fresh release media was added to the microbeads to keep the total volume constant.

The cumulative DOX release was calculated by Equation 4:

$$\text{Cumulative DOX release (\%)} = \frac{M_t}{M_\infty} \times 100\% \quad (4)$$

where M_t is the amount of DOX released at time t , M_∞ is the amount of DOX loaded on the microbeads.

3.2.10 Statistical Analysis

For DOX loading study, a sample size of six was used. For DOX release and microbeads degradation study, a sample size of three was used at each experimental condition.

Statistical analysis was performed using Microsoft Excel and OriginLab 2019b (OriginLab Corporation, MA). Results are reported as the mean \pm standard deviation.

3.3 Results

3.3.1 Droplets Generation and Size Analysis

The dispersed phase was broken into droplets at the narrow orifice by continuous phase (Figure 3.1). The droplets solidified in the NaOH solution and retained a teardrop shape. All the microbeads exhibited brownish-yellow color (Figure 3.2 A). The microbeads followed a relatively narrow size distribution with an equivalent spherical diameter of $95 \pm 22 \mu\text{m}$ (Figure 3.2 B).

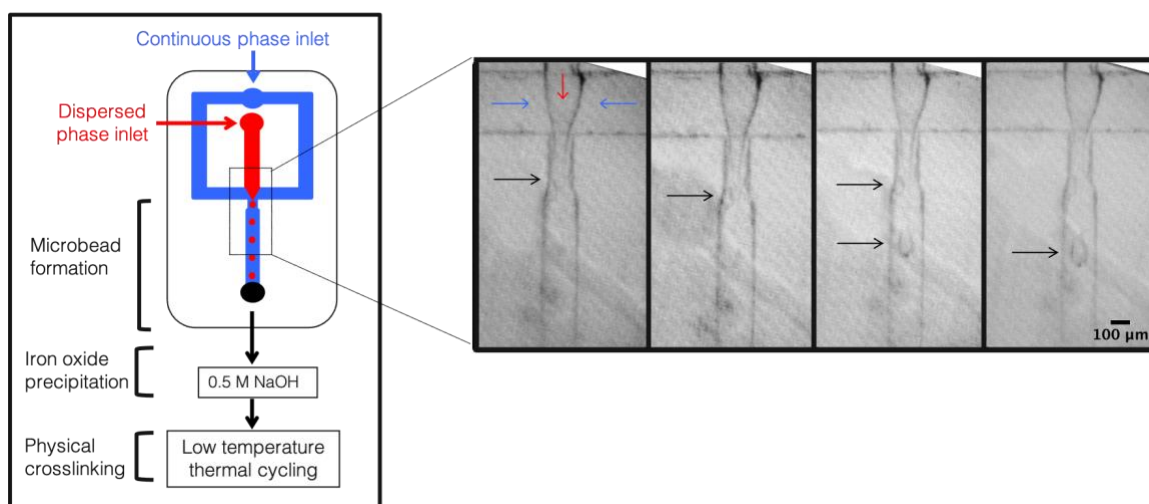


Figure 3.1 Fabrication of PVA-IONP microbeads using a flow-focusing microfluidic channel. The red arrow indicates flow of the dispersed phase, the blue arrow indicates flow of the continuous phase, and the black arrow indicates the generated microbeads. Droplets were successfully fabricated using a flow-focusing microfluidic device.

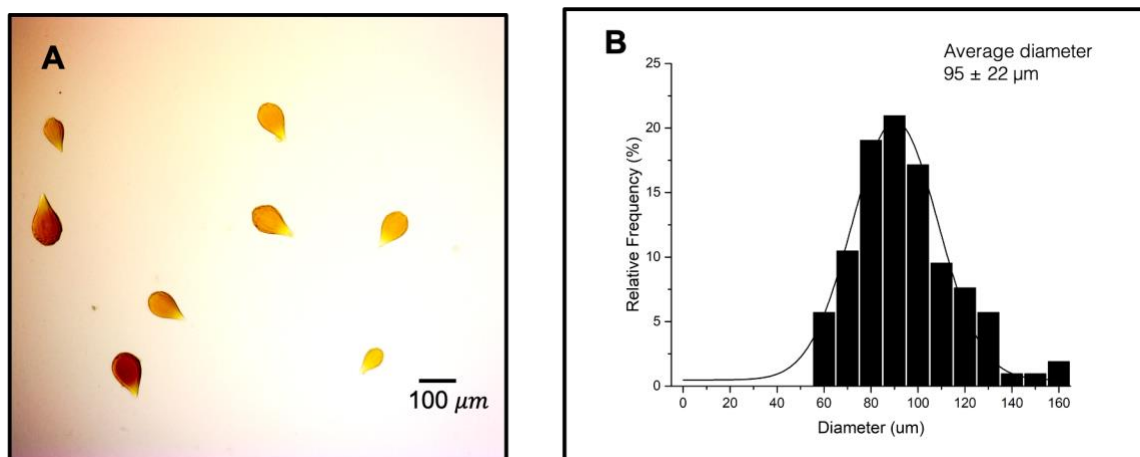


Figure 3.2 (A) Optical microcopy image of fabricated PVA-IONP microbeads and (B) histogram of microbead equivalent spherical diameter fit to a Gaussian distribution. Microbeads were in a teardrop shape with a relatively narrow size distribution.

3.3.2 Morphological, Elemental and Structural Features of Microparticles

The morphology of the beads was examined using SEM and results are shown in Figure 3.3 A-C. EDX analysis of the microbeads confirmed the presence of iron inside of the beads (Figure 3.3 D-E).

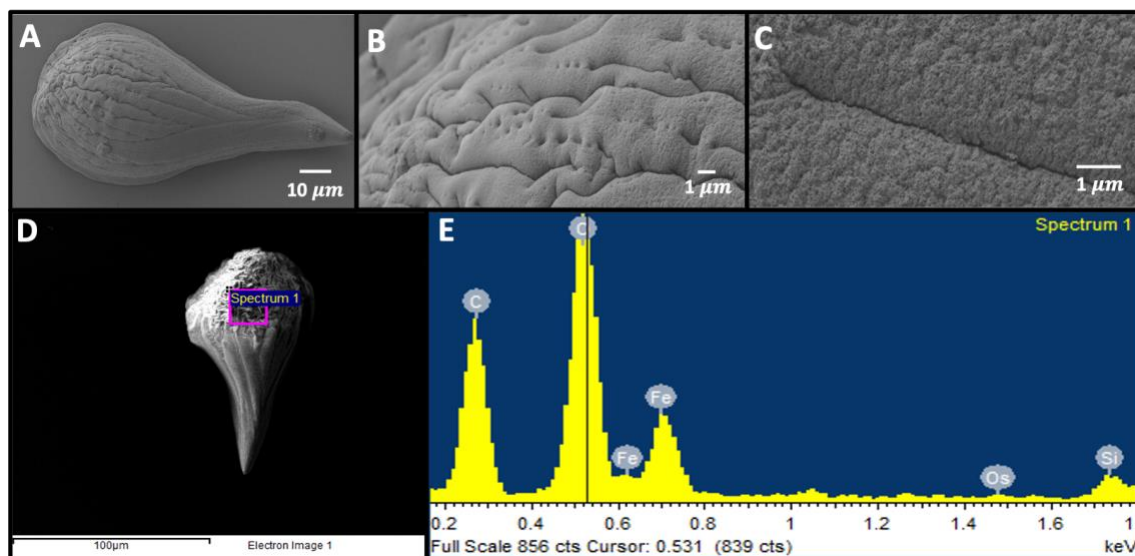


Figure 3.3 (A)-(C) SEM images of PVA-IONP microbeads. (A) displays a whole bead, (B) and (C) show surface morphology. (D) Whole microbead with a square specifying the location of EDX sampling. (E) EDX spectrum indicating the presence of iron in the PVA-IONP microbeads.

Inspection of beads by TEM revealed the presence of iron in the form of IONPs with a uniform spherical shape (Figure 3.4 A) with minimum aggregation. The size distribution histogram showed a narrow size distribution of IONPs with a mean diameter of 11 nm (Figure 3.4 B). IONPs were distributed at the interface of polymer-rich and polymer-poor regions.

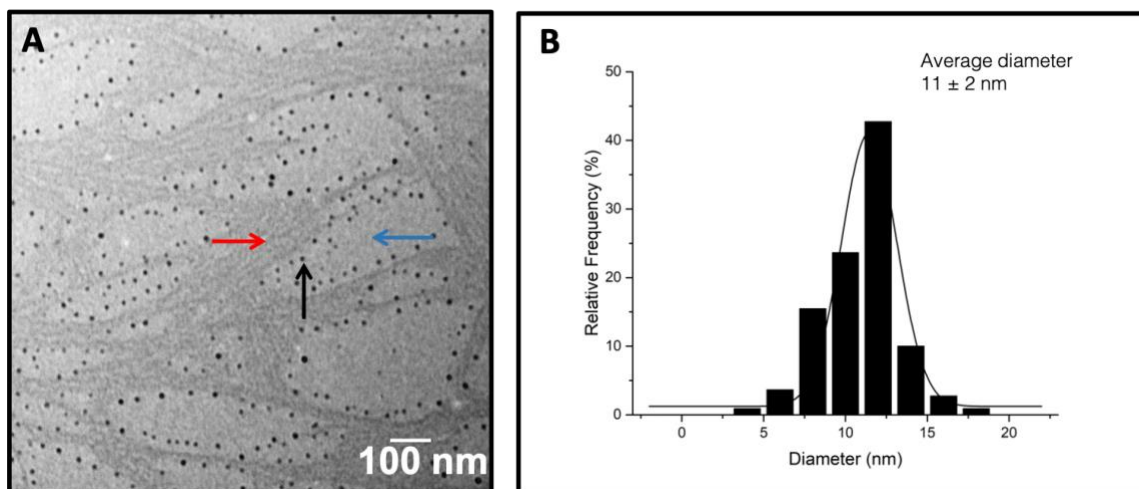


Figure 3.4 (A) TEM micrograph of PVA-IONP microbeads. The black arrow indicates an individual iron oxide nanoparticle, the red arrow indicates a polymer-rich region, and the blue arrow indicates a polymer-poor region. (B) Histogram of diameter of dispersed IONPs fit to a Gaussian distribution. IONPs were in spherical shape with minimum aggregation. IONPs were observed to distribute at the interface of polymer-rich and polymer-poor regions.

3.3.3 Magnetic Properties

The magnetic properties of microbeads were first examined visually in stagnant PBS. Upon introducing the magnet, the beads moved towards it. Once the magnet was removed, all beads slowly settled down due to gravity (Figure 3.5 A).

The magnetization study of PVA-IONP microbeads was performed at 25 °C. The symmetrical sigmoidal shape of the magnetization curve in the absence of a hysteresis loop indicated a superparamagnetic behavior (Figure 3.5 B). A saturation magnetization (M_s) of 9.36 emu/g was obtained from the curve.

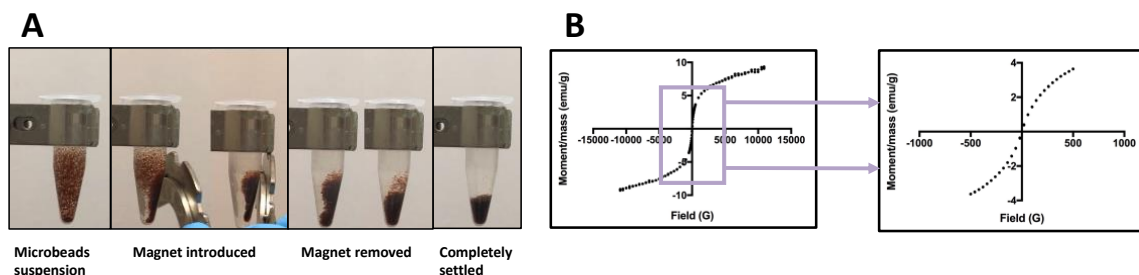


Figure 3.5 (A) Magnetic responsiveness of PVA-IONP microbeads upon introducing of a permanent magnet close to the sample. The microparticles were attracted by the magnet and would completely settle down due to gravity after the magnet was removed. (B) Magnetic susceptibility of the microbeads. The absence of a hysteresis loop indicates a superparamagnetic behavior of the PVA-IONP microbeads. The saturation magnetization M_s of the microbeads was measured to be 9.36 emu/g.

3.3.4 MR Contrast Effect

As shown in Figure 3.6, a darkening effect was observed in the T_2 -weighted images. An enhanced contrast against background was observed relative to a control sample of neat PVA, thus confirming the effectiveness of iron oxide as a contrast agent. In addition, a more prominent darkening effect was observed with a greater amount of microbeads, indicating the contrast effect is correlated to the density of microbeads hence the IONPs.

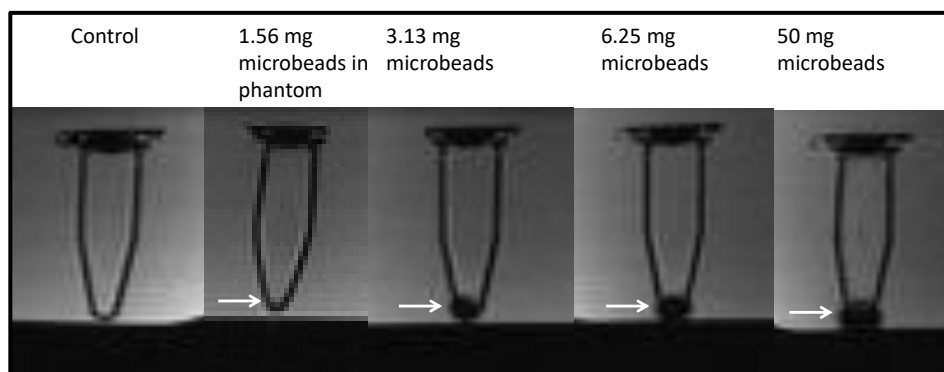


Figure 3.6 T_2 -weighted MRI images of microbeads at different quantities (3T, repetition time 350 ms, echo-time 3.5-15 ms). The white arrow indicates the presence of PVA-IONP microbeads and their contrast effect on T_2 -weighted images.

3.3.5 *In vitro* Degradation

Degradation of PVA-IONP microbeads was studied in DMEM at pH 7.4 and 5.5 for more than 50 days. The degradation is measured quantitatively as iron release and qualitatively as PVA matrix disintegration.

As depicted in Figure 3.7 A, iron release from microbeads appeared to be a two-stage release with non-significant dependence on pH. Iron release rate remained slow at the first stage (day 0-day 17), with less than 2.5% of total iron was released from microbeads under both conditions. The release rate was faster at the second stage (day 18-day 52) without reaching a plateau by the end of the measurements. After day 17, more than 20% of total iron was released in 5 weeks, resulting in a ~26% cumulative release for microbeads under acidic pH, while this number reached ~23% for samples under physiological pH.

Due to the small value of the sample weight, we were not able to measure the weight loss of the sample directly. However, the development of transparent beads (Figure 3.7 B and C) revealed the release of IONPs, which can be taken as part of mass loss hence degradation of PVA-IONP beads. In addition, SEM images of the beads at day 30 (Figure 3.7 D) showed changes in morphology, which confirmed the dissolution and disintegration of the polymer matrix.

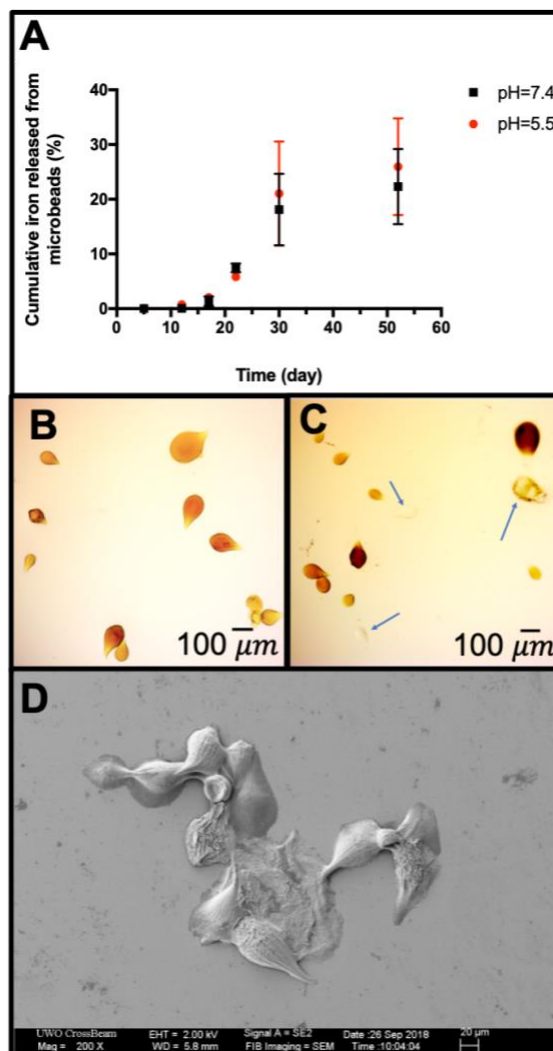


Figure 3.7 Degradation of the PVA-IONP beads. (A) Cumulative iron released from the microbeads. (B) and (C) are optical images of beads at day 0 and day 30, respectively. (D) SEM micrograph of beads at day 30. Degradation study was performed in DMEM at pH 5.5, 7.4 and 37 °C. More than 20% of total iron was released in 5 weeks for both conditions. The removal of IONPs can be further visualized through the color change of the microparticles. The PVA-IONP microparticles lost the original teardrop shape during the incubation. The release of IONPs and disintegration of the polymeric matrix indicate the degradation of the microbeads.

3.3.6 DOX Loading and *in vitro* Release

Due to the abundant presence of hydroxyl groups in the PVA matrix, the microbeads are anticipated to be capable of loading with hydrophilic drugs such as DOX, through van der Waals interaction and hydrogen bonding [19]. The PVA-IONP microbeads allowed a DOX loading capacity of 0.49 ± 0.02 mg/mL with a loading efficiency of $48.8 \pm 2.5\%$.

As shown in Figure 3.8, a sustained and pH-dependent DOX release profile was observed during the course of 7 days. For microparticles at pH 7.4, ~20% of DOX was released within 1 hour and a maximum release of 32% was reached within 7 days. Acidic environment significantly accelerated the DOX release such that ~33% of the drug was released within the first hour and ~ 53% of Dox was released within a week.

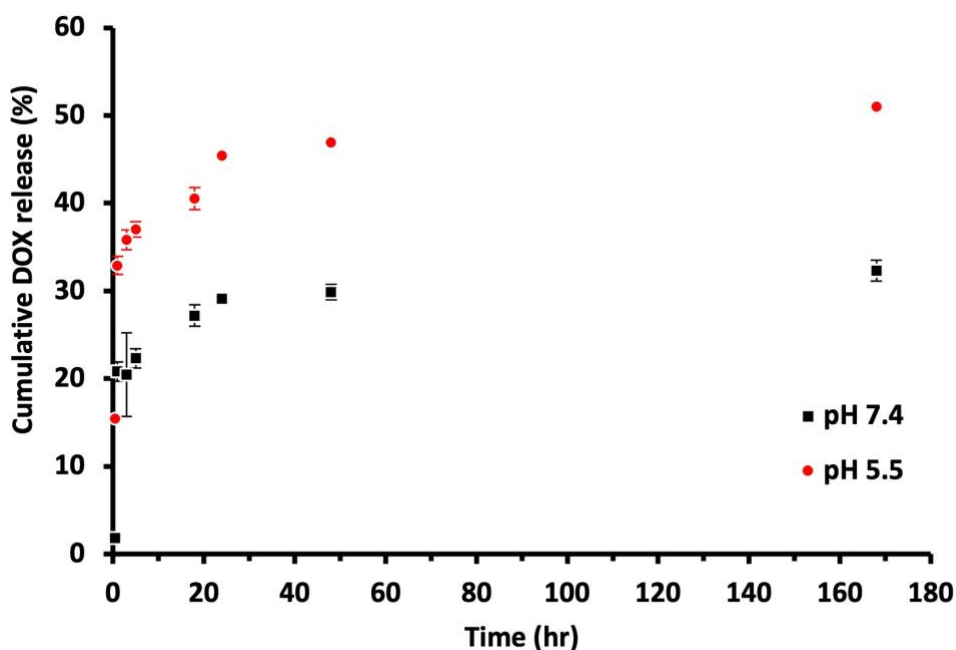
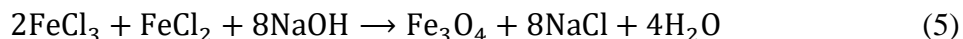


Figure 3.8 Profiles of cumulative percent doxorubicin release with time from PVA-IONP beads in PBS at pH 7.4, 5.5 and 37 °C. The DOX loading was 0.49 ± 0.02 mg/mL with a loading efficiency of $48.8 \pm 2.5\%$. Microparticles can provide a controlled release for DOX for 7 days. Acidic environment contributes to a faster and greater DOX release.

3.4 Discussion

3.4.1 Fabrication of PVA-IONP Microparticles

Microfluidic fabrication was effective in producing PVA-IONP microparticles, resulting in an equivalent spherical diameter of $95 \pm 22 \mu\text{m}$. In a flow-focusing geometry, at the intersection, the central fluid (dispersed phase, PVA with IONP precursors) was hydrodynamically flow focused by the fluid (oil phase, 1 wt.% Span80 in undecane) in the two side channels. A pressure gradient along the long axis of the device forced two liquids through the narrow orifice. Due to the wettability of the two phases to the hydrophobic PMMA channel [20], only the oil phase can adhere to the channel wall, hence the flow of the dispersed phase was pinched off by the oil phase to create droplets [21,22], forming downstream water-in-oil droplets. These iron salts containing droplets fell into the NaOH solution, which triggered the reaction shown in Equation 5, leading to the formation of Fe_3O_4 nanoparticles inside the solidified PVA hydrogel microbeads. These beads were further processed using the LTTC process to impart enhanced stability.



Interestingly, the shape of the PVA-IONP microparticles was non-spherical. The initial generation of non-spherical droplets was suspected to result from the viscous dispersed phase. According to Nie et al. [23], for high viscosity liquids, the surface tension-driven collapse of the neck at the last stage is slow, which would take longer for droplets to break up. In addition, the planar design of the microchannel only allows quasi-2-D contact of fluids. While fully shearing off the viscous disperse phase, the flow of disperse phase was elongated into a teardrop shape due to the combined outcome of shear force and viscoelastic effect [23–26]. Although the droplets would attempt to recover a spherical shape in order to minimize the interfacial free energy after leaving the microchannel [27], as the droplet fell into the NaOH solution, the combined forces applied to the surface of the droplet (e.g., gravity, buoyancy, interfacial tension and drag force), as well as the rigidity change induced by the co-precipitation, would preserve the teardrop shape of the microdroplets [27].

Apart from the shape, the size and size distribution of the microbeads must also be considered. The equivalent spherical diameter of the beads was measured as $95 \pm 22 \mu\text{m}$, which size falls in the range of large arteries and capillaries [28,29]. For TACE therapy, particles with a diameter smaller than $500 \mu\text{m}$ would be desired [30], as they can be easily administered by a catheter and reach the reach in close proximity to a tumor and adequately occlude the vessels [12,31,32].

Despite the teardrop geometry, the PVA-IONP microparticles were fairly uniform in shape with a reproducible size, making them suitable for serving as embolic agents. Some irregularly shaped materials, such as ContourTM (Boston Scientific/Target Therapeutics, USA) and Ivalon[®] PVA blocks, have been used for artery embolization [33]. Although it has been suggested that particles with uniform size and shape may reach more distal locations and has a low probability to form proximal aggregates than irregular materials or material with irregular shape [34–36]. Modifications to address the irregular shape can be made by diluting dispersed phase to reduce the viscosity of the fluid, or by adopting a 3-D coaxial design for the flow-focusing channel [37].

3.4.2 Morphological, Elemental and Structural Features of Microparticles

EDX confirmed the successful incorporation of IONPs into the PVA matrix. The size, shape and dispersity of IONPs were further examined by TEM. IONPs formed were very uniform in size with little or no aggregation (Figure 3.4 A). They were also found to be distributed at the water-rich regions, adjacent to the interface of polymer-rich and water-rich regions. This type of distribution could be explained by the partition behavior of IONP precursors between the two phases, as iron salts have higher solubility and diffusivity in the aqueous phase (i.e., polymer-poor region) [15].

Size uniformity and good dispersity of IONPs are crucial factors as they govern the magnetic behavior and the performance as a T_2 contrast agent [39]. From the TEM micrographs, the size of IONPs in the PVA matrix was $11 \pm 2 \text{ nm}$ with minimum aggregation. IONPs at this size range are anticipated to be single domain particles hence

behave superparamagnetically [40], which was confirmed by the VSM result (Figure 3.5 B).

3.4.3 Magnetic Properties

The magnetic property of PVA-IONP beads was confirmed by their movements towards a permanent magnet, which indicated the potential application in magnetically-guided drug delivery (Figure 3.5 A). Kumar et al. [28] were able to steer a group of microparticles ($D=200\ \mu\text{m}$) with a cylindrical magnet ($B=2\text{T}$) in a simulated body fluid. The beads can be propelled in parallel, antiparallel and angular directions in a linear assembly. It is to be expected that these magnetic particles will be exposed to a more complicated *in vivo* hydrodynamic environment where a combined effect of gravity, drag force, magnetic force and intermolecular repulsive force will govern the locomotion of particles [28,41]. However, with a deeper understanding of fluid dynamics and mechanics and proper MRI gradient coil and designed algorithm, the particle trajectory can be designed and controlled. For example, Chanu et al. [42] has successfully applied a closed-loop control scheme and achieved automatic guidance of a single magnetic bead ($D=1.5\ \text{mm}$) in the carotid artery of a 25 kg living swine.

The superparamagnetic property of the PVA-IONP microparticles was evident from the absence of coercivity and remanence magnetization, suggesting the *in situ* co-precipitation was effective in preparing superparamagnetic hydrogels. During the reaction, the PVA network can potentially prevent agglomeration of IONP and makes it low nanometer in size and well-dispersed [43]. In addition, PVA can serve as a stabilizer to prevent Fe_3O_4 nanoparticles from exposure to O_2 , therefore prevent them from oxidization [44].

A decrease in the M_s value (9.36 emu/g) compared to bulk magnetite (~ 90 emu/g) was apparent [45]. This can be contributed by the reduced particle size of superparamagnetic IONPs [46,47] and the dilution effect from adsorbed water and hydroxyl (-OH) content [45]. Also, the PVA matrix could act as a dead layer to restrict the magnetic coupling interaction and diminish the net moment, resulting in a reduction in M_s [48,49].

Taken all together, the development of superparamagnetic microparticles is useful in magnetic field-related applications such as magnetically-guided drug delivery. These particles can follow the pre-designed route to reach the targeted site through a fine spatial control [50]. This superparamagnetic property can potentially be helpful in MRI, as it can filter background effects of biological paramagnetic materials (e.g., deoxymyoglobin and deoxyhemoglobin) to obtain images with better contrast [51].

3.4.4 MR Contrast Effect

With an increased IONPs weight in the sample, a darkening effect in T_2 image was observed as expected. It was reported by Wabler et al. [52] that T_2 -weighted contrast positively correlated with a total iron concentration in the samples, this can be understood that the transverse proton relaxation rate (R_2) increased with an increased IONP concentration due to the signal dephasing effects of magnetic nanoparticles [53–55].

The detectability of beads will be extremely helpful in clinical practice to address the lack of feedback during DEB-TACE procedure [56]. The distribution of beads can provide a real-time location to guide the intervention. More importantly, since the drugs and the IONPs are co-localized in the microbeads, the location of beads can serve as a surrogate to report on local drug concentrations.

3.4.5 *In vitro* Degradation

It was found that negligible iron content (less than 2.5%) was released in the first 17 days, indicating a strong binding between the IONPs and PVA (Figure 3.7 A). The relatively faster release in the following weeks could be a result of fast dissolution and diffusion of IONP at the outmost layer of the gel beads [19]. However, this iron release profile could still be helpful in TACE therapy, as imaging is usually required after 2-7 days and 3-6 weeks after the first treatment to assess the tumor response [57]. This IONP release rate can potentially provide sufficient amount of IONPs for each imaging session [4,57,58].

It is worth noting that the pH effect on IONP release was not significant, which may be caused by the complex nature of such a process. In this regard, we hypothesized that

IONP release from swellable hydrophilic PVA matrix could be contributed by a series of physical and chemical process, involving liquid penetration into the polymer network, the hydration and swelling of PVA matrix, dissolution reaction, solubilized iron content diffusion throughout swollen matrix and, possibly with, the degradation of polymer matrix [59]. Among all the processes, the diffusion process can be rate-controlling. Therefore, all IONPs accessed by HCl can be reacted and converted to soluble iron salts within the sampling interval. However, dissolved iron content was retained in the PVA hydrogel and diffused into the medium at a pace determined by the diffusivity, hence the degradation of the polymer matrix [60].

In our previous study on the PVA-IONP bulk material, we have demonstrated the removal of iron mechanically weakens the hydrogel and contributes to the total mass loss of the sample [16]. The authors hypothesized that the stability of the hydrogel was provided by the IONP crosslinking and the physical crosslinking by the LTTC process. The degradation of the material can be regarded as the total mass loss of the hydrogel contributed by the loss or release of iron and the material dissolution.

In this study, the release of IONPs was quantified by the AAS. The SEM observation (Figure 3.7 D) provided qualitative evidence. The shape loss and polymer matrix disintegration were clearly observed on the microparticles at day 30, indicating the degradation of PVA-IONP microbeads.

Degradable materials could be advantageous in tumor embolization as they provide transient embolic effects, which can potentially prevent the occurrence of the post-embolization syndrome, tissue inflammation and fibrosis, and risks from non-target embolization [13,14]. Particularly for patients with HCC, it is reported that over 90% of patients need repeated treatments. As such, degradable microparticles would ideally permit multiple TACE procedures hence better treatment outcomes [33].

3.4.6 DOX Loading and *in vitro* Release

The PVA-IONP microbeads supported sustained DOX release at pH 7.4 and pH 5.5, and the trend suggested the drug release was pH-responsive. The released anticancer drug

contents reached $51.0 \pm 2.2\%$ by 7 days, almost 1.6 times of the release at healthy physiological pH. This greater release may be resulted from the protonation of the primary amine groups ($-\text{NH}_2$) of DOX under an acidic environment, depriving the sites available for hydrogen bonding with PVA.

The microparticles developed incomplete DOX release at both pH conditions, indicating the solute release may be controlled by hydrogen bonding and degradation of microparticles. Taken the degradation measurements together, it is likely that the slow degradation of PVA contributes to the incomplete release of DOX. Nevertheless, the DOX release was in a controlled manner for one week, which could potentially result in a more significant impact on tumor kill.

3.5 Conclusion

This work successfully synthesized novel composite hydrogel microbeads using microfluidic fabrication and *in situ* co-precipitation for IONP synthesis within the PVA matrix. The resulting drug delivery systems were in a teardrop shape with a relatively narrow size distribution. The microparticles exhibited superparamagnetic properties and were effective in producing a contrast-enhancing effect on MR images. Such properties also suggest the feasibility of magnetically-guided drug delivery and *in vivo* imaging during/post the intervention. Moreover, PVA-IONP microparticles were degradable, allowing repeatable TACE to be applied. Degradation occurred in the form of iron release and matrix disintegration. Moreover, these microparticles acted as a suitable carrier for DOX and rendered a controlled release for a course of one week. All these outstanding characteristics make PVA-IONP microparticles an improved DEB system in TACE therapy.

3.6 References

- [1] T. Baere, Y. Arai, R. Lencioni, J.-F. Geschwind, W. Rilling, R. Salem, O. Matsui, M. Soulen, Treatment of Liver Tumors with Lipiodol TACE: Technical Recommendations from Experts Opinion, CardioVascular and Interventional Radiology. 39 (2016) 334–343.

- [2] C.-Y. Huang, D.-T. Ju, C.-F. Chang, P. Muralidhar Reddy, B.K. Velmurugan, A review on the effects of current chemotherapy drugs and natural agents in treating non-small cell lung cancer, *Biomedicine (Taipei)*. 7
- [3] K. Fuchs, R. Duran, A. Denys, P.E. Bize, G. Borchard, O. Jordan, Drug-eluting embolic microspheres for local drug delivery – State of the art, *Journal of Controlled Release*. 262 (2017) 127–138.
- [4] J.H.M. Luz, P.M. Luz, H.S. Martin, H.R. Gouveia, R.B. Levigard, F.D. Nogueira, B.C. Rodrigues, T.N. de Miranda, M.H. Mamede, DEB TACE for Intermediate and advanced HCC - Initial Experience in a Brazilian Cancer Center, *Cancer Imaging*. 17 (2017) 5.
- [5] M. Pompili, G. Francica, F.R. Ponziani, R. Iezzi, A.W. Avolio, Bridging and downstaging treatments for hepatocellular carcinoma in patients on the waiting list for liver transplantation, *World J Gastroenterol*. 19 (2013) 7515–7530.
- [6] H.J. Prajapati, P. Kavali, H.S. Kim, Transcatheter arterial chemoembolization in recurrent unresectable hepatocellular carcinoma after orthotopic liver transplantation, *Hepatoma Research*. 3 (2017) 182–188.
- [7] Q.-Q. Zu, S. Liu, C.-G. Zhou, Z.-Q. Yang, J.-G. Xia, L.-B. Zhao, H.-B. Shi, Chemoembolization of Recurrent Hepatoma After Curative Resection: Prognostic Factors, *American Journal of Roentgenology*. 204 (2015) 1322–1328.
- [8] J.-L. Raoul, A. Forner, L. Bolondi, T.T. Cheung, R. Kloeckner, T. de Baere, Updated use of TACE for hepatocellular carcinoma treatment: How and when to use it based on clinical evidence, *Cancer Treatment Reviews*. 72 (2019) 28–36.
- [9] M. Varela, M.I. Real, M. Burrel, A. Forner, M. Sala, M. Brunet, C. Ayuso, L. Castells, X. Montañá, J.M. Llovet, J. Bruix, Chemoembolization of hepatocellular carcinoma with drug eluting beads: Efficacy and doxorubicin pharmacokinetics, *Journal of Hepatology*. 46 (2007) 474–481.
- [10] A.L. Lewis, M.V. Gonzalez, A.W. Lloyd, B. Hall, Y. Tang, S.L. Willis, S.W. Leppard, L.C. Wolfenden, R.R. Palmer, P.W. Stratford, DC bead: in vitro characterization of a drug-delivery device for transarterial chemoembolization, *J Vasc Interv Radiol*. 17 (2006) 335–342.
- [11] A.L. Lewis, S.L. Willis, M.R. Dreher, Y. Tang, K. Ashrafi, B.J. Wood, E.B. Levy, K.V. Sharma, A.H. Negussie, A.S. Mikhail, Bench-to-clinic development of imageable drug-eluting embolization beads: finding the balance, *Future Oncology*. 14 (2018) 2741–2760.
- [12] R. Lencioni, T. de Baere, M. Burrel, J.G. Caridi, J. Lammer, K. Malagari, R.C.G. Martin, E. O’Grady, M.I. Real, T.J. Vogl, A. Watkinson, J.-F.H. Geschwind, Transcatheter Treatment of Hepatocellular Carcinoma with Doxorubicin-loaded DC

- Bead (DEBDOX): Technical Recommendations, *Cardiovasc Intervent Radiol.* 35 (2012) 980–985.
- [13] A. Al Haj Zen, P. Madeddu, Notch signalling in ischaemia-induced angiogenesis, *Biochem Soc Trans.* 37 (2009) 1221–1227.
- [14] C.R. Ingraham, G.E. Johnson, A.V. Nair, S.A. Padia, Nontarget Embolization Complicating Transarterial Chemoembolization in a Patient with Hepatocellular Carcinoma, *Semin Intervent Radiol.* 28 (2011) 202–206.
- [15] W. Wan, A.D. Bannerman, L. Yang, H. Mak, Poly(Vinyl Alcohol) Cryogels for Biomedical Applications, in: O. Okay (Ed.), *Polymeric Cryogels*, Springer International Publishing, Cham, 2014: pp. 283–321.
- [16] A.D. Bannerman, X. Li, W. Wan, A ‘degradable’ poly(vinyl alcohol) iron oxide nanoparticle hydrogel, *Acta Biomaterialia.* 58 (2017) 376–385..
- [17] Preparation of Buffer Solutions : Pharmaceutical Guidelines, (n.d.).
<https://www.pharmaguideline.com/2010/09/preparation-of-buffer-solutions.html> (accessed April 5, 2021).
- [18] A.F. Khan, J.J. Drozd, R.K. Moreland, R.M. Ta, M.J. Borrie, R. Bartha, Alzheimer’s Disease Neuroimaging Initiative, A novel MRI-compatible brain ventricle phantom for validation of segmentation and volumetry methods, *J Magn Reson Imaging.* 36 (2012) 476–482.
- [19] L. Zhou, B. He, F. Zhang, Facile One-Pot Synthesis of Iron Oxide Nanoparticles Cross-linked Magnetic Poly(vinyl alcohol) Gel Beads for Drug Delivery, *ACS Appl. Mater. Interfaces.* 4 (2012) 192–199.
- [20] J.H. Xu, S.W. Li, J. Tan, Y.J. Wang, G.S. Luo, Controllable Preparation of Monodisperse O/W and W/O Emulsions in the Same Microfluidic Device, *Langmuir.* 22 (2006) 7943–7946.
- [21] M. Seo, C. Paquet, Z. Nie, S. Xu, E. Kumacheva, Microfluidic consecutive flow-focusing droplet generators, *Soft Matter.* 3 (2007) 986–992.
- [22] R.K. Shah, H.C. Shum, A.C. Rowat, D. Lee, J.J. Agresti, A.S. Utada, L.Y. Chu, J.W. Kim, A. Fernandez-Nieves, C.J. Martinez, D.A. Weitz, Designer emulsions using microfluidics, *Materials Today.* 11 (2008) 18–27.
- [23] Z. Nie, M. Seo, S. Xu, P.C. Lewis, M. Mok, E. Kumacheva, G.M. Whitesides, P. Garstecki, H.A. Stone, Emulsification in a microfluidic flow-focusing device: effect of the viscosities of the liquids, *Microfluidics and Nanofluidics.* 5 (2008) 585–594.
- [24] P. Garstecki, H.A. Stone, G.M. Whitesides, Mechanism for Flow-Rate Controlled Breakup in Confined Geometries: A Route to Monodisperse Emulsions, *Phys. Rev. Lett.* 94 (2005) 164501.

- [25] L. Derzsi, M. Kasprzyk, J.P. Plog, P. Garstecki, Flow focusing with viscoelastic liquids, *Physics of Fluids*. 25 (2013) 092001.
- [26] R. Hernández, A. Sarafian, D. López, C. Mijangos, Viscoelastic properties of poly(vinyl alcohol) hydrogels and ferrogels obtained through freezing–thawing cycles, *Polymer*. 45 (2004) 5543–5549.
- [27] Y. Hu, Q. Wang, J. Wang, J. Zhu, H. Wang, Y. Yang, Shape controllable microgel particles prepared by microfluidic combining external ionic crosslinking, *Biomicrofluidics*. 6 (2012) 026502.
- [28] Kumar, Magnetic navigation and tracking of multiple ferromagnetic microrobots inside an arterial phantom setup for MRI guided drug therapy, *Biocybernetics and Biomedical Engineering*. 37 (2017) 347–356.
- [29] J.-B. Mathieu, S. Martel, Steering of aggregating magnetic microparticles using propulsion gradients coils in an MRI Scanner, *Magn Reson Med*. 63 (2010) 1336–1345.
- [30] A. Facciorusso, Drug-eluting beads transarterial chemoembolization for hepatocellular carcinoma: Current state of the art, *World J. Gastroenterol*. 24 (2018) 161–169.
- [31] R.A. Sheth, S. Sabir, S. Krishnamurthy, R.K. Avery, Y.S. Zhang, A. Khademhosseini, R. Oklu, Endovascular Embolization by Transcatheter Delivery of Particles: Past, Present, and Future, *Journal of Functional Biomaterials*. 8 (2017) 12.
- [32] T. Amer, A.M. Abd El-khalek, G. Sheha, Intra-arterial chemoembolization with hepasphere 50–100 μ m for patients with unresectable hepatocellular carcinoma: Initial experience in Egyptian Liver Hospital, *The Egyptian Journal of Radiology and Nuclear Medicine*. 46 (2015) 957–965.
- [33] A. Poursaid, M.M. Jensen, E. Huo, H. Ghandehari, Polymeric materials for embolic and chemoembolic applications, *J Control Release*. 240 (2016) 414–433.
- [34] K. Osuga, N. Maeda, H. Higashihara, S. Hori, T. Nakazawa, K. Tanaka, M. Nakamura, K. Kishimoto, Y. Ono, N. Tomiyama, Current status of embolic agents for liver tumor embolization, *Int J Clin Oncol*. 17 (2012) 306–315.
- [35] B. Kim, S.W. Han, S.-E. Choi, D. Yim, J.-H. Kim, H.M. Wyss, J.W. Kim, Monodisperse Microshell Structured Gelatin Microparticles for Temporary Chemoembolization, *Biomacromolecules*. 19 (2018) 386–391.
- [36] D. Kocur, W. Ślusarczyk, N. Przybyłko, M. Hofman, T. Jamróz, K. Suszyński, J. Baron, S. Kwiek, Endovascular Approach to Glomus Jugulare Tumors, *Polish Journal of Radiology*. 82 (2017) 322–326.

- [37] S. Takeuchi, P. Garstecki, D.B. Weibel, G.M. Whitesides, An Axisymmetric Flow-Focusing Microfluidic Device, *Advanced Materials*. 17 (2005) 1067–1072.
- [38] J. Schulze, S. Hendrikx, M. Schulz-Siegmund, A. Aigner, Microparticulate poly(vinyl alcohol) hydrogel formulations for embedding and controlled release of polyethylenimine (PEI)-based nanoparticles, *Acta Biomater*. 45 (2016) 210–222.
- [39] L. Li, W. Jiang, K. Luo, H. Song, F. Lan, Y. Wu, Z. Gu, Superparamagnetic Iron Oxide Nanoparticles as MRI contrast agents for Non-invasive Stem Cell Labeling and Tracking, *Theranostics*. 3 (2013) 595–615.
- [40] I.M. Obaidat, B. Issa, Y. Haik, Magnetic Properties of Magnetic Nanoparticles for Efficient Hyperthermia, *Nanomaterials (Basel)*. 5 (2015) 63–89.
- [41] A.K. Hoshidar, T.-A. Le, F.U. Amin, M.O. Kim, J. Yoon, Studies of aggregated nanoparticles steering during magnetic-guided drug delivery in the blood vessels, *Journal of Magnetism and Magnetic Materials*. 427 (2017) 181–187.
- [42] A. Chanu, S. Martel, Real-time software platform design for in-vivo navigation of a small ferromagnetic device in a swine carotid artery using a magnetic resonance imaging system, *Conf Proc IEEE Eng Med Biol Soc*. 2007 (2007) 6585–6588.
- [43] G.R. Bardajee, Z. Hooshyar, One-pot synthesis of biocompatible superparamagnetic iron oxide nanoparticles/hydrogel based on salep: Characterization and drug delivery, *Carbohydrate Polymers*. 101 (2014) 741–751.
- [44] A.K. Bajpai, R. Gupta, Synthesis and characterization of magnetite (Fe₃O₄)—Polyvinyl alcohol-based nanocomposites and study of superparamagnetism, *Polymer Composites*. 31 (2010) 245–255.
- [45] M. Nadeem, M. Ahmad, M.S. Akhtar, A. Shaari, S. Riaz, S. Naseem, M. Masood, M.A. Saeed, Magnetic Properties of Polyvinyl Alcohol and Doxorubicine Loaded Iron Oxide Nanoparticles for Anticancer Drug Delivery Applications, *PLOS ONE*. 11 (2016) e0158084.
- [46] X. Guo, Z. Wu, W. Li, Z. Wang, Q. Li, F. Kong, H. Zhang, X. Zhu, Y.P. Du, Y. Jin, Y. Du, J. You, Appropriate Size of Magnetic Nanoparticles for Various Bioapplications in Cancer Diagnostics and Therapy, *ACS Appl. Mater. Interfaces*. 8 (2016) 3092–3106.
- [47] Y.-W. Jun, Y.-M. Huh, J.-S. Choi, J.-H. Lee, H.-T. Song, S. Kim, S. Yoon, K.-S. Kim, J.-S. Shin, J.-S. Suh, J. Cheon, Nanoscale size effect of magnetic nanocrystals and their utilization for cancer diagnosis via magnetic resonance imaging, *J. Am. Chem. Soc*. 127 (2005) 5732–5733.
- [48] M.P. Kesavan, S. Ayyanaar, N. Lenin, M. Sankarganesh, J.D. Raja, J. Rajesh, One pot synthesis of new poly(vinyl alcohol) blended natural polymer based magnetic

- hydrogel beads: Controlled natural anticancer alkaloid delivery system, *Journal of Biomedical Materials Research Part A*. 106 (2018) 543–551.
- [49] D.L. Leslie-Pelecky, R.D. Rieke, *Magnetic Properties of Nanostructured Materials*, *Chem. Mater.* 8 (1996) 1770–1783.
- [50] B. Hallmark, N. Darton, T. James, P. Agrawal, N. Slater, Magnetic field strength requirements to capture superparamagnetic nanoparticles within capillary flow, *Journal of Nanoparticle Research*. 12 (2010) 2951–2965.
- [51] S.R. Iyer, S. Xu, J.P. Stains, C.H. Bennett, R.M. Lovering, Superparamagnetic Iron Oxide Nanoparticles in Musculoskeletal Biology, *Tissue Engineering Part B: Reviews*. 23 (2016) 373–385.
- [52] M. Wabler, W. Zhu, M. Hedayati, A. Attaluri, H. Zhou, J. Mihalic, A. Geyh, T.L. DeWeese, R. Ivkov, D. Artemov, Magnetic resonance imaging contrast of iron oxide nanoparticles developed for hyperthermia is dominated by iron content, *Int J Hyperthermia*. 30 (2014) 192–200.
- [53] X. Guo, W. Li, L. Luo, Z. Wang, Q. Li, F. Kong, H. Zhang, J. Yang, C. Zhu, Y. Du, J. You, External Magnetic Field-Enhanced Chemo-Photothermal Combination Tumor Therapy via Iron Oxide Nanoparticles, *ACS Appl. Mater. Interfaces*. 9 (2017) 16581–16593.
- [54] Y. Wang, R. Zhao, S. Wang, Z. Liu, R. Tang, In vivo dual-targeted chemotherapy of drug resistant cancer by rationally designed nanocarrier, *Biomaterials*. 75 (2016) 71–81.
- [55] J. Chen, S.B. White, K.R. Harris, W. Li, J.W.T. Yap, D.-H. Kim, R.J. Lewandowski, L.D. Shea, A.C. Larson, Poly(lactide-co-glycolide) microspheres for MRI-monitored delivery of sorafenib in a rabbit VX2 model, *Biomaterials*. 61 (2015) 299–306.
- [56] A.L. Lewis, M.R. Dreher, Locoregional drug delivery using image-guided intra-arterial drug eluting bead therapy, *J Control Release*. 161 (2012) 338–350.
- [57] B. Yang, C.-L. Li, W. Guo, T. Qin, H. Jiao, Z. Fei, X. Zhou, L. Duan, Z. Liao, Intra-arterial ethanol embolization augments response to TACE for treatment of HCC with portal venous tumor thrombus, *BMC Cancer*. 18 (2018).
- [58] K. Takayasu, S. Arii, N. Matsuo, M. Yoshikawa, M. Ryu, K. Takasaki, M. Sato, N. Yamanaka, Y. Shimamura, M. Ohto, Comparison of CT Findings with Resected Specimens After Chemoembolization with Iodized Oil for Hepatocellular Carcinoma, *American Journal of Roentgenology*. 175 (2000) 699–704.
- [59] F.M. Carbinatto, A.D. de Castro, R.C. Evangelista, B.S.F. Cury, Insights into the swelling process and drug release mechanisms from cross-linked pectin/high amylose starch matrices, *Asian Journal of Pharmaceutical Sciences*. 9 (2014) 27–34.

- [60] I.J. Macha, B. Ben-Nissan, E.N. Vilchevskaya, A.S. Morozova, B.E. Abali, W.H. Müller, W. Rickert, Drug Delivery From Polymer-Based Nanopharmaceuticals—An Experimental Study Complemented by Simulations of Selected Diffusion Processes, *Front. Bioeng. Biotechnol.* 7 (2019).

Chapter 4

4 Development of a Multifunctional Bioactive Protein/Peptide Delivery System for Dry Eye Disease²

4.1 Introduction

Dry eye disease (DED) is a multifactorial disease characterized by inflammation that damages the ocular surface and tear producing glands [3,4]. Tear film instability or osmolarity changes, among others, stress underlying corneal epithelial cells, inducing further release of pro-inflammatory cytokines, including interferon- γ (IFN γ) and tumor necrosis factor (TNF) [3,5,6]. All severities of DED substantially reduce health-related quality of life [7]. Worldwide prevalence is estimated at 5.5–33.7% with Canada at 25%, but underestimates may result from patients' failure to recognize or report symptoms, indicating a large public health issue [4,8].

Eye drops are widely used to deliver artificial tears and anti-inflammatory agents to the ocular surface of DED patients [5]. This method fails to sustain drug delivery, with less than 5% of the topically applied drug dose reaching target corneal tissue. Rapid drug elimination can be attributed to blinking, the tear film barrier, reflex tearing, and drainage through tear ducts [9]. Losing over 95% of the formulation's dose during drug delivery not only impairs cost-effectiveness but also requires diligent patient compliance with frequent dosing throughout the day to maintain adequate efficacy within target tissues. Such high patient compliance is not consistently attainable, likely decreasing therapeutic effectiveness.

Current pharmaceutical agents commonly used to treat DED are also unfavorable as long-term solutions. Artificial tears provide only temporary lubrication without addressing the underlying pathology of DED, with most formulations lacking bioactive tear components [10,11]. Long-term use of corticosteroid eye drops may increase the risk of developing

² A version of this chapter will be submitted to *Clinical & Experimental Ophthalmology* under the title: Lacritin peptide (N-94)-conjugated solid silica nanoparticles as a novel drug delivery system for dry eye disease. Xinyi Li shares the co-first authorship with Angela Chang.

glaucoma, cataracts, and bacterial infections [3,5,10]. Prolonged use of cyclosporine can lead to complications such as lid maceration and corneal epitheliopathy [12]. Indeed, few physicians in White et al.'s study were satisfied with the ability of cyclosporine and lifitegrast to manage DED symptoms and improve quality of life [13].

The development of protein and peptide-based therapeutics is rapidly increasing for the treatment of a wide variety of clinical indications [14]. Inorganic nanoparticles such as gold nanoparticles (AuNPs), iron oxide NPs (IONPs), and silica NPs (SiNPs) have also been extensively investigated. They are highly biocompatible, with some formulations proceeding to the clinical trial stage [15]. Among these, SiNPs are especially promising as carriers for ophthalmic therapeutics to overcome the bioavailability limitation of traditional eye drops. Generally Recognized as Safe (GRAS) by the FDA, SiNPs are generally not cytotoxic to human corneal epithelial cells (HCECs), with larger diameters having a lower risk of cytotoxicity [16–18]. Lysozyme is widely used in the study of silica-protein interactions due to its conformational stability and similar properties to numerous bioactive proteins [19,20]. In addition to its prototypical features, lysozyme possesses antimicrobial, anti-inflammatory properties and is also a major component of the tear film [21–23].

Lacritin has many desirable properties conducive to its development as a therapeutic agent for DED. It is a human tear glycoprotein secreted by the lacrimal glands and downregulated in DED tears [24,25]. Topical application enhances basal tearing in rabbits [10,26]. It is mitogenic and cytoprotective on HCECs *in vitro* [27,28]. Its C-terminus is bactericidal and rescues HCECs stressed by inflammatory mediators IFN γ and TNF by stimulating an autophagy pathway to clear damaged organelles and proteins [29–31]. Because its C-terminus has a heparanase-dependent binding mechanism to syndecan-1, lacritin binding targets areas of the eye highly associated with DED [32,33].

Since lacritin's C-terminus mediates receptor activation and thus prosecretory, bactericidal, and cytoprotective activity, the N-94 fragment should be equipotent to the complete protein. We investigated a synthetic 25-amino acid lacritin peptide (N-94) derived from lacritin's C-terminal side as a candidate drug to be delivered by SiNPs. N-

94 is smaller and has a more suitable isoelectric point than lacritin, maximizing its loading potential onto SiNPs. Preliminary studies indicate that N-94 has a predicted isoelectric point (IEP) of 10.5 while lacritin has an IEP of 5 [34]. At physiological pH, N-94 would be positively charged to aid in its adsorption to the negatively charged SiNP surface [35].

The use of SiNPs as a controlled release delivery system for the N-94 offers several advantages for the treatment of DED. Since the N-94 fragment decomposes readily on the inflammatory and oxidative ocular surface, the N-94-SiNPs would allow for sustained availability of N-94 over time [2]. Furthermore, the loading, release time profile, and dosage can be tuned based on clinical needs.

While an existing study found that lacritin reduces HCEC death induced by pro-inflammatory cytokines, it was unconfirmed whether N-94 had similar cytoprotective effects [29]. The biocompatibility of N-94 and N-94-conjugated SiNPs (N-94-SiNPs) with HCECs was also yet to be elucidated.

In this study, we synthesized the SiNPs using the Stöber method. Their drug loading and controlled release properties were characterized using lysozyme as a model protein. Dissolution of the SiNPs was also demonstrated. N-94 was subsequently conjugated to SiNPs, its release profile, presence of toxicity to HCECs, and cytoprotective activity were also studied to assess the feasibility of the conjugated system for treating DED.

4.2 Materials and Methods

4.2.1 Materials

All chemicals were used as received without further purification. Tetraethylorthosilicate (TEOS, 99+%) and lysozyme from chicken egg white (minimum 23,500 units/mg protein) were purchased from Alfa Aesar, ammonium hydroxide (28%-30% NH₃ in H₂O) was obtained from Caledon. Phosphate buffered saline tablets and dimethylsulfoxide (DMSO) were purchased from Sigma-Aldrich. Ethanol (95%) was obtained from Commercial Alcohols. Inflammatory cytokines IFN γ and TNF were acquired from Thermo Fisher Scientific. Peptide N-94 was obtained from GenScript (Piscataway, NJ),

custom-made with fluorescein isothiocyanate (FITC) and a seven-atom aminohexanoyl spacer covalently conjugated to the peptide's N-terminus to allow for quantification via fluorescence spectrophotometry. Distilled water was used for all experiments.

4.2.2 Preparation and Characterization of Protein/Peptide-SiNPs Conjugates

SiNPs were synthesized by the Stöber method [217]. In a typical synthesis, solution containing 5 mL ethanol and 10 mL ammonia was prepared. After equilibration at room temperature ($23 \pm 1^\circ\text{C}$), 100 μL TEOS was added dropwise and the reaction was maintained at the same temperature for 1 hour under constant stirring. The resulting white precipitate was separated by centrifugation (Sorvall RC5C, Sorvall Instruments, USA), washed with water and ethanol, and dried at 60°C under vacuum overnight for future use.

To prepare lysozyme loaded SiNPs for characterization, conjugates were prepared from a relatively concentrated lysozyme solution (10 mg/mL, 1 mL) and 15 mg SiNPs. To load N-94 onto the SiNPs, a 20:1 ratio (w/w) of SiNP:N-94 each suspended in equal volumes of PBS were combined in Eppendorf tubes. Adsorption was allowed for 48 hours at room temperature for both formulations. Pellets were separated and rinsed with PBS to remove loosely attached lysozyme molecules. FTIR (Bruker Vector, USA) and scanning electron microscopy (SEM, LEO1540XB FIB/SEM, ZEISS, USA) were performed on both air-dried bare SiNPs and protein/peptide-SiNPs conjugates.

4.2.3 Protein Adsorption Kinetics and Isotherms

For the adsorption kinetics studies, lysozyme-SiNP conjugates were prepared by mixing 100 mg of SiNPs in a beaker containing 12 mL of a 0.5 mg/mL lysozyme in 1x PBS solution (pH 7.4). Adsorption was performed at room temperature in an orbital shaker (New Brunswick Scientific) at 75 rpm. All experiments were performed in triplicate.

At pre-determined time points, 0.5 mL supernatant was retrieved. Lysozyme concentration in the supernatant was determined by a Cary UV-vis spectrophotometer (Agilent Technologies) at $\lambda=280$ nm.

The amount of lysozyme adsorbed onto SiNPs at time t , Q_t was determined by the concentration difference between the stock solution and supernatant:

$$Q_t = \frac{(C_0 - C_e)V}{m} \quad (1)$$

where C_0 and C_t are the concentration of lysozyme in the stock solution and in the suspension at time t (mg/L), respectively. V is the total volume of the solution (in L), and m is the weight of SiNPs (g).

Isotherm studies were performed with a constant dosage of SiNPs (15 mg/mL in the final mixture) and varying concentrations of lysozyme (C_0) in the range of 133 mg/L to 3000 mg/L. The mixture was shaken at 160 rpm for 48 h at ambient temperature. Finally, samples were centrifuged for 5 minutes at 8,000 rpm to retrieve supernatant, which was subject to UV-vis for lysozyme quantification.

4.2.4 Protein/Peptide Release in the Absence of Cells

The release of bioactive protein/peptide from SiNPs were characterized using lysozyme and N-94 as the prototypical molecules. Lysozyme-SiNP and N-94-SiNP conjugates were prepared separately by mixing SiNPs and corresponding adsorbates at a 20:1 ratio (w/w). Adsorption was maintained at room temperature in an orbital shaker at 75 rpm for 48 hours. The resulting conjugates were rinsed with PBS and transferred to microcentrifuge tubes (Sigma-Aldrich) containing 1 mL PBS in each. Release was then carried out at 37°C in the orbital shaker at 75 rpm. At pre-determined time points, supernatant was replaced with fresh PBS to maintain the total volume constant.

The amount of adsorbed/released adsorbates was determined by UV-vis in the case of lysozyme, while for N-94 quantification, a SpectraMax M3 Multi-Mode Microplate Reader (Molecular Devices, LLC, CA) was used. Samples were excited at 496 nm and emission intensity at 520 nm was acquired. In addition, matrix assisted laser desorption ionization-time of flight mass spectrometry (MALDI-TOF MS) was used to verify the integrity of pre-conjugated and released N-94 samples obtained at 8 hours, suspended in ultrapure water. Samples were mixed at a 1:1 ratio (v/v) with an α -cyano-4-hydroxycinnamic acid MALDI matrix (5 mg/mL in 50% acetonitrile and 0.1%

trifluoroacetic acid) and spotted on the MALDI plate in duplicates. MS data were obtained using an AB Sciex 5800 TOF/TOF System (Framingham, MA). Data acquisition and processing were done using an AB Sciex TOF/TOF Series Explorer and Data Explorer.

4.2.5 Dissolution of SiNPs in the Absence of Cells

In vitro degradation was studied in PBS at 37°C with SiNPs alone. Typically, 10 mg of SiNPs were added into 5 mL of PBS and samples were incubated in a shaker at 75 rpm. PBS was replaced every 5 days to prevent solution saturation. At pre-determined time points, solid SiNPs were retrieved, washed, and resuspended in water. Transmission electron microscopy (TEM, PhillipsCM10) graphs were taken to examine the structural changes of SiNPs during the degradation. TEM samples were prepared by dropping this suspension onto a Formavar carbon-coated copper grid.

4.2.6 Cell Culture

Primary human corneal epithelial cells (HCECs) obtained from three different donors were purchased from American Type Culture Collection (ATCC, Manassas, VA). HCECs at the second passage at the time of purchase were cultured in colorless, keratinocyte-serum free Corneal Epithelial Cell Basal Medium with Corneal Epithelial Cell Growth Kit supplements (ATCC). For all experiments, cultured cells were seeded in 24-well plates directly into the wells or into trans-well inserts at a density of 2×10^5 cells/cm² and treated when 80% confluent.

4.2.7 Determination of Optimal Pro-inflammatory Cytokines IFN γ & TNF Concentration

Using Wang et al.'s study as a guideline, a fixed IFN γ concentration of 100 U/mL was combined with varying concentrations of TNF to insult HCECs for 16 or 20 hours [29]. The combination that reduced cellular metabolic activity from 100% to about 65–75% was used to stress HCECs. The 3-(4,5-dimethylthiazol-2-yl)-2,5-diphenyltetrazolium bromide (MTT) assay was used to measure cellular metabolic activity.

4.2.8 Effects of N-94 on HCECs

Effect of N-94 on HCECs was evaluated in terms of cytotoxicity and cryoprotection. To detect potential cytotoxicity, HCECs were treated with 1–10 000 nM of N-94 for 1–24 hours. Cells cultured in medium without the addition of N-94 were used as negative controls (“vehicle control”).

At designated times, cell viability was determined by the measurement of cellular metabolic activity using the MTT assay. Briefly, cells were incubated in 24-well plates in serum-free conditions with 450 µg/mL MTT solution (Sigma-Aldrich) for 3 hours at 37°C. After aspirating excess MTT, dimethylsulfoxide (DMSO, Sigma-Aldrich) was added and plates were shaken. Samples were transferred to 96-well plates in triplicate, with a few wells reserved for DMSO only. Absorbances were read at 575 nm by the iMark Microplate Reader (Bio-Rad Laboratories). The DMSO absorbance was subtracted from all other absorbances. The cellular metabolic activity of experimental groups was normalized by the vehicle control group (100%) in all cellular studies and expressed as percentages.

To investigate the cytoprotective effects of N-94 on HCECs, HCECs were simultaneously treated with 1–10 000 nM of N-94 and pro-inflammatory cytokines of the optimal concentration combination for 16 and 20 hours. The positive control consisted of HCECs stressed by cytokines in the absence of N-94 (“insult only”). The negative control was untreated, healthy HCECs incubated in cell medium only (“vehicle control”). The MTT assay was performed to determine cellular metabolic activity.

4.2.9 Effect of N-94-SiNPs on HCECs

Cytotoxicity and cytoprotective effect of the complete delivery system (i.e., N-94-SiNPs) on HCECs were assessed. N-94-SiNPs were prepared as per section 2.4 in concentrations of 5.6–5600 nM. Based on preceding experiments, it was assumed that 90% is adsorbed and 40% is maximally released, along with a 50% dilution during treatment, yielding final treatment concentrations of 1–1000 nM. Release of N-94 was conducted in a water bath shaker at 37 °C for 8 hours. The resulting mixtures were vortexed and used as the treatments.

N-94-SiNPs treatments were then performed in a non-contact manner. HCECs were cultured in trans-well inserts (0.4 μm pores, Falcon, Canada) placed into compatible 24-well plates. Each well contained treatment basolateral to the cells and cell culture medium apical to the cells. The controls were cell culture medium with PBS only (“vehicle control”) and SiNP treatment only.

At designated times, cells in the culture inserts were subjected to the MTT assay, while apical and basolateral supernatants were combined from each well and subjected to the lactate dehydrogenase (LDH) assay. LDH standards were prepared and loaded with supernatant samples in triplicate into 96-well plates. Reaction solution was prepared using an LDH assay kit (Sigma-Aldrich) then added to each sample and standard. Plates were incubated for 10 minutes at 37 °C and absorbances were read using a dual filter at 490 nm and 655 nm by the iMark Microplate Reader. LDH concentrations were calculated using the standard curve. LDH release of experimental groups was normalized by the vehicle control group (100%) and expressed as percentages.

To evaluate the cytoprotective property of released N-94, N-94 loading and release were performed as per section 4.2.4. After release was complete, tubes were centrifuged and supernatant samples containing the released N-94 were extracted as the treatment. HCECs were then co-treated with 100 U/mL of IFN γ and 12.5 ng/mL of TNF and 1–1000 nM of released N-94 in PBS for 16 and 20 hours. The controls were cell culture medium with PBS only (“vehicle control”) and cytokine insult only (“insult only”). Afterwards, apical supernatants were collected and analyzed using LDH and MTT assays.

4.2.10 Statistics

A one-way analysis of variance (ANOVA) was performed on the diameter of the silica nanoparticles using OriginLab 2019b (OriginLab Corporation, MA). For protein/peptide release and biological studies, three biological replicates (i.e., cell lines from distinct donors) and three technical replicates of each cell line were performed for each cellular experiment. GraphPad Prism v8.01 (La Jolla, CA) was used to conduct one- and two-way

ANOVAs and post-hoc tests. Values of $P < 0.05$ were considered statistically significant. All results are reported as the mean \pm standard deviation.

4.3 Results

4.3.1 Preparation and Characterization of Protein/Peptide-SiNPs Conjugates

SiNPs were synthesized using a Stöber procedure [36]. The product nanoparticles were characterized in terms of their morphology, size, and size distribution. The SEM micrograph in Figure 4.1 A shows that the SiNPs are spherical and non-porous with a fairly uniform size and minimum aggregation. Uniformity of the SiNPs' size was confirmed by the narrow size distribution shown in the insert. The average diameter was determined to be 251 ± 19 nm. In the N-94 study, a new batch of SiNPs with good size uniformity (374 ± 15 nm) was prepared and used (Figure 4.1 B). Particle size can be tuned by varying a combination of reaction time, temperature and reactants ratio [37].

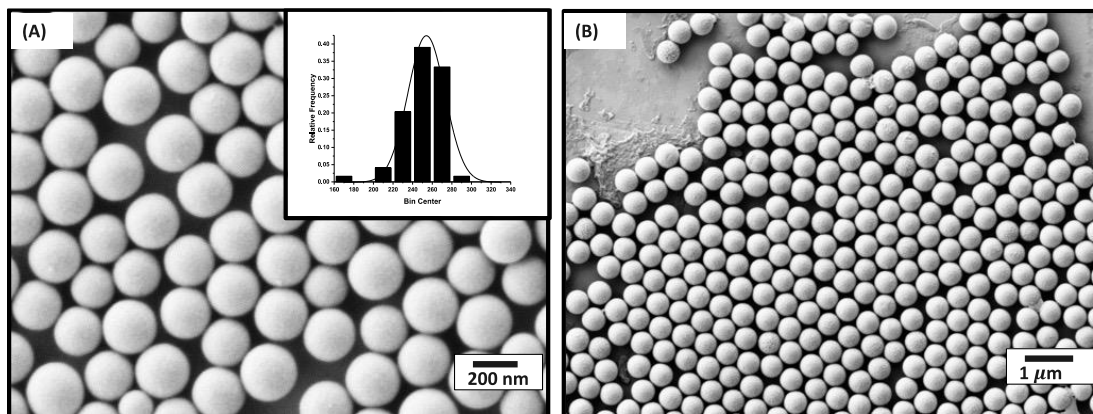


Figure 4.1 SEM of SiNPs used in (A) lysozyme and (B) N-94 study. Insert is the particle size distribution.

Lysozyme and N-94 molecules were conjugated to the SiNPs by batch adsorption. The adsorption of such molecules onto the surface of the SiNPs is visible (Figure 4.2 A). Lysozyme loading was further confirmed by FTIR. The absorption band at ~ 1650 cm^{-1} in the FTIR spectrum corresponds closely to the amide I peak for proteins [38]. The major band for silicon dioxide is located at ~ 1077 cm^{-1} . As seen in Figure 4.2 B, the peptide N-

94 was also successfully conjugated onto the SiNPs. The amount of N-94 conjugated was too small for FTIR analysis. However, characterization of the N-94 recovered in controlled release experiments shown in Figure 4.4 D serves as indirect evidence of loading success.

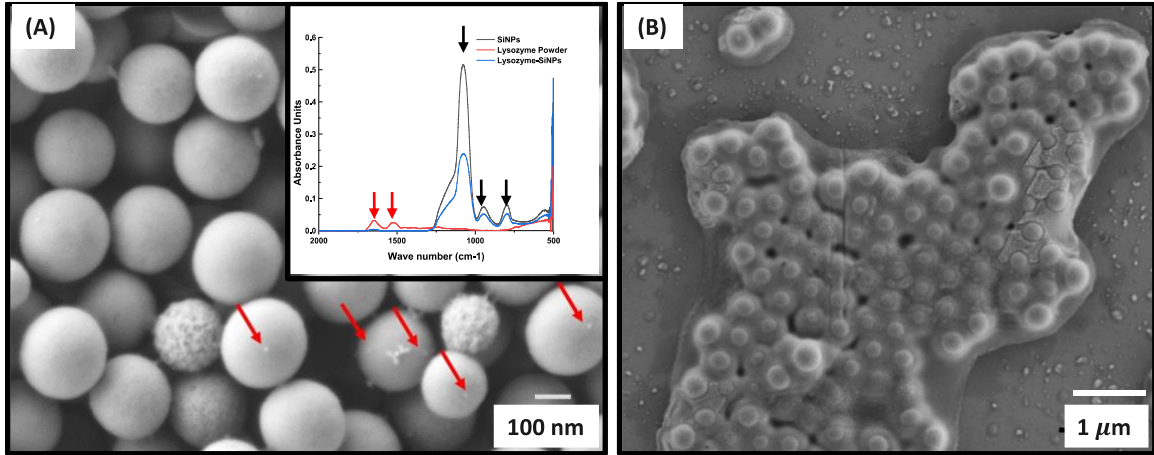


Figure 4.2 (A) SEM of lysozyme-loaded SiNPs. The red arrow indicates the presence of lysozyme. Insert: FTIR spectrum of SiNPs, lysozyme powder and lysozyme-SiNPs. The red arrow indicates the characteristic bands of proteins, and the black arrow indicates the characteristic bands of silica. (B) SEM of N-94-loaded SiNPs. The SEM micrographs and FTIR spectrum confirm the loading of lysozyme and N-94 onto the SiNPs surface.

4.3.2 Adsorption Kinetics and Isotherms

To better understand the adsorption mechanism, kinetic data was analyzed using pseudo-first-order and pseudo-second-order models, according to ref. [39]

Pseudo-first-order kinetic:

$$\log(Q_e - Q_t) = \log Q_e - \frac{k_1 t}{2.303} \quad (2)$$

Pseudo-second-order kinetic:

$$\frac{t}{Q_t} = \frac{1}{k_2 Q_e^2} + \frac{t}{Q_e} \quad (3)$$

where Q_e (mg/g) represents the amount of lysozyme being adsorbed at equilibrium. k_1 (h^{-1}) and k_2 ($g \cdot mg^{-1} \cdot h^{-1}$) are the rate constants of pseudo-first- and second- order adsorption respectively.

Time dependent adsorption data was collected for up to 72 hours at room temperature (23 ± 1 °C). Results are shown in Figure 4.3 A. Kinetic data is found to be best fitted to the pseudo-second order model ($R^2 > 0.99$). The parameters, Q_e and k_2 , derived for Equation 3 were determined to be 34.97 mg/g and $0.012 g \cdot mg^{-1} \cdot h^{-1}$ respectively, the calculated adsorption time course curve is also shown in Figure 4.3 A, demonstrating the validity of the kinetic model.

Isotherm data were fitted into Freundlich and Langmuir models. The linearized forms of these two models are shown in below [39,40]:

Freundlich isotherm:

$$\log Q_e = \log k_f + \frac{1}{n} \log C_e \quad (4)$$

where C_e is the equilibrium concentration of lysozyme (mg/L) in the solution, and k_f (mg/g) and n are the Freundlich isotherm constants related to adsorption capacity and intensity respectively.

Langmuir isotherm:

$$\frac{C_e}{Q_e} = \frac{C_e}{Q_m} + \frac{1}{Q_m b} \quad (5)$$

where Q_e (mg/g) is adsorbed lysozyme at equilibrium, Q_m (mg/g) is the maximum adsorption amount at complete monolayer coverage, and b (L/mg) is the Langmuir constant representing the energy of adsorption.

Fitting results are shown in Figure 4.3 B. Among the two adsorption isotherm models, it was found that the data fit well with the Langmuir model ($R^2=0.94$) as shown by the line in Figure 3B. The fitting parameters for the Langmuir isotherm were determined to be $Q_m=76.34$ mg/g, $b=0.0026$ L/mg. The complete fitting parameters and curves for adsorption kinetics and isotherms can be found in Appendix D.

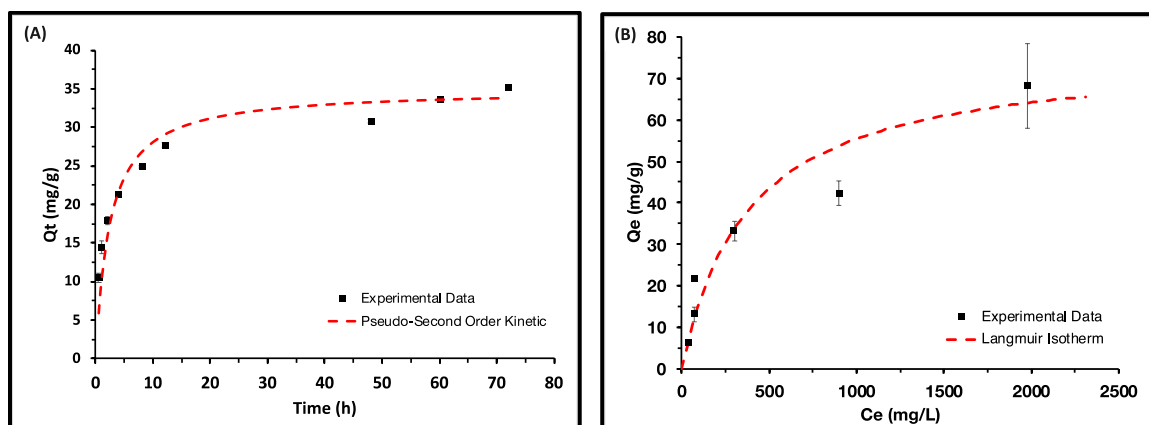


Figure 4.3 (A) Adsorption kinetics and (B) isotherm at 296 K. Error bars for some data points are too small to be displayed. The black square shows the experimental data, and the red dash curve shows the best-fit curve. Kinetic data is fit with pseudo-second order kinetic ($R^2 > 0.99$). Isotherm data fits well with the Langmuir isotherm ($R^2 = 0.94$).

4.3.3 Protein/Peptide Release in the Absence of Cells

SiNPs provided controlled release for both lysozyme and N-94 over the course of 8 hours. Approximately 50% of the loaded lysozyme was released within the first 3 hours with complete release from SiNPs within 24 hours (Figure 4.4 A). N-94 exhibited a similar release profile (Figure 4.4 B). ~30% release was achieved within the first 3 hours, while a plateau was reached after 8 hours, where ~45% of the total loaded N-94 was released.

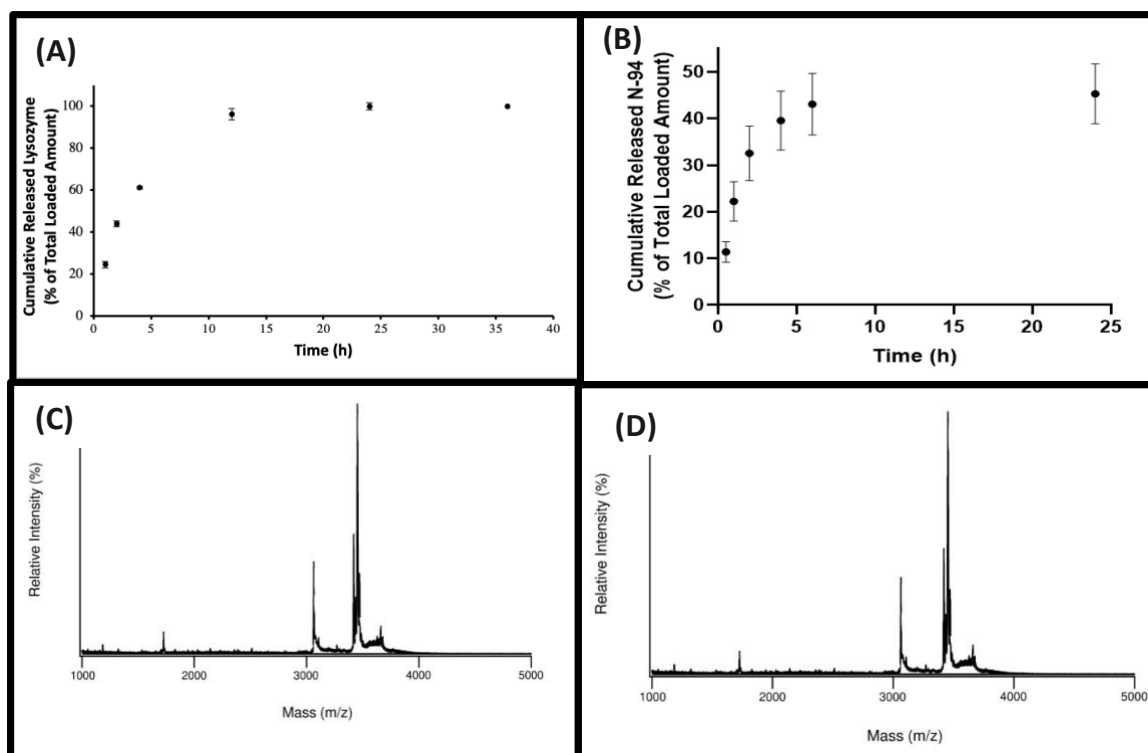


Figure 4.4 (A) Lysozyme release from SiNPs in PBS at pH 7.4 and 37 °C in the absence of cells. Lysozyme loading (i.e., M_{∞}) was 21.74 ± 2.32 mg/g. (B) N-94 release from SiNPs, N-94 loading (i.e., M_{∞}) was 44.94 ± 0.42 mg/g. SiNPs can provide controlled release for both lysozyme and N-94 over the course of 8 hours. Representative spectra of various masses (m/z or Da) of lacritin peptide (N-94) (C) prior to its conjugation to SiNPs, and (D) after release from SiNPs. The conjugation to SiNPs and release do not affect peptide integrity.

The integrity of N-94 was maintained throughout its release. MALDI-TOF mass spectrometry of pre-conjugated N-94 (Figure 4.4 C) as well as N-94 that was released after being conjugated to SiNPs (Figure 4.4 D) revealed high intensity peaks of the full 25-amino acid long peptide, both with FITC at 3400 Da and without FITC at 3000 Da. There were no peptide fragments of less than 3000 Da in either spectrum, indicating that conjugation to SiNPs does not affect peptide integrity.

4.3.4 Dissolution of SiNPs in the Absence of Cells

SiNPs degradation was studied under physiological conditions in PBS for up to 30 days. Progress of the degradation process was monitored in terms of SiNPs diameters as a function of time using TEM (Figure 4.5). Results for Days 0, 10 and 30 were found to be 113 ± 15 nm, 103 ± 20 nm and 98 ± 15 nm, respectively. One-way ANOVA confirmed that the size reduction of SiNPs was statistically significant over the period of the experiment ($P < 0.05$).

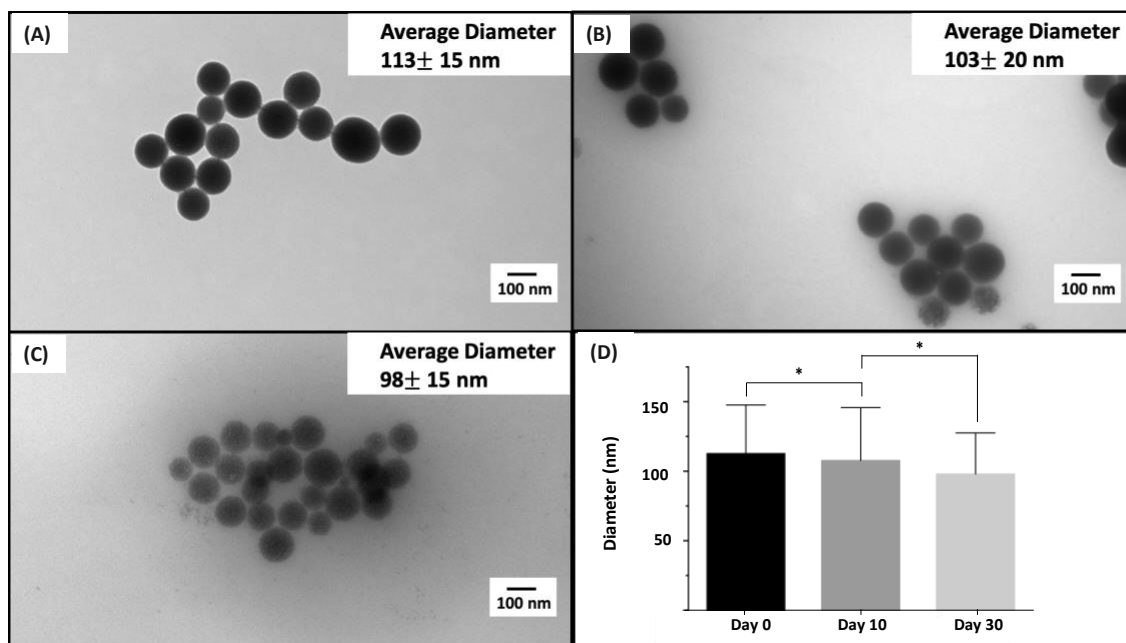


Figure 4.5 SEM images of SiNPs with an increasing immersion time in PBS, (A) $t=0$, (B) $t=10$ days, and (C) $t=30$ days. (D) Size variation of SiNPs after immersion in PBS for 0, 10, and 30 days. Each value is presented as mean \pm SD. Based on the one-way ANOVA test, size of SiNPs significantly decreased with a prolonged immersion time (*, $P < 0.05$), indicating the degradation of the nanoparticles.

4.3.5 Toxicity of N-94 to HCECs

Toxicity of N-94 to HCECs was examined over a N-94 concentration range of 1–10 000 nM for up to 24 hours and measured using cellular metabolic activity. Exposure of HCEC to N-94 up to the maximum peptide concentration and exposure time used did not result in significant changes in cellular metabolic activity (Figure 4.6).

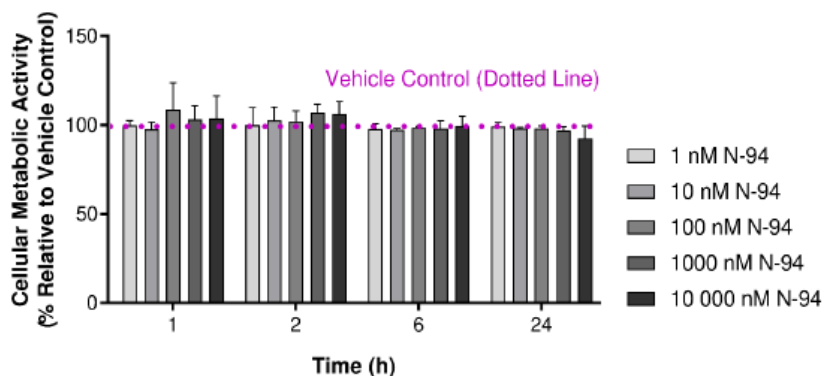


Figure 4.6 Mean cellular metabolic activity (% relative to vehicle control \pm SD) of primary human corneal epithelial cells obtained from three donors (N=3) following treatment of lacritin peptide (N-94) (1, 10, 100, 1000, 10 000 nM). Vehicle control (dotted line, 100%) was cell culture medium treatment only. MTT assays were performed after 1, 2, 6, and 24-hour treatment durations. There were no significant differences in cellular metabolic activity between the varying concentrations and durations of N-94 treatment, including vehicle control.

4.3.6 Cytoprotective Effects of N-94 to HCECs

The concentration of pro-inflammatory cytokines used to insult cells were first optimized to decrease cellular metabolic activity to 65–75% of that of “healthy” vehicle control cells to test the cytoprotective effects of N-94 (Figure 4.7 A). Treatment of HCECs with an insult combination of 100 U/mL IFN γ and 12.5 ng/mL TNF for 16 and 20 hours respectively decreased cellular metabolic activity to $74.80 \pm 6.25\%$ and $66.09 \pm 1.92\%$.

HCECs insulted with the optimized concentrations of IFN γ and TNF were co-treated with N-94 (Figure 4.7 B). Compared to insult only by IFN γ and TNF, there were significant increases in cellular metabolic activity when co-treated with 1 nM ($P < 0.05$) or 10 nM ($P < 0.001$) of N-94 after 20 hours. The effect of co-treatment with 100 nM and 1 000 nM N-94 on insulted HCECs were statistically non-significant. However, treatments of 10 000 nM of N-94 at 16 and 20 hours significantly ($P < 0.01$) decreased cellular metabolic

activity in comparison to insult only. This higher N-94 concentration was removed from the subsequent experiments that tested with N-94-SiNPs.

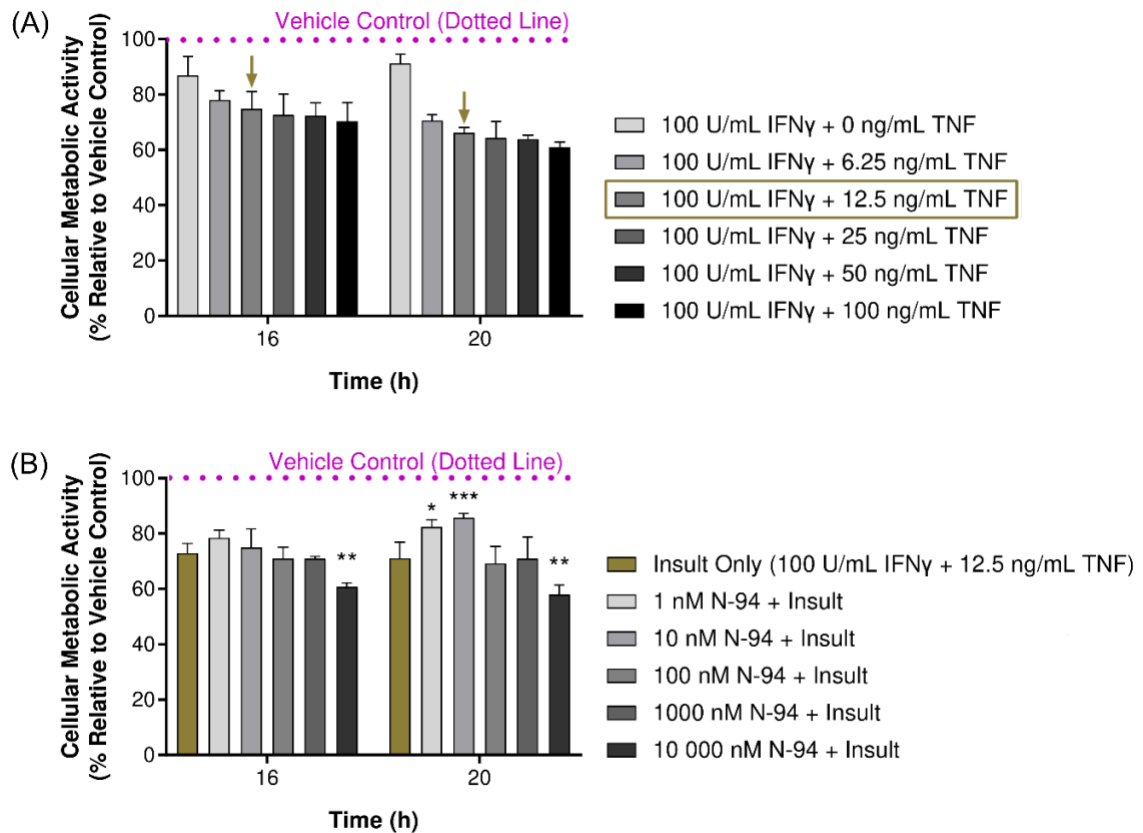


Figure 4.7 . Mean cellular metabolic activity (% relative to vehicle control \pm SD) of primary human corneal epithelial cells obtained from three donors (N=3) following (A) insult by 100 U/mL of IFN γ and varying concentrations of TNF (0, 6.25, 12.5, 25, 50, 100 ng/mL) and (B) co-treatment of lacritin peptide (N-94) (0, 1, 10, 100, 1000, 10 000 nM) along with insult by 100 U/mL IFN γ and 12.5 ng/mL TNF. In both, vehicle control (dotted line, 100%) was cell culture medium treatment only. MTT assays were performed after 16- and 20-hour treatment durations. *, **, and * indicate statistical significance versus insult only. ***, $P < 0.001$; **, $P < 0.01$; *, $P < 0.05$.**

4.3.7 Toxicity of N-94-SiNPs to HCECs

HCECs were treated with the mixture containing SiNPs, released N-94, and any potential dissolution products of SiNPs. Statistical analysis showed no significant differences in cellular metabolic activity between treatments of any concentration of N-94-SiNPs up to 1 000 nM or SiNPs and vehicle control at 16 and 20 hours (Figure 4.8 A). There were also no significant differences in LDH release between treatments of any concentration of N-94-SiNPs up to 1 000 nM or SiNPs and vehicle control at either time point (Figure 4.8 B).

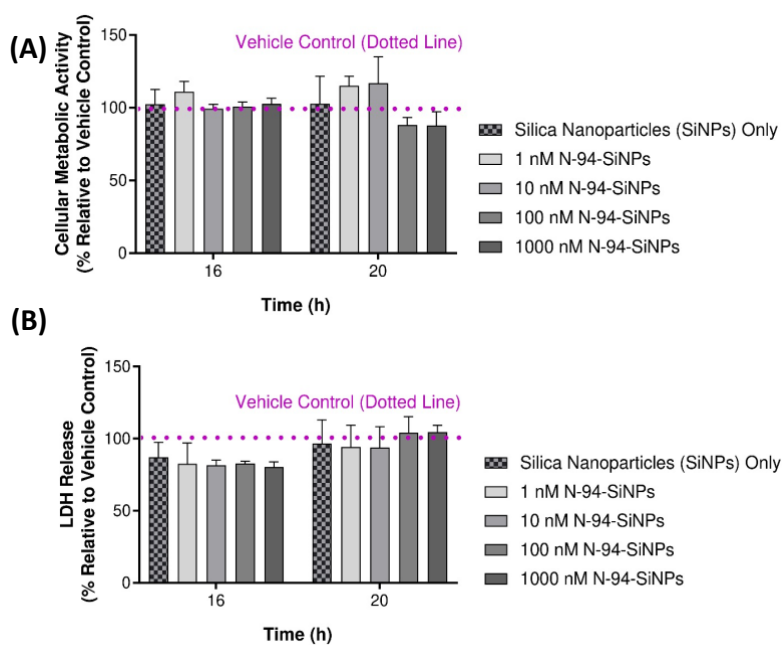


Figure 4.8 (A) Mean cellular metabolic activity (% relative to vehicle control \pm SD) and (B) mean lactate dehydrogenase (LDH) release (% relative to vehicle control \pm SD) of primary human corneal epithelial cells obtained from three donors (N=3) following treatment of lacritin peptide-conjugated silica nanoparticles (N-94-SiNPs) (1, 10, 100, 1000 nM). There was a vehicle control (dotted line, 100%) of phosphate-buffered saline and cell culture medium treatment only and a group of bare SiNP treatment only. MTT and LDH assays were performed after 16- and 20-hour treatment durations. There were no significant differences in cellular metabolic activity and LDH release between the various treatments and vehicle control at either time point.

4.3.8 Cytoprotective Effect of Released N-94 on Stressed HCECs

Compared to insult only, treatment equivalent to 1 nM of released N-94 significantly ($P < 0.05$) increased the cellular metabolic activity of insulted cells at 16 and 20 hours while 10 nM of released N-94 significantly ($P < 0.001$) increased the cellular metabolic activity of insulted cells at 20 hours (Figure 9A). Compared to insult only, co-treatment with 10 nM ($P < 0.01$) and 1000 nM ($P < 0.05$) of released N-94 significantly reduced the LDH release of HCECs at 20 hours (Figure 4.9 B).

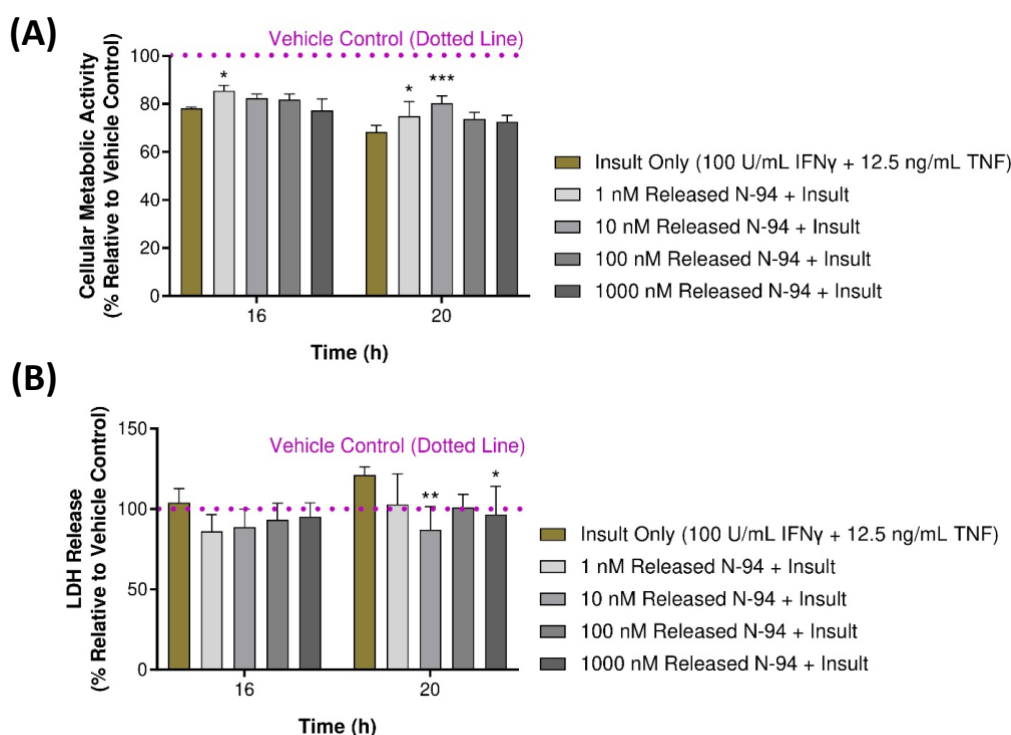


Figure 4.9 (A) Mean cellular metabolic activity (% relative to vehicle control \pm SD) and (B) mean lactate dehydrogenase (LDH) release (% relative to vehicle control \pm SD) of primary human corneal epithelial cells obtained from three donors (N=3) following co-treatment of lacritin peptide (N-94) (0, 1, 10, 100, 1000 nM) released from silica nanoparticles along with 100 U/mL IFN γ and 12.5 ng/mL TNF. Vehicle control (dotted line, 100%) was phosphate-buffered saline and cell culture medium treatment only. MTT and LDH assays were performed after 16- and 20-hour treatment durations. *, **, and * indicate statistical significance versus insult only. ***, $P < 0.001$; **, $P < 0.01$; *, $P < 0.05$.**

4.4 Discussion

The Stöber process provides a facile pathway towards the synthesis of fairly uniform SiNPs using the silica precursor TEOS [36]. Uniformity in size (Figure 4.1) allows for precise drug loading. SiNP size can be tuned as a function of reaction pH and temperature. SiNPs in the size range of 100-400 nm are promising for drug delivery applications, as they render a sufficient surface area to volume ratio to enable a high loading and would not induce significant cytotoxicity [16].

Lysozyme loading onto SiNPs is demonstrated by both SEM and FTIR. Aggregation of lysozyme can be seen which has been attributed to lysozyme-SiNP interaction on the particle surface [41]. Lysozyme conjugation to SiNPs is further confirmed by the FTIR spectrum (inset, Figure 4.2 A). For lysozyme, the amide I peak intensity is low at 1649 cm^{-1} , likely due to its low concentration relative to the SiNPs, but its presence serves as direct evidence of successful conjugation of lysozyme to SiNPs [42]. The amide II peak at 1550 cm^{-1} was not observed due to its lower intensity compared to the amide I peak [43].

Results of adsorption experiments over a 72-hour period are shown in Figure 3A. The results indicated that equilibrium adsorption was attained at around 45–50 hours. At the early stage (0–12 hours), adsorption was fast due to the high concentration of lysozyme and the number of binding sites. As adsorption proceeded, the rate slowed down, possibly due to the depletion of lysozyme and occupation of binding sites [40].

Pseudo-second order kinetics suggests that chemisorption is the rate controlling step throughout the adsorption process [44], the adsorption of lysozyme on SiNPs is most likely a combined effect of both physical and chemical interactions.

Equilibrium loading capacity is an important parameter in assessing the suitability of SiNPs as a carrier for the controlled release of a protein for therapeutic applications as it can be used to determine the maximum loading capacity for the release of a protein within the therapeutic dose range by a carrier. Among the several models available, the Langmuir model was found to be the best to describe the experimental data ($R^2 = 0.94$)

[41,45,46]. This adsorption isotherm assumes monolayer adsorption with minimal interaction among the adsorbate molecules. With macromolecular proteins such as lysozyme with surface functional groups, the process is more complex. The difference IEPs between SiNPs (IEP ~3.0) and lysozyme (IEP=10.9) would lead to the adsorption of positively charged protein onto SiNPs, resulting a protein monolayer on the surface SiNPs [38,47]. The existence of intermolecular repulsive electrostatic interactions will prevent second layer of adsorption. The maximum monolayer adsorption capacity (Q_m) of lysozyme on silica nanoparticles typically falls in the range of 50-520 mg/g, depending on the pH and ionic strength, with the greatest Q_m achieved at a pH near the IEP of lysozyme in the absence of electrolyte [46,48]. The deviation from this maximum loading could be explained by the salts in PBS and the suboptimal loading pH.

The release process of cargo is governed by the concentration gradient of the protein/polypeptide at the SiNPs surface followed by its rapid diffusion into the medium (Figure 4.4 A and B). This type of release profile makes this system a promising candidate in the topical treatment of ailments such as DED which require relatively rapid drug release at the target site that is still sustained for a few hours. The release rate can be tuned by varying the initial protein loading on the SiNPs or by silica surface modification for other clinical applications. In contrast to the lysozyme-SiNP system where all the adsorbed protein was released over time, only about half of the N-94 was released from the N-94-SiNPs. N-94 is a much smaller and flexible molecule than lysozyme. This could allow for more than one conformation of the adsorbed N-94. The relative stability of these conformations could lead to the incomplete release observed. This could be a concern that has to be addressed in the design and development of a N-94-SiNP treatment system for DED. Nevertheless, the molecular integrity of N-94 was retained during the release, as demonstrated by the MALDI results. Overall, the sustained delivery of N-94 can increase its bioavailability when applied to the cornea as compared to the current drop treatment approach.

The SiNPs degradation was evident from the time dependent change of the particle diameter. The degradation rate of SiNPs can be tuned to meet the requirements of a particular delivery application. According to Yamada et al., in general, smaller sizes

particles have higher degradation rates [49]. The ultimate dissolution time *in vivo* is dependent on the particle size, synthesis method, and the properties of fluid it is subjected to [49,50]. The degradation of the material is favorable for drug delivery application as the carriers serve no other useful purposes after the therapeutics are delivered.

The clinical significance of the N-94-SiNP delivery system was supported by experiments demonstrating that neat N-94 was non-toxic to HCECs and can effectively reduce cell damage imparted by pro-inflammatory cytokines across a wide time and concentration range (Figure 4.7 B). We found that release products from N-94-SiNPs were non-cytotoxic, and N-94 released from SiNPs remained cytoprotective (Figure 8 and 9). We observed optimal cytoprotective effects at 10 nM and potentially 1 nM. This corroborates existing lacritin studies that determined a 10 nM optimal concentration for cytoprotective effects on HCECs and a 1–10 nM optimum for bactericidal activity [29,30]. We applied N-94 for 16 and 20 hours to check cytoprotective effects over a long period of cell stress and found that an exposure to 10 nM of N-94 for 20 hours was most effective in our model. It is possible that the autophagy pathway that restores homeostasis during inflammation was gradually triggered by increasing amounts of N-94 binding syndecan-1 on the HCECs, reaching an optimum at 20 hours [29].

A limitation in the translatability of our study is the gap between the complete release of N-94 from SiNPs after 8 hours and its optimal cytoprotective effects at 20 hours after release. As mentioned, it may be worthwhile to study release kinetics in a solvent containing tear proteins such as lacritin to possibly prolong release. Treating cells with the conjugated N-94-SiNPs without first inducing release would also be useful in studying optimal treatment durations once release kinetics are established in tear-mimicking cell culture media. Future studies should also extend the study duration: supplementing with additional N-94 daily as it is depleted can mimic daily drug administration. In addition, other cell models could be explored to investigate the preventative effect and rescue ability of N-94. More specifically, pre-treating HCECs with N-94 before cytokine and post-treating insulted cells with N-94 could be employed.

Trans-well inserts were used to separate N-94-SiNPs from HCECs to avoid the endocytosis of SiNPs [17]. In clinical application, it must be ensured that the N-94-SiNPs can remain on the ocular surface for the entire duration of N-94 release. This challenge presents opportunities to create novel approaches for implementation. Future studies could explore a secondary drug carrier for our proposed drug delivery system, such as silicone hydrogel contact lenses. Embedding N-94-SiNPs into contact lens would further ensure sustained drug delivery. While hydrogel contact lens itself can be considered as a primary drug carrier, the SiNPs intermediate confers flexibility: it may be difficult to synthesize different types of complex hydrogen matrices personalized for different amounts of drug release, but we can more easily vary the amount of SiNPs embedded into contact lenses for patients with varying degrees of dry eye.

4.5 Conclusions

As an excellent option for bioactive protein and peptide delivery, the SiNP-based delivery system mediated the controlled release of cargo for a period of eight hours. This type of release profile could be useful in dry eye treatment, as it could allow patients to encounter the drug-elution at night, ideally while sleeping, and then to have 16 hours of relief during waking hours. We have demonstrated that N-94 is functionally equipotent to its parent protein lacritin and cytoprotective of stressed HCECs in its free dosage form. The constitution of the N-94-SiNP delivery system successfully retained the peptide's molecular integrity and biological functionality. The peptide carrier was degradable and was non-toxic to cells. The system has potential for incorporation into other ophthalmic devices such as silicone hydrogel contact lens or new multifunctional devices. Overall, the N-94-SiNPs delivery system represents a promising approach that can be further developed for the treatment of DED.

4.6 References

- [1] A. Nasajpour, S. Ansari, C. Rinoldi, A.S. Rad, T. Aghaloo, S.R. Shin, Y.K. Mishra, R. Adelung, W. Swieszkowski, N. Annabi, A. Khademhosseini, A. Moshaverinia, A. Tamayol, A Multifunctional Polymeric Periodontal Membrane with Osteogenic and Antibacterial Characteristics, *Advanced Functional Materials*. 28 (2018).

- [2] J.L. Holloway, A.M. Lowman, G.R. Palmese, The role of crystallization and phase separation in the formation of physically cross-linked PVA hydrogels, *Soft Matter*. 9 (2012) 826–833.
- [3] M.E. Stern, J. Gao, K.F. Siemasko, R.W. Beuerman, S.C. Pflugfelder, The role of the lacrimal functional unit in the pathophysiology of dry eye, *Exp Eye Res*. 78 (2004) 409–416.
- [4] A.D. Pucker, S.M. Ng, J.J. Nichols, Over the counter (OTC) artificial tear drops for dry eye syndrome, *Cochrane Database Syst Rev*. 2 (2016) CD009729.
- [5] T. Vijmasi, F.Y.T. Chen, S. Balasubbu, M. Gallup, R.L. McKown, G.W. Laurie, N.A. McNamara, Topical Administration of Lacritin Is a Novel Therapy for Aqueous-Deficient Dry Eye Disease, *Invest. Ophthalmol. Vis. Sci*. 55 (2014) 5401–5409.
- [6] W. Stevenson, S.K. Chauhan, R. Dana, Dry eye disease: an immune-mediated ocular surface disorder, *Arch Ophthalmol*. 130 (2012) 90–100.
- [7] R.M. Schiffman, J.G. Walt, G. Jacobsen, J.J. Doyle, G. Lebovics, W. Sumner, Utility assessment among patients with dry eye disease, *Ophthalmology*. 110 (2003) 1412–1419..
- [8] J.L. Gayton, Etiology, prevalence, and treatment of dry eye disease, *Clin Ophthalmol*. 3 (2009) 405–412.
- [9] R. Gaudana, H.K. Ananthula, A. Parenky, A.K. Mitra, Ocular Drug Delivery, *AAPS J*. 12 (2010) 348–360.
- [10] S. Samudre, F.A. Lattanzio, V. Lossen, A. Hosseini, J.D. Sheppard, R.L. McKown, G.W. Laurie, P.B. Williams, Lacritin, a novel human tear glycoprotein, promotes sustained basal tearing and is well tolerated, *Invest. Ophthalmol. Vis. Sci*. 52 (2011) 6265–6270.
- [11] Management and therapy of dry eye disease: report of the Management and Therapy Subcommittee of the International Dry Eye WorkShop (2007), *Ocul Surf*. 5 (2007) 163–178.
- [12] M. Hingorani, L. Moodaley, V.L. Calder, R.J. Buckley, S. Lightman, A randomized, placebo-controlled trial of topical cyclosporin A in steroid-dependent atopic keratoconjunctivitis, *Ophthalmology*. 105 (1998) 1715–1720.
- [13] D.E. White, Y. Zhao, H. Jayapalan, P. Machiraju, R. Periyasamy, A. Ogundele, Treatment Satisfaction Among Patients Using Anti-Inflammatory Topical Medications for Dry Eye Disease, *Clin Ophthalmol*. 14 (2020) 875–883.

- [14] H.A.D. Lagassé, A. Alexaki, V.L. Simhadri, N.H. Katagiri, W. Jankowski, Z.E. Sauna, C. Kimchi-Sarfaty, Recent advances in (therapeutic protein) drug development, *F1000Res.* 6 (2017) 113.
- [15] A. Anselmo, S. Mitragotri, A Review of Clinical Translation of Inorganic Nanoparticles, *The AAPS Journal.* 17 (2015) 1041–1054..
- [16] D. Napierska, L.C.J. Thomassen, V. Rabolli, D. Lison, L. Gonzalez, M. Kirsch-Volders, J.A. Martens, P.H. Hoet, Size-dependent cytotoxicity of monodisperse silica nanoparticles in human endothelial cells, *Small.* 5 (2009) 846–853.
- [17] J.-H. Park, H. Jeong, J. Hong, M. Chang, M. Kim, R.S. Chuck, J.K. Lee, C.-Y. Park, The Effect of Silica Nanoparticles on Human Corneal Epithelial Cells, *Scientific Reports.* 6 (2016) srep37762.
- [18] A. Watermann, J. Brieger, Mesoporous Silica Nanoparticles as Drug Delivery Vehicles in Cancer, *Nanomaterials (Basel).* 7 (2017) E189.
- [19] R.C. de Guzman, S.Y. Rabbany, PEG-Immobilized Keratin for Protein Drug Sequestration and pH-Mediated Delivery, *Journal of Drug Delivery.* 2016 (2016) e7843951.
- [20] D.J. McClements, Encapsulation, protection, and delivery of bioactive proteins and peptides using nanoparticle and microparticle systems: A review, *Advances in Colloid and Interface Science.* 253 (2018) 1–22.
- [21] X. Zhang, V. Jeyalatha M, Y. Qu, X. He, S. Ou, J. Bu, C. Jia, J. Wang, H. Wu, Z. Liu, W. Li, Dry Eye Management: Targeting the Ocular Surface Microenvironment, *Int J Mol Sci.* 18 (2017).
- [22] C.A. Rubio, Increased Production of Lysozyme Associated with Bacterial Proliferation in Barrett's Esophagitis, Chronic Gastritis, Gluten-induced Atrophic Duodenitis (Celiac Disease), Lymphocytic Colitis, Collagenous Colitis, Ulcerative Colitis and Crohn's Colitis, *Anticancer Res.* 35 (2015) 6365–6372.
- [23] J.G. Lawrenson, 2 - Anterior Eye, in: N. Efron (Ed.), *Contact Lens Practice (Third Edition)*, Elsevier, 2018: pp. 10-27.e2.
- [24] S.V. Aluru, S. Agarwal, B. Srinivasan, G.K. Iyer, S.M. Rajappa, U. Tatu, P. Padmanabhan, N. Subramanian, A. Narayanasamy, Lacrimal proline rich 4 (LPRR4) protein in the tear fluid is a potential biomarker of dry eye syndrome, *PLoS One.* 7 (2012) e51979.
- [25] M.D.P. Willcox, P. Argüeso, G.A. Georgiev, J.M. Holopainen, G.W. Laurie, T.J. Millar, E.B. Papas, J.P. Rolland, T.A. Schmidt, U. Stahl, T. Suarez, L.N. Subbaraman, O.Ö. Uçakhan, L. Jones, TFOS DEWS II Tear Film Report, *Ocul Surf.* 15 (2017) 366–403.

- [26] R. Karnati, V. Talla, K. Peterson, G.W. Laurie, Lacritin and other autophagy associated proteins in ocular surface health, *Experimental Eye Research*. 144 (2016) undefined-undefined.
- [27] J. Wang, N. Wang, J. Xie, S.C. Walton, R.L. McKown, R.W. Raab, P. Ma, S.L. Beck, G.L. Coffman, I.M. Hussaini, G.W. Laurie, Restricted epithelial proliferation by lacritin via PKC α -dependent NFAT and mTOR pathways, *J Cell Biol*. 174 (2006) 689–700.
- [28] M.M. Feng, J. Baryla, H. Liu, G.W. Laurie, R.L. McKown, N. Ashki, D. Bhayana, C.M.L. Hutnik, Cytoprotective Effect of Lacritin on Human Corneal Epithelial Cells Exposed to Benzalkonium Chloride In Vitro, *Current Eye Research*. 39 (2014) 604–610.
- [29] N. Wang, K. Zimmerman, R.W. Raab, R.L. McKown, C.M.L. Hutnik, V. Talla, M.F. Tyler, J.K. Lee, G.W. Laurie, Lacritin Rescues Stressed Epithelia via Rapid Forkhead Box O3 (FOXO3)-associated Autophagy That Restores Metabolism, *J Biol Chem*. 288 (2013) 18146–18161.
- [30] R.L. McKown, E.V. Coleman Frazier, K.K. Zadrozny, A.M. Deleault, R.W. Raab, D.S. Ryan, R.K. Sia, J.K. Lee, G.W. Laurie, A cleavage-potentiated fragment of tear lacritin is bactericidal, *J Biol Chem*. 289 (2014) 22172–22182.
- [31] M. Azkargorta, J. Soria, C. Ojeda, F. Guzmán, A. Acera, I. Iloro, T. Suárez, F. Elortza, Human Basal Tear Peptidome Characterization by CID, HCD, and ETD Followed by in Silico and in Vitro Analyses for Antimicrobial Peptide Identification, *J. Proteome Res*. 14 (2015) 2649–2658.
- [32] P. Ma, S.L. Beck, R.W. Raab, R.L. McKown, G.L. Coffman, A. Utani, W.J. Chirico, A.C. Rapraeger, G.W. Laurie, Heparanase deglycanation of syndecan-1 is required for binding of the epithelial-restricted prosecretory mitogen lacritin, *J. Cell Biol*. 174 (2006) 1097–1106.
- [33] Y. Zhang, N. Wang, R.W. Raab, R.L. McKown, J.A. Irwin, I. Kwon, T.H. van Kuppevelt, G.W. Laurie, Targeting of heparanase-modified syndecan-1 by prosecretory mitogen lacritin requires conserved core GAGAL plus heparan and chondroitin sulfate as a novel hybrid binding site that enhances selectivity, *J. Biol. Chem*. 288 (2013) 12090–12101.
- [34] P. Ma, N. Wang, R.L. McKown, R.W. Raab, G.W. Laurie, Focus on molecules: lacritin, *Exp Eye Res*. 86 (2008) 457–458.
- [35] M.L. Hair, W. Hertl, Acidity of surface hydroxyl groups, *J. Phys. Chem*. 74 (1970) 91–94.
- [36] W. Stöber, A. Fink, E. Bohn, Controlled growth of monodisperse silica spheres in the micron size range, *Journal of Colloid and Interface Science*. 26 (1968) 62–69.

- [37] J.W. Kim, L.U. Kim, C.K. Kim, Size Control of Silica Nanoparticles and Their Surface Treatment for Fabrication of Dental Nanocomposites, Biomacromolecules. 8 (2007) 215–222.
- [38] N. Henry, J. Clouet, C.L. Visage, P. Weiss, E. Gautron, D. Renard, T. Cordonnier, F. Boury, B. Humbert, H. Terrisse, J. Guicheux, J.L. Bideau, Silica nanofibers as a new drug delivery system: a study of the protein–silica interactions, Journal of Materials Chemistry B. 5 (2017) 2908–2920.
- [39] H.-Y. Zhu, Y.-Q. Fu, R. Jiang, J. Yao, L. Xiao, G.-M. Zeng, Novel magnetic chitosan/poly(vinyl alcohol) hydrogel beads: preparation, characterization and application for adsorption of dye from aqueous solution, Bioresour. Technol. 105 (2012) 24–30.
- [40] Z.S. Pour, M. Ghaemy, Removal of dyes and heavy metal ions from water by magnetic hydrogel beads based on poly(vinyl alcohol)/carboxymethyl starch-g-poly(vinyl imidazole), RSC Adv. 5 (2015) 64106–64118.
- [41] F. Felsovalyi, P. Mangiagalli, C. Bureau, S.K. Kumar, S. Banta, Reversibility of the Adsorption of Lysozyme on Silica, Langmuir. 27 (2011) 11873–11882.
- [42] E.F. dos Reis, F.S. Campos, A.P. Lage, R.C. Leite, L.G. Heneine, W.L. Vasconcelos, Z.I.P. Lobato, H.S. Mansur, Synthesis and characterization of poly(vinyl alcohol) hydrogels and hybrids for rMPB70 protein adsorption, Materials Research. 9 (2006) 185–191.
- [43] A. Barth, Infrared spectroscopy of proteins, Biochimica et Biophysica Acta (BBA) - Bioenergetics. 1767 (2007) 1073–1101.
- [44] D. Robati, Pseudo-second-order kinetic equations for modeling adsorption systems for removal of lead ions using multi-walled carbon nanotube, J Nanostruct Chem. 3 (2013) 55.
- [45] K.-C. Kao, T.-S. Lin, C.-Y. Mou, Enhanced Activity and Stability of Lysozyme by Immobilization in the Matching Nanochannels of Mesoporous Silica Nanoparticles, J. Phys. Chem. C. 118 (2014) 6734–6743.
- [46] B. Bharti, J. Meissner, G.H. Findenegg, Aggregation of Silica Nanoparticles Directed by Adsorption of Lysozyme, Langmuir. 27 (2011) 9823–9833.
- [47] H. Lam, L. Bleiden, C.S. de Paiva, W. Farley, M.E. Stern, S.C. Pflugfelder, Tear cytokine profiles in dysfunctional tear syndrome, Am J Ophthalmol. 147 (2009) 198–205.
- [48] J. Meissner, A. Prause, B. Bharti, G.H. Findenegg, Characterization of protein adsorption onto silica nanoparticles: influence of pH and ionic strength, Colloid Polym Sci. 293 (2015) 3381–3391.

- [49] H. Yamada, C. Urata, Y. Aoyama, S. Osada, Y. Yamauchi, K. Kuroda, Preparation of Colloidal Mesoporous Silica Nanoparticles with Different Diameters and Their Unique Degradation Behavior in Static Aqueous Systems, *Chem. Mater.* 24 (2012) 1462–1471.
- [50] J.P. Icenhower, P.M. Dove, The dissolution kinetics of amorphous silica into sodium chloride solutions: effects of temperature and ionic strength, *Geochimica et Cosmochimica Acta.* 64 (2000) 4193–4203.

Chapter 5

5 Development of Multifunctional PVA-SiO₂-IONP Microparticles for TACE³

5.1 Introduction

Drug-eluting microparticles are characterized as matrix systems in which the drug is homogeneously dispersed, either in dissolved or suspended form [1]. These micron-sized delivery packages hold great utility in the clinical management of numerous diseases. Plentiful microparticles composed of biocompatible polymers, such as chitosan, alginate, poly(vinyl alcohol) (PVA) and poly(lactic-*co*-glycolic acid) (PLGA) were developed for treating gastric diseases, lung cancer and hepatocellular carcinoma (HCC) [2–4]. Such particles could be prepared via a wide array of processing techniques, including microfluidics, electrospray and spray drying [1,5,6]. In addition to being used solely, such particles can be used as a component in existing platforms, such as microfibers, scaffolds, or bulk hydrogels for many applications, including drug delivery and tissue regeneration [7–10].

Multifunctional drug-eluting microparticles have been a center of research in the past decade. Such particles can fulfill two or more functions after administration, making them promising in treating complex systems, such as tumors [11]. Targeted drug delivery can localize the drug to the site of action, minimizing the unwanted toxicity to healthy tissue [12]. Controlled release capability can avoid burst release and maintain an effective drug concentration for a prolonged time [13,14]. Degradation of the delivery system is beneficial as drug release can be modulated by the degradation rate of the carrier. In addition, device removal is not required. Repeatable treatment is possible because the carriers can be broken down into innocuous products and eliminated from the body after the therapeutic is depleted [15]. Furthermore, imageable drug carriers facilitate the

³ A paper under the title: Microfluidic fabrication of drug-eluting composite hydrogel microparticles is in the preparation stage. Xinyi Li will be the first author.

diagnosis and postoperative feedback, which is particularly advantageous in interventional radiology for cancer treatment [16].

Composite hydrogels provide a powerful platform to construct multifunctional drug-eluting systems. The idea behind it is to use nanoparticle fillers, biological factors, or a combination of polymers to enhance and diversify the properties of traditional hydrogels [17,18]. Poly(vinyl alcohol) (PVA) is one of the most commercially important biocompatible polymers in use. PVA can be stabilized via physical crosslinking through the freezing-thawing technique, in which no toxic chemical crosslinkers are required. The porosity and mechanical properties can be altered by adjusting the process parameters, polymer concentration in the solution and molecular weight of PVA [19]. The non-toxic crosslinking approach, along with the tunable properties, renders PVA widespread biomedical applications, including drug delivery, wound dressing and orthopedic implants [20]. Iron oxide nanoparticles (IONPs) have gained particular interests due to their excellent magnetic properties, making them good candidates as magnetic resonance imaging (MRI) contrast agents and drug carriers for targeted delivery [21]. Furthermore, the incorporation of IONPs into the PVA could endow the system with degradability. Bannerman et al. introduced IONPs to the PVA hydrogels through *in situ* co-precipitation [22]. IONPs were allowed to form hydrogen bonding with PVA chains and participate in hydrogel crosslinking during the subsequent freezing-thawing cycles. As a result, the gradual dissolution of IONPs in an acidic environment would weaken the linkages, and therefore the stability of the matrix, leading to the 'degradation' of PVA. Silica (also known as silicon dioxide, SiO₂) has been "generally recognized as safe" by the FDA for more than five decades and is widely used in the food industry as a color or formulation stabilizer [23,24]. The presence of abundant surface silanols (Si-OH) allows the conjugation to various organic functional groups, rendering silica nanoparticles (SiNPs) with a wide range of applications in disease diagnosis and controlled drug release [25]. In addition to SiNPs, silica-based materials in the form of composite hydrogels have attracted significant attention. For example, silica-PVA hydrogels derived from acid-catalyzed sol-gel synthesis possess improved permeability and mechanical properties compared to neat PVA hydrogels [26–28]. It is speculated that the relatively slow hydrolysis step resulted in molecular chains contain sufficient silanol groups to

participate in hydrogen bonding with the hydrogel polymers [29]. The formation of silica-hydrogel interaction affects the intramolecular binding of the polymeric chains and could reduce the crystallinity while improving the PVA's diffusivity [27,30]. This improvement is particularly beneficial for drug delivery as it would facilitate the permeation of drug molecules [31,32].

In this chapter, we continued the previous work on multifunctional PVA-IONP microparticles (Chapter 3). However, we introduced silica to the composite hydrogel to modify the loading and release ability of the delivery system. This material was prepared via the acid-catalyzed sol-gel process and *in situ* co-precipitation. The microparticulate PVA-SiO₂-IONP system was fabricated by microfluidics and stabilized by the low temperature thermal cycling (LTTC). The detailed scheme of the preparation of the particles is presented in Figure 5.1. Various flow rates of the continuous phase and dispersed phase were explored to make microparticles of adjustable sizes. The resulting PVA-SiO₂-IONP microparticles were comprehensively characterized in the aspects of morphology, composition, magnetic properties, drug loading/release and degradation. This multifunctional delivery system can potentially be used as drug-eluting microparticles in different interventional radiology therapies, such as transarterial chemoembolization (TACE) treatment of HCC.

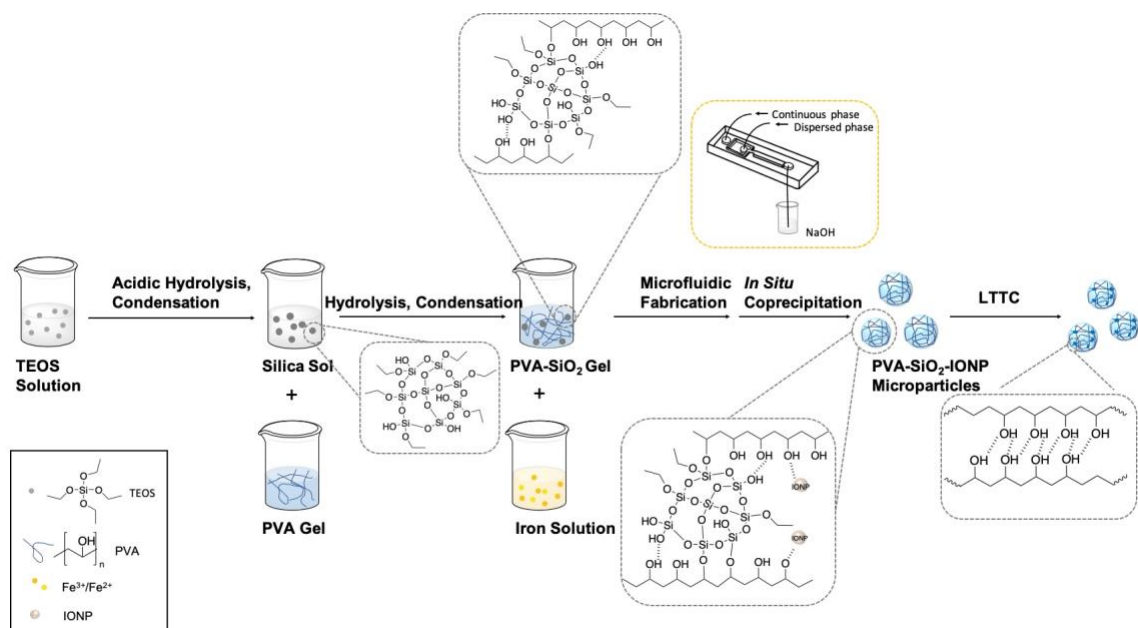


Figure 5.1 Schematic illustration for the preparation of PVA-SiO₂-IONP microparticles.

5.2 Materials and Methods

5.2.1 Materials

PVA (MW 146,000-186,000, 99+% hydrolyzed), iron (III) chloride (FeCl₃), iron (II) chloride tetrahydrate (FeCl₂•4H₂O) were purchased from Sigma-Aldrich.

Tetraethylorthosilicate (TEOS, 99+%) was acquired from Alfa Aesar. Hydrochloric acid (36.5%-38%, HCl) was obtained from Caledon. Sodium hydroxide (NaOH) pellets were purchased from ThermoFisher Scientific. Doxorubicin hydrochloride was obtained from Cayman Chemicals. Span80 was purchased from Fluka. Ethanol (95%) was acquired from Commercial Alcohols. Phosphate buffer solution (pH 5.5) was prepared by a procedure reported elsewhere [33]. All other chemicals were purchased from Sigma-Aldrich and were used without any purification.

5.2.2 Preparation of PVA Solution

A 2.99 wt% PVA solution was prepared at 90 °C under mechanical stirring (rpm 100). The temperature was maintained for at least 3 h. The PVA was stored at room temperature overnight to degas naturally.

5.2.3 Preparation of Iron Chloride Solution

An iron chloride solution containing 20.66 wt% FeCl₃ and 12.66 wt% FeCl₂·4H₂O (2:1 molar ratio) in distilled water was prepared at room temperature.

5.2.4 Preparation of PVA-SiO₂-Fe (II, III) Gel

First, a silica sol was prepared by slowly adding 2.76 mL TEOS into a solution containing 2.7 mL of H₂O, 2.95 mL of ethanol and 70 μL concentrated HCl. The resulting mixture was maintained at 60 °C under magnetic stirring (rpm 150) for one hour. To prepare the PVA-SiO₂ gel, 1.36 g of silica sol was mixed with 13.64 g 2.99 wt% PVA solution. The resultant gel was then aged at 60 °C under magnetic stirring (rpm 150) for five hours. The PVA-SiO₂ gel, after cooling, was blended with 2.78 g iron chloride solution. The resulting PVA-SiO₂-Fe (II, III) gel was filtered through a 5 μm filter (Acrodisc[®] syringe filter, Pall Laboratory) and stored at room temperature.

5.2.5 Fabrication of the Flow-focusing Microfluidic Device

A planar microfluidic system, comprising a flow-focusing configuration, was prepared using poly(methyl methacrylate) (PMMA) slab (50 x 25 x 12 mm) by milling. The width of the continuous phase and dispersed phase channels were 500 μm and 200 μm, respectively. A second PMMA slab (50 x 25 x 12 mm) was sealed onto the channel slab by screws. Two needles (20 gauge, Hamilton Company) attached with silicone tubes (0.062 x 0.125'', VWR International) were inserted into the inlet of the top slab to allow independent injection of continuous phase and dispersed phase at selected rates controlled by two syringe pumps (NE-1000, New Era Pump Systems Inc.). The droplets generated were directed into a NaOH tank through an outlet tubing (0.023 x 0.038'', Intramedic[™] PE tubing, BD).

5.2.6 Fabrication of PVA-SiO₂-IONP Microparticles

Undecane containing 1 wt.% Span80 was used as the continuous phase, while the PVA-SiO₂-Fe (II, III) gel was used as the dispersed phase. Microparticles were fabricated at various flow conditions. The microfluidic fabrication was first conducted at a fixed continuous phase flow rate ($Q_c=20$ mL/h) while different dispersed phase flow rate

($Q_d=1-9$ mL/h). Subsequently, the fabrication was conducted at two different Q_d 's ($Q_d=1$ mL/h and 3 mL/h) with various continuous phase flow rates ($Q_d=5-45$ mL/h). The produced droplets were collected in a reservoir containing 1.0 mol/L NaOH for solidification. The resulting PVA-SiO₂-IONP microparticles were collected and thoroughly cleaned by 50 v/v% ethanol.

In later experiments (section 5.2.7-5.2.14), dispersed phase ($Q_d=3$ mL/h) was focused by the continuous phase ($Q_c=20$ mL/h). The droplets were guided into NaOH, collected and washed as stated before. The cleaned microparticles were subsequently placed into a programmed cryobath for three freeze-thaw cycles (FTCs) (from 20°C to -20°C then to 20°C at $0.1^\circ\text{C}/\text{min}$, held for one hour at the temperature limits). The microbeads were stored in phosphate buffered saline (PBS) at room temperature until future use.

5.2.7 Drug Concentration Effect on DOX loading

Doxorubicin (DOX) was loaded into microparticles by immersion approach. Briefly, 0.25 mL microparticles were added into 1 mL of DOX stock solution of various concentrations ($C_0=0.125$ mg/mL, 0.25 mg/mL and 0.50 mg/mL) under mild shaking condition overnight. Afterwards, the loading solution was retrieved and subject to UV-vis measurements (Cary 60 UV-Vis, Agilent Technologies Inc.) at 485 nm. The drug-loaded microbeads were carefully washed with PBS to remove the surface-associated DOX.

The loading capacity of doxorubicin was determined by Equation 1:

$$\text{Doxorubicin loading}\left(\frac{\text{mg}}{\text{mL}}\right) = (W_0 - W_t)/V_b \quad (1)$$

Loading efficiency was determined according to Equation 2:

$$\text{Loading efficiency (\%)} = \frac{(W_0 - W_t)}{W_0} \times 100\% \quad (2)$$

where W_0 is the initial amount of DOX in solution, W_t is the amount of DOX in the supernatant, and V_b is the volume of hydrated PVA-SiO₂-IONP beads in each sample. Results were expressed as mean \pm standard deviation ($n=9$).

5.2.8 *In vitro* Release of DOX

The *in vitro* release profiles of DOX from PVA-SiO₂-IONP microbeads were studied in three release media at 37 °C with shaking at 110 rpm (shaking water bath, New Brunswick Scientific). Microparticles with various DOX loading (i.e., C₀=0.125 mg/mL, 0.25 mg/mL and 0.50 mg/mL) were added into 15 mL corresponding release media (PBS pH 7.4, phosphate buffer pH 5.5 and acidic water pH 5.5). At predetermined time intervals, 1 mL of liquid was retrieved from each sample, and 1 mL of fresh media was replenished. The DOX concentration in the liquid was quantified, as stated before.

5.2.9 Degradation of PVA-SiO₂-IONP Microparticles

The degradation of microbeads was studied at 37 °C in PBS and phosphate buffer. In detail, 0.25 mL blank PVA-SiO₂-IONP microbeads were incubated with 15 mL corresponding buffer. The degradation medium was replaced with a fresh one every 5 days. At designated time points, samples were retrieved and dried for microscopic imaging.

5.2.10 Size Analysis

The size of microparticles was measured by an optical microscope (Olympus BX60) coupled to an OMRX A35100U camera. Samples were prepared by dropping microbeads suspension on the microscope glass slides. The sectional area of the beads was measured manually using Image J software for over 100 samples and then converted into an equivalent spherical diameter using Equation 3:

$$d = 2\sqrt{A/\pi} \quad (3)$$

where d is the equivalent spherical diameter and A is the measured sectional area of the microbead. Results are expressed as the mean \pm standard deviation of more than 100 particles in each sample.

5.2.11 Scanning Electron Microscopy (SEM)/Energy-Dispersive X-ray (EDX)

Samples were critical point dried (K850 Critical Point Dryer, Electron Microscopy Sciences) and fixed on a carbon tape. A layer of 5 nm osmium coating was sputtered onto the surface of the samples using a plasma coater (OPC80T, Filgen) before imaging. Scanning electron micrographs and elemental mapping were obtained using an SEM coupled with energy EDX spectroscopy (LEO (Zeiss) 1540XB FIB/SEM).

5.2.12 Transmission Electron Microscopy (TEM)

To visualize the silica particles, silica sol was properly diluted using water, sonicated and dripped onto a Formvar carbon-coated 400 mesh copper grid (Electron Microscopy Sciences), air-dried and observed under TEM (CM10, Philips).

The internal structure of PVA-SiO₂-IONP microbeads was analyzed using TEM. Samples were dehydrated in acetone and embedded in epoxy resin. After that, embedded beads were ultramicrotomed (Reichert-Jung Ultracut E) with a diamond knife and the resulting slices were placed on copper grids (Electron Microscopy Sciences) for imaging at 80 kV.

5.2.13 Fourier Transform Infrared Spectroscopy (FTIR)

The samples of neat PVA, PVA-SiO₂ gel and PVA-SiO₂-IONP microparticles were dried in an oven at 60 °C overnight. FTIR analysis (Perkin-Elmer, Massachusetts, USA) was then performed in the region of 4000-500 cm⁻¹ at a resolution of 2 cm⁻¹.

5.2.14 Vibrating Sample Magnetometry (VSM)

PVA-SiO₂-IONP microparticles were oven-dried at 60 °C overnight. The magnetization curve of the microparticles was obtained using a vibrating sample magnetometer (LakeShore 7407, Lake-ShoreCryotronics Inc.) at 298 K.

5.2.15 Statistical Analysis

For DOX loading and release experiments, a sample size of three or nine was used for each condition. For degradation study, a sample size of three was used for each buffer

condition. Statistical analysis was performed using Microsoft Excel and GraphPad Prism v9 (La Jolla, CA). Results are reported as the mean \pm standard deviation.

5.3 Results

5.3.1 Microfluidic Fabrication of Size-tunable PVA-SiO₂-IONP Microparticles

The flow-focusing microfluidic device was effective in producing tadpole-shaped PVA-SiO₂-IONP microbeads with tunable sizes (129-272 μm). The polydispersity index (PDI), defined as the ratio between the standard deviation and the mean diameter of particles multiplied by 100, was calculated for each flow condition. The droplets developed PDI values \sim 10%, suggesting that a reasonably monodisperse population [34,35].

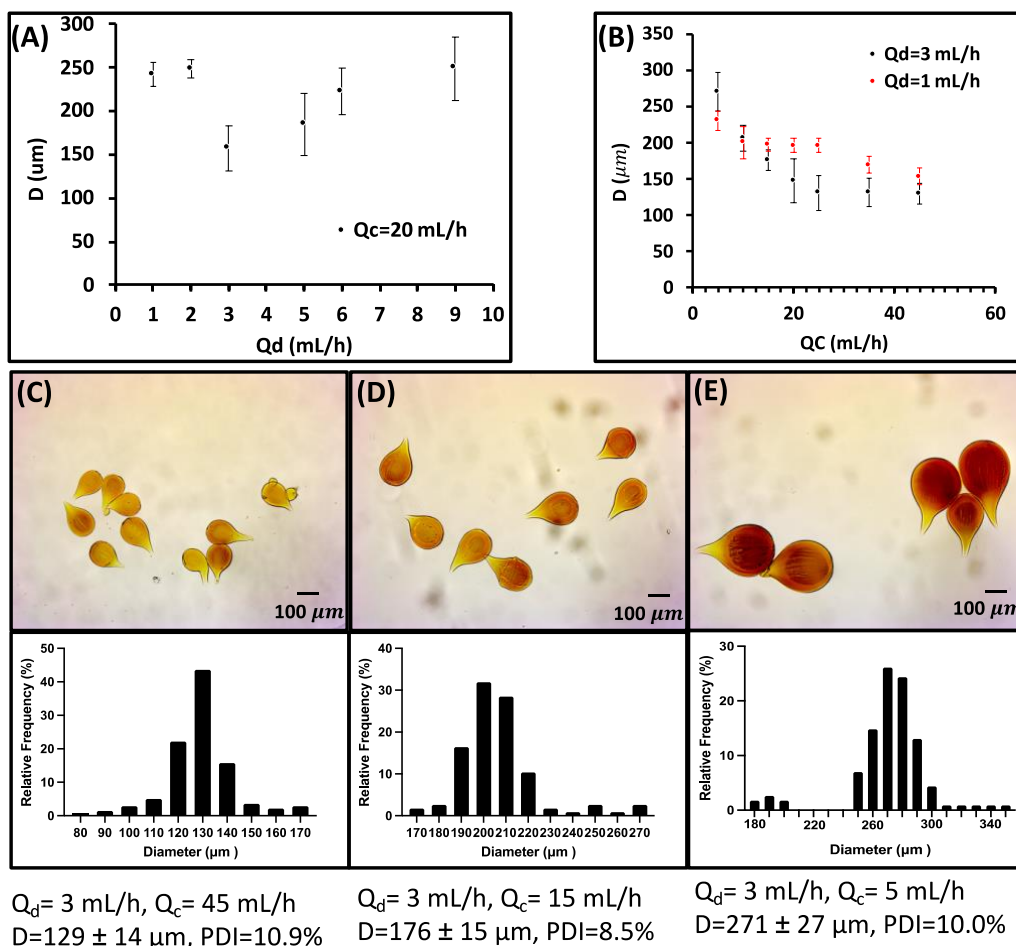


Figure 5.2 Relationship between particle diameter and flow rates. (A) Diameter as a function of dispersed phase, $Q_c=20$ mL/h, $Q_d=1-9$ mL/h. (B) Diameter as a function

of continuous phase, $Q_d=1$ mL/h, 3 mL/h, $Q_c=5-45$ mL/h. (C)-(E): Optical microscope images and size distributions of microbeads fabricated under different flow rate conditions. For a fixed $Q_c=20$ mL/h, the particle size decreased first and then increased as the Q_d increased. At a fixed Q_d , the particle size decreased with an increased Q_c .

5.3.2 Characterization of PVA-SiO₂-IONP Microparticles

The morphology of PVA-SiO₂-IONP microbeads was shown in Figure 5.3 A. The EDX analysis (Figure 5.3 D) confirmed the co-existence of iron oxide and silica throughout the microparticles.

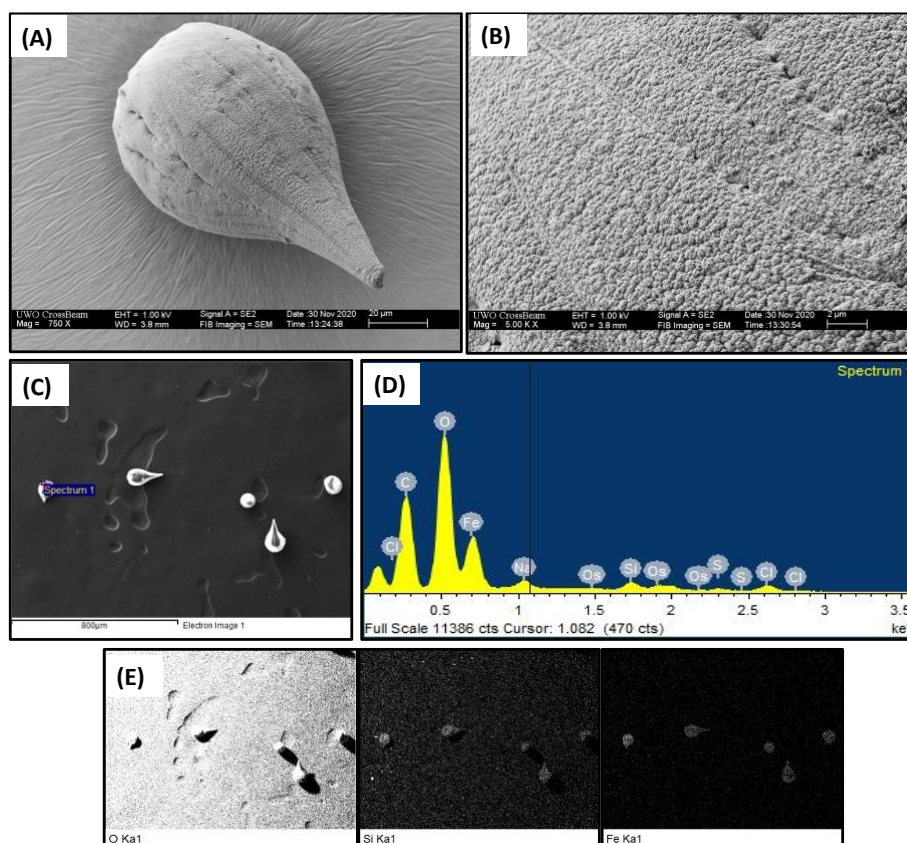


Figure 5.3 (A) and (B): surface morphology of microparticles ($Q_d=3$ mL/h, $Q_c=20$ mL/h). (C) and (D): EDX spectrum of microparticles with a square indicating the area of analysis. (E) is the EDX elemental mapping of the entire sample in (C). The EDX analysis confirmed the presence of iron and silica content in the PVA-SiO₂-IONP microparticles.

The silica and iron oxide components were visualized by TEM (Figure 5.4). Silica microparticles were found in a spherical shape with a diameter of $1.3 \pm 0.5 \mu\text{m}$. IONPs were well dispersed in the PVA matrix. The diameter of IONPs was measured to be $2.3 \pm 0.8 \text{ nm}$.

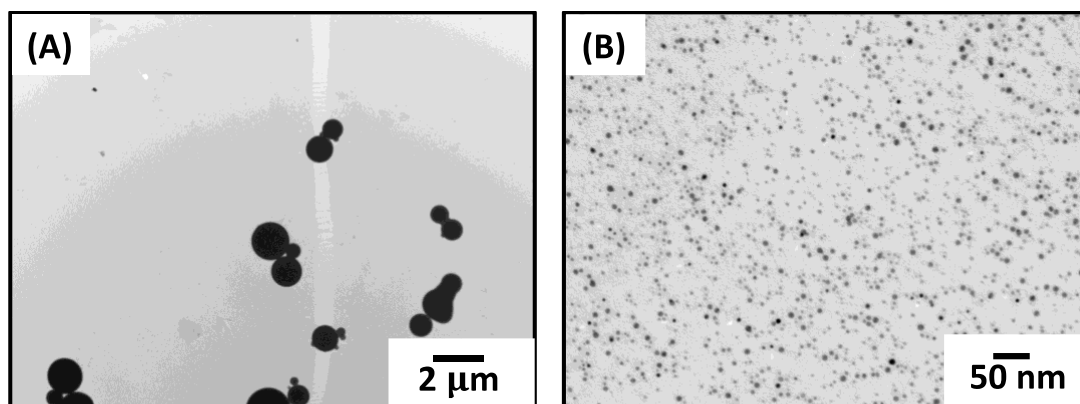


Figure 5.4 TEM images of (A) silica sol and (B) PVA-SiO₂-IONP microbeads. Acid-catalyzed sol-gel process contributed to spherical silica microparticles with a diameter of $1.3 \pm 0.5 \mu\text{m}$. IONPs were $2.3 \pm 0.8 \text{ nm}$ in diameter and were well-dispersed in the microbeads. Due to the large variance of the dimension of silica microparticles and IONPs, individual silica microparticle cannot be displayed in (B) with IONPs.

The FTIR spectrum of neat PVA, PVA-SiO₂ gel, PVA-SiO₂-IONP microparticles were shown in Figure 5.5. The neat PVA sample showed characteristic bands at 3220 cm^{-1} , 2897 cm^{-1} and 1078 cm^{-1} due to the O-H stretching, C-H stretching, and C-O-C, respectively [36].

The PVA-SiO₂ composite gels showed a new band at 946 cm^{-1} , attributed to the Si-OH stretching [37]. The spectra in the range of $1040\text{-}1100 \text{ cm}^{-1}$ indicated the co-existence of C-O-C, Si-O-Si and C-O-Si stretching [36,37]. The increase in the width of the peaks and its slight shift towards a lower wavenumber could be associated with the formation of Si-O-Si groups ($\sim 1060 \text{ cm}^{-1}$) and intermolecular reaction between TEOS and PVA (C-O-Si stretching, $1080\text{-}1120 \text{ cm}^{-1}$) [37,38]. This hypothesis was supported by the considerable reduction of the intensity of the O-H band (3220 cm^{-1}), which might be attributed to a

condensation reaction between the hydroxyl groups from silicate (i.e., silanol groups) and PVA [39]. Compared with the O-H bands (3220 cm^{-1}) of PVA and PVA-SiO₂ gels, an increase in the width of O-H band after IONPs incorporation was observed for PVA-SiO₂-IONP beads, indicating a possible formation of intermolecular bonding between the IONPs and PVA through hydroxyl groups.

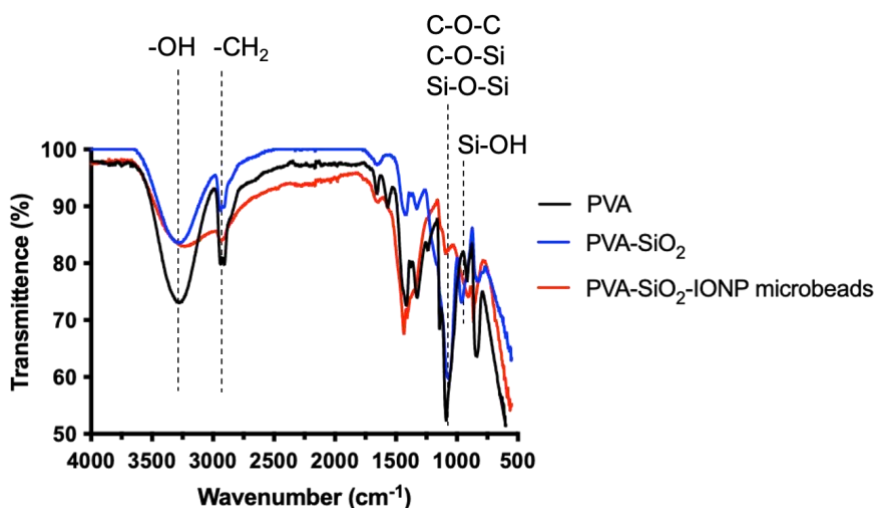


Figure 5.5 FTIR spectra of neat PVA, PVA-SiO₂ gel, and PVA-SiO₂-IONP microbeads. The emergence of C-O-Si peak and reduction of O-H peak indicates the condensation reaction between -OH groups of PVA and surface silanols of silica.

To characterize the magnetic properties of the delivery system, VSM was performed on the PVA-SiO₂-IONP microparticle sample. The magnetization curve (Figure 5.6 A) revealed the paramagnetic nature of the microparticles.

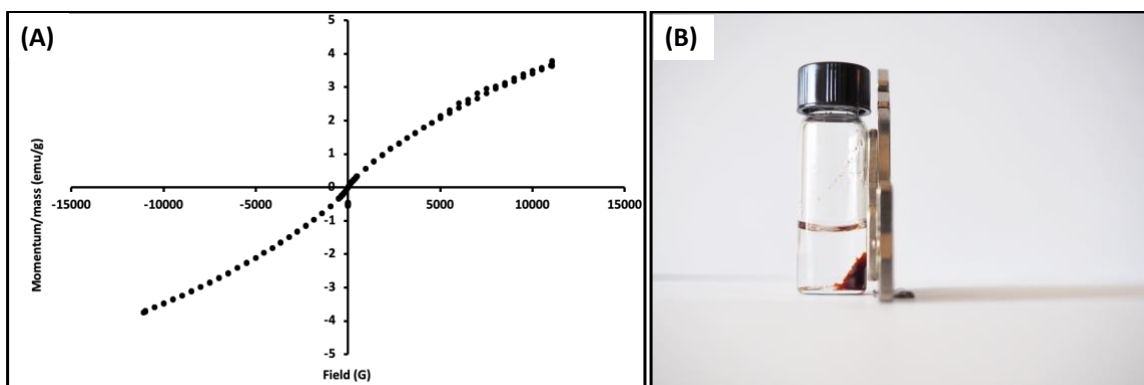


Figure 5.6 Magnetization curve of PVA-SiO₂-IONP microparticles. The microparticles exhibited paramagnetic behavior. (B) Microparticles dispersed in PBS attracted by a permanent magnet.

5.3.3 Drug Concentration Effect on DOX Loading

PVA-SiO₂-IONP microparticles were incubated with DOX solution of 0.125 mg/mL, 0.25 mg/mL and 0.50 mg/mL, the results of drug loading were summarized in Table 5.1. A higher loading while lower entrapment efficiency was observed when a more concentrated DOX stock solution was used. The DOX loading was 0.45 ± 0.03 , 0.79 ± 0.08 and 1.34 ± 0.09 mg/mL, respectively. Under these loading conditions, the entrapment efficiency was $89.8 \pm 6.6\%$, $79.3 \pm 7.9\%$ and $66.9 \pm 4.5\%$, respectively.

Table 5.1 Drug concentration effect on DOX loading.

DOX loading solution conc. (C ₀ , mg/mL)	DOX loading (mg/mL beads)	Entrapment efficiency (%)
0.125	0.45 ± 0.03	$89.8 \pm 6.6\%$
0.25	0.79 ± 0.08	$79.3 \pm 7.9\%$
0.50	1.34 ± 0.09	$66.9 \pm 4.5\%$

5.3.4 *In vitro* Release of DOX

Figure 5.7 shows the release profile of PVA-SiO₂-IONP microparticles with various DOX loading (i.e., 0.45 ± 0.03 , 0.79 ± 0.08 and 1.34 ± 0.09 mg/mL) in different release buffers. The drug release was fast on the first day and sustained release was

observed afterwards. The release plateau was reached at 7 days for all subgroups. Within the same DOX loading group, the release rate increased with a higher ionic concentration in buffer or a lower pH value.

The loading effect on DOX release was illustrated in Figure 5.7 D. PVA-SiO₂-IONP microspheres with a higher loading rendered a slower release. At day 21, the cumulative release for microspheres with 0.45 ± 0.03 , 0.79 ± 0.08 and 1.34 ± 0.09 mg/mL loading were $44.94 \pm 0.88\%$, $45.33 \pm 2.82\%$ and $33.50 \pm 1.62\%$, respectively.

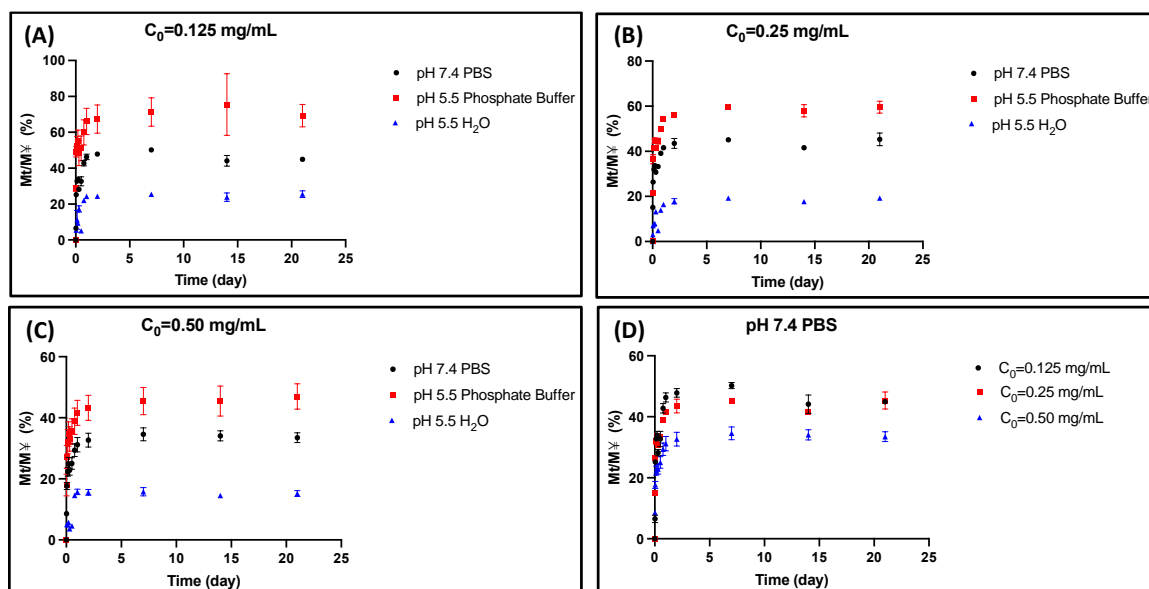


Figure 5.7 *In vitro* drug release from DOX-loaded PVA-SiO₂-IONP microparticles: (A)-(C) effect of release conditions on DOX release; (B) effect of drug loading on DOX release. Within the same DOX loading subgroup, the release rate increased with a higher ionic concentration in buffer or a lower pH value. At the same buffer condition, microparticles with a higher DOX loading contributed to a slower and lower percentage of release.

5.3.5 Degradation of Microparticles

The degradation of microparticles was evidenced by the morphological change during the test period (Figure 5.8). PVA-SiO₂-IONP microbeads degraded faster in acidic phosphate

buffer than in PBS, as the uneven surface and deformation of the original tadpole shape were more apparent from SEM images.

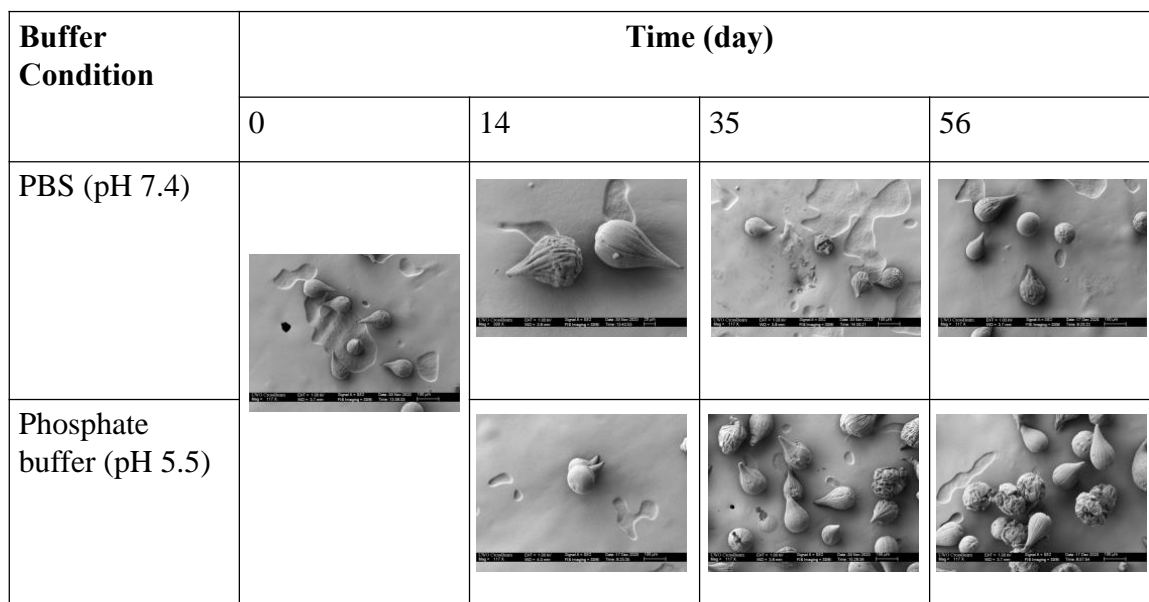
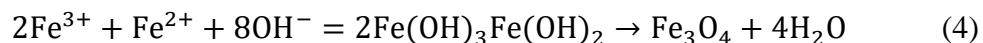


Figure 5.8 SEM images of the PVA-SiO₂-IONP microparticles at two buffer conditions. Pictures were obtained after 0, 14, 35 and 56 days' immersion in the corresponding buffer. Error bar: 20 μm , except for day 14 PBS (error bar 100 μm). The degradation of microparticles at both buffer conditions was evidenced by the morphological change during the test period.

5.4 Discussion

5.4.1 Microfluidic Fabrication of Size-tunable PVA-SiO₂-IONP Microparticles

During the microfluidic fabrication process, a dispersed fluid composed of PVA, SiO₂ and iron oxide precursors was sheared by the two continuous oil streams at the junctions of three microfluidic channels to form droplets. The resulting droplets were directed into the NaOH bath, where ferric and ferrous iron salts co-precipitate to form magnetite (Fe₃O₄) nanoparticles. The co-precipitation reaction can be represented by:



The flow rate of the dispersed phase and continuous phase are important parameters in determining the diameter of the microbeads. The size of the droplets decreased with an increased Q_c at a fixed Q_d , which was consistent with the literature [283,297]. It has been reported that within a certain Q_c range, a greater Q_c value would result in more rapid thread collapse and the breakup of the dispersed phase, leading to a reduced particle size [42]. The literature also suggests that the increase in Q_d will increase the size of microparticles [40], which was partially contradicted to our results, where the particle diameter first decreased with a larger Q_d . When Q_d exceeded the threshold value (i.e., 3 mL/h), larger microparticles with broader size deviation were generated. The initial downward trend could be resulted from the instability of droplet breakup at the early operating conditions or the transition of breakup pattern (e.g., from dripping to jetting) [43]. However, the droplet generation process must be microscopically examined along with the computation of relevant parameters (i.e., capillary number and Weber number) to fully understand fluid mechanics and the effect of flow rates on the size of final droplets [42,44].

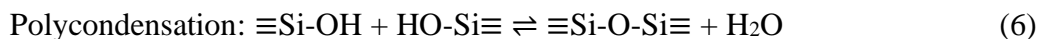
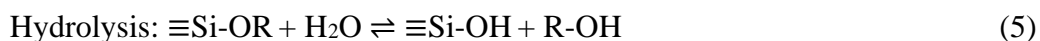
The tadpole shape of PVA-SiO₂-IONP microparticles could be attributed by the solidification process that emerged at the oil phase/NaOH interface. In the NaOH collection bath, the continuous phase (i.e., oil phase) would form a separate layer on the top of the NaOH phase with extended fabrication time. It was speculated that during the slow passage of PVA-SiO₂-Fe (II, III) droplets through the oil phase/NaOH interface, the droplets deformed into tail shape due to the combined effect of gravity, interfacial tension, impact and tangential stress [45,46]. The co-precipitation of iron precursors proceeds in the presence of PVA and gradually increased the rigidity of microgel, which would prevent further changes in particle morphology. Indeed, non-spherical hydrogel microparticles are expected in droplet generation with a subsequent “external gelation” procedure. Alginate microparticles with different tailed morphologies have been intentionally produced by changing the viscosity of the polymer solution, the concentration of the crosslinker and collecting distance [47,48].

Monodisperse, size-controlled and tail-shaped PVA-SiO₂-IONP microparticles are attractive as drug-eluting microparticles for TACE. The uniform morphology could

facilitate the catheter delivery, which could potentially avoid the off-target embolization and allow a more proximal occlusion [49,50]. The non-spherical microparticles render a higher surface area compared to spherical ones, which makes faster drug release possible [48].

5.4.2 Characterization of PVA-SiO₂-IONP Microparticles

Silica microparticles were formed in the acid-catalyzed sol-gel process. The reaction is generally carried out through simultaneous or successive reactions of hydrolysis and polycondensation of silica precursors in the presence of an organic cosolvent [29]. The net reactions can be described by:



The size of generated silica particles was found to be similar to what was developed using the acidic catalysis procedure [51] but much larger than the particles derived from basic conditions [52]. The large diameter and broad size distribution can be explained by the gel formation scheme. In an acid-catalyzed sol-gel procedure, the hydrolysis rate is greater than the condensation rate. The silica tends to form linear polymeric networks that are occasionally crosslinked. In contrast, hydrolysis is a lot faster than condensation under basic conditions, which results in uniform and discrete silica particles [29].

The incorporation of silica into the PVA is beneficial as it can potentially improve the drug loading and release capability of the delivery system. In a hydrogel-based delivery system, the microscopic structure of the polymeric network governs inward and outward molecular diffusion [53]. It was believed that the crystalline regions of polymers are impermeable to solutes [30,31]. This was supported by the reduction in diffusion coefficients through PVA gels with a greater degree of crystallinity or denser polymeric network. Moreover, PVA with a denser network has stronger intermolecular interactions displays a smaller degree of swelling and, therefore pore expansion. This was believed to hinder drug penetration and release from the PVA matrix. The incorporation of silica components could reduce the density of polymer mesh and the degree of crystallinity, therefore improve the permeation of drug molecules [54–56]. It was evidenced that the

incorporation of silica nanoparticles (SiNPs) can interact with -OH groups from PVA and interfere with the PVA chain arrangement, which would diminish the crystallinity of PVA and contribute to an improved solute permeability [26–28].

TEM micrographs confirmed the formation of well-dispersed and relatively uniform IONPs ($D=2.3 \pm 0.8$ nm). The ultrasmall size (<50 nm) and good dispersity could be attributed by the protective effect of PVA [57]. In a study conducted by Lee et al., IONPs of average diameter 4-7 nm were synthesized via *in situ* co-precipitation. The ferric and ferrous ions co-precipitate in the PVA solution, during which PVA irreversibly adsorbed on the surface of IONPs [58]. It was hypothesized that the interaction of PVA hydroxyl groups with IONPs could protect the nanoparticles from growth and aggregation through steric stabilization [59,60].

The formation of IONPs within the microparticles is desirable for their applications as DEBs. First, IONPs could contribute to the crosslinking of the hydrogel and allow the delivery system to ‘degrade’ [22]. IONPs could provide contrast enhancement to magnetic resonance (MR) images [61]. More importantly, the co-localization of the contrast agent with drug contributes to more definitive and precise location of the drug, which could be useful for intraprocedural guidance and post-operative assessment. Moreover, the IONPs endow the microparticles with magnetic properties, making them promising in magnetically-guided drug delivery [62].

The PVA-SiO₂ interaction was revealed by the FTIR spectrum. Through the acidic hydrolysis of TEOS in the presence of PVA, the silanol groups not only condense with each other but also react with the hydroxyl groups of PVA to form C-O-Si bonds [26,39,63]. This PVA-SiO₂ interaction could be desirable as it would affect the overall crosslinking of the hydrogel and render a more drug-permeable matrix. The contribution of SiO₂ to the PVA crosslinking should also be considered for the degradation process.

Compared with the O-H peak of PVA-SiO₂ samples, the PVA-SiO₂-IONP gave a peak with a weaker intensity and broader width. This could be attributed by the consumption of -OH groups during the crosslinking between PVA and IONPs [22]. Furthermore, a significant reduction of the peak in the range of 1040-1100 cm⁻¹ was observed. The

variation in this peak was consistent with the decrease in the concentration of PVA, SiO₂ in the PVA-SiO₂-IONP formulation, as compared to neat PVA and PVA-SiO₂ gels. This could also be an indication that the complex interactions among PVA, SiO₂ and IONP have weakened certain interactions.

The near-linear magnetization curve implied the paramagnetic property of the PVA-SiO₂-IONP microparticles, which was commonly found in FeO and Fe₂O₃ [64–66]. The formation of non-magnetite impurities could be due to the presence of oxygen and/or the unconfined stoichiometric and pH condition [67]. In a co-precipitation reaction, stoichiometry and pH are crucial to ensure the formation of Fe₃O₄ nanoparticles. The ideal ratio of Fe²⁺/Fe³⁺ is approximately 0.5, while the optimal pH window remains 8.5–10 [68,69]. The presence of oxygen and strong alkaline solutions could induce the oxidation of Fe²⁺ ions to Fe³⁺ ions, making the effective Fe²⁺/Fe³⁺ < 0.5 [67]. In the context of the pH effect, re-dissolutions of Fe(OH)₃ and Fe(OH)₂ begin at pH >11, which could change the composition of formed IONPs [70]. To ensure the formation of Fe₃O₄ nanoparticles, excess Fe²⁺ ions (e.g., Fe²⁺:Fe³⁺=2:3) could be used. An alternative approach would be to employ argon or nitrogen to eliminate the oxygen in the system [71]. Nevertheless, PVA-SiO₂-IONP microparticles demonstrated magnetic response and zero residual magnetization was produced. This suggests that these microparticles do not retain any magnetization after the external magnetic field is removed, which can potentially avoid the particle agglomeration *in vivo* [72]. Magnetic PVA-SiO₂-IONP microparticles may find their application in MRI contrast enhancement and magnetic targeting.

5.4.3 Drug Concentration Effect on DOX Loading

PVA-SiO₂-IONP microparticles could achieve a greater DOX loading and lower entrapment efficiency at a higher initial DOX concentration. This phenomenon could be attributed to the finite number of binding sites when the amount of microparticles was fixed. Moreover, the increase in loading (in percentile) was smaller than in the DOX concentration, indicating a longer incubation time might be necessary. The competition between DOX molecules would need a longer time to reach equilibrium.

5.4.4 *In vitro* Release of DOX

The effect of ionic concentration and pH on DOX elution was shown in Figure 7 A-C. At all loading levels, DOX release was faster in pH 5.5 phosphate buffer than in the H₂O of the same pH, indicating the presence of ions in elution medium can accelerate the release. Acidic phosphate buffer rendered faster release compared with saline. As the ionic concentration and pH were different for the two buffers, it is challenging to claim the pH effect on DOX release. However, we believe that an acidic pH plays an essential role in DOX release. DOX is an amphoteric drug that presents predominantly in its cationic form [73]. It contains deprotonable phenolic groups (-OH, pKa 9.5) and a protonable amine group (-NH₂, pKa 8.2) [74]. Yang et al. assembled a DOX-loaded delivery system using graphene oxide. DOX elution profile was studied at three pHs (2, 7 and 10), and the acidic pH environment provided the fastest and greatest release. It was hypothesized that the DOX interacted with the carrier through the hydrogen bonding between the -OH groups on the graphene sheet with the -OH and -NH₂ groups in DOX. In an acidic environment, the protonation of amine groups accelerates the DOX release by reducing the number of functional groups available for hydrogen bonding [75]. Such pH-dependent release is particularly attractive for drug delivery applications. It can potentially allow tumor-specific release, because the pH value in tumor tissue (pH 6.5-6.8) is different from healthy tissue (pH 7.35-7.45) [76].

As shown in Figure 7 D, PVA-SiO₂-IONP microparticles with a higher loading provide a slower DOX release. This could be explained by the increased hydrophobicity of the microparticles after loading. It was found that the DOX molecules could introduce $\pi - \pi$ drug-drug interactions, which increased the hydrophobicity of the drug carriers [4]. As such, microparticles with greater DOX loading became more hydrophobic than those with lower loading. As a consequence, the water penetration hence drug diffusion would be retarded, resulting in a slower drug release [77].

For all subgroups, an incomplete drug release was observed, which could possibly be explained by the entrapment of DOX in the hydrogel matrix and/or the adsorption of DOX to the surface of the glass vials [78,79]. The plateau phase in DOX release could be followed by a sustained but slow release of the rest of the payload as the degradation

progresses. Future study could be conducted for an extended period of time to fully reveal the drug release profile. Nevertheless, the release was sustained for 7 days, and the release rate was adjustable by altering the DOX loading. Such release profile could be engineered to comply with the frequency of TACE treatments and provide a better tumor response due to the prolonged drug release [16].

5.4.5 Degradation of Microparticles

It has been hypothesized that the degradation of microbeads was contributed by the iron dissolution and PVA matrix disintegration (Chapter 3). This study provides additional quantitative data to support the hypothesis. However, we are not able to conclude the degradation mechanism of PVA-SiO₂-IONP microbeads because the impact of silica dissolution on degradation is yet to be elucidated. Future studies on sample weight loss, thermal properties, compositional analysis of the degradation medium are required to understand the degradation process fully. The degradation data should also be compared with DOX release profile to better understand the role of carrier degradation in drug release.

5.5 Conclusion

Multifunctional microparticles were successfully prepared from poly(vinyl alcohol), silica and iron oxide via sol-gel synthesis, *in situ* co-precipitation and microfluidics. The size of the microparticles was tunable by adjusting the flow rate of the continuous phase and dispersed phase. The PVA-SiO₂-IONP microparticles were able to load DOX and provide a controlled release for 7 days. This could be followed by a sustained but slow release of the rest of the payload as the degradation progresses. The release profile was adjustable by altering the drug loading. It was speculated that the DOX release from the system was co-dependent on the ionic concentration and pH of the release medium. Furthermore, the microparticles were subject to degradation in physiological conditions. Taken together, multifunctional PVA-SiO₂-IONP microparticles can be potentially used as drug-eluting agents for locoregional therapy, such as transarterial chemoembolization and wound healing. Further research in the PVA-silica interaction and microparticle degradation is required to comprehensively evaluate this drug delivery system.

5.6 References

- [1] M. Lengyel, N. Kállai-Szabó, V. Antal, A.J. Laki, I. Antal, *Microparticles, Microspheres, and Microcapsules for Advanced Drug Delivery*, Scientia Pharmaceutica. 87 (2019) 20.
- [2] J.-Y. Hou, L.-N. Gao, F.-Y. Meng, Y.-L. Cui, *Mucoadhesive microparticles for gastroretentive delivery: preparation, biodistribution and targeting evaluation*, Mar Drugs. 12 (2014) 5764–5787.
- [3] D.A. Edwards, J. Hanes, G. Caponetti, J. Hrkach, A. Ben-Jebria, M.L. Eskew, J. Mintzes, D. Deaver, N. Lotan, R. Langer, *Large porous particles for pulmonary drug delivery*, Science. 276 (1997) 1868–1871.
- [4] T. de Baere, S. Plotkin, R. Yu, A. Sutter, Y. Wu, G.M. Cruise, *An In Vitro Evaluation of Four Types of Drug-Eluting Microspheres Loaded with Doxorubicin*, J Vasc Interv Radiol. 27 (2016) 1425–1431.
- [5] F.Y. Han, K.J. Thurecht, A.K. Whittaker, M.T. Smith, *Bioerodable PLGA-Based Microparticles for Producing Sustained-Release Drug Formulations and Strategies for Improving Drug Loading*, Front. Pharmacol. 7 (2016).
- [6] W. Li, L. Zhang, X. Ge, B. Xu, W. Zhang, L. Qu, C.-H. Choi, J. Xu, A. Zhang, H. Lee, D.A. Weitz, *Microfluidic fabrication of microparticles for biomedical applications*, Chem. Soc. Rev. 47 (2018) 5646–5683.
- [7] V.N. Chamundeswari, Y.J. Chuah, S.C.J. Loo, *Multidrug-eluting bi-layered microparticle-mesh scaffolds for musculoskeletal tissue regeneration*, J. Mater. Chem. B. 6 (2018) 3340–3347.
- [8] S.-Q. Gao, T. Maeda, K. Okano, K. Palczewski, *A Microparticle/Hydrogel Combination Drug-Delivery System for Sustained Release of Retinoids*, Invest Ophthalmol Vis Sci. 53 (2012) 6314–6323.
- [9] S. Shkarina, R. Shkarin, V. Weinhardt, E. Melnik, G. Vacun, P.J. Kluger, K. Loza, M. Epple, S.I. Ivlev, T. Baumbach, M.A. Surmeneva, R.A. Surmenev, *3D biodegradable scaffolds of polycaprolactone with silicate-containing hydroxyapatite microparticles for bone tissue engineering: high-resolution tomography and in vitro study*, Sci Rep. 8 (2018).
- [10] F. Hejazi, H. Mirzadeh, *Roll-designed 3D nanofibrous scaffold suitable for the regeneration of load bearing bone defects*, Prog Biomater. 5 (2016) 199–211.
- [11] D. Bannerman, W. Wan, *Multifunctional microbeads for drug delivery in TACE*, Expert Opinion on Drug Delivery. 13 (2016) 1289–1300.

- [12] A. Nacev, C. Beni, O. Bruno, B. Shapiro, The behaviors of ferromagnetic nanoparticles in and around blood vessels under applied magnetic fields, *Journal of Magnetism and Magnetic Materials*. 323 (2011) 651–668.
- [13] R.T.P. Poon, W.K. Tso, R.W.C. Pang, K.K.C. Ng, R. Woo, K.S. Tai, S.T. Fan, A Phase I/II Trial of Chemoembolization for Hepatocellular Carcinoma Using a Novel Intra-Arterial Drug-Eluting Bead, *Clinical Gastroenterology and Hepatology*. 5 (2007) 1100–1108.
- [14] M. Varela, M.I. Real, M. Burrel, A. Forner, M. Sala, M. Brunet, C. Ayuso, L. Castells, X. Montañá, J.M. Llovet, J. Bruix, Chemoembolization of hepatocellular carcinoma with drug eluting beads: Efficacy and doxorubicin pharmacokinetics, *Journal of Hepatology*. 46 (2007) 474–481.
- [15] K.R. Kamath, K. Park, Biodegradable hydrogels in drug delivery, *Advanced Drug Delivery Reviews*. 11 (1993) 59–84.
- [16] A. Rammohan, J. Sathyanesan, S. Ramaswami, A. Lakshmanan, P. Senthil-Kumar, U.P. Srinivasan, R. Ramasamy, P. Ravichandran, Embolization of liver tumors: Past, present and future, *World J Radiol*. 4 (2012) 405–412.
- [17] Z. Zhao, C. Vizetto-Duarte, Z.K. Moay, M.I. Setyawati, M. Rakshit, M.H. Kathawala, K.W. Ng, Composite Hydrogels in Three-Dimensional in vitro Models, *Front. Bioeng. Biotechnol*. 8 (2020).
- [18] P.N. Dave, A. Gor, Chapter 3 - Natural Polysaccharide-Based Hydrogels and Nanomaterials: Recent Trends and Their Applications, in: C. Mustansar Hussain (Ed.), *Handbook of Nanomaterials for Industrial Applications*, Elsevier, 2018: pp. 36–66.
- [19] W. Wan, A.D. Bannerman, L. Yang, H. Mak, Poly(Vinyl Alcohol) Cryogels for Biomedical Applications, in: 2014.
- [20] M.I. Baker, S.P. Walsh, Z. Schwartz, B.D. Boyan, A review of polyvinyl alcohol and its uses in cartilage and orthopedic applications, *J Biomed Mater Res B Appl Biomater*. 100 (2012) 1451–1457.
- [21] D. Zhi, T. Yang, J. Yang, S. Fu, S. Zhang, Targeting strategies for superparamagnetic iron oxide nanoparticles in cancer therapy, *Acta Biomater*. 102 (2020) 13–34.
- [22] A.D. Bannerman, X. Li, W. Wan, A ‘degradable’ poly(vinyl alcohol) iron oxide nanoparticle hydrogel, *Acta Biomaterialia*. 58 (2017) 376–385.
- [23] M. Younes, P. Aggett, F. Aguilar, R. Crebelli, B. Dusemund, M. Filipič, M.J. Frutos, P. Galtier, D. Gott, U. Gundert-Remy, G.G. Kuhnle, J.-C. Leblanc, I.T. Lillegaard, P. Moldeus, A. Mortensen, A. Oskarsson, I. Stankovic, I. Waalkens-Berendsen, R.A. Woutersen, M. Wright, P. Boon, D. Chrysafidis, R. Gürtler, P.

- Mosesso, D. Parent-Massin, P. Tobback, N. Kovalkovicova, A.M. Rincon, A. Tard, C. Lambré, Re-evaluation of silicon dioxide (E 551) as a food additive, *EFSA Journal*. 16 (2018) e05088.
- [24] J.G. Croissant, Y. Fatieiev, N.M. Khashab, Degradability and Clearance of Silicon, Organosilica, Silsesquioxane, Silica Mixed Oxide, and Mesoporous Silica Nanoparticles, *Advanced Materials*. 29 (2017) 1604634.
- [25] C. Xu, C. Lei, C. Yu, Mesoporous Silica Nanoparticles for Protein Protection and Delivery, *Front. Chem.* 7 (2019).
- [26] R. Guo, X. Du, R. Zhang, L. Deng, A. Dong, J. Zhang, Bioadhesive film formed from a novel organic–inorganic hybrid gel for transdermal drug delivery system, *European Journal of Pharmaceutics and Biopharmaceutics*. 79 (2011) 574–583.
- [27] H. Pingan, J. Mengjun, Z. Yanyan, H. Ling, A silica/PVA adhesive hybrid material with high transparency, thermostability and mechanical strength, *RSC Advances*. 7 (2017) 2450–2459.
- [28] C. Shao, H.-Y. Kim, J. Gong, B. Ding, D.-R. Lee, S.-J. Park, Fiber mats of poly(vinyl alcohol)/silica composite via electrospinning, *Materials Letters*. 57 (2003) 1579–1584.
- [29] A.M. Buckley, M. Greenblatt, The Sol-Gel Preparation of Silica Gels, *J. Chem. Educ.* 71 (1994) 599.
- [30] S.J. Lue, D.-T. Lee, J.-Y. Chen, C.-H. Chiu, C.-C. Hu, Y.C. Jean, J.-Y. Lai, Diffusivity enhancement of water vapor in poly(vinyl alcohol)–fumed silica nanocomposite membranes: Correlation with polymer crystallinity and free-volume properties, *Journal of Membrane Science*. 325 (2008) 831–839.
- [31] R.S. Harland, N.A. Peppas, Solute diffusion in swollen membranes, *Polymer Bulletin*. 18 (1987) 553–556.
- [32] K.A. Walters, Trends and Future Perspectives in Peptide and Protein Drug Delivery (Drug Targeting and Delivery Volume 4) Edited by Vincent H. L. Lee, Mitsuru Hashida and Yutaka Mizushima Published 1995 Harwood Academic Publishers GmbH, Chur, Switzerland xiv + 378 pages ISBN 3 7186 5641 8 \$120.00, £78.00, ECU 100.00, *Journal of Pharmacy and Pharmacology*. 48 (1996) 881–881.
- [33] Preparation of Buffer Solutions : Pharmaceutical Guidelines, (n.d.). <https://www.pharmaguideline.com/2010/09/preparation-of-buffer-solutions.html> (accessed April 5, 2021).
- [34] Q. Xu, M. Hashimoto, T.T. Dang, T. Hoare, D.S. Kohane, G.M. Whitesides, R. Langer, D.G. Anderson, Preparation of Monodisperse Biodegradable Polymer Microparticles Using a Microfluidic Flow-Focusing Device for Controlled Drug Delivery, *Small*. 5 (2009) 1575–1581.

- [35] M. Danaei, M. Dehghankhold, S. Ataei, F. Hasanzadeh Davarani, R. Javanmard, A. Dokhani, S. Khorasani, M.R. Mozafari, Impact of Particle Size and Polydispersity Index on the Clinical Applications of Lipidic Nanocarrier Systems, *Pharmaceutics*. 10 (2018).
- [36] H.S. Mansur, C.M. Sadahira, A.N. Souza, A.A.P. Mansur, FTIR spectroscopy characterization of poly (vinyl alcohol) hydrogel with different hydrolysis degree and chemically crosslinked with glutaraldehyde, *Materials Science and Engineering: C*. 28 (2008) 539–548.
- [37] P. Hajji, L. David, J.F. Gerard, J.P. Pascault, G. Vigier, Synthesis, structure, and morphology of polymer–silica hybrid nanocomposites based on hydroxyethyl methacrylate, *Journal of Polymer Science Part B: Polymer Physics*. 37 (1999) 3172–3187.
- [38] T. Pirzada, S.A. Arvidson, C.D. Saquing, S.S. Shah, S.A. Khan, Hybrid Silica–PVA Nanofibers via Sol–Gel Electrospinning, *Langmuir*. 28 (2012) 5834–5844.
- [39] Y. Zhang, L. Ye, Structure and property of polyvinyl alcohol/precipitated silica composite hydrogels for microorganism immobilization, *Composites Part B: Engineering*. 56 (2014) 749–755.
- [40] D.-H. Kim, T. Choy, S. Huang, R.M. Green, R.A. Omary, A.C. Larson, Microfluidic fabrication of 6-methoxyethylamino numonafide-eluting magnetic microspheres, *Acta Biomaterialia*. 10 (2014) 742–750.
- [41] B. Amoyav, O. Benny, Controlled and tunable polymer particles’ production using a single microfluidic device, *Appl Nanosci*. 8 (2018) 905–914.
- [42] J.H. Xu, G.S. Luo, S.W. Li, G.G. Chen, Shear force induced monodisperse droplet formation in a microfluidic device by controlling wetting properties, *Lab Chip*. 6 (2006) 131–136.
- [43] N.M. Kovalchuk, M. Sagisaka, K. Steponavicius, D. Vigolo, M.J.H. Simmons, Drop formation in microfluidic cross-junction: jetting to dripping to jetting transition, *Microfluid Nanofluid*. 23 (2019) 103.
- [44] Y. Mahdi, K. Daoud, L. Tadrist, Two-phase flow patterns and size distribution of droplets in a microfluidic T-junction: Experimental observations in the squeezing regime, *Comptes Rendus Mécanique*. 345 (2017) 259–270.
- [45] Q. Wang, S. Liu, H. Wang, J. Zhu, Y. Yang, Alginate droplets pre-crosslinked in microchannels to prepare monodispersed spherical microgels, *Colloids and Surfaces A: Physicochemical and Engineering Aspects*. 482 (2015) 371–377.
- [46] L. Capretto, S. Mazzitelli, C. Balestra, A. Tosi, C. Nastruzzi, Effect of the gelation process on the production of alginate microbeads by microfluidic chip technology, *Lab Chip*. 8 (2008) 617–621.

- [47] Y. Hu, G. Azadi, A.M. Ardekani, Microfluidic fabrication of shape-tunable alginate microgels: Effect of size and impact velocity, *Carbohydrate Polymers*. 120 (2015) 38–45.
- [48] Y.-S. Lin, C.-H. Yang, Y.-Y. Hsu, C.-L. Hsieh, Microfluidic synthesis of tail-shaped alginate microparticles using slow sedimentation, *Electrophoresis*. 34 (2013) 425–431.
- [49] J. Handa, S. Nakasu, I. Matsuda, Facial nerve palsy following therapeutic embolization, *Surg Neurol*. 14 (1980) 377–380.
- [50] S. Vaidya, K.R. Tozer, J. Chen, An Overview of Embolic Agents, *Semin Intervent Radiol*. 25 (2008) 204–215.
- [51] null Silva, null Airoidi, Acid and Base Catalysts in the Hybrid Silica Sol-Gel Process, *J Colloid Interface Sci*. 195 (1997) 381–387.
- [52] C.K. Dixit, S. Bhakta, A. Kumar, S.L. Suib, J.F. Rusling, Fast nucleation for silica nanoparticle synthesis using a sol–gel method, *Nanoscale*. 8 (2016) 19662–19667.
- [53] J. Li, D.J. Mooney, Designing hydrogels for controlled drug delivery, *Nat Rev Mater*. 1 (2016).
- [54] S.M. Shaheen, K. Yamaura, Preparation of theophylline hydrogels of atactic poly(vinyl alcohol)/NaCl/H₂O system for drug delivery system, *Journal of Controlled Release*. 81 (2002) 367–377.
- [55] H. Matsuyama, M. Teramoto, H. Urano, Analysis of solute diffusion in poly(vinyl alcohol) hydrogel membrane, *Journal of Membrane Science*. 126 (1997) 151–160.
- [56] C.M. Hassan, N.A. Peppas, Structure and Applications of Poly(vinyl alcohol) Hydrogels Produced by Conventional Crosslinking or by Freezing/Thawing Methods, in: *Biopolymers · PVA Hydrogels, Anionic Polymerisation Nanocomposites*, Springer Berlin Heidelberg, 2000: pp. 37–65.
- [57] A. Nemmar, S. Beegam, P. Yuvaraju, J. Yasin, S. Tariq, S. Attoub, B.H. Ali, Ultrasmall superparamagnetic iron oxide nanoparticles acutely promote thrombosis and cardiac oxidative stress and DNA damage in mice, *Particle and Fibre Toxicology*. 13 (2016) 22.
- [58] J. Lee, T. Isobe, M. Senna, Preparation of Ultrafine Fe₃O₄ Particles by Precipitation in the Presence of PVA at High pH, *Journal of Colloid and Interface Science*. 177 (1996) 490–494.
- [59] J.S. Gonzalez, C.E. Hoppe, P.M. Zelis, L. Arciniegas, G.A. Pasquevich, F.H. Sanchez, V.A. Alvarez, Simple and Efficient Procedure for the Synthesis of Ferrogels Based on Physically Cross-Linked PVA, *Ind. Eng. Chem. Res*. 53 (2014) 214–221.

- [60] D. Kovář, A. Malá, J. Mlčochová, M. Kalina, Z. Fohlerová, A. Hlaváček, Z. Farka, P. Skládal, Z. Starčuk, R. Jířík, O. Slabý, J. Hubálek, Preparation and Characterisation of Highly Stable Iron Oxide Nanoparticles for Magnetic Resonance Imaging, *Journal of Nanomaterials*. 2017 (2017) e7859289.
- [61] J.X.J. Zhang, K. Hoshino, Chapter 7 - Nanomaterials for molecular sensing, in: J.X.J. Zhang, K. Hoshino (Eds.), *Molecular Sensors and Nanodevices (Second Edition)*, Academic Press, 2019: pp. 413–487.
- [62] O. Felfoul, A.T. Becker, G. Fagogenis, P.E. Dupont, Simultaneous steering and imaging of magnetic particles using MRI toward delivery of therapeutics, *Scientific Reports*. 6 (2016) 33567.
- [63] X. Luo, M.Y. Akram, Y. Yuan, J. Nie, X. Zhu, Silicon dioxide/poly(vinyl alcohol) composite hydrogels with high mechanical properties and low swellability, *Journal of Applied Polymer Science*. 136 (2019) 46895.
- [64] *Magnetic Properties of Materials*, (n.d.).
<https://www.sigmaaldrich.com/CA/en/technical-documents/technical-article/materials-science-and-engineering/solid-state-synthesis/properties> (accessed June 15, 2021).
- [65] P.A. Petrov, A. Ali, D.K. Potter, Diamagnetic Behavior in Nanoparticle Hematite?, *Journal of Modern Physics*. 8 (2017) 1013–1019.
- [66] H.M. Lu, X.K. Meng, Morin Temperature and Néel Temperature of Hematite Nanocrystals, *J. Phys. Chem. C*. 114 (2010) 21291–21295.
- [67] G. Gnanaprakash, S. Mahadevan, T. Jayakumar, P. Kalyanasundaram, J. Philip, B. Raj, Effect of initial pH and temperature of iron salt solutions on formation of magnetite nanoparticles, *Materials Chemistry and Physics*. 103 (2007) 168–175.
- [68] N.M. Griбанov, E.E. Bibik, O.V. Buzunov, V.N. Naumov, Physico-chemical regularities of obtaining highly dispersed magnetite by the method of chemical condensation, *Journal of Magnetism and Magnetic Materials*. 85 (1990) 7–10.
- [69] P. Berger, N.B. Adelman, K.J. Beckman, D.J. Campbell, A.B. Ellis, G.C. Lisensky, Preparation and Properties of an Aqueous Ferrofluid, *J. Chem. Educ.* 76 (1999) 943.
- [70] N. Ajinkya, X. Yu, P. Kaithal, H. Luo, P. Somani, S. Ramakrishna, Magnetic Iron Oxide Nanoparticle (IONP) Synthesis to Applications: Present and Future, *Materials (Basel)*. 13 (2020).
- [71] Y.M. Wang, X. Cao, G.H. Liu, R.Y. Hong, Y.M. Chen, X.F. Chen, H.Z. Li, B. Xu, D.G. Wei, Synthesis of Fe₃O₄ magnetic fluid used for magnetic resonance imaging and hyperthermia, *Journal of Magnetism and Magnetic Materials*. 323 (2011) 2953–2959.

- [72] A. Singh, S.K. Sahoo, Magnetic nanoparticles: a novel platform for cancer theranostics, *Drug Discovery Today*. 19 (2014) 474–481.
- [73] B. Manocha, A. Margaritis, Controlled Release of Doxorubicin from Doxorubicin/-Polyglutamic Acid Ionic Complex, *Journal of Nanomaterials*. 2010 (2010) e780171.
- [74] Z. Fülöp, R. Gref, T. Loftsson, A permeation method for detection of self-aggregation of doxorubicin in aqueous environment, *International Journal of Pharmaceutics*. 454 (2013) 559–561.
- [75] X. Yang, X. Zhang, Z. Liu, Y. Ma, Y. Huang, Y. Chen, High-Efficiency Loading and Controlled Release of Doxorubicin Hydrochloride on Graphene Oxide, *J. Phys. Chem. C*. 112 (2008) 17554–17558.
- [76] W. Guo, L. Deng, J. Yu, Z. Chen, Y. Woo, H. Liu, T. Li, T. Lin, H. Chen, M. Zhao, L. Zhang, G. Li, Y. Hu, Sericin nanomicelles with enhanced cellular uptake and pH-triggered release of doxorubicin reverse cancer drug resistance, *Drug Deliv.* 25 (2018) 1103–1116.
- [77] R.R. Taylor, Y. Tang, M.V. Gonzalez, P.W. Stratford, A.L. Lewis, Irinotecan drug eluting beads for use in chemoembolization: In vitro and in vivo evaluation of drug release properties, *European Journal of Pharmaceutical Sciences*. 30 (2007) 7–14.
- [78] D.C. Wu, C.M. Ofner, Adsorption and Degradation of Doxorubicin from Aqueous Solution in Polypropylene Containers, *AAPS PharmSciTech*. 14 (2012) 74–77.
- [79] D. Curry, H. Scheller, M. Lu, M. Mkandawire, M.R. Servos, S. Cui, X. Zhang, K.D. Oakes, Prevention of doxorubicin sorptive losses in drug delivery studies using polyethylene glycol, *RSC Adv*. 5 (2015) 25693–25698.

Chapter 6

6 Conclusion and Recommendations

6.1 Summary and Conclusion

The overall objectives of this thesis are to develop multifunctional drug delivery systems for locoregional therapy (Figure 6.1). Nano- and microparticulate systems were prepared using organic or inorganic biomaterials. These delivery systems were characterized in their composition, morphology, drug loading/release and degradation. The results demonstrated sustained drug release capacity and *in vitro* degradability. The summary of each delivery system is presented below.

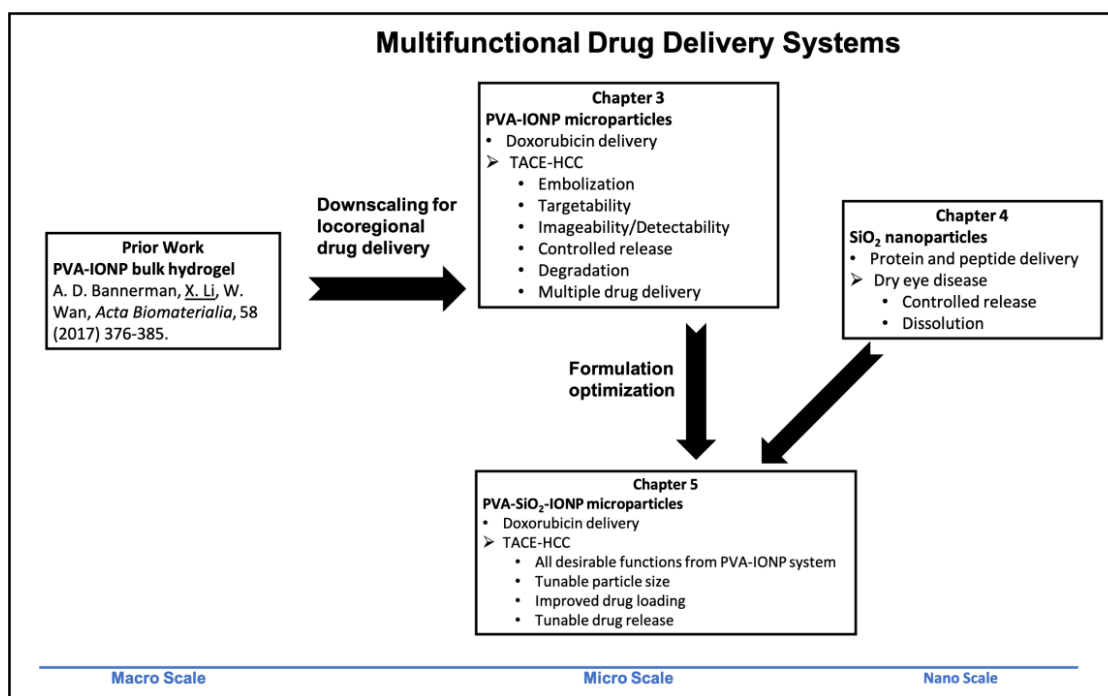

Macro Scale
Micro Scale
Nano Scale

Figure 6.1 Schematic of the research work described in Chapter 3-5.

In Chapter 3, multifunctional PVA-IONP microparticles were developed as DEBs for TACE treatment. The superparamagnetic IONPs were entrapped in the PVA matrix through *in situ* coprecipitation and freezing-thawing cycles. Droplet microfluidics was employed to fabricate microparticles. The resulting beads were in a teardrop shape with a relatively narrow size distribution. PVA-IONP microbeads have demonstrated multiple

functionalities relevant to the application as DEBs, including targetability, detectability, controlled DOX release and degradation. The highlights of this project are:

1. Targetability. PVA-IONP microparticles were superparamagnetic and can be attracted by a permanent magnet.
2. Imageability/Detectability. Microparticles were effective in producing a contrast enhancing effect on T₂-weighted MRI images.
3. DOX loading and release. PVA-IONP microparticles provided a DOX loading of 0.49 ± 0.02 mg/mL. The release was in a sustained manner during the course of one week.
4. Degradability. The degradation of the microbeads was in the form of iron release and PVA matrix disintegration.
5. Co-localization of contrast agent with DOX. This would about a precise location of the carrier and drug in relevance to tumor site.

Chapter 4 described the development of bioactive proteins and peptides delivery system using non-porous SiNPs. The system was first assembled using lysozyme as the model protein. The adsorption kinetics and isotherm were studied to reveal the loading mechanism. Protein release and the dissolution of SiNPs in PBS were investigated. The SiNPs were then loaded with N-94, the peptide derived from a tear glycoprotein, lacritin, that is effective in dry eye treatment. The SiNP system is attractive as a drug delivery formulation for treating dry eye disease.

The highlights of this work are shown below:

1. Protein loading is driven by chemisorption and will form a monolayer on SiNP surface at low protein concentration. As such, it is expected to be a maximum loading capacity determined by the number of binding sites and hindrance effect.
2. SiNPs can provide a controlled release for proteins and peptides for 8 hours.
3. The nanocarriers can protect molecular integrity and biofunctions of the peptides.
4. SiNPs are dissolvable in PBS. The dissolution is time-dependent and results in reduced particle size and a porous structure.
5. N-94 is functionally equipotent to its parent protein, lacritin.
6. SiNPs are non-toxic to cells.

Chapter 5 introduced the development of PVA-SiO₂-IONP system, which gives improved performance over the PVA-IONP microparticles in terms of increased loading capacity and tunable drug release. The multifunctional PVA-SiO₂-IONP beads were in a tadpole shape and developed a paramagnetic response. SiO₂ microparticles participated in the hydrogen bonding with PVA and improved the loading and release capacity of the delivery system. These microparticles are attractive as DEBs for locoregional treatment of diseases. The highlights of this work are listed below:

1. The size of the microparticle could be tuned by varying the flow rates of the continuous and dispersed phase.
2. PVA-SiO₂-IONP microparticles rendered a 61.2% increase in DOX loading capacity compared with the original system.
3. PVA-SiO₂-IONP microparticles can provide a controlled release of DOX for 7 days. The release profile is tunable by varying the drug loading.
4. DOX release is dependent on the pH and ionic concentration of the release media. A more acidic pH and higher ion concentration would contribute to a faster and greater drug release.

6.2 Significance of Research

This thesis explored the development of nanoscopic and microscopic drug delivery systems. In Chapter 3 and Chapter 5, chemical (e.g., coprecipitation and sol-gel process) and physical routes (e.g., freezing-thawing cycling) were employed to prepare multifunctional drug carriers. Material processing techniques such as droplet microfluidic demonstrated efficiency and stability in producing hydrogel microparticles. The resulting particles exhibited the integration of several desirable properties, including targetability, visibility/detectability, co-localization of contrast agent with drug, sustained drug release and degradation. The robust and scalable microfluidic fabrication of microparticles would aid the success of clinical translation. The physical crosslinking method allows the stabilization of the hydrogel without using toxic crosslinkers, which would make the resulting system advantageous for *in vivo* applications. The resulting multifunctional delivery platform holds the promise to address the limitations of current DEBs, which would ultimately lead to improved efficacy and safety of TACE treatments.

In Chapter 4, a simple drug nanocarrier composed of SiNPs was developed using Stöber synthesis. The protein adsorption kinetics and isotherms were studied to reveal the loading mechanism. The adsorption pattern is helpful in determining, altering the loading and regulating the protein release. The SiNPs are effective in protecting molecular integrity and biofunction of protein therapeutics during release. The SiNP-protein system is a proof-of-concept design towards many applications for ocular drug delivery.

In summary, my Ph.D. work involved significant research work in the design, synthesis, and processing of multifunctional materials for drug delivery applications. The choice of materials and fabrication techniques would guide future work in developing novel delivery systems. The delivery formulations we developed could be used as drug carriers alone. The primary application would be in TACE-HCC treatment. Other potential applications include TACE therapy for colorectal liver metastases and hyperthermia treatment for brain tumor. The application could be further expanded if they were combined with other delivery platforms, such as microfibers, scaffolds and contact lens to serve as drug-eluting medical devices.

6.3 Future Studies

Based on the length scale of the delivery system we designed, this thesis could be aggregated into two main projects. Chapter 3 and Chapter 5 described the development of multifunctional ‘nano-on-micro’ microparticles. Chapter 4 involved work on the development of silica-based nanocarriers for protein delivery. Future studies will be discussed for Chapter 3 and 5 together, and separately for Chapter 4, due to the similarity of the work.

Development of multifunctional hydrogel microparticles (Chapter 3 and Chapter 5)

The co-flow or three-dimensional (3D) flow-focusing microcapillary devices should be explored to produce the microparticles [1]. This architecture would allow a better sealing than quasi-2D planar devices, which is expected to secure the driving force (i.e., the relative pressure difference between the inlet and outlet of the microfluidic channel) in

robustly delivering the fluids [2]. In addition, a 3D geometry would circumvent the unstable breakup of droplets, as the fluids do not contact the walls [3].

To examine the targetability of the multifunctional ‘nano-on-micro’ microparticles, MR steering could be tested in bifurcated fluidic tubing using a clinical MRI scanner [4]. The distribution of particles should be recorded to evaluate the spatial control of system. Steering ratio and mass loss can be quantified to assess the sensitivity and reliability of this approach.

In the degradation study, additional quantitative and qualitative experiments could be conducted. Size exclusion chromatography (SEC) can be employed to examine the microbeads. Changes in molecular weight and molecular weight distribution could indicate the degradation of PVA [5]. Differential scanning calorimetry (DSC) could be performed to monitor the changes in glass transition temperature during the degradation. Dynamic light scattering (DLS) can be utilized to measure the size reduction caused by the disintegration of the matrix. Moreover, the degradation could be quantified gravimetrically.

Future work should also be dedicated to revealing the biocompatibility and efficacy of the drug eluting microparticles. For biocompatibility study, normal cells (e.g., epithelial cells) could be incubated with drug-free microparticles. Cell apoptosis should be analyzed by flow cytometry. To study the efficacy of the delivery system, cancer cells (e.g., HepG2 cells) could be treated with drug-loaded particles. The antitumor effect of the system against HepG2 cells could be evaluated using a methyl thiazolyl tetrazolium (MTT) assay. Morphological changes of cells in response to the treatments will be microscopically examined to reveal the apoptosis pathway [6].

To explore the full application spectrum of our multifunctional delivery systems, studies on drug release and heating effect could be conducted with the presence of an alternating magnetic field (AMF). This would allow the assessment of their clinical applicability in magnetic-responsive drug release and magnetic hyperthermia cancer therapy [7].

Development of silica nanocarriers for bioactive protein delivery (Chapter 4)

This study demonstrated the feasibility of using SiNPs as protein carriers. Future work should focus on improving the loading capacity and demonstrating the superiority of the drug delivery systems over free drugs. In detail, porous SiNPs could be synthesized to improve the loading capacity. Alternatively, non-porous SiNPs could be functionalized to introduce more surface binding sites. A cell study could be performed to examine the effectiveness of delivery systems. Stressed corneal cells could be treated with free bioactive proteins and SiNP-protein systems separately. A comparative study on cell viability and metabolism should be performed.

6.4 References

- [1] R.K. Shah, H.C. Shum, A.C. Rowat, D. Lee, J.J. Agresti, A.S. Utada, L.Y. Chu, J.W. Kim, A. Fernandez-Nieves, C.J. Martinez, D.A. Weitz, Designer emulsions using microfluidics, *Materials Today*. 11 (2008) 18–27.
- [2] L. Shang, Y. Cheng, Y. Zhao, Emerging Droplet Microfluidics, *Chem. Rev.* 117 (2017) 7964–8040.
- [3] S. Takeuchi, P. Garstecki, D.B. Weibel, G.M. Whitesides, An Axisymmetric Flow-Focusing Microfluidic Device, *Advanced Materials*. 17 (2005) 1067–1072.
- [4] J.-B. Mathieu, S. Martel, Steering of aggregating magnetic microparticles using propulsion gradients coils in an MRI Scanner, *Magn Reson Med*. 63 (2010) 1336–1345.
- [5] S. D'Souza, J.A. Faraj, R. Dorati, P.P. DeLuca, Enhanced Degradation of Lactide-co-Glycolide Polymer with Basic Nucleophilic Drugs, *Advances in Pharmaceutics*. 2015 (2015) e154239.
- [6] K.S. Kim, C.H. Cho, E.K. Park, M.-H. Jung, K.-S. Yoon, H.-K. Park, AFM-Detected Apoptotic Changes in Morphology and Biophysical Property Caused by Paclitaxel in Ishikawa and HeLa Cells, *PLOS ONE*. 7 (2012) e30066.
- [7] M. Häring, J. Schiller, J. Mayr, S. Grijalvo, R. Eritja, D.D. Díaz, Magnetic Gel Composites for Hyperthermia Cancer Therapy, *Gels*. 1 (2015) 135–161.

Appendices

Appendix A: PVA-IONP microbeads size measurement



Equivalent spherical diameter is calculated using the following equation:

$$d = 2\sqrt{A/\pi}$$

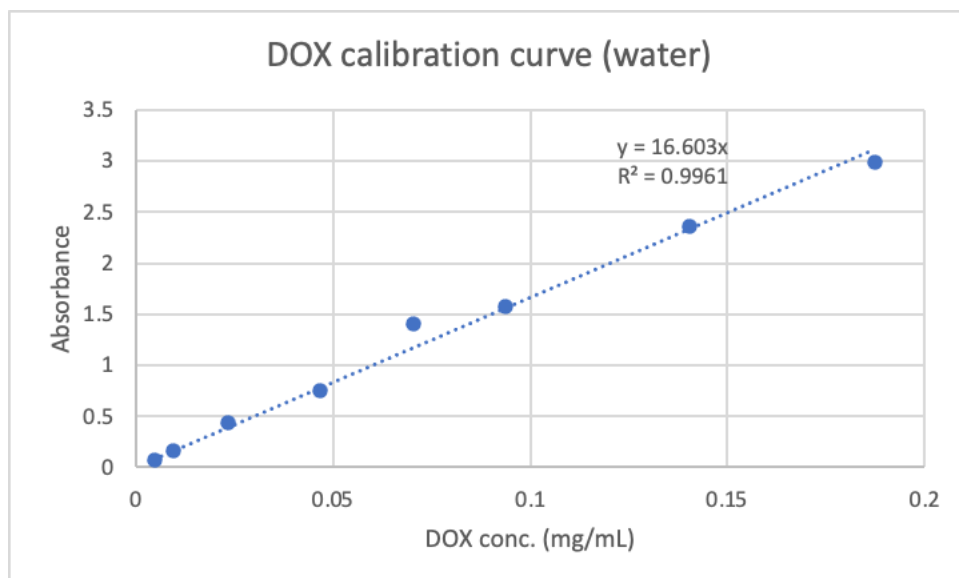
where d is the equivalent spherical diameter, while A is the measured sectional area of a microbead.

Appendix B: Preparation of pH 5.5 phosphate buffer

Solution I: dissolve 13.61 g of potassium dihydrogen phosphate (KH_2PO_4) in distilled water and dilute to 1000 mL.

Solution II: Dissolve 35.81 g of disodium hydrogen phosphate (Na_2HPO_4) in distilled water and dilute to 1000 mL.

Mix 96.4 mL of solution I and 3.6 mL of solution II.

Appendix C: Calibration curve for doxorubicin at 485 nm

Appendix D: Fitting parameters and curves for lysozyme adsorption kinetics and isotherms

Adsorption kinetics:

Pseudo-first order

$$\log_{10}(Q_e - Q_t) = \log_{10}Q_e - k_1 t$$

Pseudo-second order

$$\frac{t}{Q_t} = \frac{1}{k_2 Q_e^2} + \frac{t}{Q_e}$$

Dynamic Model	Pseudo-First Order			Pseudo-Second Order		
	Q _e (mg/g)	k ₁ (h ⁻¹)	R ²	Q _e (mg/g)	k ₂ (g mg ⁻¹ h ⁻¹)	R ²
	17.77	0.016	0.90	34.97	0.012	>0.99

Table S1 Pseudo-first-order, pseudo-second-order parameters for lysozyme adsorption.

Adsorption isotherms:

Langmuir isotherm

$$\frac{C_e}{Q_e} = \frac{1}{Q_m} C_e + \frac{1}{Q_m b}$$

Freundlich isotherm

$$\log_{10} Q_e = \frac{1}{n} \log_{10} C_e + \log_{10} K_F$$

Redlich-Peterson isotherm

$$Q_e = \frac{K_R C_e}{1 + \alpha_R C_e^\beta}$$

θ (K)	Freundlich Isotherm			Langmuir Isotherm			Redlich-Peterson			
	n (mg/g)	K_f	R^2	Q_m (mg/g)	b (L/mg)	R^2	K_R	α^R	β	R^2
294	1.98	1.57	0.88	76.34	0.0026	0.94	1.14	0.31	0.61	0.93

Table S2 Fitting parameters for Freundlich, Langmuir and Redlich-Peterson isotherms.

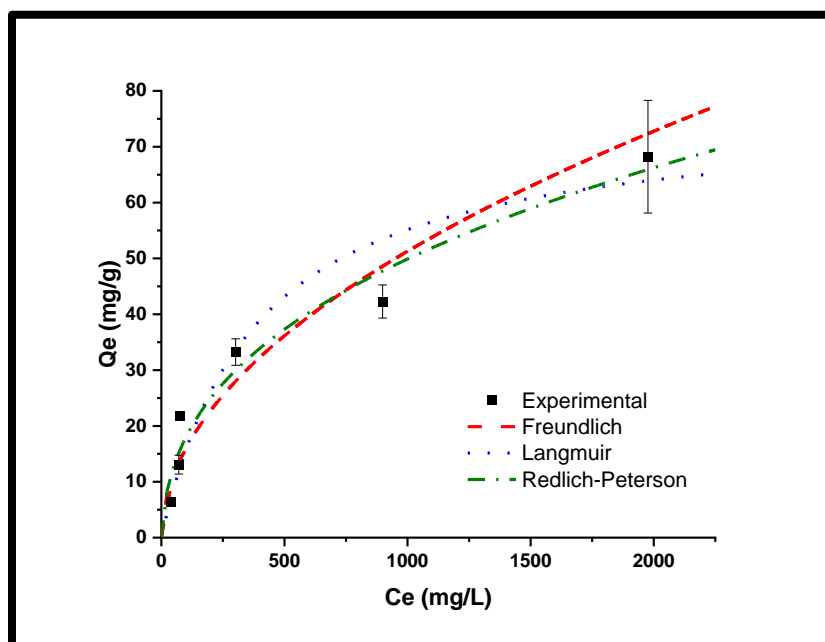


Figure S1 Comparison between the measured and modelled equilibrium isotherm profile.

Appendix E: Copyright permission

Figure 2.1

RightsLink Printable License

<https://s100.copyright.com/App/PrintableLicenseFrame.jsp?publisherID...>

ELSEVIER LICENSE TERMS AND CONDITIONS

Jun 08, 2021

This Agreement between Ms. Xinyi Li ("You") and Elsevier ("Elsevier") consists of your license details and the terms and conditions provided by Elsevier and Copyright Clearance Center.

License Number	5084000738908
License date	Jun 08, 2021
Licensed Content Publisher	Elsevier
Licensed Content Publication	Journal of Controlled Release
Licensed Content Title	Locoregional drug delivery using image-guided intra-arterial drug eluting bead therapy
Licensed Content Author	Andrew L. Lewis,Matthew R. Dreher
Licensed Content Date	Jul 20, 2012
Licensed Content Volume	161
Licensed Content Issue	2
Licensed Content Pages	13
Start Page	338
End Page	350

Curriculum Vitae

Name: Xinyi Li

Post-secondary Education and Degrees: East China University of Science and Technology
Shanghai, China
2011-2015 B.Eng.

The University of Western Ontario
London, Ontario, Canada
2015-2016 M.Eng.

The University of Western Ontario
London, Ontario, Canada
2016-2021 Ph.D.

Honours and Awards: First Prize Poster Award (Canadian Ophthalmological Society)
2018

Trainee Travel Award (CAMBR, Western University)
2019

Western Medical Innovation Fellowship (WORLDiscoveries®, Western University, 2021)

Related Work Experience Teaching Assistant
The University of Western Ontario
2016-2020

Publications:

1. M. Gong, X. Li, and A. Bassi, "Investigation of simultaneous lutein and lipid extraction from wet microalgae using Nile Red as solvatochromic shift probe," *J. Appl. Phycol.*, 31, 1-11, 2018.
2. D. Bannerman, X. Li, and W. Wan, "A 'degradable' poly(vinyl alcohol) iron oxide nanoparticle hydrogel," *Acta Biomater.*, 58, 376–385, 2017.